Author:
Al Nussairi, Alaa

Title:
Characterising the Static and Impact Load Resistance of One-Way RC Slabs Strengthened by NSM CFRP Rods

Characterising the Static and Impact Load Resistance of One-Way RC Slabs Strengthened by NSM CFRP Rods

by

ALAA NAJM ABBOOD Al-NUSSAIRI

Department of Civil Engineering
UNIVERSITY OF BRISTOL

A dissertation submitted to the University of Bristol in accordance with the requirements of the Degree of Doctor of Philosophy in the Faculty of Engineering.

2018

Word account: 44429

ABSTRACT

This study aims to enhance the blast resistance of reinforced concrete slabs which are commonly encountered in modern buildings. The focus is on preventing their collapse by increasing their ductility and energy dissipation by strengthening them with near surface mounted (NSM) carbon fibre reinforced polymer (CFRP) rods.

Laboratory experiments were conducted to study the entire responses of one-way RC slabs with and without NSM CFRP strengthening with different loading rates (quasi-static and impact load). The quasi-static tests showed that strengthening both faces of the slab contributes to increasing the load capacity and ductility of the slab. In addition, the dissipated energy of the control slab was doubled in the strengthened slab. In the impact tests, the dissipated energy enhanced by a factor of 2.1 when only the compression face of the slab was strengthened by 7 CFRP bars. Also, applying the external strengthening technique led to a change in the crack pattern from one opened crack to multiple cracks in the tension face.

Analytical and numerical models were also provided in this study to simulate the static and impact responses of the one-way NSM CFRP RC slabs. The analytical model was developed by modifying the traditional nonlinear layered analysis to incorporate CFRP bars and the various strain rate values. The modification in the nonlinear layered method comprised deriving and including the effect of the crack patterns on the entire response of the slabs, and combining a single-degree-of-freedom (SDOF) method to estimate the maximum response of the slab under blast and impact loads. The commercial software Abaqus was utilized in the numerical analysis. Results from both these models show a good agreement with the experimental results in terms of the entire load-deflection behaviour for both quasi-static and impact tests.

The developed models were used to investigate the effects of the potential relevant factors on the entire response of the NSM CFRP system. The results show that the dissipated energy achieved by strengthening both faces of the slab depends on the ratio of the strengthening in each face, and the optimum dissipated energy was obtained when the CFRP in the tension face was allowed to rupture by increasing the CFRP strengthening ratio in the compression face if the shear resistance is controlled. The results also showed that the enhancing factor of the energy dissipation was almost strain rate independent.

DEDICATION

For the sake of Allah, my master and creator

To the memory of my father

To all members of my family

To all the people in my life

I dedicate this research

ACKNOWLEDGMENTS

My utmost gratitude to Allah, my creator and master for giving me the health and the ability to overcome all the challenges that I endured during my PhD journey.

I would like to express my sincere gratitude to Dr Wendel Sebastian for his valuable support, guidance and advices during his supervision period for the first three years of my study which was continued even after that. Special thanks to my supervisor Dr Jitendra Agarwal for his critical assessing and his valuable reviewing of my thesis. Thanks also go to my co-supervisor Dr. John Macdonald for his help and ideas that led to improve the work.

I also would like to thank the technician staff in the structural laboratory in University of Bristol for their help and assistance during my laboratory work which I really appreciate, especially Peter, Guy and Dave.

Special gratitude and love to my wife Noor for been patient and for her support during my study journey. Thanks to my kids Mustafa and Yasser for their love and smile and for giving me the motivation to complete my PhD study. My thanks also go to others family members for their unconditional support.

Thanks to the ministry of higher education and scientific research in Iraq and the University of Baghdad for their financial support that allows me to fulfill my dream and to obtain my PhD degree at Bristol University.

AUTHOR'S DECLARATION

I declare that the work in this dissertation was carried out in accordance with the requirements of the University's Regulations and Code of Practice for Research Degree Programmes and that it has not been submitted for any other academic award. Except where indicated by specific reference in the text, the work is the candidate's own work. Work done in collaboration with, or with the assistance of, others, is indicated as such. Any views expressed in the dissertation are those of the author.

SIGNED: .....

DATE:.....

TABLE OF CONTENTS

Abstract i

Dedication ii

Acknowledgment iii

Author's Declaration iv

Table of Contents v

List of Figures viii

List of Tables xvi

List of Symbols xvii

1 CHAPTER 1: INTRODUCTION 1

1.1 Background 1

1.2 Aims of the current study 3

1.3 Objectives 4

1.4 Outline of the thesis 4

2 CHAPTER 2: LITERATURE REVIEW 6

2.1 Introduction 6

2.2 Blast events 6

2.2.1 Explosion and Blast Phenomenon 6

2.2.2 Explosive air blast loading on the buildings 7

2.2.3 Response of structures to different types of loads 8

2.2.4 Strain rate effect on the response of structures 9

2.2.5 Prediction of blast pressure 12

2.2.6 Simulating the blast events 13

2.3 Protection techniques for structures against blast loading 14

2.3.1 Externally strengthening by using EB technique 15

2.3.2 Near Surface Mounted (NSM) technique 16

2.4 FRPs materials for strengthening against blast loading 18

2.4.1 Glass fibre reinforced polymer (GFRP) 19

2.4.2 Carbon fibre reinforced polymer (CFRP) composites 27

2.4.3 Fibre reinforced concret (FRC) 34

2.4.4 Aramid fibre reinforcement (ARFR) 36

2.4.5 Polyurea (PU) 38

2.4.6 Sandwich composite panels 40

2.5 Theoretical modeling of the blast response of FRPs composite 42
2.6 Numerical Modelling of blast response of FRPs composite 45
2.7 Summary and discussion 51
3 CHAPTER 3: EXPERIMENTAL PROGRAM 57
3.1 Introduction 57
3.2 Experimental program 57
3.2.1 Description of specimens 57
3.2.2 Material properties 59
3.2.3 Construction and specimen preparation 64
3.3 Instrumentation 69
3.3.1 Strain gauge installation 69
3.4 Test setup 71
3.5 Analysis of the experimental data 73
3.5.1 The quasi-static results 75
3.6 Discussion of the quasi-static test 81
3.6.1 The impact test results 83
3.7 Discussion of the impact test 106
4 CHAPTER 4: ANALYTICAL AND NUMERICAL MODELLING 109
4.1 Introduction 109
4.2 The analytical solution 110
4.2.1 Basic assumptions 110
4.2.2 Constitutive materials modelling 111
4.2.3 Strain rate dependency of the structural materials 116
4.2.4 The relationship between Mid-span Deflection Rate and Curvature Rate 120
4.2.5 Analytical Moment-Curvature Relationship 121
4.2.6 Analytical Load-Mid span Deflection Relationship 122
4.2.7 Effect of the opened cracks 123
4.2.8 Structural response to the impact loading 131
4.3 The numerical analysis 139
4.3.1 Modelling of reinforced concrete member 139
4.3.2 Material constitutive modelling 141
4.3.3 Simulating the applied load 146
4.3.4 Predicting the crack pattern 146
4.4 Summary 147

5 CHAPTER 5: RESULTS AND DISCUSSION 148
5.1 Introduction 148
5.2 Validating the nonlinear analysis procedures in the quasi-static regime 149
5.2.1 The load-deflection behaviour 149
5.2.2 The total and the dissipated energy 150
5.2.3 The crack patterns 154
5.3 Validating the nonlinear solution procedures in the high strain rate regime 161
5.3.1 The impact maximum deflection 161
5.3.2 The Resistance-deflection behaviour 162
5.3.3 The crack patterns 166
5.4 Strength and limitations of the two used procedures 168
5.5 Parametric study 169
5.5.1 Effect of strengthening ratio of CFRP 170
5.5.2 Effect of deflection rate on the total and the dissipated energy 182
5.5.3 Effect of the stiffness of CFRP on the energy dissipation 184
5.5.4 Effect of dimensions of the one-way slab on the energy dissipation 187
5.5.5 Effect of the reinforcing area of steel and CFRP on the energy dissipation 189
5.6 Conclusion 192
6 CHAPTER 6: SUMMARY AND CONCLUSION 194
6.1 Summary 194
6.2 Conclusion 195
6.2.1 Literature review study 195
6.2.2 Physical experiments 196
6.2.3 Analytical and numerical results 197
6.2.4 Parametric study 198
6.3 Limitation of the work 199
6.4 Future work 200
REFERENCES 199
Appendices 211

LIST OF FIGURES

Figure 1-1: Schematic of NSM FRP strengthening system (Zhang et al., 2017). 3
Figure 2-1: Blast wave propagation with distance and typical blast pressure profile (Ngo et al., 2007a)..... 7
Figure 2-2: Blast load on a building (Ngo et al., 2007a)..... 8
Figure 2-3: DIF of concrete and steel under various strain rates (Silva and Lu, 2007)..... 10
Figure 2-4: Stress-strain relationship of concrete and steel under various strain rates (Silva and Lu, 2007)..... 10
Figure 2-5: Strain rate dependency in the stress-strain relationship of glass fibre reinforced polymer GFRP (Langdon et al., 2014). 11
Figure 2-6: Spectrum of the approximated strain rates corresponding to different loading environments (Adhikary et al., 2015). 12
Figure 2-7: Strengthening technique approaches in RC beam; a) EB technique, b) NSM technique..... 15
Figure 2-8: Comparison of Steel and FRPs properties (Ewen, 2005). 19
Figure 2-9: Details of retrofitting method used by Tolba et al (Razaqpur et al., 2007). 20
Figure 2-10: Effect of different retrofitting types; E-glass and Carbone fibre laminates with two (U1) and three (U2) layers (Mosallam and Mosalam, 2003). 22
Figure 2-11: Comparison between computational and experimental results of the study conducted by (Mosalam and Mosallam, 2001). 23
Figure 2-12: Validating the adopted numerical model for the blast load retrofitting and as-built slabs (Mosalam and Mosallam, 2001). 24
Figure 2-13: Retrofitting schemes a) scheme 1 and b) scheme 2 of the strengthened slabs (Guo et al., 2017)..... 25
Figure 2-14: The historical a) central displacement and b) strain of steel of the control slab PB1 (Guo et al., 2017). 26
Figure 2-15: The reflected pressure-time history curves recorded in slab a) PB1 and b) SB3 under different explosive charge weight (Guo et al., 2017). 27

Figure 2-16: Details of retrofitting NSM procedure adopted by Wu et al (Wu et al., 2007). 29
Figure 2-17: Details of the retrofitting method used by Wu et al (Wu et al., 2009). 30
Figure 2-18: Shape of failure and setup of the test conducted by Wu et al (Wu et al., 2009) 31
Figure 2-19: Spalling of concrete due to blast load effect (Tabatabaei et al., 2012) 34
Figure 2-20: Different shapes of steel fibres (wave cut, hoked end, enlarged end and deformed). 35
Figure 2-21: : Polymer reinforced compact reinforced composite column (Riisgaard, 2007). 37
Figure 2-22: Test set up and post-test observation of the strengthened columns (Riisgaard, 2007). 38
Figure 2-23: Comparison of maximum and residual displacement of RC slabs with different strengthening FRP material (CFRP, PU and CPU) compared to the control panel NSC (Ha et al., 2011). 39
Figure 2-24: Procedure of applying the CFRP sheet, the PU and the hybrid CPU on RC panels (Ha et al., 2011). 40
Figure 2-25: pattern of failure of the sandwich panels with different configuration (Gardner and Shukla, 2011). 42
Figure 3-1: Details of the internal and the external reinforcement in the cross-section of the test slabs. 59
Figure 3-2: Concrete compressive test of the cubes. 60
Figure 3-3: Details of the steel reinforcement mesh in the specimens. 61
Figure 3-4: Stress-strain relationship of the steel bars obtained from coupon tension test. 62
Figure 3-5: The measured stress-strain behaviour of CFRP rod under uniaxial tensile stress. 63
Figure 3-6: Formwork for concrete slab specimens 65
Figure 3-7: Process of casting the specimens and the concrete cubes used to define strength of the concrete at the testing day of each slab. 66
Figure 3-8: Processing of applying the NSM CFRP technique. 68

Figure 3-9: The instruments used in the test; a) the data logger system, b) the load cell and c) the LVDT. 70
Figure 3-10: Strain gauge of both a) steel reinforcement and b) concrete that used in the specimens. 70
Figure 3-11: The two rigs adopted to spread the load on the specimens a) airbag and b) whiffletree rigs..... 72
Figure 3-12: Frame and rigs of the impact test..... 73
Figure 3-13: Load-deflection curves for slabs QC1, QC2 and QS1 under quasi-static loading test. 76
Figure 3-14: Stress-strain behaviour of concrete and steel and the crack pattern in the strengthened slab (QC1) under quasi-static test. 78
Figure 3-15: Stress-strain behaviour of concrete and steel and the crack pattern in the strengthened slab (QC2) under quasi-static test. 79
Figure 3-16: Stress-strain behaviour of concrete and steel and the crack pattern in the strengthened slab (QS1) under quasi-static test..... 80
Figure 3-17: Modes of failure in slabs; a) QC1, b) QC2 and QS1. 81
Figure 3-18: Effect of the stiffness of the contact surface on (a) the impulse and (b) the deflection of the slab with the same impact energy applied on slab MC0..... 86
Figure 3-19: History of deflection, impact load and reaction of a) the control (MC1-1) and b) the strengthened (MS1-1) slabs during the first impact blow. 89
Figure 3-20: Different reaction-deflection behaviour (atypical) of slabs MC2 and MS2 under different impact drops with the same impact energy. 90
Figure 3-21: History of deflection, impact load and reaction of a) the control (MC2-1) and b) the strengthened (MS2-1) slabs during the first impact blow. 91
Figure 3-22: The obtained history profiles of the impact force and the mid-span deflection of the control slab (MC) under various heights of dropping mass. 92
Figure 3-23: History of steel and concrete strain in the mid-span location of the control slabs MC1-1 and MC2-1 during the 1st impact drop. 94

Figure 3-24: History of steel and concrete strain in the mid-span location of the strengthened slabs MS1-1 and MS2-1 during the 1st impact drop..... 95
Figure 3-25: History of steel and concrete strain in the mid-span location of the strengthened slabs MS1-2 and MS2-2 during the 2nd impact drop. 96
Figure 3-26: The damage of concrete at: a) the compression and b) the tension face of the control slabs (MC1 &MC2) after the first and the final impact drop test..... 98
Figure 3-27: The damage of concrete at: a) the compression and b) the tension face of the strengthened slabs (MS1 &MS2) after the first and the final impact drop test. 99
Figure 3-28: Impact (P) & Reaction (R) versus deflection (Δ) behaviour of slabs MC and Ms under 1st and 2nd..... 103
Figure 4-1: Details of the layered analysis method for the RC section without FRP strengthening material (Fujikake et al., 2009). 111
Figure 4-2: Stress-strain curves of different type of concrete based on the adopted model. 112
Figure 4-3: Stress-strain behaviour of concrete under compression and tension stresses. 113
Figure 4-4: a) the proposed multi-linear stress-strain model of steel and b) the validation with the experimental results. 115
Figure 4-5: Stress-strain relationship of CFRP bar under direct tensile test: a) Experimental behavior, b) Idealized model 116
Figure 4-6: The dynamic increase factor (DIF) for both steel and concrete (Mutalib and Hao, 2010). 117
Figure 4-7: Dynamic increase factor of concrete in compression and tension based on the adopted CEB model. 119
Figure 4-8: Variation of forces in steel and concrete at different stages of loading in a uniaxial tension test of an RC prism (Wu and Gilbert, 2008). 124
Figure 4-9: Deflection of Beam and curvature of segments with localized and non-localized crack (Shin et al., 2015) 125
Figure 4-10: Strain distribution as measured by BOCDA-based optical fiber sensor (Imai et al., 2010) 126

Figure 4-11: Geometrical factors in the ACI approach for control of flexural crack width (Abou-Zeid et al., 2001)..... 127
Figure 4-12: Model for computing slip length (Carino and Clifton, 1995b)..... 128
Figure 4-13: Effect of the width of the crack on the curvature. 130
Figure 4-14: General load function of the dynamic applied load.(Biggs and Biggs, 1964)..... 133
Figure 4-15: Maximum response of one-degree elastic systems (undamped) subjected to equilateral triangular load pulse, a) the DLF curve, b) time of the maximum response (Biggs and Biggs, 1964)..... 136
Figure 4-16: Simplified resistance function of an elasto-plastic SDOF system (Biggs and Biggs, 1964). 137
Figure 4-17: Maximum response of elasto-plastic SDOF system to a triangular load (Ngo et al., 2007b). 138
Figure 4-18: Eight node hexahedron brick element (Sangi, 2011, Barros et al., 2006). 140
Figure 4-19: Representation of reinforcement in concrete model (Sangi, 2011). 140
Figure 4-20: The adopted FE model of the RC slab showing concrete, steel and CFRP bars. 141
Figure 4-21: The Modified stress-strain curve of concrete in the CDP model (Abaqus, 2011). 143
Figure 4-22: The relationship between the plastic and the inelastic strain with the consideration of the damage parameter dc (Sinha et al., 1964). 144
Figure 4-23: The typical crack pattern of the slabs based on the average crack spacing. 147
Figure 5-1: Comparison of the analytical and the numerical load-deflection behaviour with the experimental behaviour of the control slab (QC1) 152
Figure 5-2: Validation of the analytical and the numerical load-deflection behaviour with the experimental behaviour of the strengthened slab (QS1) 152
Figure 5-3: Comparison of the a) total and b) dissipated energy of each slab (QC1 & QS1) obtained from each procedure. 154
Figure 5-4: The observed Crack patterns in the tension face under quasi-static load for slabs QC1 and QS1. 155

Figure 5-5: Comparison between the analytically predicted width of the four sequent cracks at each slab (QC1 &QS1) at the ultimate state of the analytical method. 156
Figure 5-6: The numerical plastic strain distribution at the ultimate state at the bottom face of slab (a) QC1 and (b) QS1 157
Figure 5-7 The predicted strain distribution of a) concrete and b) steel along half of the span length of slab (QC1) under quasi-static load at the ultimate state. 158
Figure 5-8: The predicted strain distribution of a) concrete and b) steel along half of the span length of slab (QS1) under quasi-static load at the ultimate state. 159
Figure 5-9: Comparison between the a) analytical and b) the numerical predicted steel strain distribution along half of the span of the control QC1 and the strengthened slab QS1 under static load. 160
Figure 5-10: Validation of the analytical and the numerical maximum response with the experimental results under different impact load magnitudes for slab MC2 and MS2. 164
Figure 5-11: The predicted analytical load-deflection response of the control slab (MC2) under different strain rate values. 165
Figure 5-12: Comparison between the predicted reaction-deflection behaviour with the recorded behaviour of slab MC2 165
Figure 5-13: The analytical width of the four consequent cracks at the ultimate state of slabs MC and MS under rapid loading..... 166
Figure 5-14: The actual crack pattern which observed at the ultimate state of the impact test of each slab (MC2 and MS2). 167
Figure 5-15: The numerical crack pattern of slab MC2 and MS2 at the ultimate state of the impact analysis. 167
Figure 5-16: The compression strain at the top fibre of concrete at the mid-span section at the ultimate state of case MS2. 168
Figure 5-17: The analytical load-deflection response of the slab under different strengthening ratio in the compression face only with no CFRP bars in the tension face. 175
Figure 5-18: The analytical load-deflection response of the slab under different strengthening ratio of CFRP in the tension face only. 175

Figure 5-19: The analytical load-deflection response of the slab under different compression strengthening ratio with 3 CFRP bars in the tension face..... 176
Figure 5-20: The analytical load-deflection response of the slab under different compression strengthening ratio with 5 CFRP bars in the tension face..... 176
Figure 5-21: The analytical load-deflection response of the slab under different compression strengthening ratio with 7 CFRP bars in the tension face..... 177
Figure 5-22: Comparison between the analytical and the numerical Reaction-deflection behaviour of case S(0,0) which is used to calculate the energy. 179
Figure 5-23: Comparison between the analytical and the numerical Reaction-deflection behaviour of case S(0,7) which is used to calculate the energy. 179
Figure 5-24: The predicted ultimate deflection value at each case study obtained from the analytical and the numerical procedures. 180
Figure 5-25: The predicted ultimate Load at each case study obtained from the analytical and the numerical procedures..... 180
Figure 5-26: The total and the dissipated energy of different cases with different number of CFRP bars obtained from the analytical and the numerical procedures..... 181
Figure 5-27: The load-deflection behaviour of slab S(0,7) for different deflection rate values where t_m refers to the time of the maximum deflection. 183
Figure 5-28: The total and the dissipated energy of slab S(0,7) for different deflection rate value..... 185
Figure 5-29: The relationship between the normalized total and dissipated energy (to the quasi-static state) and the deflection rate value of slab S(0,7)..... 185
Figure 5-30: Effect of the modulus of the elasticity of the CFRP on: a) the amount and b) the enhancing factor of the dissipated energy of the slab by using different compression strengthening ratio. 186

Figure 5-31: The amount of (a) the energy dissipation and (b) its enhancing factor of the strengthened slab S(0,7) compared to the control slab S(0,0) for different values of thickness and shear length. 188
Figure 5-32: The amount and the enhancing factor of the energy dissipated of the strengthened slab with different steel and CFRP reinforcing area. 190
Figure 5-33: The amount and the enhancing factor of the energy dissipated of the strengthened slab with different ratio of CFRP to steel reinforcing. 191

LIST OF TABLES

Table 2-1: The measured peak central displacement and its corresponding time (Guo et al., 2017). 27
Table 3-1: Scheme of the strengthening in each specimen. 58
Table 3-2: Proportions of constituent materials in the concrete mixture. 60
Table 3-3: Mechanical properties of the structural materials. 64
Table 3-4: Results of the quasi-static tests. 75
Table 3-5: Results of effect of thickness of the rubber pad on the load and deflection behaviour. 85
Table 3-6: Crack patterns and failure modes of the specimens in the impact tests. 101
Table 3-7: Results of the total and dissipated energy of both the control (MC1) and the strengthened (MS1) slabs based on both the impact and the reaction forces. 104
Table 4-1: Default parameter of CDP model under compound stress (Kmiecik and Kamiński, 2011) 142
Table 5-1: The experimental and the predicted results of the tested slabs QC1 and QS1 153
Table 5-2: the experimental and the predicted maximum deflection Ym and the corresponding time t_m. 163
Table 5-3: Comparison between the measured and the predicted maximum response of the control slab (MC2) under different impact load values. 164
Table 5-4: The analytical results of different cases study with different strengthening ratio of NSM CFRP bars in both faces. 174
Table 5-5: The numerical results of different cases study with different strengthening ratio of NSM CFRP bars in both faces. 178

LIST OF SYMBOLS

Z	Scaled distance of the explosion event
R	Distance from the explosive charge to the target
W	Weight of the explosive charge
$p(t)$	The time dependent load function
t_d	Duration of the transient load
fc'	Compression strength of concrete
F_m	Peak force of the transient impulse
y_m	Yielding dynamic displacement response
y_e	Ultimate dynamic displacement response
R_u	Maximum elastic dynamic strength of the member
Δ_{max}	Maximum impact response of the specimen
t_m	Time of the maximum impact response of the specimen
W_{cr}	Width of the crack
Pu	Ultimate strength
Pu	Yielding strength
ε_c	Strain of concrete
ε_s	Strain of steel
$\dot{\varepsilon}$	Strain rate in the range Of $3x10^{-6}$ To 300 S^{-1}
ε'_c	Strain rate in the concrete
ε'_s	Strain rate in the steel
$\dot{\varepsilon}_{avr}$	The average strain rate
$\dot{\varepsilon}_{max}$	The maximum strain rate (the peak value)
Δ_y	Yielding deflection
Δ_u	Ultimate deflection
μ	Ductility factor
E_t	Total absorbed energy
E_d	Dissipated energy
A-CFRP	The total area of the carbon fibre reinforced bars
As	The total area of the main steel bars
t	Thickness of the concrete slab
σ_c	Compressive stress in concrete
Eo	Young modulus of concrete

f_{sy}	The yield strength of steel
f_{su}	The ultimate strength of steel
f_{cd}	Dynamic compression strength at any strain rate
f_{cs}	Static compression strength at $\dot{\varepsilon}_s$
$\dot{\varepsilon}_s$	Static Strain Rate ($30x10^{-6}$ S^{-1})
f_{td}	The dynamic tensile strength of concrete at any strain rate value
f_{ts}	The static tensile strength of concrete at any strain rate
$\sigma_{c.i}$	Stress acting on the individual concrete layer (i)
nL	Number of concrete layers over the cross-section
I	Moment of inertia of the section
m	Number of the reinforcement layers over the cross-section
$M(x)$	Moment at any distance along the span length
w	Factor of the uniformly distributed load
$\varepsilon_{c.x}$	Strain in the top fiber of concrete at distance x from the support
$\varepsilon_{c.m}$	Strain in the top fiber of concrete at the mid-span section (l/2)
L	The shear length of the slab (mm)
x	Distance from the element to the support (mm)
$\dot{\varepsilon}_{c,x}$	Strain rate of the top fibre of concrete at each element.
$\dot{\varepsilon}_{c,m}$	Strain rate of the top fibre of concrete at mid-span.
$\varepsilon_{cm(\max)}$	Strain of concrete at crushing
$\dot{\emptyset}_{mid}$	Average curvature rate at mid-span.
β	Ratio of the distance between the neutral axis and tension face to the distance between the neutral axis and reinforcing steel.
d_c	Thickness of cover from the extreme tension fibre to the closest bar
A	Area of concrete symmetric with reinforcing steel divided by number of bars (sq. In)
Ac_{ef}	Equivalent to a in the ACI approach
$l_{s,\max}$	The maximum distance between cracks.
$l_{s,avr}$	The average distance between cracks.
$\rho_{s,ef}$ =	Area of steel divided by effective area of concrete in tension (As/Ac_{ef}).
θ_{SG1}	The curvature at any segment of element along the span
dx	Length of the segment along the span
Mf	Magnifying factor due to the opened crack

$\theta_{SG1(cr)}$	Theta in segment 2 including the width of the crack.
R_c	Curvature length along segment at the n.a line.
K_n	Curvature at node n along the span length
K	Stiffness of the member
ω	Natural frequency of the element
T	Natural periodic time

CHAPTER 1: INTRODUCTION

1.1 Background

Over the last few decades, numerous explosion events due to military or terrorist activities have happened over the entire world. Structures in urban areas like government and civilian buildings, such as military camps, airports, historical and strategic building, bridges, parliaments, dams and official buildings, have been targeted to inflict damage and casualties. Oklahoma City (1995), Word Trade Centre in New York City (2001) (Musselman, 2007)UN headquarters in Iraq (2003) are some examples of the massive damage to the buildings and the loss of civilian lives resulting from such events. Normally conventional buildings are incapable to resist out-of-plane loads and such events have brought the topic of strengthening important buildings against the blast load to the forefront.

This goal can be achieved by increasing their strength, ductility or energy absorption. In some cases, especially in residential buildings or shelters, enhancing the ductility and the energy dissipation of the elements may not have any substitute for the safety of the occupants.

Whilst many techniques have been introduced to achieve the above demand, the cost and the feasibility of any implementation method should also be considered. Increasing the stand-off distance by using fences or barrels, enlarging the mass of the strengthened elements (Buchan and Chen, 2007), using a capture system to hold the fragments of the failed elements from targeting the occupants and other elements following the blast wave by using cables, fabrics or thin gauge steel sheets (Ha et al., 2011), installing sacrificial panels on the façade of the building to mitigate the magnitude of the blast pressure (Su and McConnell, 2013) and externally strengthening the element by utilizing stiff or ductile materials are some of the conventional methods used for this purpose. Steel with different shapes (plate and bar) used to be the conventional material to improve the blast resistance of structures. Recently, with the invention of FRP materials, steel is being replaced with new stiff and lightweight FRP materials as an external retrofitting material.

FRPs are accepted to be utilized to enhance the physical properties of the structures by improving their strength, stiffness and ductility or energy absorption capacity (Sayed-Ahmed et al., 2009, Teng et al., 2003, Pichandi et al., 2013). The high strength to weight and corrosion-free behaviour of the FRPs make them competitive to be considered as effective retrofitting materials.

However, limited studies have been conducted on using FRPs (for all forms and approaches)to enhance the blast resistance of concrete structures due to the expensive experimental works and the security issues related to blast load tests. Majority of the reviewed studies have focused on enhancing the bearing capacity of the strengthened elements by externally bonding CFRP strips (EB) on their tension face by using epoxy resin which gave good enhancing factors in terms of the short-term bearing capacity. But this strengthening technique has many drawbacks such as the low resistance to external environmental factors and vandalism of both the CFRP strips and the epoxy resin, the premature debonding of the CFRP strips, and the high cost of both the materials and the installation process. In addition to that, this technique is found to enhance the bearing capacity of the strengthened elements at the expense of their ductility, which leads to a brittle failure. As a result of these drawbacks and to overcome the above-mentioned problems with the EB system, a new strengthening technique, namely the Near Surface Mounted (NSM) technique has been developed as a promising alternative to the EB FRP method.

The NSM FRP strengthening technique comprises of cutting slits or grooves in the concrete cover of the RC member that needs to be strengthened, then to insert and bond the FRP composite material inside the grooves with an adhesive. Different FRP material with different geometrical shapes can be used in this technique as shown in Figure 1-1. This is considered to have distinct advantages over the externally bonded (EB) FRP techniques, such as less preparation work in the strengthened area (in terms of the amont of work, the strengthened area, the prepared surface, the disruption to the finishing materials and the need to remove the corrosion in the concrete cover), less exposure to the aggressive environment agents or acts of vandalism, and less prone to debonding or delamination of the FRP, especially when small size CFRP bars are used (Coelho et al., 2015).

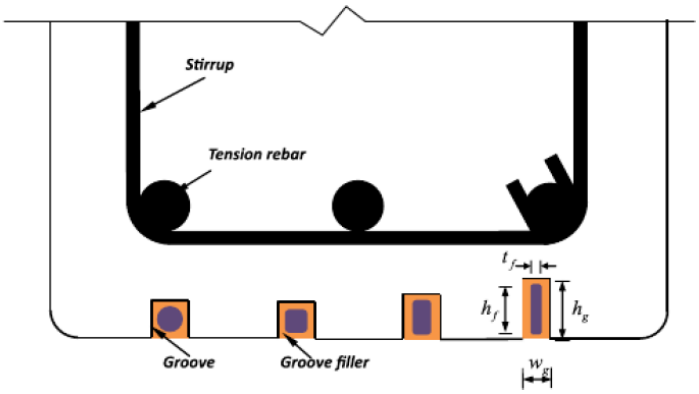

Figure 1-1: Schematic of NSM FRP strengthening system (Zhang et al., 2017).

These advantages of the NSM system have inspired researchers to study and investigate this system in depth in many aspects. The failure mode, bearing capacity, ductility, long term behaviour, and properties of bond have been addressed in their studies. A critical review of the NSM technique has been provided by (De Lorenzis and Teng, 2007). Most of the studies they included deal with strengthening of RC beams in flexure or shear. They reported that significant research has also been done on the debonding process associated with the NSM technique. However, limited research on NSM has been done with respect to RC slabs.

Most of the studies mentioned above have been conducted under quasi-static conditions. Limited research has been conducted to enhance the response of the structures to blast loads (Pichandi et al., 2013). Most of the work to date has focused on increasing the load capacity of new and existing members with very few studies covering other factors such as failure modes, crack patterns, ductility and energy dissipated in the strengthened member, which are known to be critical in preventing collapse of the whole structure.

1.2 Aims of the current study

This research aims to enrich the existing knowledge of the structural blast load resistance by conducting experimental and simulation programs related to the blast load resistance of RC slabs by covering some important aspects that have not been studied in depth before, such as the energy dissipation, failure modes, and the ductility of the NSM CFRP system. The NSM CFRP system as a strengthening method in one-way RC slab against blast and impact loads was considered in this research to investigate and interpret

its behaviour under short transient loadings such as blast and impact loadings. The slabs were selected to be strengthened as they represent the weakest and the most vulnerable part in the structure to the blast loading effect due to their wide surface which subjucts to the blast pressure for all form of the slabs such as as floors, wall panels, cladding panels.

1.3 Objectives

The main objectives of this research are as follows:

1. To investigate the adequacy of the NSM CFRP system to enhance the blast resistance of RC one-way slabs in terms of the bearing capacity, ductility, failure modes and energy dissipation under different strain rate factors.

2. To design and conduct an experimental program to study the behaviour of NSM CFRP strengthened RC slabs.

3. To develop an analytical model to simulate the behaviour of the one-way RC NSM CFRP system under loads with different loading rates.

4. To introduce a numerical model to simulate the NSM CFRP system and to compare with the developed analytical model.

5. To investigate the potential effects of the relevant factors on the system for the optimum performance.

1.4 Outline of the thesis

In Chapter 2, basic concepts about explosions and blast waves are presented. Then a literature review of the blast resistance field is provided. Both the experimental and the nonlinear simulation studies are presented in this chapter. Finally, a summary of the previous work is presented highlighting the areas that need further work.

Chapter 3 presents the methodology and the results of the experimental program that was conducted in this study. One-way RC slabs with and without NSM CFRP strengthening were tested under load with low (quasi-static) and high (impact) loading rates. The measured results are presented and discussed in detail in this chapter.

Chapter 4 presents details of nonlinear simulation models used in this study to simulate the response of the one-way RC slab NSM CFRP system under loads with different loading rates. The procedure of developing the analytical model and the basic assumptions adopted in this model are provided. In addition to the analytical model, a numerical model was also adopted in this study by using the commercial software Abaqus in both the standard and the explicit versions to simulate the quasi-static and dynamic behaviour. Details of the numerical modeling are also presented in this chapter.

Chapter 5 presents the results obtained from both the analytical and the numerical models. These results are compared and validated with the experimental results. After validation of the nonlinear simulation models, the relevant factors that affect the one-way RC slab NSM CFRP system are investigated in this chapter by conducting parametric studies.

Chapter 6 provides a summary and conclusions of the present study. Some suggestions and recommendations for the future research are also indicated.

CHAPTER 2: LITERATURE REVIEW

2.1 Introduction

As this study aims to enrich the existing knowledge of the structural blast load resistance and the protection methods used to enhance the resistance of the existing structural elements to mitigate the blast loading effects, exploring the existing knowledge about the natural effect of the blast loading and the protection methods used up to date in this area is needed. Thus, this chapter aims to present basic information about the explosions and the resulting blast loads and their effect on buildings. Also, the structural response of the buildings to the blast load and the contributing factors are presented. To review the existing knowledge in this area, a review of the studies that have been done so far on enhancing the structural response to the blast loading is presented as well and their results are discussed highlighting their strengths and limitations. In this chapter, the methods and the materials that have been used in the blast strengthening is highlighted with a focus on the pros and cons of each one. Both experimental and numerical studies that were conducted in this area are covered in this chapter. Finally, the areas that have not been covered well and need further research are identified.

2.2 Blast events

2.2.1 Explosion and Blast Phenomenon

An explosion is defined as a sudden and rapid release of a large amount of energy within a limited space. Explosions are categorized into three types: physical, nuclear and chemical. Failure of a cylinder of a compressed gas is an example of the physical explosion. The nuclear explosion is caused by the nuclear energy that is released by the formation of different atomic nuclei. The energy released from rapid oxidation of fuel elements (carbon and hydrogen atoms) is the source for the chemical explosion. This type of explosion is the most common for the terrorist attacks.

As the chemical explosion happens, mass of hot gases (3000-4000^{O}C) is produced under a high pressure of about 300 kilo bar (Ngo et al., 2007b). These gases expand outward of their occupied space. As a result, the surrounding air particles are compressed then pushed out of the explosion point with pressure above the ambient atmosphere called

overpressure. After that, the pressure decays in a regular manner within a very short time (duration time) to reach to the ambient pressure again. This changing of the transferring pressure with time is called a shock wave (blast wave). The maximum overpressure occurs at the front of the blast wave which is called the peak overpressure (incident pressure or side-on pressure). With a distance from the explosion point, the decay of the pressure continues and becomes less than the ambient pressure (negative phase) which then rises to reach to the ambient pressure (see Figure 2-1). During the negative phase, a partial vacuum is initiated with an air sucked in (high suction wind) carrying the debris from the explosion venue to long distances (Ngo et al., 2007a).

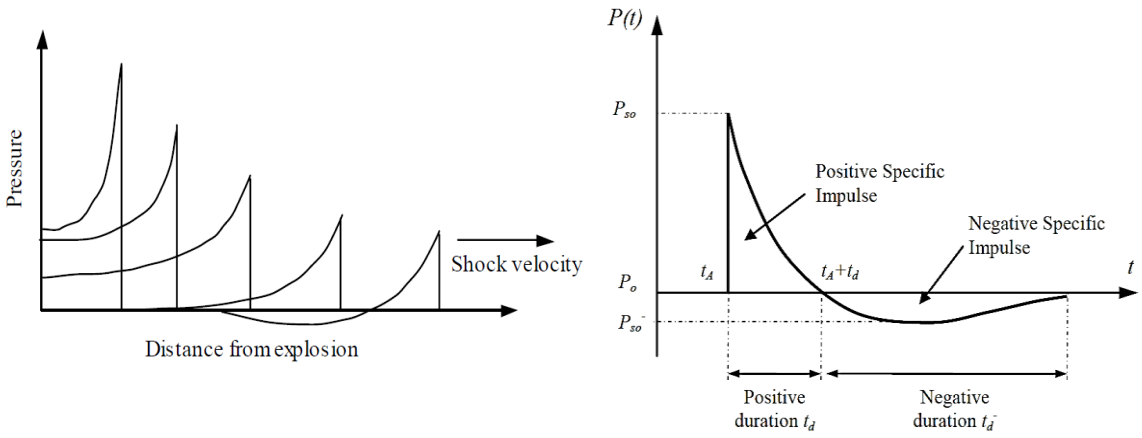

Figure 2-1: Blast wave propagation with distance and typical blast pressure profile (Ngo et al., 2007a)

2.2.2 Explosive air blast loading on the buildings

As the blast wave propagates within the surrounding space, any object or structure in its path will be submitted to its effect. In some cases, the applied incident pressure is amplified by a reflection factor making the pressure more intensive (reflected pressure). This reflection factor depends on the angle between the plane of the impacted surface and the direction of the wave (angle of incident), and the distance to the explosion source (stand-off distance). The reflected factor is typically greatest when the impacted surface is facing the direction of the blast wave, whilst it is zero when the impacted surface is parallel to the direction of the blast wave. Figure 2-2 illustrates the blast loading on a building.

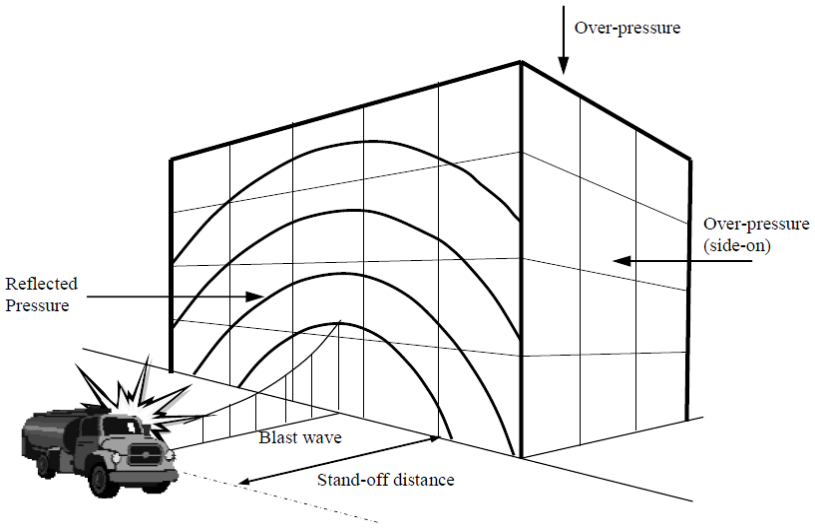

Figure 2-2: Blast load on a building (Ngo et al., 2007a)

With the increase of the stand-off distance, the duration of the positive phase (duration time) increases while the amplitude of the incident pressure decreases. Explosive charge situated very close to a target (close-in distance) impose high incident pressure over a localized region of the target. While further away explosive charge imposes lower incident pressure which distributed uniformly over the entire structure.

When the blast wave impinges structure, if the external elements (walls, columns, etc.) are strong enough to resist the blast effect, the shock penetrate inside through the weak elements such as windows or doors, leading to subjecting the interior elements such as slabs and floors and the occupants to high pressure and shreds of broken glass. While if the external elements were incapable to resist the blast load, collapse or localized failure is the potential scenario with lots of fragments of the crushed concrete or stones which will enter inside the building following the blast wave making further loses in the building and the occupants.

2.2.3 Response of structures to different types of loads

Loads on structures are mostly classified into two categories: static load and dynamic load. The static load is insensitive to the time effect, while the dynamic load is sensitive to the time effect. According to that, the static load may be defined as any load which is applied constantly for relatively long time (compared to the natural period of the member), while dynamic load may be defined as the transient and changeable load that

occurs within a short duration (milliseconds) such as vibration, seismic, impact and blast load. Applying the load within very short time results in a higher loading rate leads to an increase in the deflection rate of the loaded member, and as a result, increasing the strain rate of the structural materials inside the member. Typically, blast and impact loads produce high strain rates due to the high loading rates associated.

Some materials have different mechanical properties under different strain rate values. These are referred to as strain rate dependent materials and the strain rate effect of the dynamic loads, especially with high strain rates, should be considered well in any design procedure.

2.2.4 Strain rate effect on the response of structures

With the strain rate dependent materials, an enhancement in the mechanical properties, such as yielding and ultimate strength, is achieved when they deform with high strain rate values. The enhancing factor of these materials is called the dynamic increase factor (DIF), which is defined as the ratio of the dynamic to the static strength value. For the structural buildings, both concrete and steel are found to be strain rate dependent materials (Silva and Lu, 2007), where the DIF of steel and concrete each is found to be proportional to the strain rate value. The enhancing factor of the concrete compression strength could exceed 4 under high strain rate values as shown in Figure 2-3. Figure 2-4 shows the DIF of both the concrete and the steel with various strain rate values. It shows that a linear function is obtained for the steel and multi-linear function for the compression strength of concrete.

Fibre reinforced composite are essentially strain rate dependent material where the stress-strain relationship varies with the varying of the strain rates (Langdon et al., 2014). And the strain rate dependency depends on the type of the composite material. For GFRP and CFRP, increasing the strain rates induces enhancing the ultimate strength for both the tension and the compression stresses while the modulus of elasticity stays constant (Langdon et al., 2014). However, no significant enhancing in the mechanical properties of the GFRP can be obtained when the strain rates are less than 100 s^{-1} as shown in Figure 2-5. Therefore, the strain rate dependency of the CFRP and GFRP is commonly neglected in most of the numerical analysis studies of the structural blast response (Mutalib and Hao, 2010). This is reasonable for most of the blast structural response

where the strain rates obtained is within this limit. In some cases when higher strain rate is expected (more than 100 s^{-1}) in the elements when they have low natural period and are subjected to intensive blast loadings, the strain rate effect on the FRP need to be considered.

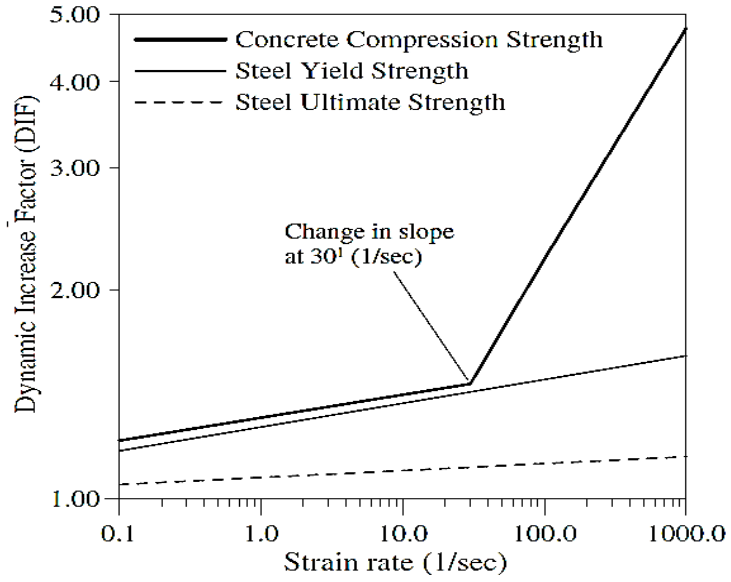

Figure 2-3: DIF of concrete and steel under various strain rates (Silva and Lu, 2007)

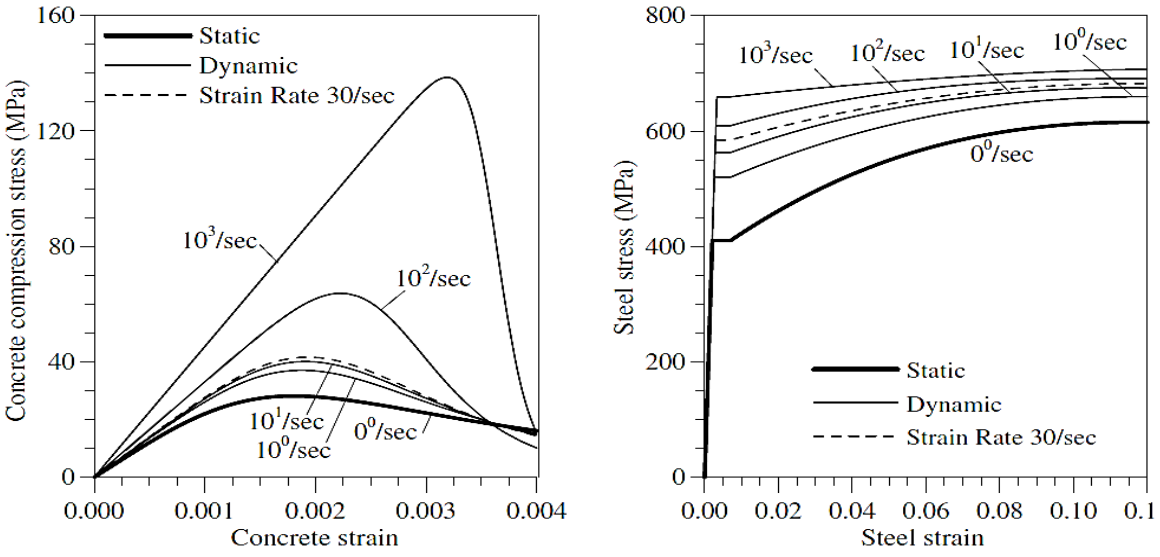

Figure 2-4: Stress-strain relationship of concrete and steel under various strain rates (Silva and Lu, 2007).

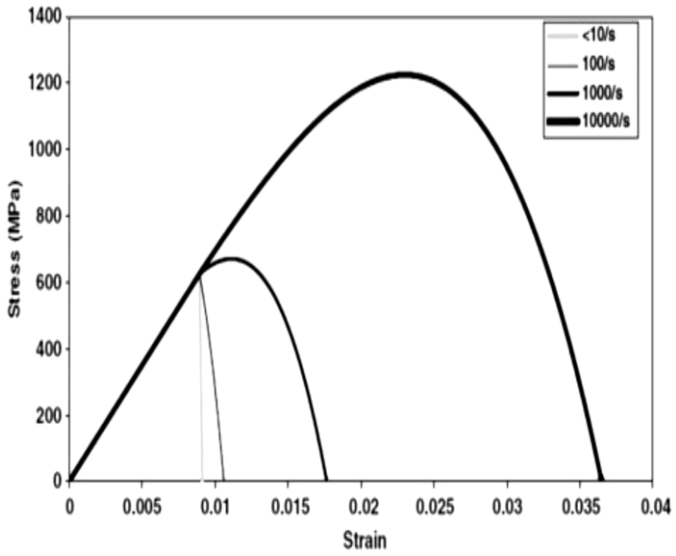

Figure 2-5: Strain rate dependency in the stress-strain relationship of glass fibre reinforced polymer GFRP (Langdon et al., 2014).

Since the response of the structural materials under dynamic load depends on the strain rate value, the dynamic loads can be classified into many regimes based on the strain rate values. Figure 2-6 shows the approximate range of the expected strain rate produced from different loading conditions. Blast and impact loads typically produce high strain rates in the range of $1\text{-}10^4$ s^{-1}, whereas strain rates for static loading have a range of about $10^{-6}\text{-}10^{-5}$ s^{-1} (Ngo et al., 2007a). The structural behaviour including ductility, failure mode, strength and energy absorption is found to be affected by the strain rates (Alhadid et al., 2014). So, investigating each loading regime from low to high strain rate values is needed for a better understanding of the structural behaviour. Much research has been done in the quasi-static regime while less research has focused on the high strain rate regimes such as impact and blast loading due to the destructive nature of such these tests which make it difficult to quantify and measure the obtained results instrumently. A recent review (Pham and Hao, 2016) found that structures behave inconsistently under either impact or blast loads. The result is a complete absence of any design guideline for the protection against blast events. So, more research into the high strain rate regime should be done to enrich available guidance on the blast-resistance topic.

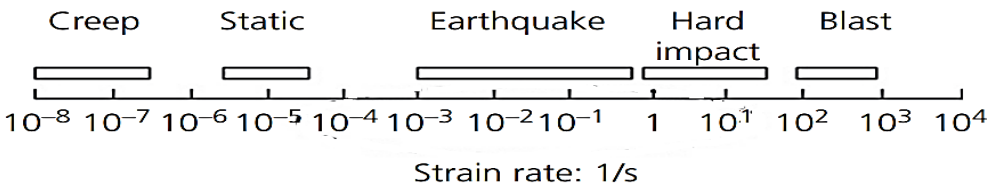

Figure 2-6: Spectrum of the approximated strain rates corresponding to different loading environments (Adhikary et al., 2015).

When a structural reinforced concrete member is subjected to a very short transient load, such as blast and impact load, the reinforced concrete member oscillates producing a periodic displacement-time function with multiple peaks. The first peak of the displacement which occurs in the first phase of the displacement wave has the highest magnitude and the highest effect on the member as the peak deflection reduces in the consequent phases of the oscillation due to the damping effect. So, only the first peak of the displacement is considered in analysing the structural response to the blast and impact loading (Alhadid et al., 2014).

2.2.5 Prediction of blast pressure

To design a structure against blast loading, prediction of the blast pressure is needed. Many studies have been conducted to provide adequate prediction of blast load. The blast pressure on any target is related to the energy of the blast and to the stand-off distance. While the explosive energy is related to the type of explosive charge and its weight. A universal normalized description for the blast effect can be given as scaled distance:

$$Z = \frac{R}{W^{1/3}} \qquad 2\text{-}1$$

where R refers to the stand-off distance (m), and W refers to the TNT equivalent charge weight (kg) of an explosive (Moon, 2009).

Many studies have been conducted to predict the blast load pressure. Theoretical and empirical equations are provided with charts by (Mays, 1995). Other methods such as numerical, empirical and some adopted software are explained well elsewhere (Baker et al., 1981, Remennikov, 2003).

2.2.6 Simulating the blast events

To overcome the difficulties of conducting a real explosion test, non-explosive tests are used to simulate the blast load effect on structures. Dropping weight with low velocity or applying hydraulic pressure with different loading rates are widely used by researchers (Musselman, 2007); (Yoo and Yoon, 2014); (Mosallam and Mosalam, 2003). But the strain rate achieved from such these methods (less than 1 s^{-1}) is not located in the same regime of the blast load (high strain rate of 100 s^{-1} and more as shown in Figure 2-6), whereas the performance of the structure is related to the type of loading which is in turn related to the strain rates. A shock wave tube machine (Hopkinson machine) was used in some studies to simulate the blast load effect (Chock, 1999, Kristoffersen et al., 2018). This machine can apply shock waves with high strain rates (1000 s^{-1} or more), but the magnitude of the shock wave depends on the volume of the tube, which means the size of the test specimen depends on the size of the tube which is small. For all these reasons, research on producing easy methods to simulate the blast load effect is required to give an extra impetus for the blast load protection field. Dropping a mass with high velocity by either increasing the dropping hight or by imposing an initial velocity in the dropping mass, such as by using the INSTRON DYNATUP 9250 hv impact tower also can be used in simulating the blast loading due to the high impact impule with short duration of loading produced by this type of hard impact action. The main difference between the blast and the hard impact loading is in the loading way where the blast loading tends to act in a distributed way compared to concentrated way in case of the impact loading. This difference can be mitigated if a proper loading layout rig is used in the contact surface between the impactor and the impacted bodies.

Due to security and integrity factors, the real blast experimental tests have been conducted in the free space area. This means that the interaction between the blast wave and the surrounding buildings was neglected. This interaction was found to have a significant effect (mitigated or intensified) on the blast wave that applied on the individual element which depends on the interacting in the pressures that are reflected from the surrounding buildings (Draganić and Sigmund, 2012). Till now, it has been difficult to simulate blast load either experimentally or numerically due to the complexity involved. This simplification affects the accuracy of the obtained results making them applicable to

limited structures. Understanding the interaction effect and what it means is important, especially for simulating structures in urban areas.

2.3 Protection techniques for structures against blast loading

Protecting the civil structures from the blast load effect is crucial to reduce the financial or human losses caused by building collapse or from the flying debris. Many strategies, discussed below, can be applied to increase the blast resistance of structures. Cost and ease of implementation are the main factors to select the suitable method of the protection.

Increasing the strength of the structure by extra concrete or reinforcement is an old strategy to reduce the progressive collapse. However, the high cost and duration of installation in addition to the extra weight make it an unfavorable solution (Buchan and Chen, 2007). Surrounding the structures with fences, walls or bollards to keep them away from the explosion point may help to mitigate the blast effect due to reduced pressure. This strategy is not feasible in the urban area where space is not available or is very expensive (Longinow and Alfawakhiri, 2003).

Fabric catcher systems are also introduced to be effective with walls to catch the failure of the in-fill wall units such as masonry, block, glazing or window frames, to reduce the casualties or damage to properties caused by shards and fragments. Cables, thin gauge steel sheet, and fabrics are examples of typical catcher systems (Ha et al., 2011). Increasing ductility and energy absorption capacity of existing walls could be augmented by using steel studs in the connection between the walls and the floor or ceiling since steel behaves in a ductile manner when it fails. These elements and the stud as well should be designed so as not to fail. The disadvantage of this technique is in loss of space and the long time needed for installation (Longinow and Alfawakhiri, 2003).

External bonding of steel plates (EB) to the RC structural elements can improve their mechanical properties, such as the flexural strength or shear strength, based on the strengthened member and positions of the EB plates. Lateral confinement of RC columns by EB steel plates enhances their compressive strength and improves their ductility as well. Corrosion of the steel plates, extra weight, and costly maintenance are the common

problems with this technique (Buchan and Chen, 2007); (Frangou et al., 1995); (Giménez et al., 2009b); (Giménez et al., 2009a); (Su et al., 2010).

In the last decades, fibre reinforced polymer materials (FRP) have progressively replaced the above traditional strengthening methods for existing concrete structures due to their advantages in terms of high strength, corrosion resistance and easy installation (Alkhrdaji et al., 1999, ACI, 2008) ; (Pichandi et al., 2013).

2.3.1 Externally strengthening by using EB technique

FRPs have been used as an external reinforcing material in fabric or laminate form to be bonded to the surface of the original concrete structure using two-part epoxy adhesives (see Figure 2-7). Many studies have been produced for this type of strengthening technique for different structural components (Sebastian, 2001, Lee et al., 2008, Mukhopadhyaya and Swamy, 2001, Foret and Limam, 2008, Shahawy et al., 1996). Although this method is highly competitive against the conventional methods, it does have some drawbacks such as low resistance at high or low temperatures (Pantuso et al., 2000) and low resistance to damage caused by accidents or vandalism.

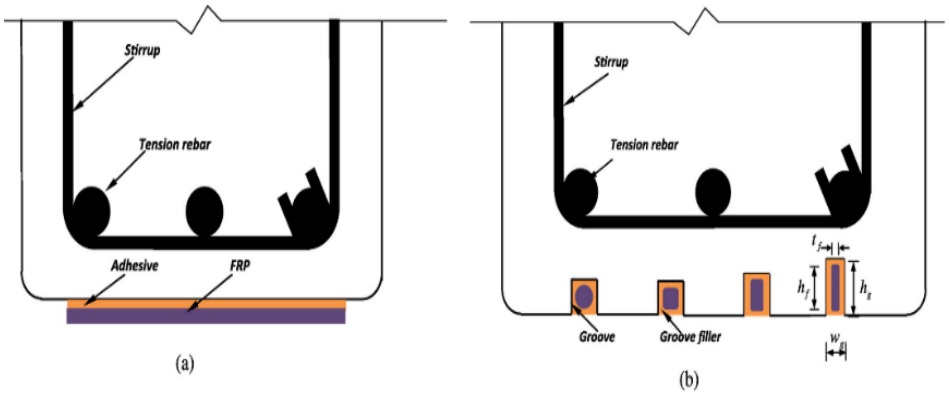

Figure 2-7: Strengthening technique approaches in RC beam; a) EB technique, b) NSM technique.

Also, an intensive and time-consuming pre-treatment process is needed to prepare the surface for bonding. In addition, researchers have reported that the bond integrity over the interface area has a significant impact on the overall performance of the strengthened structure and debonding of the laminates is connected major issue with this technique (Limam et al., 2003, Rabinovitch and Frostig, 2002).It has also been reported that even

after implementing a proper bonding process debonding of the EB reinforcement still occurs through a thin or thick layer of the cover concrete due to the low tensile strength of concrete (Bakis et al., 2002) or due to the propagation of flexural cracks (Sebastian, 2001).

(David and Neuner, 2001) have studied the influence of the environment in the long term on the externally bonded glass fibre reinforced polymer EB GFRP system and they reported a reduction in the tensile strength of the E-glass externally bonded system under high humidity and temperature with time-based on the durability of the epoxy resin, where the reduction in the durability of the epoxy resin leads to reduce the bonding properties provided by the resin with the time and as a result mitigating the efficiency of the EB CFRP system.

To overcome these drawbacks with the EB system, a new strengthening technique namely the Near Surface Mounted (NSM) technique has been developed (De Lorenzis and Teng, 2007); (Coelho et al., 2015). This is considered to have distinct advantages over EB FRP techniques (Alkhrdaji and Nanni, 1999).

2.3.2 Near Surface Mounted (NSM) technique

In the NSM technique, reinforcing FRP rods or strips are bonded into grooves cut into the cover concrete. This is found to be effective in enhancing the anchorage capability of FRP and in mitigating the environmental effects on the strengthening system. The NSM approach was firstly introduced in 1950 for strengthening RC bridges in Sweden by using steel rods and cement mortar (Asplund, 1949). But, due to the low corrosion-resistance of the steel and the mortar it became outdated. Later on, the NSM technique has received renewed attention with the entry of FRP materials due to their high corrosion resistance (Alkhrdaji et al., 1999). High-performance FRP rods and epoxy resin have replaced the steel rods and cement mortar. Since external bonding of the CFRP is found to be sensitive to the environment conditions (David and Neuner, 2001), the NSM system is highlighted as a solution to mitigate the environmental impacts by taking the CFRP system away from the ambient exposure.

To assess the effectiveness of the NSM technique, Barros et al (Barros et al., 2006) have carried out static tests on RC columns, RC beams and masonry panels by using NSM

CFRP rods. Their results showed that the NSM technique is very effective in terms of increasing flexural resistance. The use of cement mortar as a groove filler in the NSM approach was explored by (Täljsten et al., 2003). The results identified limitations of cement mortar as a groove material due to problems with bonding properties.

(Hosseini et al., 2014) investigated the efficiency of strengthening RC slabs by using prestressed NSM CFRP laminates. In this study, the laminates were placed in grooves cut into the concrete cover of the tension zone with different prestressing levels, namely 0%, 20% and 40% of the maximum CFRP tensile strength. It was found that relative to 0% prestressing, 40% prestressing increased the service and ultimate loads by 119% and 152% respectively.

Many studies have been carried out to compare the overall structural ductility achieved between the EB and NSM approaches after strengthening the negative moment zone of continuous members. (Liu et al., 2006) reported that more ductility is achievable with the NSM approach due to the slipping of the FRP rods, compared to the EB system where the premature debonding of FRP plates leads to the common brittle failure mode.

A critical review of the NSM technique has been provided by (De Lorenzis and Teng, 2007). Most of the studies they included deal with strengthening of RC beams in flexure or shear. They reported that significant research has also been done on the debonding process associated with the NSM technique. However, limited research on NSM has been done with respect to RC slabs. There is an important distinction between the two i.e., unlike beams one-way slabs do not contain embedded shear links, which can render them more prone to the possibility of shear failure.

In the seismic field, enhancing the moment capacities of RC columns has been investigated by adopting both EB and NSM techniques. Both were found to be effective in increasing column strength against seismic loads (Bournas and Triantafillou, 2008, Seyhan et al., 2015, Kaptan, 2017). Combining both techniques is more effective in terms of the strength and the ductility for columns where confining the member by EB plates can be achieved.

Most of the studies mentioned above have been conducted under quasi-static loading. Limited research has been conducted to enhance the response of the structures

to blast loads (Pichandi et al., 2013). Most of the work to date has focused on increasing the load capacity of new and existing members with very few studies covering other factors such as failure modes, crack patterns, ductility and energy dissipated in the strengthened member which are known to be critical in preventing the collapse of the whole structure.

2.4 FRPs materials for strengthening against blast loading

Different types of FRPs materials are widely used in retrofitting structures against the blast load effect. The properties of the FRP composite depends on the type of the polymer and its proportional volume in the composite. Selection of the polymer is normally connected to the desired cost and the behaviour of the composite. Researchers have considered the following materials and composites in their studies to be implemented in the blast load retrofitting: carbon fibre reinforced polymer, glass fibre reinforced polymer, aramid fibre polymer, polypropylene fibre (PP), steel fibre reinforced polymer, polyuria, textile sandwich composite and hybrids of different types of composites (Buchan and Chen, 2007); (Pichandi et al., 2013). Most of the studies have used GFRP and CFRP, while recent studies have included hybrid materials in terms of the blast load resistance(Ha et al., 2011). However, in most of the conducted studies, the reason for choosing the material or the method for the study was not provided which make it difficult to assess and evaluate the best FRPs material for retrofitting against the blast loading. Figure 2-8 shows the mechanical properties of some polymers compared to steel.

The following sections provide details of various types and forms of fibrous and composite materials used in the blast protection of structures, literature of related study is presented as well.

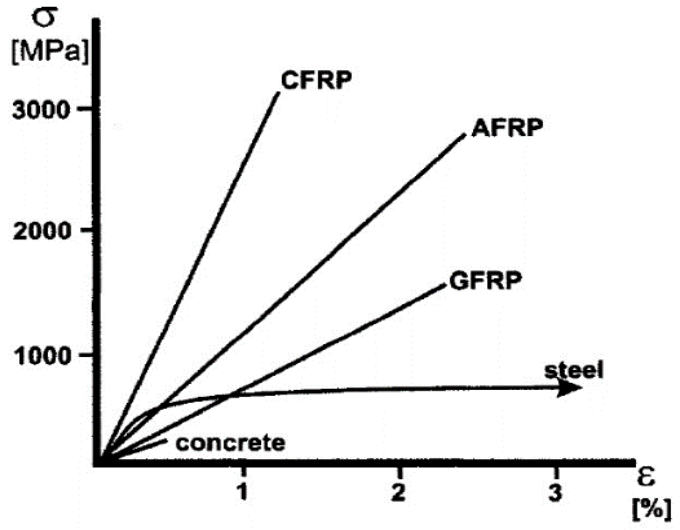

Property	Steel	FRP
Corrosion resistance	low	high
Ultimate tensile strength, σ_{uts}	400-700 MPa	up to 3200 MPa (CFRP)
Tensile elastic modulus, E	206 GPa	varies with V_f (200 GPa obtainable)
Temperature resistance	maintains strength up to several hundred degrees	poor (oxidation above degradation temperature of polymer matrix)
Yield strength, σ_{yp}	400-700 MPa	no yielding apparent - brittle failure at ultimate tensile strength
Ductility (% elongation)	up to 50%	<4.5%

Figure 2-8: Comparison of Steel and FRPs properties (Ewen, 2005).

2.4.1 Glass fibre reinforced polymer (GFRP)

GFRP composite is used in the strengthening of structures to improve their resistance to out of plane loadings such as impact and blast loads. Members like walls, beams, slabs, and columns have been retrofitted with this material. There are different types of glass fibre such as S-glass, E-glass, R-glass, and C-glass. E-Glass and S-glass are found to be suitable for fabricating reinforcement. Although S-glass has higher ultimate strength and stiffness, E-glass outweighs it in terms of the cost and stability under high temperature (Benmokrane et al., 1995). With epoxy resin, many shapes of glass fibre reinforced polymer components are made such as strips, rods, rebar and sandwich panels. The stiffness and strength of the FRP come from the fibres, while the resin protects the

fibres from mechanical abrasion and weathering, while also performing the important function of distributing loads between fibres.

The validity of using GFRPs as retrofitting materials for blast load resistance has been studied by few researchers. (Razaqpur et al., 2007) studied the blast load performance of RC slabs retrofitted by GFRP strips. Eight (1000 x 1000 x 70 mm) panels were tested under real blast load. Five of them left without external strengthening to be used as a reference slabs while the remaining four were strengthened on both faces with two layers on each face in orthogonal directions as shown in Figure 2-9 . The strips were made of E-glass in the main direction with a small amount of aramid in the other direction. All the panels were subjected to explosions with charge weight of 22.4 kg and 33.4 kg of ANFO with a standoff distance of 3 m.

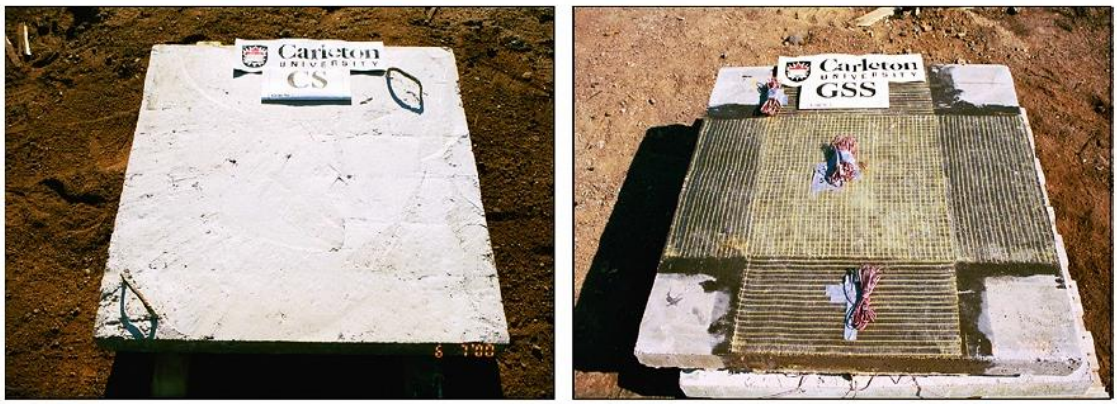

Typical test panels: (a) Control specimen; (b) retrofitted specimen.

Figure 2-9: Details of retrofitting method used by Tolba et al (Razaqpur et al., 2007).

The obtained results of this study (Razaqpur et al., 2007) showed that under low explosive charge (22.4 kg) the GFRP composite enhanced the blast resistance of the panels by providing more residual strength when tested statically later. The enhancing factor was about 75%. While under the higher explosive charge (33.4 kg), the results were found to be scattered with no clear trend. The reporters stated that using GFRP for the close-in explosion (i.e. a small scaled distance of about 1 $m/kg^{1/3}$) may not be advantageous. The failure of the strengthened panels was dominated by shear cracks rather than delamination of the composite. The non-delaminated composite was the key factor for the improvement in the residual strength of the panels. Based on the results they

stated the need for more experimental work to assess the effectiveness of the GFRP in mitigating the blast effect.

(Mosallam and Mosalam, 2003) investigated the effect of retrofitting two-way unreinforced concrete slabs (2640 x 2640 x 76 mm) with GFRP and CFRP strips under increasing hydraulic pressure (non-explosive test) with a slow loading rate of 3.45 kPa min^{-1}.Two slabs were retrofitted by bonding two layers of unidirectional CFRP strips in each direction on the tension zone, while three layers of GFRP strips were bonded to the tension zone of another group of the strengthened slabs (equivalent to the two layers of the CFRP since GFRP has lower stiffness compared to CFRP). According to the obtained results (shown in Figure 2-10), both the retrofitted slabs exhibited similar behaviour up to failure. In the case of slab retrofitted by GFRP (E-RET-U1) a sudden drop of load happened due to localized debonding of the GFRP strip, but the load then again increased up to failure. This atypical behaviour was suspected to be a result of poor workmanship or/and material variability leading to a degree of uncertainty. According to the reported failure pattern, crushing of the concrete in the compression zone was the dominant failure mode.

The same researchers analysed their experimental case numerically by using DIANA code (Mosalam and Mosallam, 2001, Mosallam and Mosalam, 2003). A layered shell element of 8 nodes with 5 DOF for each node was used to model the concrete, the steel reinforcement and the FRPs retrofitting strips with independent properties for each layer. As the bonding between the layered was assumed to be perfect, the delamination of the FRPs strips and slip or reinforcement could not be modeled which led to reduced accuracy of the results as a delamination in the FRPs strips occurred in the actual test. Also, the strain rate effect was neglected in this model due to the lack of experimental data.

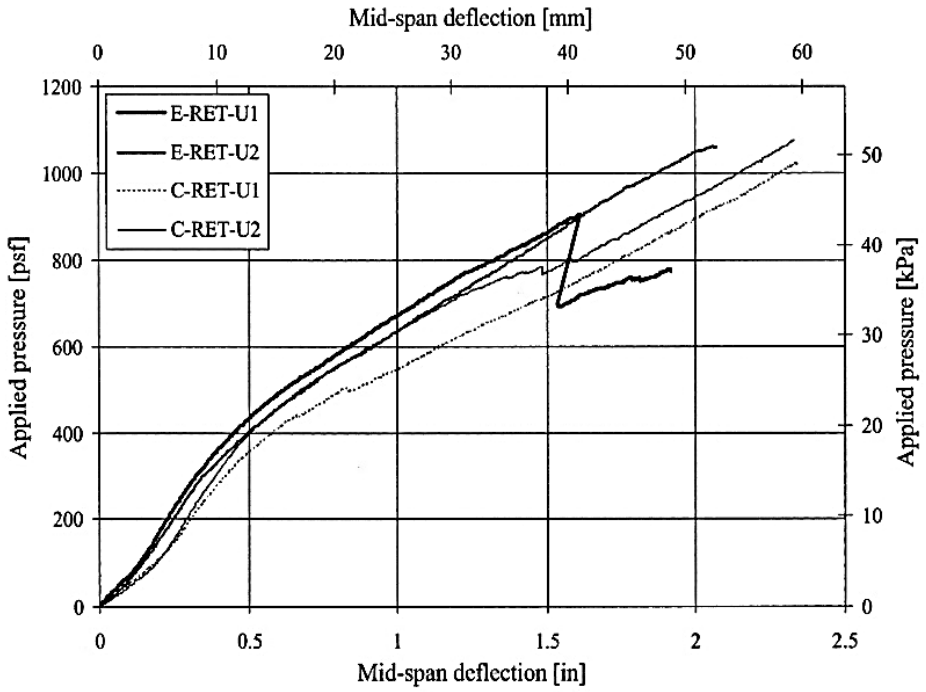

Figure 2-10: Effect of different retrofitting types; E-glass and Carbone fibre laminates with two (U1) and three (U2) layers (Mosallam and Mosalam, 2003).

To study the accuracy of the adopted model, the predicted results were compared with the experimental results for both tests (Mosalam and Mosallam, 2001, Mosallam and Mosalam, 2003). The obtained results indicated that the increase in the loading capacity was about 500% for the unreinforced retrofitted slab and 200% for the reinforced retrofitted slab compared to the as-built slab as shown in Figure 2-11.

To investigate their model for the dynamic analysis validation under blast load effect, the same slab was subjected to hypothetical blast load caused by an explosive charge of 453.44 kg of TNT with an estimated scale distance of ($Z=0.348$ m $kg^{-1/3}$). The impulse and the time duration resulting from this charge were predicted based on approximation charts proposed by (Tedesco et al., 1999). The function of the blast load on the element was idealized as a triangular pulse rather than an exponential decay function, also the negative phase of the load was neglected too. These simplifications lead to decrease the accuracy of the results by an unknown level (Mosalam and Mosallam, 2001, Mosallam and Mosalam, 2003).

The maximum strain rate obtained numerically for this charge was $0.4/s^{-1}$. They argued that this strain rate value is low to make any significant enhancement in the

strength. Thus, they suggested that using strain rate independent model for relatively low strain rate cases is acceptable. The numerical results indicated the validity of retrofitting the slab by FRPs strips. This was indicated by reducing the historical displacement of the retrofitted slab compared to the control slab. Figure 2-12 shows the results. The study also tested retrofitting the slab on both sides. The results showed that using FRPs strips on both sides reduced the maximum displacement of the slab from 37.5 mm for the as-built slab to 16.55 mm for the retrofitted slab (Mosalam and Mosallam, 2001, Mosallam and Mosalam, 2003). This is reasonable since strengthening the tension face of the slab leads to enhance its absorping energy in the early stages of the response (elastic energy) due to the enhancing in the stiffness of the element which as a result lead to absorb more energy under lower displacement magnitude compared to the control slab.

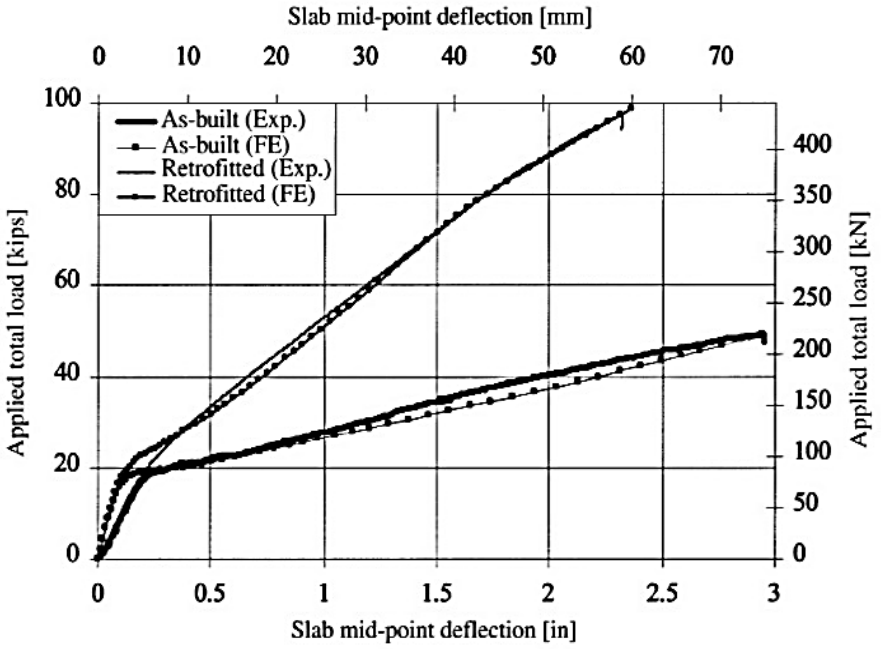

Figure 2-11: Comparison between computational and experimental results of the study conducted by (Mosalam and Mosallam, 2001).

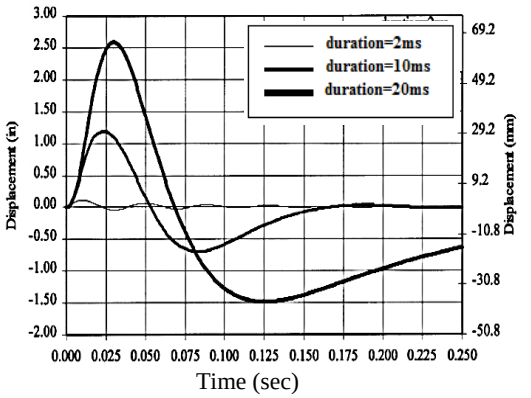

Displacement time histories for the as-build slab at different blast loading duration (t_d).

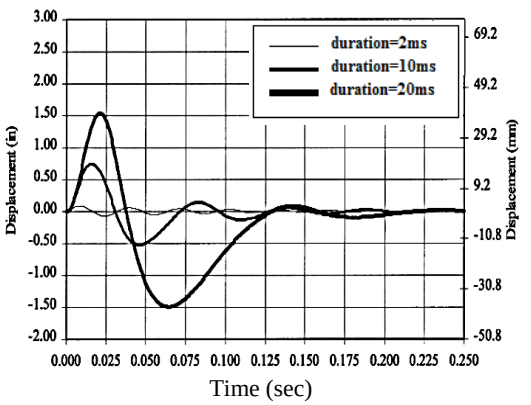

Displacement time histories for the retrofitted (top side) slab at different blast loading duration (t_d).

Figure 2-12: Validating the adopted numerical model for the blast load retrofitting and as-built slabs (Mosalam and Mosallam, 2001).

In a recent study (Guo et al., 2017) retrofitting the bottom face of the two-way RC slab by EB GFRP strips against underground blast has been investigated as shown in Figure 2-13 . In this study, both the explosive charges and the specimens were buried in the soil to simulate the response to underground explosions. The explosive charge used was TNT with charge weight varied from 400 to 1000 gm and located on the top of the slab with a standoff distance of 200 and 500 mm. Two retrofitting schemes were adopted in this study by bonding GFRP strips on the bottom face of the slab. Figure 2-13 shows the adopted retrofitting schemes.

The obtained results reported by (Guo et al., 2017) stated that the strengthened slabs experienced much less damage than the control slabs. Also, a reduction in the width of the cracks on the bottom face of the strengthened slab (the negative moment zone) was observed. There were only minor cracks of a width no more than 1.5 mm in the strengthened slabs as compared to many cracks with a width of 2.5 mm in the control slab. Therefore, they reported the feasibility of externally bonding GFRP strips to mitigate and control the cracking of the concrete. Delamination and/or rupture in some GFRP strips was commonly observed in these tests; the rupture occurred at the mid-span while the observed delamination radiated from centre to the end of the strengthened slab in some strips.

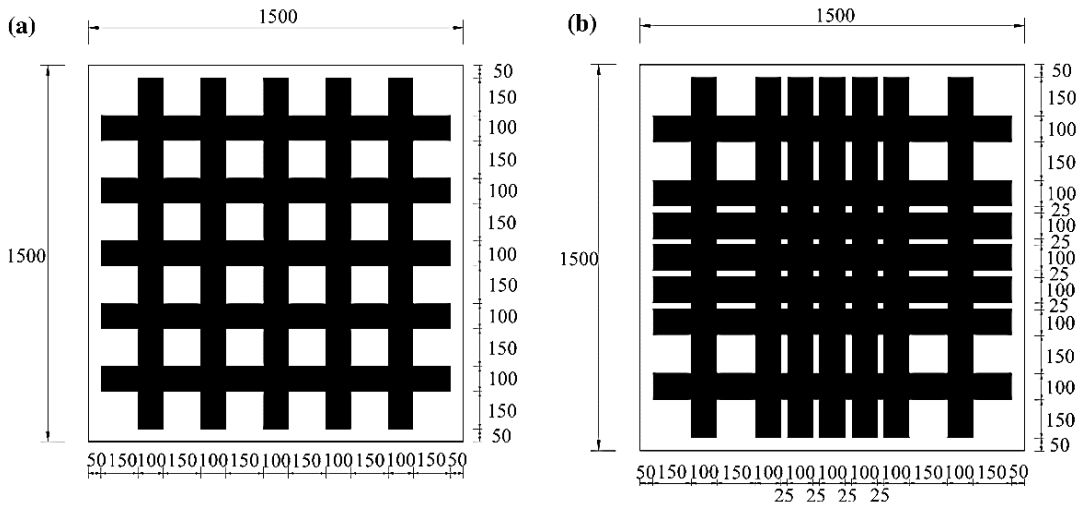

Figure 2-13: Retrofitting schemes a) scheme 1 and b) scheme 2 of the strengthened slabs (Guo et al., 2017).

(Guo et al., 2017) noted that the reflected pressure on the slab takes different function shape based on the weight of explosive charge. A periodic multi-peak load function was recorded for the small charge weights (400 and 600 gm) compared to a periodic single peak load function when 1000 gm of explosive charge weight was used (see Figure 2-15). In terms of the response, the reported results indicated that the maximum displacement of the strengthened slabs was lower than that of the control slab by 32.3%. Also, increasing the GFRP strips led to a more reduction in the maximum displacement where the recorded maximum displacements were 7.9, 5.6 and 4.9 mm for control (PB1), scheme 1 strengthening (SB1, SB2) and scheme 2 strengthening (SB3, SB4) respectively. However, a scattered result was obtained for slab SB1 which experienced displacement higher than the control slab (PB1) when 400 g of TNT was detonated (7.9 and 8.1 mm respectively). In contrast, the maximum displacement declined from 12.4 to 10.2 mm when 600 g of TNT was detonated. This was attributed to the different out of control conditions for each blast test (see Table 2-1). It should be noted that the reinforcement ratio used in SB1 was 0.6% compared to 0.8% was used for all the other slabs. The reported response curves indicate that the displacement function depends on the properties of the slab rather than the shape of the load function. Similar shape of displacement function with different peak values was recorded in the control slab PB1 for different shape of load function. As shown in Figure 2-14a, periods of the response wave

during the first phase and the time at the peak displacement were constant despite the change in the reflected pressure function.

Figure 2-14b shows that the historical strain curve was a harmonic with the historical deflection curve whatever the load function, indicating that the strain rate value which has effect on the mechanical properties of the structural material is affected by the function of the applied load and controlled by the natural frequency of the structural member. In this real blast test, the calculated strain rate value in the critical section of the steel bar was about 0.3 s^{-1} based on Figure 2-14b. This indicates that the strain rates are sensitive to both the loading rate and the geometrical shape of the element where the strain rate value depends on the relative position of the structural materials to the neutral axes in the cross-section. This strain rate value is close to what has been obtained in the current study by conducting impact test as presented in chapter 3.

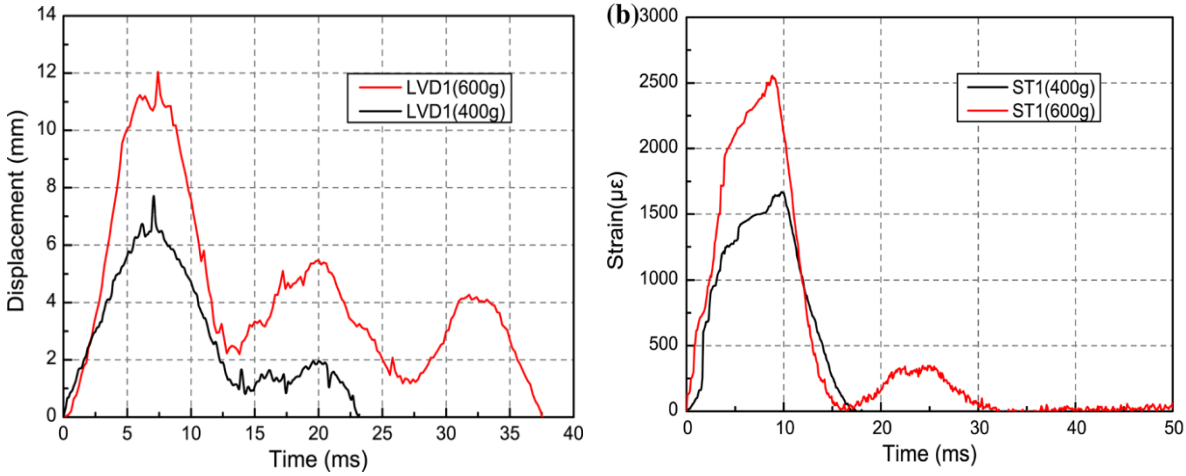

Figure 2-14: The historical a) central displacement and b) strain of steel of the control slab PB1 (Guo et al., 2017).

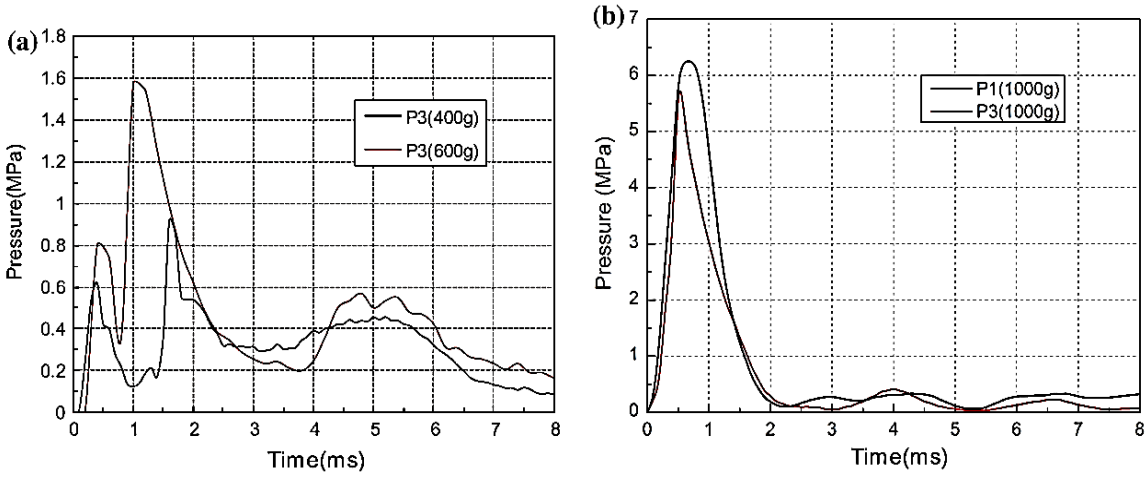

Figure 2-15: The reflected pressure-time history curves recorded in slab a) PB1 and b) SB3 under different explosive charge weight (Guo et al., 2017).

Table 2-1: The measured peak central displacement and its corresponding time (Guo et al., 2017).

Specimen	Displacement measuring point	TNT weight (400 g)		TNT weight (600 g)		TNT weight (1000 g)		TNT weight (1400 g)	
		Peak displacement (mm)	Arrival time (ms)	Peak displacement (mm)	Arrival time (ms)	Peak displacement (mm)	Arrival time (ms)	Peak displacement (mm)	Arrival time (ms)
PB1	LVDT1	7.9	6.8	12.4	7.4				
SB1	LVDT1	8.1	7.0	10.2	7.6				
SB2	LVDT1	5.6	6.2	8.4	7.2				
SB3	LVDT1	4.9	8.4	7.2	8.2	15.7	8.2	21.5	7.0
SB4	LVDT1	–	–	6.9	8.6	16.8	7.3	17.9	7.4

2.4.2 Carbon fibre reinforced polymer (CFRP) composites

Many types of polymer are used in CFRP composites. Epoxy is very often used, but other resins include polyester, nylon, and vinyl ester. CFRP composite is widely used in strengthening the structural elements due to the high mechanical properties it possesses which in turn are attributed to the Carbon fibres. The pure carbon fibre has a tensile strength reaches to 3000 MPa, which is 10 times more than the tensile strength of the mild steel, and stiffness of about 500 GPa. This means only small amount of material is needed in the strengthening to enhance the mechanical properties of the strengthened member, mainly the strength. This also means no extra weight is added or extra space is needed to apply it as compared to other techniques such as using steel or concrete.

CFRP has many advantages which inspired the researchers to consider it as a competitive retrofitting material for the new and the existing buildings to cope with any extra loads. The easy installation process, the high resistance to the alkali attack and to corrosion, and the low cost as compared to the conventional materials are some of the advantages of the CFRP in the retrofitting field. CFRP is found to be strain rate dependent material, which means its ultimate strength gets enhanced under high strain rate effect making it more suitable to be used in the retrofitting against blast and impact loads. However, the enhancing factor of the mechanical properties of the CFRP itself is much less than that of the concrete and steel, therefore it is commonly neglected in most of the analytical calculations (Mutalib and Hao, 2010).

Over the last two decades, CFRP composites have been used by researchers to retrofit structures against high loading rates in many different shapes, such as fabric, rods, strips, and fibres. Retrofitting slabs, beams and columns by CFRP are studied and qualified by researchers. Wrapping some reinforced concrete (RC) elements like columns or beams with CFRP fabric was found to be adequate in term of enhancing ability to resist blast loading effects, where both the ultimate strength and the ductility of the strengthened members were enhanced by wrapping them with CFRP fabric (Wang and Wang, 2013, Berger et al., 2008, Frangou et al., 1995). (Muszynski and Purcell, 2003) studied interior columns and walls against real blast load after retrofitting them with autoclaved three-ply carbon fibre laminates. An explosive charge weight of 860 kg of TNT was detonated at a standoff distance varied from 13 to 16 m. They reported that the retrofitted system failed under higher displacement value than the control system, indicating the ability of this CFRP strengthening technique to enhance the structural resistance to the blast loading.

(Wu et al., 2007) studied the performance of RC panels strengthened by NSM system with CFRP strips on both faces. Details of the retrofitting are shown in Figure 2-16. The specimens were subjected to blast loading of two detonations equivalent to 0.08 and 2.1 kg of TNT with a stand-off distance of 0.6 m, where the lower charge was dedicated to study the elastic response of both the control and the retrofitted slab while the higher charge was dedicated to study the mechanism of failure in both slabs. The evaluation of the retrofitting method was made based on the post-observation and post-test to measure the residual strength statically as no instruments were used during the explosion tests except high-speed camera. The results indicate that no significant change

in behaviour between the slabs in terms of the permanent displacement and the scabbing of concrete, where similar size of hole of scabbing was observed in both slabs indicating no effect of the retrofitting material on the scabbing behaviour. Slight increase in the permanent displacement was recorded with the retrofitted slab by about 7% compared to the unretrofitted slab which is attributed to the wider plastic hinge area. Similar crack pattern was observed on both faces of the slabs. Crushing of concrete in the mid-span of the top face was also observed at the end of the blast test for both slabs. Rupture of FRPs strips was observed in some CFRP strips in both faces, while debonding in the adhesive was observed for the remaining CFRP strips at the end of the blast test. In the post monotonic test, the unretrofitted slab showed higher residual strength than the retrofitted slab with small difference (119 and 108 kN respectively). In general, they reported that no significant enhancing in the blast resistance of the slab when retrofitting by a specific amount of NSM CFRP strips on both faces. Due to the absence of any instrument during the blast test and the distractive nature of the explosive charge, it is difficult the asses and evaluate the difference in the blast response between both slabs quantitively. Also, the scabbing behaviour which was observed in both slabs, which was attributed to the close-in explosion, cannot be prevented by retrofitting the slab with CFRP strips.

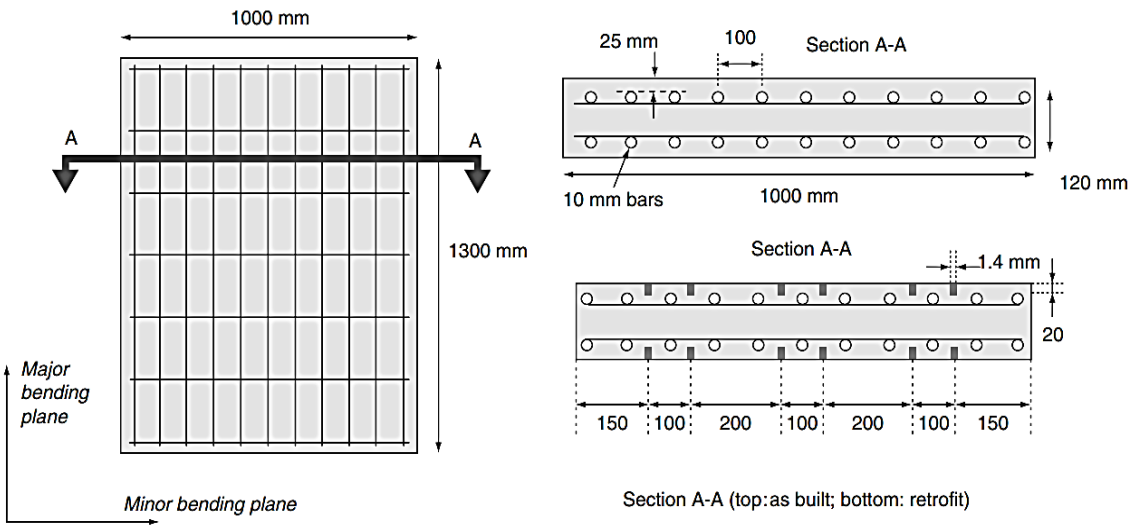

Figure 2-16: Details of retrofitting NSM procedure adopted by Wu et al (Wu et al., 2007).

In another study, Wu et al (Wu et al., 2009) tested RC slabs retrofitted with EB CFRP strips on the compression face only.

Figure 2-17 presents the cross-sectional details of the slab. Two layers of 240mm wide and 1.4 mm thick CFRP strips were externally bonded using Epoxy resin on reinforced and unreinforced concrete slabs. Different explosive charge with different stand-off distance was used for each slab test which makes it difficult to compare the results quantitively as each explosion test gives different reflected impulse on each slab. Thus, the obtained results for each slab were presented separately. The comparison between the obtained results was made based on the predicted absorption energy capacity for each slab which was estimated based on a proposed equation derived from the equation of motion.

The obtained results of the retrofitted panel were compared with the control panel results. It was reported that under larger blast pressure or close-in explosion (a scaled distance of 0.92 m/kg$^{1/3}$) the panel failed by debonding of CFRP strips with cracks in the tension face and no crushing of concrete was observed. Also, direct shear failure was observed near the support which is attributed to the near-field charge. The observed failure pattern is presented in Figure 2-18. It was reported that retrofitting the compression face with CFRP strips enhanced its ability to absorb energy, but it was not quantified as the slabs were not tested to the point of failure. So, further study is needed to evaluate the validity and the feasibility of adopting this strengthening technique and to investigate the entire behaviour quantitively by avoiding all the limitations that preventing this aim in this study as mentioned above.

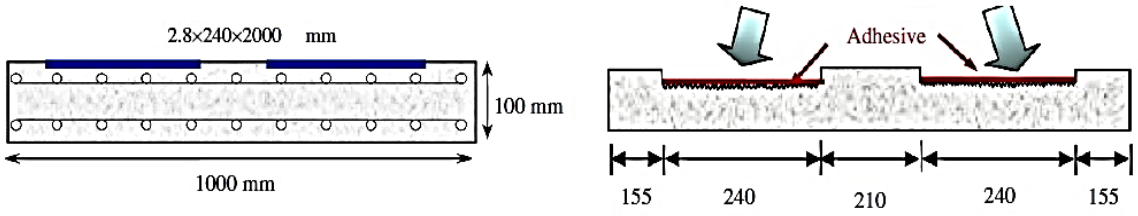

Figure 2-17: Details of the retrofitting method used by Wu et al (Wu et al., 2009).

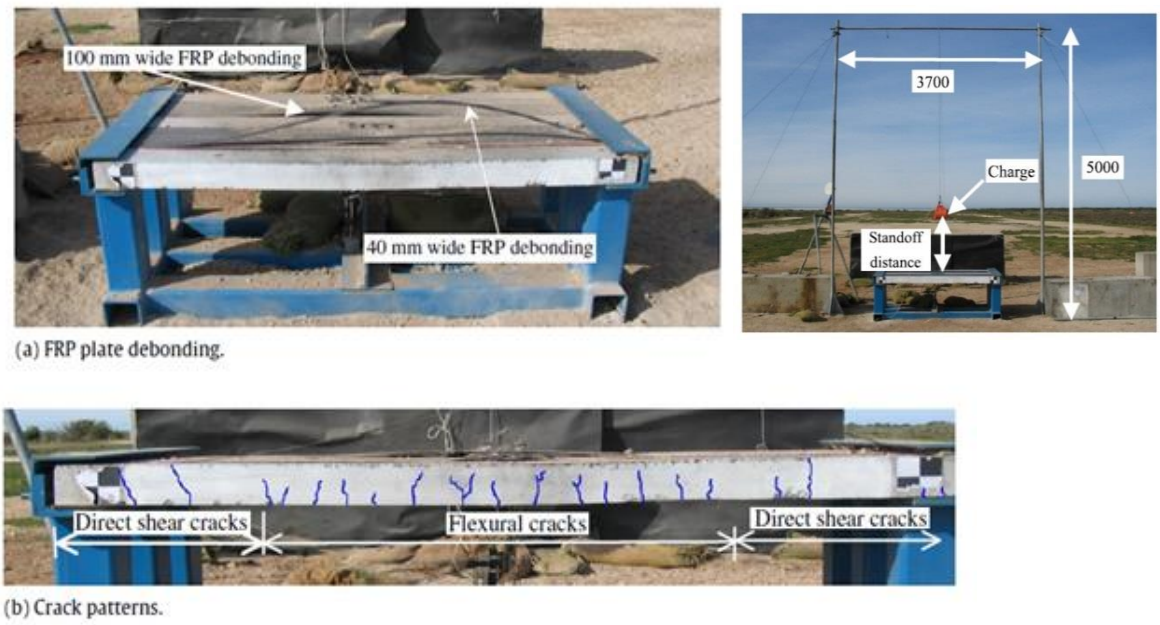

Figure 2-18: Shape of failure and setup of the test conducted by Wu et al (Wu et al., 2009)

Silva and Lu (Silva and Lu, 2007) studied the effect of the CFRP sheets as a retrofitting material against the blast load. 0.165mm thick CFRP sheets were externally bonded to one face or both faces of 1200x1200x90 mm one-way RC slabs reinforced with 3ϕ9.5 mm steel bars (0.18%) with yielding strength of 414 MPa. All the specimens were subjected to a real blast load equivalent to 1.35 kg of TNT explosive charge at a stand-off distance of 300 mm. No instruments were installed to record either the strain or the displacement of the slabs during the test (to avoid damage of the instruments). Based on the post-test observation, they reported that strengthening the slab on one side only led to a slight increase in the blast load resistance compared to a significant increase in the blast resistance when both faces are strengthened. They attributed that to the negative moments that developed under the blast waves (the second phase of the displacement wave) which causes cracking and serious damage in the non-reinforced compression face of the slab due to the rebounding behaviour. The shear failure was found to be dominant for the retrofitted panels. Due to the absence of any recorded data, and the low strength of the slab as a result of the low steel reinforcing ratio accompanied by low yielding strength, it is difficult to determine the gains in the resistance of the slab to the blast loading.

Retrofitting of RC panels with CFRP sheets against blast load was also studied by (Razaqpur et al., 2009). In their study, both faces of the 1m square RC slabs of 70 mm

thickness were retrofitted with two unidirectional laminates of CFRP strips of 500 mm wide in a cross form. These panels were subjected to blast load tests by detonating free air explosive charge of 22.4 and 33.4 kg of ANFO with a stand-off distance of 3 m resulting scale distance of 1.06 and 0.93 m/kg$^{1/3}$ respectively, which is equivalent to 1.13 and 0.98 m/kg$^{1/3}$ of TNT where the equivalent TNT weight factor of ANFO explosive charge is approximately 0.82 as cited in this study. Theoretically, expositions with similar scaled distance produce similar blast pressure. The obtained results were used to assess the validity of using CFRP strips as a retrofitting material against the blast loading. To achieve that the partially damaged panels were then tested under increasing static load to measure the residual strength. By comparing the results obtained from the retrofitted panels with the control panels, they reported that the retrofitted slabs performed better in term of the residual strength under the low explosive charge. The residual strength for the retrofitted panels is almost 188% and 220% higher than that of the control panel. The results were found to be scattered under the large explosive charge (small scaled distance) as the close-in explosion events produce non-uniform pressure. So, they reported that for the future test the charge should be positioned at a scaled distance greater than 1 m/kg$^{1/3}$.

The observed failure pattern of the slabs showed the shear failure to be the dominant mode. No delamination of the CFRP strips was seen. By increasing CFRP layers, an increase in the stiffness of the structure was achieved, which as a result increased the structural resistance against the blast load. Increasing stiffness on the other hand, led to an increase in the natural frequency of the structure which led to increasing the ratio of the blast wave duration to the natural period of the structure (t_d/T), which increases the effect of the blast load and as a result increases the maximum displacement response of the slab under the same explosive charge. Also, increasing layers of CFRP led to reducing the ductility in the slab which will counteract the benefits of the improving the strength. So, they concluded that before applying CFRP to enhance the blast resistance, a proper analysis should be used to assess the effect of the CFRP laminates on the various properties of the slab such as strength, ductility, stiffness and natural frequency. The ultimate response of the structure is a complex function of all these parameters.

Other studies (Kim JHJ, 2009) , (Ha et al., 2011) investigated the performance of RC slab retrofitted with one of the three: EB CFRP, Polyuria (PU) or the hybrid material

CFRP-PU. All the 1 m square specimens were subjected to blast loading from 15.88 kg of ANFO at 1.5 m ($Z= 0.6$ m/kg$^{1/3}$). The hybrid material led to the smallest displacement, while the CFRP led to the highest value of the dissipated energy of about 79.9% compared to 71.8%, 67.14 and 51.4% for the CFRP-PU, PU and the non-retrofitted slab NSC, respectively. The hybrid material enabled the benefit of high strength and stiffness of CFRP with the ductility of PU.

Debonding of the FRP laminates or strips is the most common failure mode in the retrofitted RC structures (Sayed-Ahmed et al., 2009). This undesirable failure mode happens due to the low strength (tensile or shear) of the adhesive or concrete as compared to the FRP. Thus, prohibiting debonding of FRP laminates is important for their successful implementation. This has been achieved by using different anchoring systems. (Eshwar et al., 2008) tested two different types of anchorage system: boundary and interval spikes anchors. Both systems were tested experimentally under static load. Both anchorage systems enhanced the bonding strength of the FRP composite to a certain limit which helps to delay the debonding failure of the FRP composite.

FE-predicted residual displacements were compared with test data from Muszynski and Purcell (Muszynski and Purcell, 2003). For non-retrofitted walls, good agreement was found, while about 16% difference occurred for the retrofitted walls although FRP-concrete failure was correctly predicted. Using this FE model, a parametric study was conducted to establish the effects of FRP-concrete anchor distribution on the blast resistance of the slab. Boundary anchors were found to reduce residual displacement, while intermediate anchors seemed to encourage early rupture of the FRP and so to adversely affect slab response. There was no test data to validate these FE predictions and so it is recognized that these results may be of limited value.

(Musselman, 2007) studied the effect of long carbon fibres on the dynamic response of concrete slabs under both blast and impact (drop-weight) loads. The CFRP-enhanced slabs were reported to fail at higher loads than did their normal concrete counterparts. The crack patterns on the CFRP-enhanced specimens were reported to have been better developed than those on the control where more cracks were propagated in the strengthened panel compared to fewer in the control, which led to the conclusion of higher energy dissipation with the inclusion of CFRP fibres. Musselman (Musselman,

2007) found that under blast loading the CFRP fibres inside the concrete reduced concrete spalling and halved the residual displacement of the slab. They attributed that to the energy dissipation in pulling out CFRP fibres.

Since longer carbon fibres appear to improve blast and impact load resistances of slabs, it seems prudent to try and investigate means of avoiding balling of the fibres which adversely affects fibre contributions at higher fibre lengths. To that end, (Tabatabaei et al., 2012) tested under impact (drop weight) both plain RC panels and panels reinforced with 100 mm long carbon fibres coated with a thermoplastic material to reduce balling of the long fibres at the wet concrete stage. The carbon fibre reinforced panels were found to outperform the normal reinforced concrete slabs on both first crack and ultimate loads, on reducing fragmentation and spalling (Figure 2-19) by 90%, on reducing residual deflection and on exhibiting more ductility.

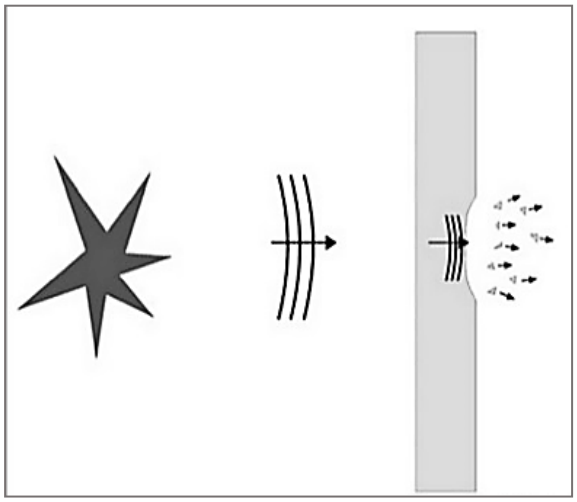

Figure 2-19: Spalling of concrete due to blast load effect (Tabatabaei et al., 2012)

2.4.3 Fibre reinforced concret (FRC)

Adding steel fibre to the concrete has been investigated by many researchers as a retrofitting technique against blast and impact load. To improve the pullout resistance of the fibres (which allows stress redistribution), fibres of different shape such as enlarged end, hooked end, straight, twisted and others (see Figure 2-20) have been investigated. Studies suggest that the hooked end shape is the best for dissipating more energy (Pichandi et al., 2013, Brandt, 2008) as the hokes help to enhance the bonding between

the steel fibre and the concrete which make it more effective in bridging the concrete between the cracks.

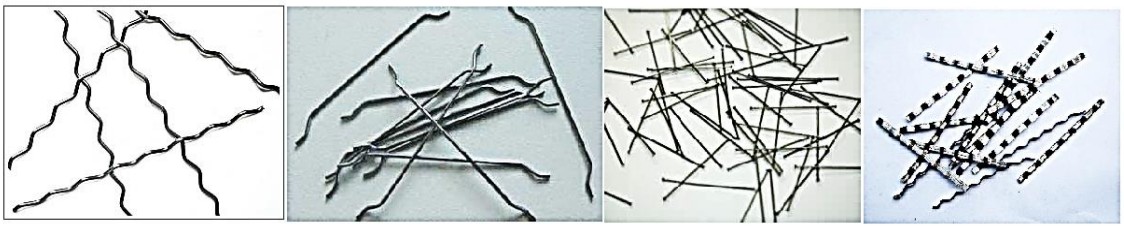

Figure 2-20: Different shapes of steel fibres (wave cut, hoked end, enlarged end and deformed).

(Lan et al., 2005) studied effect of length and ratio of the steel fibres on the blast performance of RC panels, where three different sizes (18, 30, 60 mm) with three different mixing ratios (0.5, 1.0, 1.5% by volume) was used to conduct the study. The RC panels were subjected to real blast loads by detonating 8, 20 and 30 kg of PETN. They reported that the longer fibres produced better blast resistance. They also found that the highest blast performance was obtained by using 1.0% of steel fibres. Balling of the fibre was observed related to the longest steel fibre. So, they recommended that increasing fibre lengths up to a limiting value improved the blast resistance of RC panels. Beyond this limit (a number was not suggested), balling (agglomeration) and poor dispersion of the fibres in the concrete prevailed. (Yusof MA, 2010) also investigated effect of steel fibre volume on the blast resistance by using the same proportion ratios that used by (Lan et al., 2005) (0.5, 1.0 and 1.5 %). The RC panels were subjected to a real blast test by detonating 1 kg of plastic explosive charge with a stand-off distance of 0.6 m. The post-test observation to the RC panels showed that 1.5% of fibres gave the best performance to the blast load followed by 1.0%.

(Yoo and Yoon, 2014) reported that concrete compressive strength decreased while flexural strength, maximum displacement during and residual deflection after impact testing increased with the increase of the steel fibre proportion in one-way plain concrete slabs. This was attributed to the bridging effect of the steel fibres which prevents the cracks from opening.

(Yi et al., 2012) found that, for two-way concrete slabs, using steel reinforcement with ultra-high strength concrete (UHSC) or steel fibres with reactive powder concrete enhanced ductility and led to more dissipated energy. Failure was by micro-cracking rather than by large cracks due to flexural or shear failure encountered in normal RC slab.

2.4.4 Aramid fibre reinforcement (ARFR)

Aramid is a group of Aromatic Polyimide heat-resistant synthetic fibres. Kevlar is the well-known type of Aramid which was developed by DuPont in 1971 (Hearle, 2001) . It is used in the structural applications due to its high strength-to-weight ratio. The high strength character comes from the highly oriented internally rigid molecular chains (Simonelli, 2006). The stress-strain behaviour for Kevlar is linear up to failure (brittle behaviour) like CFRP and GFRP (Figure 2-8).

The high tensile strength of Kevlar (2640 – 3040 MPa) with a modulus of elasticity of 75.5-127.5 GPa inspired the researchers to investigate it's feasibility to improve the blast resistance of structures. (Riisgaard, 2007) investigated the effect of using Kevlar reinforcement in the form of lace to strengthen compact reinforced composite (CRC) in the out of plane direction against blast load effects, as shown in Figure 2-21. In this study, two columns with a dimension of 160 x 200 x 200 mm were reinforced by longitudinal high strength wire strands as flexural reinforcement, and 8Ø 3 mm of aramid laces used for strengthening against blast load with a spacing of 50 mm and 100 mm in two different columns. The closer lace spacing was found to reduce column damage due to blast loading as shown in Figure 2-22. The strengthened columns were also analysed numerically by using LS-DYNA code and the results showed that failure of both columns was flexural, with the lace having remained intact. Unfortunately, the enhancing ratio cannot be quantified as no data was provided for both the experimental and the numerical studies.

Figure 2-21: : Polymer reinforced compact reinforced composite column (Riisgaard, 2007).

(Yoo and Yoon, 2014) investigated the strengthening of one-way plain steel fibre reinforced concrete slabs (100 x 50 x 350 mm) with either externally bonded aramid fibre polymer (AFRP) or CFRP sheets. Different ratios of steel fibres were used in the concrete varied form 0.5%-1.5% by volume. The specimens were subjected to a single impact test for each by using impact tube machine by dropping 12.9 kg from a height of 1045 mm which producing impact energy of about 133 J. Both the mid-span displacement and impact load were measured simultaneously during the test. A load-displacement curve was plotted for each drop test and the results assessed based on the peak value of the impact force. The maximum strain rates measured at the top extreme fibre in the tests ranged between 0.19 and 0.33 s^{-1}. The dissipated energy was assumed to be equal to the area under the hysteresis loop in the load-deflection curve. The obtained results revealed a drop in the peak value of the impact load and an increase in the dissipated energy by 19% and 270% respectively. Delamination of the FRP sheets was observed as a failure mode. They reported that AFRP sheets outweigh CFRP sheets in terms of the impact resistance by recording less residual deflection (30%) than that obtained with the CFRP sheets. Nonlinear FE analysis was conducted to simulate the impact response of the specimens by using LS-DYNA code. Good agreement was obtained in terms of the maximum response despite the difference in the historical displacement wave.

Experimental setup – column, steel frame and high explosive charge

Damage on *Column 1* – aramid lacing for every 50mm

Damage on *Column 2* – aramid lacing for every 100mm

Figure 2-22: Test set up and post-test observation of the strengthened columns (Riisgaard, 2007).

2.4.5 Polyurea (PU)

PU is an elastomeric material produced from the mechanical reaction of isocyanate and synthetic resin through polymerization processing. PU exists in two types; aromatic and aliphatic. The aromatic form of PU is particularly well suited to blast protection due to its cross-linked structure. Polyurea (PU) has high ultimate strain (superior to those of GFRPs and CFRPs), high ductility, high shock resistance elastomeric

material which bonds well to concrete, plastic and steel. (Tekalur et al., 2008), (Davidson et al., 2004).

Owing to these properties, PU has been investigated for its retrofit capabilities to enhance blast resistance of reinforced concrete members. For a large-scale structure comprising three rooms with concrete block walls, (Knox et al., 2000) coated the walls with unreinforced polyurea and polyurethane and subjected the structure to blast loading by detonating ANFO. Other retrofitting options investigated include open weave aramids with a spray-on polyurea on concrete walls (Johnson et al., 2004), (Stanley et al., 2005). Also, either a CPU hybrid (CFRP+PU) or PU on its own used on RC slabs (Ha et al., 2011) as shown in Figure 2-24. In all cases, blast loads were applied to the retrofitted elements. The results revealed, relative to the original un-retrofitted walls, up to 58% increase in load capacity (peak reflected pressure), over 37% decrease in peak deflection and over 63% decrease in residual displacement when the hybrid polymer (CPU) is used (see Figure 2-23). Based on that, they stated the adequacy of hybridising PU with carbon to enhance both the ductility and strength of the structural member.

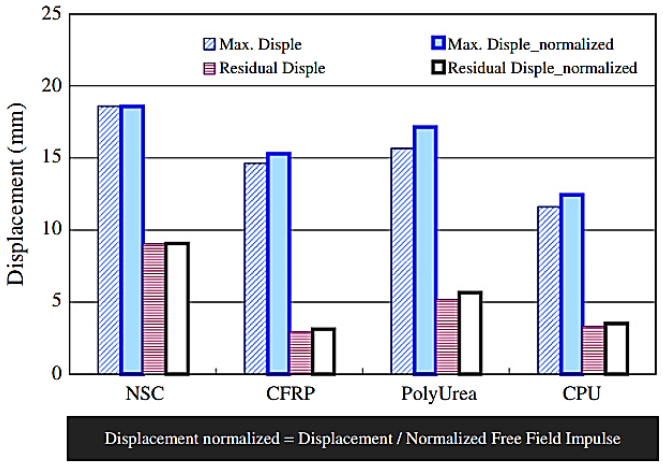

Figure 2-23: Comparison of maximum and residual displacement of RC slabs with different strengthening FRP material (CFRP, PU and CPU) compared to the control panel NSC (Ha et al., 2011).

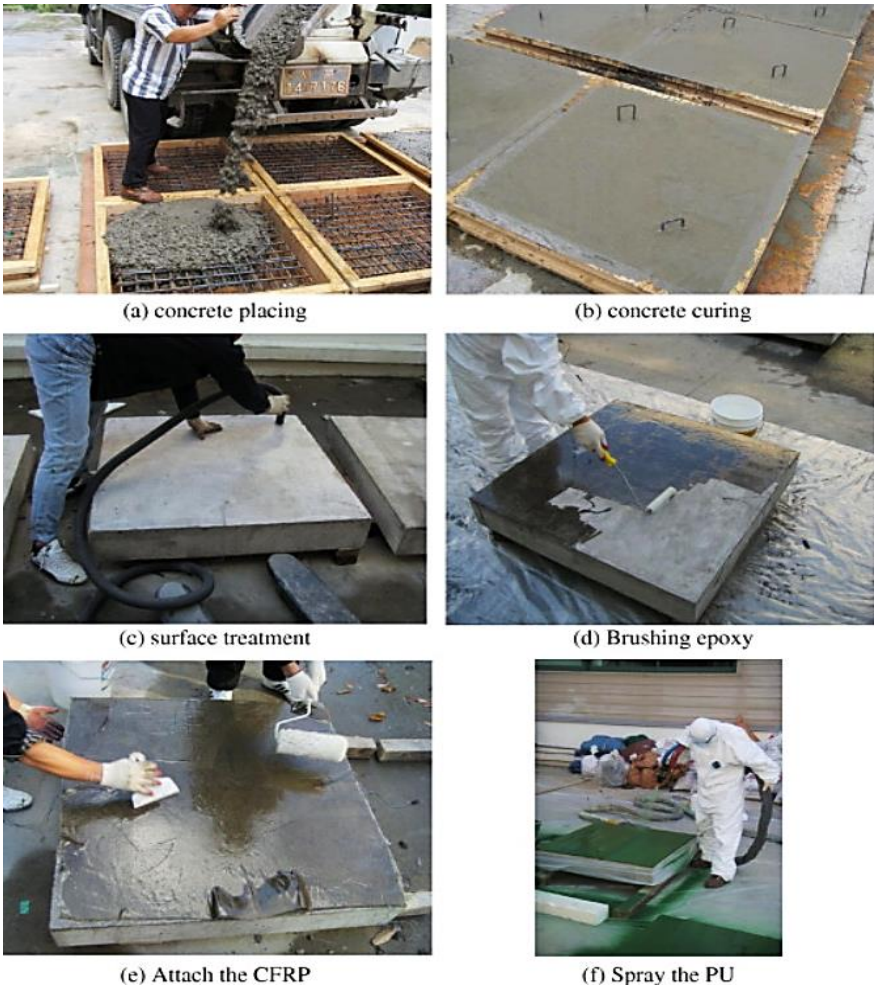

Figure 2-24: Procedure of applying the CFRP sheet, the PU and the hybrid CPU on RC panels (Ha et al., 2011).

2.4.6 Sandwich composite panels

Sandwich composite panels with two strong faces sandwiching crushable or plastic materials are often used as blast resistant material (Li et al., 2014). Such panels may work as sacrificial shields when applied to the façades of a structure facing blast waves. The core of the panel plays an important role in diluting impulses and enduring the high transient blast or impact loading, and absorbing energy (thus reducing the load on the protected element) (Hanssen et al., 2002, Gardner and Shukla, 2011). Many studies have been done to investigate different materials with different forms to be used in the core (Liu et al., 2014). Crushable and ductile materials were utilized as a core material to absorb the applied energy. Different forms of the core, such as foams, latticed cores, honeycombs or corrugated have been studied (Li et al., 2017).

Due to the high level of ductility, PU (Polyurea) has shown much promise and is a material of choice for use as a core material, with the FRPs used as facing materials (Gardner and Shukla, 2011).(Tekalur et al., 2008) studied the blast resistance of a sandwich composite panels consisting of two materials: E-glass vinyl ester (EVE) and PU. Two different forms were used in the sandwich: first, by selecting the polyurea as a core material and the second, EVE as facing sheets and vice-versa. The results showed that the sandwich composite with the PU used in the core exhibited the best blast resistance. In another study, (Wang et al., 2009) investigated the blast performance of carbon fibre-balsa wood sandwich composite where the carbon fibre was used in the faces and the balsa-wood was used in the core. They reported that the sandwich composite performed better than its individual components by about 300% in terms of the failure impact load. In another study (Gardner and Shukla, 2011), the sandwich panels comprised E-glass vinyl-ester faces and stepwise graded cores of different densities and layouts of styrene foams. Owing to the composite action, the sandwich panels were found to outperform (in one case by as much as 100%) their non-sandwich counterparts. One study (Gardner and Shukla, 2011) showed that changing the sequence of foam layers altered the failure mode from significant core fragmentation (undesirable) to virtually no fragmentation as shown in Figure 2-25.

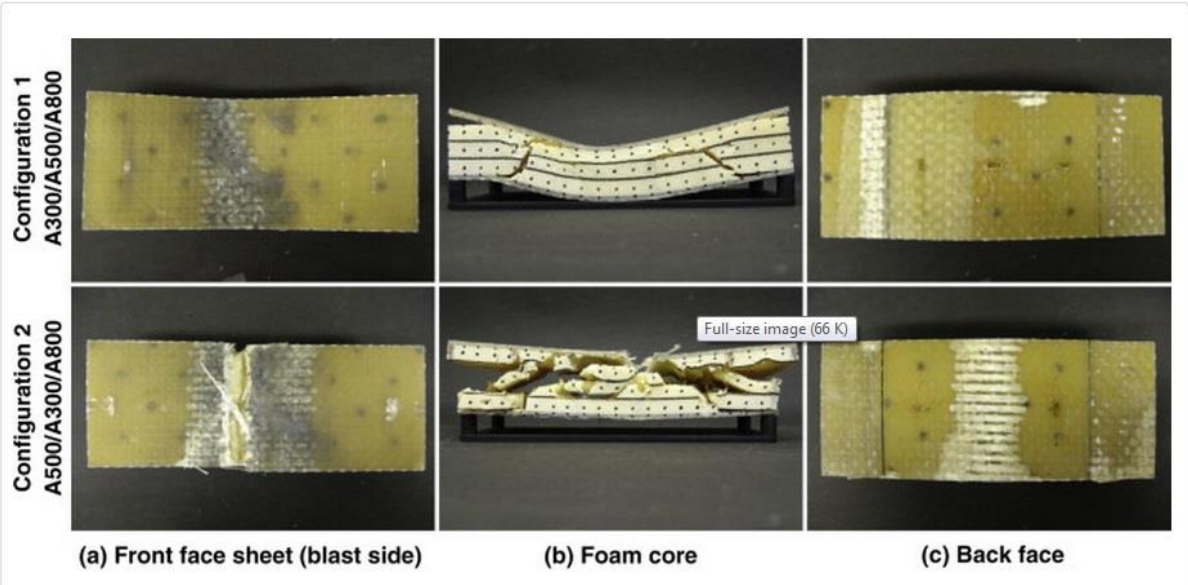

Figure 2-25: pattern of failure of the sandwich panels with different configuration (Gardner and Shukla, 2011).

2.5 Theoretical modeling of the blast response of FRPs composite

Investigating the mechanism of the FRPs composite structures response to the blast load experimentally have a great value in interpretation the mechanical behaviour of the composite materials to the blast load in terms of the failure modes and the other mechanical response to provide enough data for well understanding to the entire behaviour of the composite materials in many aspects which needed to generate a systematic design and modelling approaches. However, many difficulties are involved in the experimental investigations make it difficult to gather all the data needed before building any comprehensive guideline design for the blast protection. The difficulties involve the highly cost blast experiments in terms of the materials and the instruments, the destructive nature of loading within very short time, and the limitations of conducting the blast events for security reasons. Thus, the need to develop rational model to simulate the structural response to the blast loading is crucial as the rational modeling can provide all the data needed to provide additional insights onto the entire behaviour of the composite material structural response, particularly for the data which is challenging to measure during the experiments. Such this kind of computational model, after validated with sufficient experimental data, can be used to gather as much of data as possible to cover all the aspects that needed to build the design procedure.

Many studies have been conducted to develop and propose rational models to capture the structural response of RC elements under different strain rates. The blast resistance response of the structural components such as slabs, columns and beams is commonly predicted by adopting one of two methods; SDOF (Biggs and Biggs, 1964, Mays, 1995) and finite element analysis methods (Mosalam and Mosallam, 2001, Luccioni et al., 2004, Wang et al., 2005, Foret and Limam, 2008). In the elastic SDOF method, the system is assumed to be responding elastically as a single-degree-of-freedom system where the structure is converted to an equivalent mass having resistance and damping function subjected to time-dependent load function. The deflection response of the system at any time instant is obtained by solving the equation of motion of a rigid body. Normally the maximum deflection response in the system is used to define the structural damage (Li and Meng, 2002). Beyond the maximum elastic displacement response in the system, a pressure-impulse (*p-i*) isodamage diagram is used to distinguish level of damage in the system which was introduced based on the elastic SDOF model (Mays, 1995). The *p-i* isodamage diagrams were widely used to predict both the structural damage (Marchand et al., 1991, Merrifield, 1993) and the human injuries induced by blast events (Baker et al., 1975, Merrifield, 1993). The (*p-i*) isodamage diagram basically used to classify and estimate level of the damage in the element that subjected to a transient load (impulse) depends on both the value of the peak pressure (p) and the magnitude of the impulse (i) based on the shape of the impulse. The p-i diagram suggests that the estimated level of damage is sensitive to the peak value of the pressure in the impulse with relatively short duration and it is sensitive to the magnitude of the impulse when an impulse with relatively long duration is applied. The estimated level of damage is obtained as a ratio to the critical (reference) damage which is estimated based on specific pressure and impulse (p_1, i_1) which is calculated for each structural element by equations. More details about the p-I isodamage diagram method is provided in reference ((Li and Meng, 2002).

(Abrahamson and Lindberg, 1976) suggested a characteristic curve similar to the *p-i* diagram to estimate the damage based on both determined critical and maximum deflection. In their method, set of curves were used to determine the damage level for pulse with various loads and the same shape. In addition to that, different set of curves were suggested for different shape of pulse which found to have similar features.

(Li and Meng, 2002) have investigated the effect of the pulse shape on the *p-i* diagram based on the maximum deflection damage criterion. The blast load was idealized as a descending pressure pulse and the elastic SDOF model was used to predict the structural response. So, only the elastic response was considered in their study. Based on three types of idealized pulse shape; triangular, rectangular and exponential, they reported that the pulse shape has a considerable effect on the *p-i* diagram. They also reported that for the elastic response, this effect can be eliminated by introducing an effective impulse. Based on that, they proposed a unique effective impulse diagram insensitive to the shape of the pulse. They validated their model with experimental and numerical results gathered from literature.

(Krauthammer et al., 1993) have introduced finite difference (FD) analysis to predict the dynamic response of the structural element by dividing the element into discrete segments to find an approximate solution to the equation of motion. The proposed model can accommodate any distribution load along the member, can consider any variation in the mechanical properties across the depth of the member, can account the shear and deformation along the member based on Timoshenko beam theory. All of these characterizes were not possible to be detected in the SDOF analysis method. In their study, the dynamic increase factor (DIF) in the component materials was considered by assuming constant strain rate over the cross-section based on an average strain rate.

(Jones et al., 2009) have extended Krauthammer's FD model by considering the variation in the strain rates over the cross-section of the member. A sectional layered method with strain rate dependency was used to derive the sectional moment-curvature (m-k) relationships. To simplified the calculation a bilinear m-k relationship with linear behaviour between the yeilding and the ultimate moment was used in the analysis. The ultimate moment was obtained when the strain at the top fibre of concrete reaches to the ultimate strain which was assumed to be 0.0035. To validate their model, the predicted results were compared with the FE and SDOF results where good agreement was obtained. Based on the simplified m-k relationship, it is obvious that the nonlinear and the softening behaviour during the plastic deformation regime was neglected. This could effect on the value of the maximum deflection obtained at the ultimate state.

(Su and McConnell, 2013) introduced approach to estimate the absorbed energy of a sandwich panel used as a sacrificing element to withstand the blast loadings by imbedding Friendlander equation with the SDOF analysis method as equations in the MATLAB. Where Friendlander equation was used to calculate the blast pressure p(t) based on the charge weight and the standoff distance, and the SDOF analysis method was used to predict the dynamic response. The sandwich panel consisted of two faces with vertical webs inserted between them. The absorbed energy was calculated based on the plastic deformation and failure of the web. The elastic response of the web was predicted based on elastic SDOF based on the equation of motion. While the plastic response of the web was estimated based on elastic-perfect plastic relationship. The absorbed energy, which was considered to be the dissipated energy in the webs as a result to the plastic deformation and the failure, was calculated by taking out the reversible energy (maximum elastic energy) from the total kinetic energy applied on the front face of the panel according to Equation2-2 as follows:

$$AE_{web}^{F} = \frac{1}{2} m_{core} v_E^2 + F_y w_f - \frac{1}{2} F_y w_y \qquad 2\text{-}2$$

Where the first term in the equation represents the eroded kinetic energy at the failure of web, and the last two terms refer to the eroded internal energy in the web. The predicted results were validated with the numerical results obtained by LS-DYNA code. The provided procedure was dedicated to optimizing the energy absorption of the core in the composite panel based on different total area of the webs A.

2.6 Numerical Modelling of blast response of FRPs composite

SDOF modeling approach found to yield satisfactory overall predicting the structural response. However, predicting the localized damage in the structure, capturing a spatial transient and temporary loads with different distribution variation on the member such as blast loads, accounting the strain rate effect directly, cannot be detected by this simulating approach(Jones et al., 2009) . This type of complicated details only can be detected by following step by step finite element analysis with refined element size. This type of finite element analysis is so complicated and time-consuming if it is done manually especially for large structural element with an irregular geometrical shape where large number of elements is necessary. With the developing in the technology of

computers and the processors and the developing in the finite element analysis solutions, more detailed simulating models with more accuracy and comprehension than SDOF were developed for more reliable prediction to the static and dynamic structural response (Riedel et al., 1999, Autodyn, 2005).

Extensive numerical studies have been carried so far to simulate the blast response of the FRPs composites, However, more studies are still in needs before adopting a specific numerical model to be outstanding. The main challenges in the numerical modeling are modeling the blast loads effect on the structures and the development of suitable composite material modes covering all the potential failure mechanisms and incorporating the strain rates of the constitutive materials.

There are two approaches are used to simulate the blast loading numerically; the first approach comprises decoupling the load and the structural response, where the load is simulated separately as predefined load-time function where the distribution of the blast load is predicted based on Friedlander equation(Hetherington and Smith, 2014) as shown in equation 2-3.

$$p(t) = Pso\left[1 - \frac{t}{td}\right] exp\left\{-\frac{bt}{td}\right\} \qquad 2\text{-}3$$

Where b is the exponential decay factor of the blast load function, Pso is the peak force. Many other simplified equations were proposed by researchers based on Friedland equation which can be found in literature (Qiu et al., 2004, Mori et al., 2007, Batra and Hassan, 2007). A triangular load function and Heaviside pulse were also proposed to simulate the blast impulse(Librescu et al., 2004). The proposed pulse shape was imported into ABAQUS/Explicit code through a user-define subroutine to predict the structural response of the loaded panels (Vo et al., 2012). ConWep algorithm was also available in LS-DYNA and ABAQUS/Explicit which is used to describe air-blast loading(Thiagarajan et al., 2003, Rajamani and Prabhakaran, 1980).

The second approach which is used to model the blast pulse and the structural response is a coupled numerical simulation, where Eulerian fluid equations are used to simulate the blast wave. This has a disadvantage as it is capable to simulate the change in the blast wave resulting from displacing the responded structure due to the fluid-structure interaction. Researchers have found that Eulerian solvers are the best in modeling the

blast waves with some limitation capability in modeling the composite response. In contrast, Lagrangian solvers have more capability in simulating the composite response with some limitations in simulating the blast waves(Langdon et al., 2014). However, both Lagrangian codes (implemented in ABAQUS and LS-DYNA) and Euilerian codes (implemented in AUTODYN) are in developing to reach to fully coupled blast loading and structural response simulation models.

The blast response of the RC FRPs structures can be modeled based on the blast response of the constituent structural materials (concrete, steel and FRPs) and the bonding behaviour between them. As there are many different types of FRPs owning different mechanical properties, as discussed in the previous sections, it is difficult to provide a comprehensive numerical model to simulate the FRPs materials. Furthermore, the bonding behaviour between the FRPs layers (when multi layers are used) or with the concrete is atypical as it depends on many factors, such as type of the FRPs material, type of the adhesive, and the environmental conditions. Several constitutive material models were proposed to describe the mechanical behaviour of the FRPs composite materials in terms of the failure criteria and evolution of damage. In addition to that, several contact models are proposed to simulate the bonding behaviour between the constituent materials. However, all of the proposed models comprise factors need to be assumed or pre-defined based on the actual behaviour of each composite material.

An anisotropic linear elastic model is often used to model the elastic behaviour of the FRPs laminates before the dawn of any damage. After that, a damage evolution model is assumed based on the displacement or the fracture energy. (De Souza Neto et al., 1998, Krajcinovic, 2000) have done review study on the available failure models highlighting the important issues in this area. Hashin's failure criteria are widely used to model the mechanism of damage in the FRPs and implemented in the commercial codes Abaqus and LS-DYNA as a 2D form(Langdon et al., 2014). (Vo et al., 2012) implemented Hashin's 3D failure criteria into ABAQUS/Explicit through a user-defined subroutine to account the thickness effect in the thick or multi layers FRPs plates. Different failure criteria models were proposed and implemented in different FE codes for different FRPs materials. Details of the proposed models and the corresponding FRPs composite material are covered in a review paper published by (Langdon et al., 2014).

Extensive numerical studies have been done on investigating the structural response to the blast loading. Majority of the work done was carried out by using commercial FE codes such as ABAQUS, ANSYS and others by utilizing the built-in constitutive material models or by developing new models to implement them as a predefine models or as a subroutine.

(Dolce et al., 2010) used a 3D FE analysis to model damage of CFRP due to an air blast. A fluid-structure interaction was used in the analysis by using Eulerian equations for the blast waves and Lagrangian equations for the structures. Good agreement between the experimental and the numerical results was reported in terms of the residual displacement and the resulting failure mode. (Forghani and Vaziri, 2009) simulated the dynamic response of GFRP laminates subjected to distributed pressure by implementing a user-defined damage model in LS-DYNA. Good global structural response was indicated in this study. (Icardi and Ferrero, 2010) studied the behaviour of multi-core sandwich composite subjected to blast loading by developing FE model based on the first order shear deformation theory (FSDPT). (Hui and Oskay, 2012) simulated a woven E-glass fibre reinforced vinyl ester (EVE) composite and PU-EVE composites under blast loading by developing a computational model. In their computational model, the damage was modeled based on multiscale behaviour by including the adiabatic heating and the strain rate dependency. Extensive studies have been conducted using LS-DYNA to simulate the blast response of skull sandwich structures, composite laminates and sandwich panels (Langdon et al., 2014). Most of the numerical studies that carried out to investigate the blast response of the FRPs composite utilized the commercial codes ANSYS and ABAQUS to develop accurate numerical solutions.

(Mutalib and Hao, 2010) simulating the debonding behaviour in the interaction contact between the FRP composite plate and the RC concrete panels by adopting LS-DYNA code. The concrete material was modelled by adopting 72Rel3 model (MAT CONCRETE DAMAGE REL3) based on the parameters compression strength of the unconfined concrete which has been proven to be reliable in simulating response of concrete to the blast loading (Malvar et al., 1997). The steel reinforcement was modeled by using MAT PIECEWISE LINEAR PLASTICITY based on user-defined stress-strain data. While MAT ENHANCED COMPOSITE DAMAGE TITLE model was used to simulate FRP material based on Chang-Chang failure model. The strain rate dependency

of concrete was account based on CEB model, while Malvar's model was utilized to account the strain rate dependency in steel (Malvar, 1998). In contrast, the strain rate effect on FRP was neglected. To simulate the interaction between the constituent materials, the CONTACT option is used which is implemented in LS-DYNA code.

The bond between the steel bar and the concrete was assumed to have elastic-plastic shear stress relationship. While the bonding between the epoxy adhesive and the concrete was simulated by using AUTOMATIC SURFACE TO SURFACE TIEBREAK model in the contact nodes by defining the characters of failure based on the tensile and the shear stresses and assumed to be perfect bond between the multi-layers of the FRP plates. In addition to that, two models were developed to simulate the anchorage system which is used by fixing the FRP with the concrete by steel bolts to enhance the bonding properties by using the options CONSTRAINED TIED NODES FAILURE and CONTACT TIEBREAK NODE TO SURFACE. For the geometrical simulating, 8 nodes solid element with 6 DOF was used for the concrete block. And 2 nodes Hughes-Liu beam element was used for the steel bars. While FRP plate was simulated by using 3D Belytschko-Tsay shell element.

To validate their model, (Mutalib and Hao, 2010) compared their predicted results with the experimental results obtained from a previous study conducted by (Muszynski and Purcell, 2003) where concrete panels were subjected to close-in explosion tests. To simulate the blast load, the panel was divided into nine segments and the load was assumed to be uniform pressure with different magnitudes for each segment corresponding to its distance to the detonation node to simulate the close-in explosion effect. Based on the comparison between the predicted and the measured results, good agreement was obtained in terms of the displacement values for different points in the panels with average percentages of error about 0% and 16% for the control and the retrofitted panels.

(Nam et al., 2010) conducted numerical study to investigate the effectiveness of strengthening RC panels with GFRP plates on both faces against blast pressure by using LS-DYNA code. In their study, the predicted results were compared with the experimental results obtained by (Razaqpur et al., 2007). Solid and beam elements were used to model the concrete and the steel reinforcement. While the GFRP plates were

modeled by using shell element. The contact area between the GFRP and the concrete was modeled by using contact interfacial element with either perfect bonding or debonding failure models. In the debonding model, the strain rate dependency was also included. To control the noise in the analysis, the optimum size of the element was found to be 2.5% of the specimen length. For modeling the failure in the material, concrete damage model (MAT-72), piecewise linear plasticity (MAT-24), and orthotropic elastic model (MAT-2) were adopted for concrete, steel reinforcements, and FRP reinforcement respectively. Based on the obtained results, the comparison between the perfect bonding and the debonding models were used to evaluate the efficiency of the bonding provided. While the compression between the rate dependent and independent models was used to evaluate the dynamic enhancing factor in the bonding. The results indicate that the behaviour curve of the perfect bonding model was close to that with the rate dependent debonding model. This indicates the efficiency of the bonding system used in the retrofitting. Also, reduction in the maximum displacement of about 20% was obtained when the RC panel is retrofitted with FRP plates compared to the control slab which indicating the adequacy of the retrofitting system. The overall results showed good agreement between the numerical and the experimental results.

(Soliman et al., 2010) conducted experimental and numerical studies on strengthening the flexural behaviour of RC beams by NSM-FRP bars under concentrated static load. In this study, different parameters were investigated including internal steel ratio, size of FRP-rods, size and shape of the grooves and bonded length of the FRP-bars. The obtained results were compared with the numerical results that conducted by using nonlinear displacement-controlled 3D finite element FE analysis with the including of bond-slip relationship. Good agreement was obtained between the experimental and the numerical analysis in term of the load-deflection, ultimate capacities, load-strain, and failure modes.

(Hawileh, 2012) developed 3D FE model to predict the static response of the RC beam strengthened by NSM-FRP rods subjected to four-point loads by utilizing ANSYS code (Manual, 2000). In this study, the nonlinear constitutive material behaviour of concreted, steel and FRP rods were considered. In addition to that, the bond-slip model was used for the bonding properties between the adhesive and the FRP and the concrete. The concrete block was modeled by using 8 nodes solid element SOLID65 having three

DOF. The steel and NSM rods were modeled by using Link8 element. While the spring element type COMBIN14

The developed FE model was compared with the experimental data of seven specimens conducted by (Al-Mahmoud et al., 2009). Based on the comparison, a good agreement was obtained between the experimental and the predicted results of the load-displacement curve. Furthermore, the developed FE model was capable to predict the debonding in the NSM rod and the separation of concrete. the validated FE model then used to study the effect of different parameters such as type and shape of FRP rods.

2.7 Summary and discussion

Numerous studies have been conducted on the blast load resistance of civil structural elements with various materials and composites. Also, many techniques have been suggested to protect structures from the blast load effect. Majority of the studies have been carried out on the FRPs materials due to the effectiveness of these polymer materials in the blast protection field. The FRPs that utilized in this field are: GFRP, CFRP, Aramid, PU, FRC and hybrid composites of a different polymer. These materials were used in different forms such as fibrous, rebar, laminates, spray-on materials, composite, laces and NSM rod. Research has revealed the ability of these FRPs to enhance strength, ductility and absorbing energy of the retrofitted structures to minimize their collapse.

It is difficult to make a direct comparison between different studies due to various parametric conditions of the tests, such us different types and weights of the explosive charge used, different stand-off distance and different weather condition, as the environment conditions found to have impact on the blast wave (the free air and the reflected pressure). Also, in most of the experimental tests conducted by real blast events by using TNT or ANFO, the explosive detonating charge was installed within small stand-off distance from the target specimen to ensure a sufficient pressure to fail the specimens. This type of explosions only simulates the close-in explosions which have different effect on the structures compared to the away explosions, where localized failures (punching shear and scabbing) are associated with the former one due to the high incident pressure over a localized region of the target compared to a uniformly distributed pressure over the entire structure with the away explosion event. To simulate the away explosions large

amount of explosive charge with relatively long stand-off distance should be used which is difficult to be available for the experiments for many reasons. Thus, it is difficult to identify the best retrofitting material or technique to be adopted. Also, the retrofitting materials and the method of applying them in the previous research seems to be selected randomly due to the absence of any explanation about that (Buchan and Chen, 2007). Therefore, to make an objective assessment of the different retrofitting materials, a standard field-blast test procedure along with standard retrofitting guidelines should be developed for the future research. The Air Force Research Laboratory (AFRL) at Tyndall Air Force Base in USA is taking the lead in this type of researches as it initiated the first (Raman et al., 2011) research centre in 1999 to develop and study applications of different techniques in the blast protection area, where many research were conducted experimentally or theoretically on strengthening different structures comprises of steel, concrete and masonry structures against blast events.

Many retrofitting materials were tried and their feasibility in the blast retrofitting field were investigated, but these materials were not designed to resist blast loading. Further research is needed to understand their performance under blast loading and to develop new innovative material for the blast load resistance. The innovative material should comprise all the factors needed for the best retrofitting material against the blast loading such as stiffness, ductility, resistance to the environment and vandalism and easy installation processing.

Since the blast-resistance design is still in its infancy with the absence of any design guidelines, the reviewed literature was aiming to understand the structural performance of the retrofitted elements by conducting experimental tests under real explosion event. Researchers have tried to understand the blast performance of the retrofitted elements by measuring relevant factors such as deflection, ductility, strength, and pattern of failure. But the destructive energy produced from the explosion within very short duration (milliseconds) makes it difficult to achieve the desired accuracy by using laboratory instruments whereas it is difficult to quantify the difference or the enhancing factor of the mechanical properties of the structure after retrofitting against this type of destructive loading. Considering that, in addition to the cost and the secure nature of the explosion tests, there is a need to develop theoretical or numerical models with accepted accuracy level. Further, it is not possible to achieve all behaviours by using laboratory

instruments to validate the numerical work. Although some studies have been conducted numerically by adopting various programs and models to predict the blast-resistance behaviour (Mutalib and Hao, 2010, Mao et al., 2014, Zhou et al., 2008, Foret and Limam, 2008), many assumptions were made to simplify the calculations to reduce the cost and the time which in turn reduced the accuracy of the results, such as neglecting the strain rate dependency of FRPs, assuming perfect bond between the FRPs and the concrete and predefining the spacing between the cracks.. Considering that, the need to understand the experimental behaviour of the RC FRP composite and developing adequate and validated nonlinear numerical model is in need.

Majority of the researchers used FRPs as a retrofitting material for the existing buildings either as externally bonded laminates (EB) or Near Surface Mounted (NSM) rods to increase their strength against blast load effect due to the high strength of FRPs. But due to the brittle behaviour of FRPs materials, increasing structural strength of retrofitted element without increasing their ductility could make these elements fail in a brittle manner if they were to encounter explosion load exceeding their capacity. Using steel fibre or carbon fibre in the concrete mixture, as reported in many papers, enhanced ductility of the concrete element significantly but it is suitable for new buildings only. Therefore, enhancing the ductility and the absorbed energy of the existing building elements should be considered to prevent collapse and fragmentation of the retrofitted elements.

Most of the previous studies have focused on using EB method as a strengthening method for mobilizing the high tensile strength FRPs materials in the form of CFRP sheets. But the premature debonding failure of the CFRP sheets on both faces of the retrofitted slabs and their low resistance to the external environment factors, in addition to the complex installation method in some cases, is limiting the optimum use of the high strength CFRP materials (Sena-Cruz, 2005). Further, EB technique is rarely used to strengthening the compression zone due to the premature debonding failure of the CFRP plate which limits the gain in the ductility achieved by adopting this method. In contrast, NSM technique is found to be superior in many respects, such as the easy installation, the high resistance to the environment and safe from vandalism, the workability with all types of the structural members in all stress zones, and the reduction of the consuming materials of both FRP and adhesive.

Most of the conducted research so far have focused on utilizing the comprising FRPs in the blast protection field by investigating its efficiency in enhancing the blast resistance of the strengthened elements which was approved by all of the previous study for all types of FRPs such as CFRP, GFRP, Aramid, PU, Hybrid and others. However, there is absence of any guideline to highlight the advantages and the limitations of each application method. This also was observed by (Buchan and Chen, 2007) who have conducted review study on the FRPs blast resistance techniques stating the need to clarify and cover all the relevant factors related to each application method. Furthermore, most of the conducted studies have focused on enhancing the strength capacity of the elements by utilizing the strong and stiff FRPs materials. But in many cases enhancing the strength capacity compromising the ductility and the dissipated energy of the elements which are so important in the blast resistance filed. This could lead to a disaster and huge losses in humans and catastrophic global collapse in the buildings if the applied blast loadings exceed their ultimate strength. While the main goal of the blast protection applications is to mitigate and to control these types of losses.

Limited analytical studies were conducted to develop analytical models to simulate the blast resistance of the structural elements. The SDOF solution approach found to be efficient in detecting the overall elastic response of the structural element based on equation of motion by assuming single degree of freedom system. However, simulating the plastic response of the element was challenging which led to impose many assumptions to approximate the actual behaviour such as assuming elasto-plastic behaviour with perfect plastic trend and neglecting the effect of shear stresses and deformation. In addition to that, estimating the plastic response of the elements was estimated based on limited idealized load function which limit application of SDOF approach with specific types of load functions such as triangular, rectangular and exponential time-dependent load function. Also, the SDOF alone is incapable to detect the variation in the mechanical properties over the depth of the element. Thus, more studies are needed to validate and develop the SDOF approach in the blast response filed especially when plastic deformation is expected in the element.

With the developing in the computer technology, finite element analysis FEA solution approach was highlighted to be the compromising solution technique to solve the complexity involved in the dynamic response with more accuracy by including all the

potential affecting factors such as the variation in the thermal and mechanical properties in the element. Most of the numerical studies of the blast and impact response have been conducted by using LS-DYNA and ABAQUS explicit codes which were proven to be adequate in simulating the high-velocity impact problems. However, obtained numerical results highly depend on the constitutive material models which are simulated by using user-defined models with many assumed factors. It is so complicated to provide a comprehensive numerical model to simulate the blast resistance of the FRPs composite elements due to the various in the mechanical behaviour and the failure criteria of each FRP material which depend on many factors such as the orientation of the fibres inside the composite FRP, the geometrical shape of the FRP composite. While the commercial FE codes adopt 2D failure criteria for the material by neglecting effect of the thickness Also, the mechanical properties of the bonding area provided by the adhesive which vary based on the shape and the type of the FRP composite add complexity to the numerical modelling, while most of the FEA codes simulate the interfacial area as a cohesive element.

Similar to the experimental studies, most of the conducted numerical studies have focused on enhancing the load capacity of the element by using EB FRP plates on the tension face. As the debonding failure of this type of strengthening technique is the dominant failure mode, most of the numerical studies focused on developing models to simulate the premature debonding behaviour. Less focus was dedicated on enhancing the ductility and the dissipated energy of the element numerically. This can be obtained only by investigate the blast response in the structure with high level of plastic deformation. So, more numerical studies are needed in terms of validating the proposed numerical models with the experimental results with different parametric factors and developing numerical models by considering all the potential factors which affect the blast response of the structure.

By considering all the above-mentioned factors in the future research, the blast performance of the structures and their components can be understood properly. That, as a result, will help to produce guideline and design procedures for the blast load protection to mitigate the destructive effect of the rising terrorist explosion attacks.

To that end, this study is aiming to fill the gap that highlighted in the literature, especially in enhancing the energy dissipation and ductility of the element to cope with the out-of-plan loads, by conducting experimental studies of one-way RC slab strengthened by NSM CFRP rods subjected to loads with low and high strain rates. The one-way RC slab was selected to control the strength capacity of the specimens to reduce the impact energy needed to fail the specimen to be within the capacity of the equipment used in the lab. The low strain rates were obtained by conducting a quasi-static test while the high strain rate was obtained by conducting impact tests. The reason for imposing two different strain rate regimes is to understand the difference in the behaviour of the RC NSM CFRP system under different strain rates. The focus of the study is on ductility, load carrying capacity, dissipated energy, crack patterns and failure modes. Analytical and numerical simulation of the RC NSM CFRP rods system under load with low and high loading rate is also studied with different parameters to investigate the adequacy of the adopted nonlinear simulation models.

CHAPTER 3: EXPERIMENTAL PROGRAM

3.1 Introduction

One of the main objectives in this study is to investigate the behaviour of one-way RC slab strengthened with a near surface mounted Carbon Fibre Reinforced Polymer system (NSM CFRP) under loads with different loading rates. The main focus in this chapter is to quantify the enhancing of the dissipated energy in the RC slab when NSM CFRP strengthening approach is used. Interpretation of the entire response of the slab with and without applying the strengthening approach under load with different loading rate is another objective in this study. To achieve these objectives, an experimental programme was conducted on several slabs, with and without strengthening, subjected to loads with different strain rates. To conduct that, quasi-static loading and impact loading were applied in the tests to induce low and high strain rate effects respectively. In this study, only strengthening the flexural response of the RC slabs was considered, while strengthening the shear response was neglected. The bonding properties between the reinforcement and the concrete was neglected as well since the debonding failure was controlled by providing a sufficient bonding area. This chapter presents details of the experimental programme and the results obtained from both sets of tests with highlighting the key points and the limitations in the obtained results. The results obtained in this chapter will be used in chapter 5 to validate the analytical and the numerical models that were developed in chapter 4.

3.2 Experimental program

3.2.1 Description of specimens

In this study and in order to investigate the response of the CFRP NSM RC system under loading with low and high strain rate effects, a series of experiments were conducted. Eight one-way slabs with dimensions of 1000x500x50 mm were prepared and tested with different NSM strengthening layouts (no strengthening, strengthening with NSM CFRP on one face, strengthening with CFRP on both faces) and under different loading conditions (quasi-static and impact load). A similar main steel reinforcing scheme was adopted in all slabs with reinforcing ratio of 0.78%. This percentage was selected to be between the minimum reinforcing ratio (0.2%) and the maximum reinforcing ratio as

using the minimum reinforcing ratio led to exhaust all the ductility available in the reinforcing bar simultaneously with the crushing in the concrete which makes applying the strengthening technique adopted in this study useless, while using higher reinforcing ratio led to increase the load capacity of the slab which might exceed the limit capacity of the equipment used in the test. Thus, these parameters were selected to minimize the applied load needed to fail the slabs due to the limited capacity of the equipment used (weight and height of the dropping mass) and to ensure enough amount of the spare ductility available in the steel reinforcing bars which the main aim of this study is to use it. More details about the specification of the specimens and the justification for these specification are provided in Appendix B.

Descriptions of the specimens and experiments are given in Table 3-1. Details of the strengthening NSM technique used in this study are illustrated in Figure 3-1.

Table 3-1: Scheme of the strengthening in each specimen.

Specimen	State of the specimen	Type of testing	fc' MPa	CFRP in the comp. face	CFRP in the ten.
QC1	Control	Quasi-	28	-	-
QC2	Control	Quasi-	35	-	-
QS1	Strengthened	Quasi-	43	7φ4mm	3φ4mm
MC0	Control	Impact	23	-	-
MC1	Control	Impact	23	-	-
MC2	Control	Impact	30	-	-
MS1	Strengthened	Impact	38	7φ4mm	-
MS2	Strengthened	Impact	30	7φ4mm	-

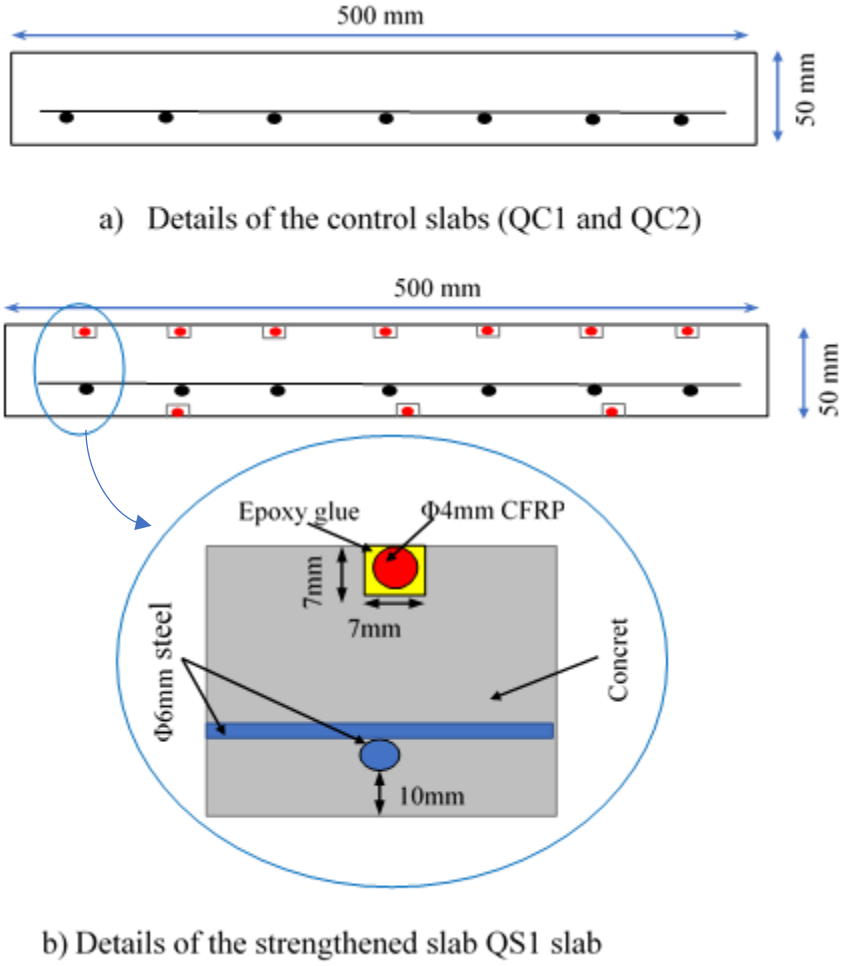

Figure 3-1: Details of the internal and the external reinforcement in the cross-section of the test slabs.

3.2.2 Material properties

3.2.2.1 Concrete

The concrete used to cast the specimens and the cubes were prepared by using Cement CEM I 32,5R, Gravel Shingle crushed limestone with a maximum size of 10mm as coarse aggregate and sharp/grit sand as a fine aggregate. A concrete mixer with a capacity of 50 liters was used to mix the constituent materials cement, sand and aggregates in proportions of 1:1.5:3. Multiple batches were needed due to the limited capacity of the mixer. Accelerator and plasticiser admixture agents were used to enhance both the workability and the early strength of concrete by reducing the water/cement ratio to 0.29%. Table 3-2 shows the ratio of materials used in each specimen.

Table 3-2: Proportions of constituent materials in the concrete mixture.

Cement (kg)	Fine aggregate (kg)	Coarse aggregate (kg)	Water (L)	Accelerator (L)	Plasticiser (ML)
16.5	25	50	4.75	0.4	50

Since the specimens were cast using a different batch of concrete and were tested at different ages, the concrete compression strength of each specimen was assessed individually by conducting compressive tests on two concrete cubes (150 x 150 x150 mm) which were cast with each specimen. The first cube was tested to estimate its strength after 7 days and the second cube was tested on the day when the corresponding specimen was tested. The latter result was used in the subsequent analytical and numerical simulations. The compression tests of the cubes (Figure 3-2) were conducted in accordance with BS1881-Part 116 (1983)(Standard, 1881).

Figure 3-2: Concrete compressive test of the cubes.

3.2.2.2 Steel reinforcement

A similar steel reinforcing layout was adopted for all the specimens by embedding two layers of steel reinforcing bars (Figure 3-3) in the concrete. The first layer consisted of 6mm deformed steel bars along the span length at a spacing of 70 mm with a clear cover of 10mm from the bottom face of the specimen to represent the longitudinal reinforcement for the flexural requirement. The second layer consisted of 6mm steel deformed bars set on the first layer spread at a spacing of 140mm to represent the transverse reinforcement. The mechanical properties of the steel bars were obtained by conducting a direct tension test by using the INSTRON 1341 machine. Figure 3-4 shows the stress-strain relationship of the steel reinforcing bar as obtained from the tension test. The obtained results indicate that the yielding strength of the steel bars is 460 MPa and modulus of elasticity is 185 GPa as listed in Table 3-3.

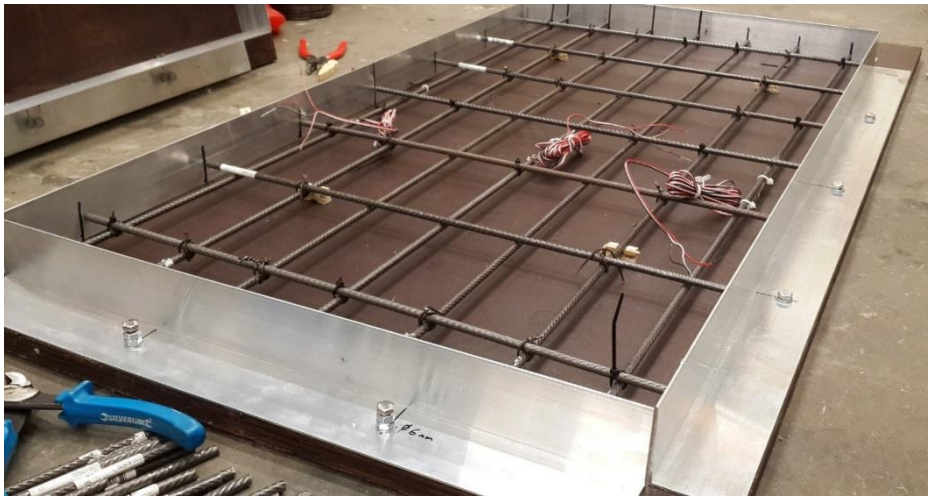

Figure 3-3: Details of the steel reinforcement mesh in the specimens.

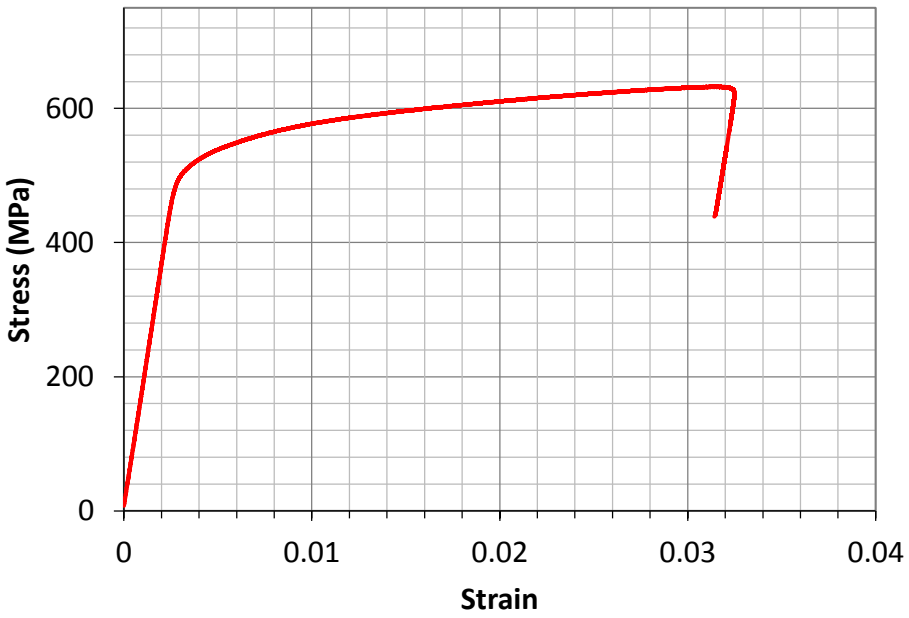

Figure 3-4: Stress-strain relationship of the steel bars obtained from coupon tension test.

3.2.2.3 CFRP bars

To strengthen the slab a composite CFRP material was used in this study. It consists of two parts - Carbon fibers and resin. The mechanical properties of this material depend on the ratio of the Carbon fibres to the resin in the composite. This composite is manufactured in the form of plates and rods with different cross-sectional shapes. In this study, CFRP rods with a diameter of 4 mm were used. The structural material of the composite is T300 carbon fiber. The percentage of carbon fiber in the composite is 60% and the rest is an epoxy resin. The maximum tensile strength, the strain at rupture and the modulus of elasticity of the CFRP rod are listed in Table 3-3 which were obtained by conducting coupon uniaxial direct tension test on a specimen by using INSTRON 1341 machine. Figure 3-5 shows the stress-strain relationship of the CFRP rod as obtained from the tension test.

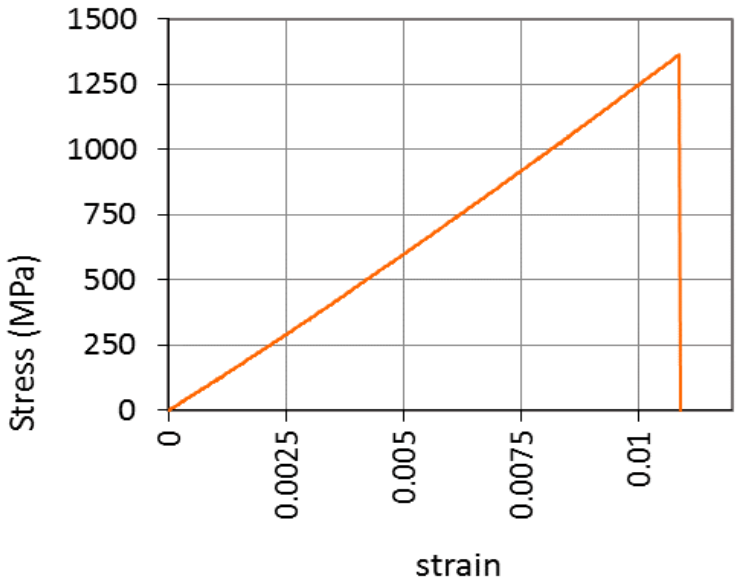

Figure 3-5: The measured stress-strain behaviour of CFRP rod under uniaxial tensile stress.

3.2.2.4 Adhesive

The adhesive material used to bond the CFRP rods inside the grooves on the top and the bottom face of the concrete slab is epoxy Sikadure-31 CF. This epoxy consists of two parts; resin and hardening with a mixing ratio of 2:1 according to the instruction catalog. This epoxy adhesive resin has a compression strength of 33-62 N/mm^2 , a tensile strength of 9-31 N/mm^2 and a bond strength with concrete of >4 N/mm^2 after 1 day of curing based on the curing temperature of 20^o C according to the manufacturer as shown in Table 3-3. The mechanical properties of the Sikadure 31-CF are provided by the manufacturer in form of data sheet which can be found online in their web page (Sikadur-31CF)

Table 3-3: Mechanical properties of the structural materials.

Property	Steel Rebar	CFRP	Epoxy (after 1-day curing) *
Type	deformed	Smooth	Sikadur 31 CF
Diameter (mm)	6	4	
Yield stress (MPa)	460	-	-
Ultimate compression strength (MPa)			33-62
Ultimate tension strength (MPa)	630	1400	>4 (concrete failure)
Modulus of elasticity in tension (GPa)	183	128	6.0
Modulus of elasticity in compression (GPa)			5.5
Fracture elongation %	3	1	50

*: according to the manufacturer

3.2.3 Construction and specimen preparation

3.2.3.1 Formwork preparation

To cast 1000x500x50 mm RC one-way slabs, four small-scale moulds were manufactured, so, four specimens could be cast with one batch of concrete. The mould consisted of plywood for the bottom face of the slab to ensure a flat and smooth face and aluminum angle sections around the borders to obtain flat and vertical edges for the specimen. The aluminum sections were fixed to the plywood using bolts, so it was easy to remove them when the concrete has cured. Figure 3-6 shows a mould used to fabricate the specimens.

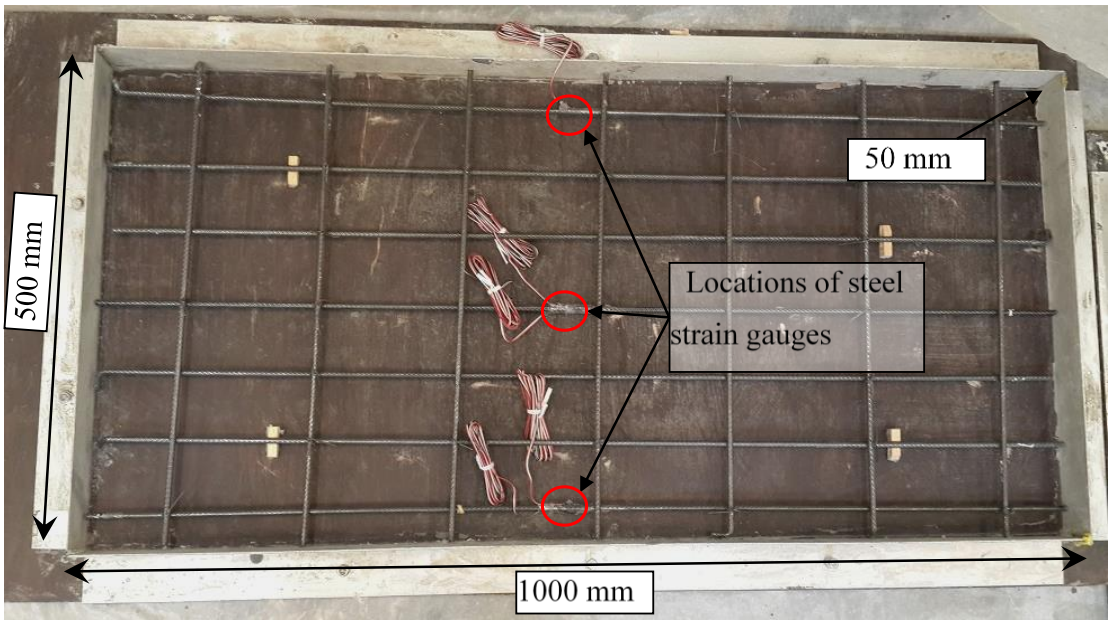

Figure 3-6: Formwork for concrete slab specimens

3.2.3.2 Concrete casting and curing

Before pouring the concrete, the mould was oiled to prevent any bonding between the mould and the concrete. Then the steel reinforcement is placed inside the mould after bonding the strain gauges on the bars and wrapping the strain gauges with a thick layer of silicon to protect them from any harsh environment. The concrete was mixed by using a concrete mixer and poured inside the mould. A hand vibrator is used to ensure good consolidation. The concrete in the top surface of the mould was leveled off and finished by using trowels to give the specimen a smooth surface. One day later, the concrete was covered with wet burlap and plastic sheet to prevent any shrinkage cracking and to allow for curing until it reached the desired strength based on a uniaxial compression test of concrete cubes which were cast simultaneously with each concrete batch and cured in water for 7 and 28 days. Figure 3-7 shows the process of casting both the specimens and the concrete cubes.

a) Casting and compacting the concrete.

b) Preparing the cubes of the concrete.

Figure 3-7: Process of casting the specimens and the concrete cubes used to define strength of the concrete at the testing day of each slab.

3.2.3.3 Applying the CFRP bars

The CFRP bars were applied to strengthen the slabs by using the NSM technique. The process of applying the CFRP in the strengthened slabs started after more than 28 days from the casting date. Two steps were followed to apply the strengthening CFRP material. The first step comprised cleaning and leveling the allocated surface on the concrete slab where the CFRP bars were installed. The location of the CFRP bars was determined by

marking the length and the spacing distance between the CFRP bars on the allocated area. Grooves were then cut after deciding the width and the depth for each groove where width and depth of each groove depend on the size of the CFRP bar and thickness of the epoxy layer used in bonding. In this study, CFRP bars with 4 mm diameter and the epoxy layer with thickness of 1.5 mm was used, therefore, a square cross-section with dimensions of 7 x 7 mm was decided for the grooves. In the present study, the grooves were cut by utilizing the wall chaser machine from Draper Expert 1500W after adjusting the width and the depth of the grooves from the adjusting buttons.

The second step in the applying the NSM CFRP method is to apply the CFRP rods inside the grooves by using epoxy resin to achieve strong bonding with the surrounding concrete. In this step, the grooves were washed down, and air gun was applied inside to remove debris and dust from the grooves. The Epoxy resin type Sikadure 31-CF was prepared and mixed according to the instructions and then applied inside the grooves by using application gun after filling the epoxy inside a cartridge. The epoxy was left to cure for at least one day to achieve the sufficient strength before conducting the test. Figure 3-8 shows the implemented steps of applying the NSM CFRP bars.

a) Preparing the grooves by using a wall chaser machine.

b) Inserting the CFRP rods inside the grooves.

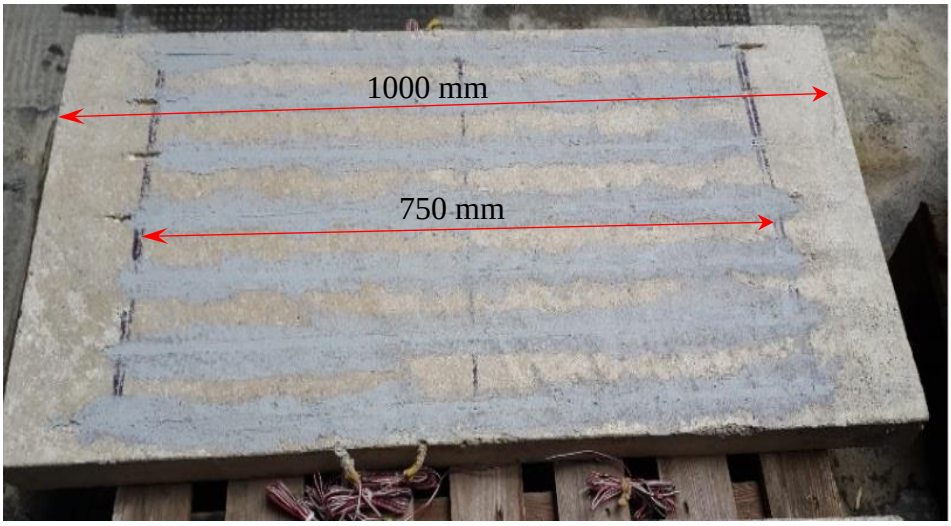

c) Bonding the CFRP rods inside the grooves by using epoxy adhesive.

Figure 3-8: Processing of applying the NSM CFRP technique.

3.3 Instrumentation

To measure the output of the experimental test accurately, several good quality devices were used in the test. The load was measured by using Sensotic strain gauge load cell sensor provided by Vishay company which is capable to detect both the quasi-static and dynamic load. The vertical displacement at the mid-span of the slab was measured by using a linear variable differential transformer (LVDT). Two types of strain gauges were used to measure the uniaxial linear strain of both the steel reinforcement and the top fiber of concrete at the mid-span of the specimens. For the steel reinforcement bars, strain gauge type C2A-06-125LW-350 with a resistance of 350 Ohms and dimension of 5 x 3 mm which is provided by Micro-Measurements company (Division of Vishay Precision Group) was fixed on the steel bars by using M-Bond AE-10 glue which is provided by Micro-Measurements company. The compression strain of concrete was measured by using linear strain gauge type PL-60-11 provided by Tokyo Sokki Kenkyujo company with the length of 60 mm and resistance of 120 Ohms. M-bond A-10 glue was used to bond the strain gauge on the concrete after preparing the surface by degreasing and smoothing the surface. All these sensors were connected to a Vishay StrainSmart System 6000 data logger with a parallel recording frequency of 1 and 5 kHz to record the output data for both the quasi-static and impact tests respectively. (see Figure 3-9). Procedure for installing the strain gauges is described in the following section.

3.3.1 Strain gauge installation

Before bonding the strain gauges, both the steel and the concrete surfaces were prepared well by following the procedure recommended by the manufacturer. Both the steel and concrete surfaces are flattned and grinded by using sand papers with different grads range from 180 to 400 grits as recommended for good preparation. To release the prepared surfaces of any loose particles and grease, an air gun and Acetone solution is used. The prepared surface in both cases the steel bars and the concrete were coated by a thin layer of the M-Bond A-10 adhesive which consists of two parts after following the instruction provided by the manufacturer. Figure 3-10 presents photos of both the steel and the concrete strain gauges which shows that both the steel and concrete strain gauges are positioned in the mid-span of the specimen to record the potential maximum strain in the critical section of the element.

a) StrainSmart data logger System 6000

b) Load cell

c) LVDT

Figure 3-9: The instruments used in the test; a) the data logger system, b) the load cell and c) the LVDT.

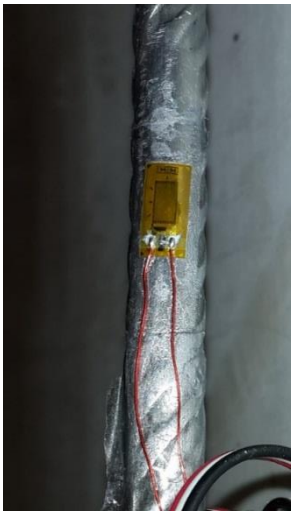

a) Steel strain gauge

b) Concrete strain gauge

Figure 3-10: Strain gauge of both a) steel reinforcement and b) concrete that used in the specimens.

3.4 Test setup

Both quasi-static and impact tests were carried out in the Structures Laboratory at the University of Bristol. The specimens were supported at both ends on rigid members to mimic a simply supported state, with a clear span of 830 mm. The quasi-static loading was applied via a manually-operated hydraulic jack in a slow loading rate (about 0.25 $kN.S^{-1}$). For simulating the uniformly distributed load in the quasi-static test and to avoid any premature shear failure due to any concentrated load, the applied load was spread on the slab by using load spread rig named an airbag. The principal idea of the airbag was using four large air-filled latex balloons confined by a steel plate from the top and wrapped by a high tensile strength woven carbon fiber twill (Mitsubishi Rayon Grafil Pyrofil TR505 12L 12K tow), as shown in Figure 3-11-a. The reason for using the airbag to spreading the load is to follow the deflection shape of the specimen for differernt stages of loading by utilizing the flexibility provided by the latex balloons.

In contrast, the impact test was conducted by dropping a mass of 25 kg from a height of 4 m guided by a 5 m long aluminum tube to impinge the specimen at its centre. For simulating the uniformly distributed blast load, the concentrated impact load was spread by using a whiffletree to avoid any premature shear failure as shown in Figure 3-11 as the airbag lead to change the impact load function by extending the duration of loading and reducing the peak impact force due to the flexibility of the balloons which makes the load function different than the blast load function. The principle idea of the whiffletree is to transform the concentrated point load to four lines loads spread on the slab with spacing distance between them. The reason for not using the airbag in the impact test

To avoid any damage in the concrete due to the hard impact, rubber pads with thickness of 12 mm were used in the contact surfaces. The impact test was conducted by applying multi-impact blows with an estimated impact energy of 1000 J. The frame was set on four corners and another load cell was set under one corner as shown in Figure 3-12 representing roughly 25% of the total reaction then to estimate the total reaction in addition to the top load cell which measures the impact load. The impact and the reaction forces on each slab were recorded in addition to the displacements and the steel and concrete strains at the mid-span section.

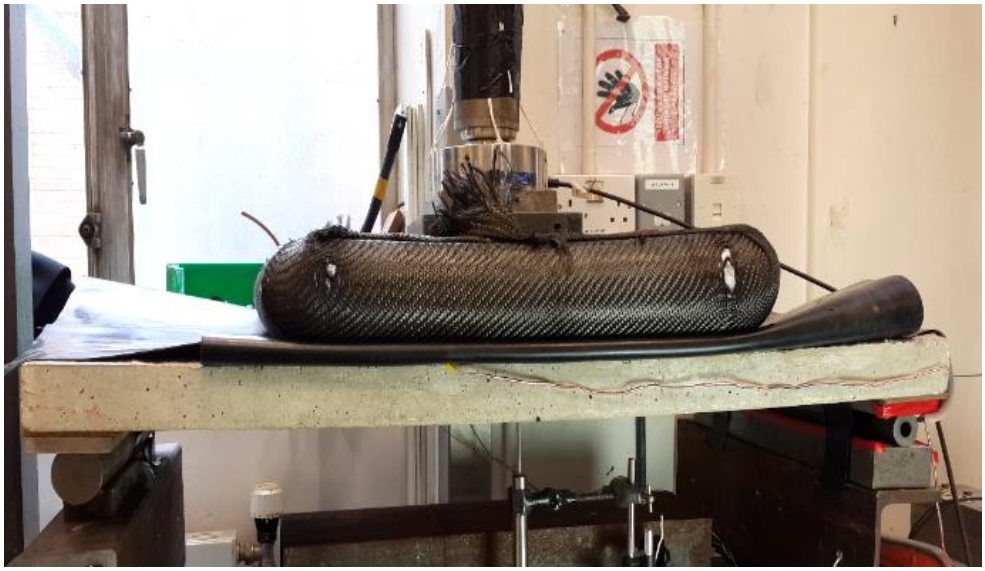

a) Airbag load layout in the quasi-static test

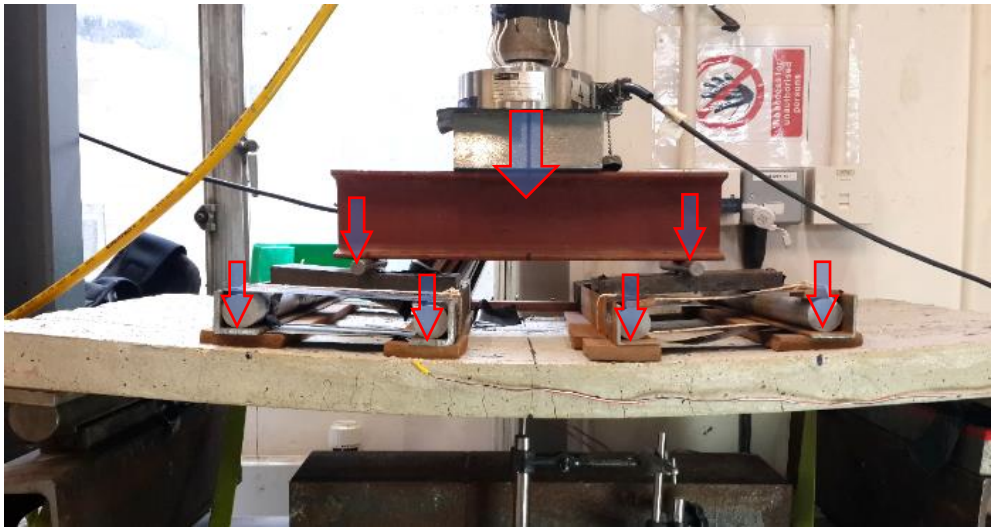

b) Whiffletree load layout

Figure 3-11: The two rigs adopted to spread the load on the specimens a) airbag and b) whiffletree rigs

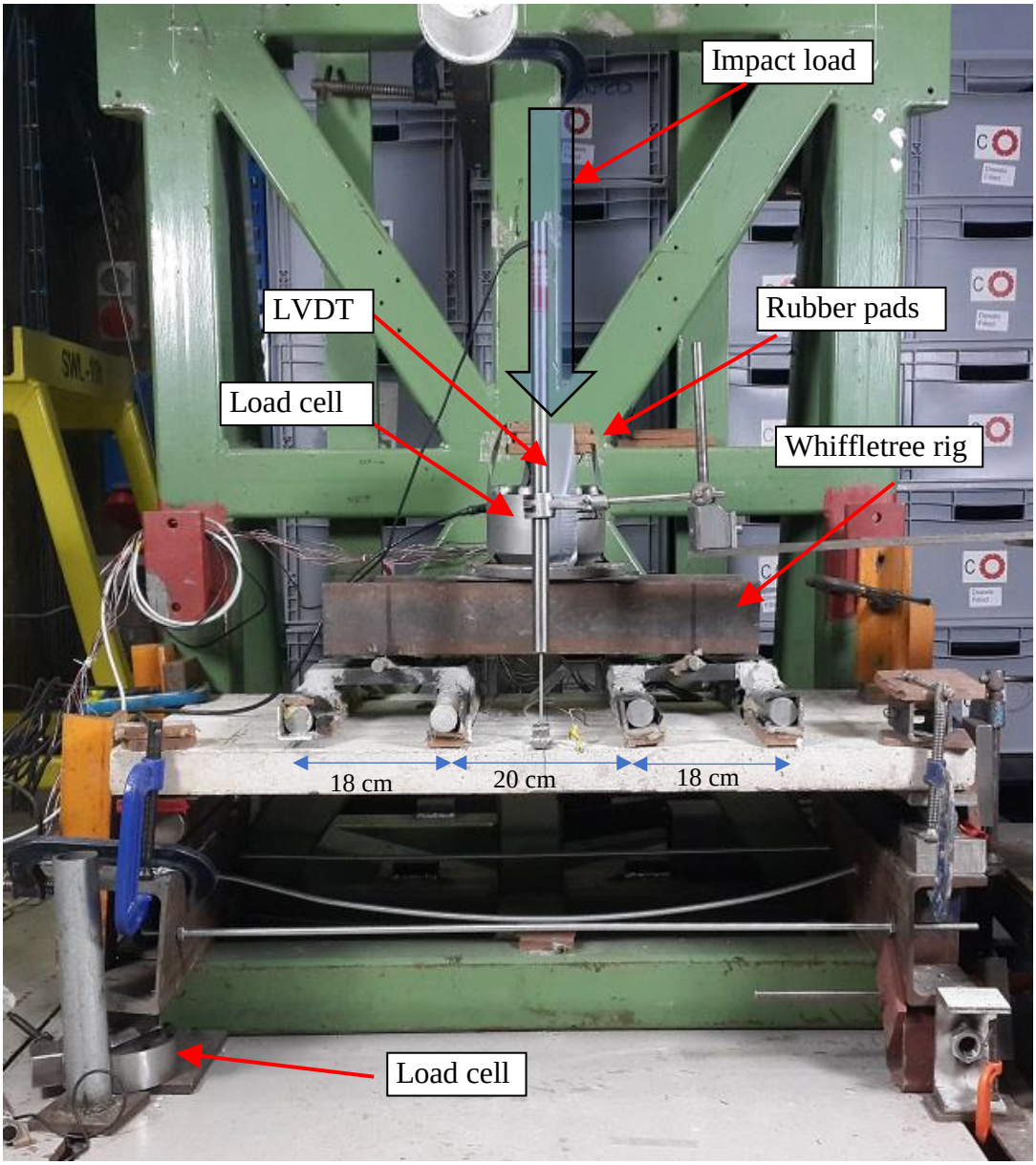

Figure 3-12: Frame and rigs of the impact test.

3.5 Analysis of the experimental data

For each type of test, comparisons were made between the control and the strengthened slabs based on many factors including load capacity, ductility, and the energy dissipation based on the measured data of load, deflection and steel and concrete strains and the post-test observation of the crack patterns and the failure mode. For the quasi-static tests, the peak applied loads were considered to compare load capacities. For the impact tests, both the impact load and the reaction at the support were considered to compare load capacities. After Meisami et al (Meisami et al., 2013), the ductility has been represented

by the ratio of the maximum displacement to the first yield displacement at mid-span of the slab. The total energy of each case was calculated by integrating the area under the load-deflection curve by applying equation (3-1) which was proposed by Sastranegara (Sastranegara et al., 2005) as following:

$$E_t = \int_0^{Ui} p_{(U)}\, dU \qquad 3\text{-}1$$

Where E_t is the total energy quantity, P and U represent the load and mid-span displacement.

Then the energy dissipation (E_d) was calculated by taking out the energy absorption (elastic) from the total energy as shown in equation3-2.

$$E_d = E_t - E_b \qquad 3\text{-}2$$

Where the energy absorption (E_b) of each case refers to the elastic energy and was calculated directly in the quasi-static test from the unloading behaviour of the load-deflection curve (p-δ). While in the impact test, due to the difficulty of obtaining the yielding load, the energy absorption was estimated approximately as the ratio of the difference between the maximum and the residual displacement to the maximum displacement as proposed by (Ha et al., 2011).

In contrast to the quasi-static tests, in the impact tests, it is difficult to obtain the actual total and the dissipated energy based on the area under the load-deflection curve, since the measured impact-time profile found to be non-synchronic with the measured reaction-time profile. This is similar to what has been reported by many previous studies (Sangi, 2011, Batarlar, 2013, Saatci, 2007). In addition to that, the impact force tends to act on the structure as an impulse rather than as an incremental force. So, for the comparison purpose of this study the total and the dissipated in the impact tests were calculated based on the area under the load-deflection curves for both the impact and the reaction forces separately.

3.5.1 The quasi-static results

3.5.1.1 Load-deflection behaviour

The quasi-static load was applied in multiple stages (two stages on the control slabs and four stages on the strengthened slab) by submitting the specimen to a loading and unloading process to obtain the unloading stiffness at any stage which is used to estimate the energy absorption (elastic energy). Figure 3-13 and Table 3-4 present the obtained results for each slab and for all loading stages except for slab QC2 where the second stage of loading was not recorded due to a problem in holding the LVDT. It is found that the load capacities were 25.1, 23.5 and 49.4 kN for the control and the strengthened slabs QC1, QC2 and QS1 respectively. This indicates a significant increase in the load capacity of about 100% by strengthening both faces of the slab (including effect of the change in the strength of concrete). The maximum mid-span deflections for slabs QC1, QC2 and QS1 were 27.3, 34.0 and 34.4mm, while the ductility factors were 3.3, 3.0 and 2.4 respectively. This suggests a reduction in the ductility factor of about 20% in the strengthened slab compared to the control slab. This reduction was expected due to the reinforcing of the tension zone externally by using 3ϕ4mm NSM CFRP rods in addition to the compression strengthening. The ductility level could be even lower if the compression face of the slab was not reinforced by 7φ4mm NSM CFRP rods since the more tension strengthening ratio the lower ductility level obtained (Ramana et al., 2000, Dias et al., 2018). Overall, this indicates that the reduction in the ductility level of the slab when only the tension face of the slab is strengthened can be overcome if the compression face is strengthened too.

Table 3-4: Results of the quasi-static tests.

Slab	State	Compression strength of concrete f_c' MPa	Yeilding load P_y kN	Ultimate load Pu kN	Yeild deflection δy mm	Ultimate deflection δu mm	Ductility (δμ/δy)	Dissipated energy E_d (J)	Failure mode
QC1	Control	28	17.4	25.1	6.3	27.3	3.3	424	CC*
QC2	Control	35	13.8	23.5	8.4	34.0	3.0	-	CC
QS1	Streng-thened	43	18.9	49.4	10.0	34.4	2.4	901	SF*
Where CC and SF mean concrete crushing and shear failure.									

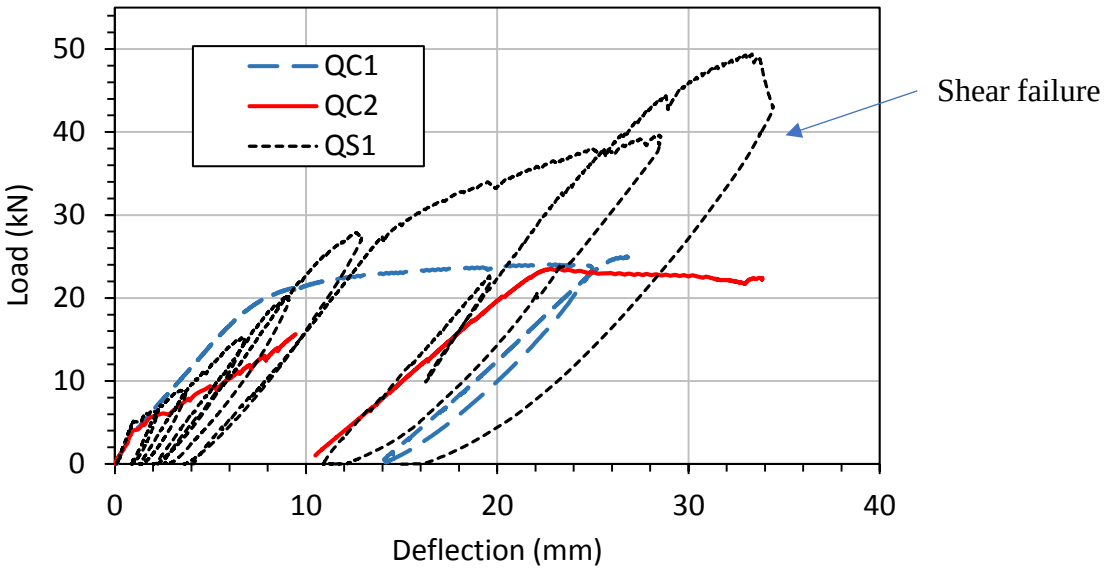

Figure 3-13: Load-deflection curves for slabs QC1, QC2 and QS1 under quasi-static loading test.

3.5.1.2 Crack pattern and failure mode

Figure 3-14-b, Figure 3-15-b and Figure 3-16 show the crack-pattern in the tension zone of both the control slabs and the strengthened slab. While Figure 3-17 shows the failure mode obtained in each slab. They show that the crack pattern was represented by one major opened crack in the tension zone of the control slabs and the failure was represented by crushing of concrete. In contrast, the shear failure was the dominant failure mode in the strengthened slab which was represented by an inclined crack near the right support as shown in Figure 3-17-c.

Figure 3-16-c shows that elsewhere along the strengthened slab, many finer cracks were spread along the span. This multi-crack pattern is desirable since it contributes to reduce the width of the major crack and as a result, reduces the maximum steel strain which is proportional to the width of the crack.

For both the control slabs, it was observed that the cracks on the lower face tended to be wavy rather than straight transversely (Figure 3-14-b and Figure 3-15-b). No debonding of any of the NSM rods was observed. There were no perceptible cracks in the epoxy bonding material either, indicating less concern regarding premature debonding failure

when using the NSM technique as compared to the Externally Bonded (EB) technique. In the latter, debonding of the composite laminate material is often the key factor of the premature failure mode (Lee et al., 2008, Mukhopadhyaya and Swamy, 2001, Sebastian, 2001). However, debonding of the CFRP NSM bars should be controlled especially when large CFRP bar size is used as the bonding area depends on the ratio of the boundary to the sectional area.

3.5.1.3 The steel and concrete strain profile

Figure 3-14, Figure 3-15 and Figure 3-16 show the load-strain plot of concrete and steel at the mid-span point of the three slabs in the quasi-static test. They show that there is similarity in the strain behaviour at the mid-point of two reinforcement bars for the three slabs up to a strain of about 8000 με. Then the trend of one or both steel bars changed showing a decreasing or increasing in the strain although the load or the mid-span deflection increased continuously. This could be attributed to the tension stiffening behaviour of concrete when a wide crack is opened which leads to make the strain along the steel bar fluctuated as will be described in 4.2.7. At the cracking load, about 4 kN, a sudden reduction in the steel strain was detected in slab QC2 while no such behaviour was noticed in slab QC1. This was found to have an impact on the entire response of the affected slab where a significant drop in the stiffness was noticed in QC2 compared to QC1 as shown in Figure 3-13. This behaviour could be attributed to the wavy crack pattern in the negative moment zone of slab QC1 as described in the previous paragraph (section3.5.1.2) where the steel strain distributed periodically along the steel bar when the surrounding concrete cracks and it jumps to the peak at the crack position and drops between cracks.

3.5.1.4 The total energy and the energy dissipation

The dissipated energy in slabs QC1 and QS1 was calculated based on the area under the load-displacement curve of each case as presented in Figure 3-13. It shows that the displacement of the first loading stage in QC2 was not recorded properly as the LVDT moved from its position during the loading stage, so the dissipated energy of QC2 was not calculated. As shown in Table 3-4 the dissipated energy of slabs QC1 and QS1 were 424.9 and 901.1 J respectively, indicating an increase in the dissipated energy of about

112% (enhancing factor of 2.24) when both faces of the slab were strengthened with NSM CFRP rods (including effect of the changing in the strength of concrete).

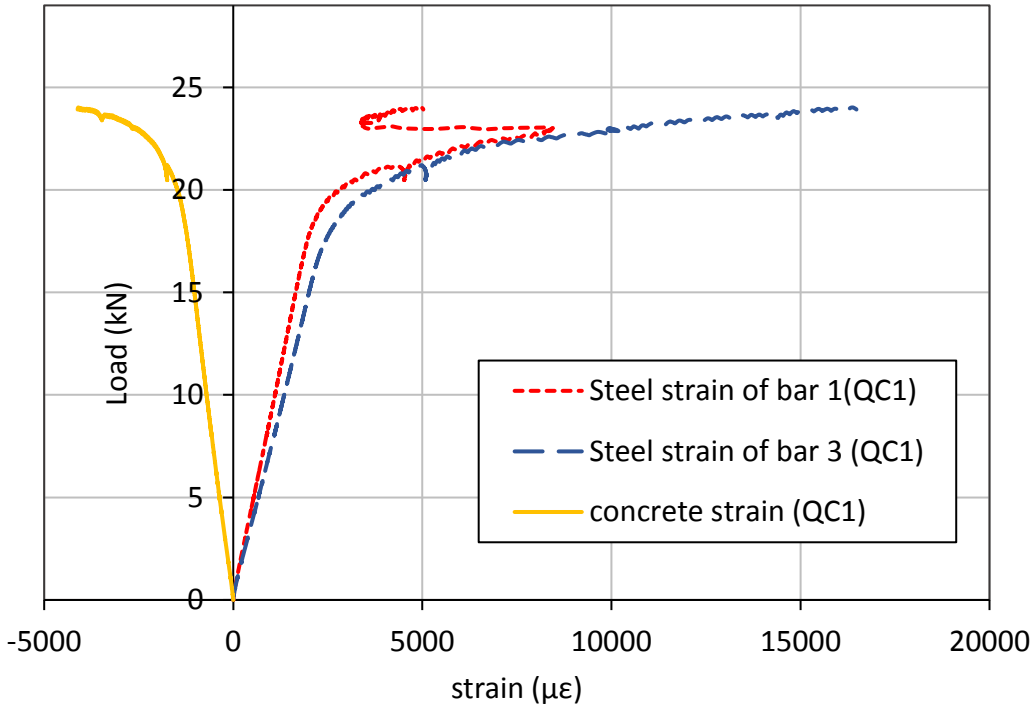

a) Stress-strain behaviour of concrete and the steel bars (bar1, bar 3) based on the position of the steel strain gauges.

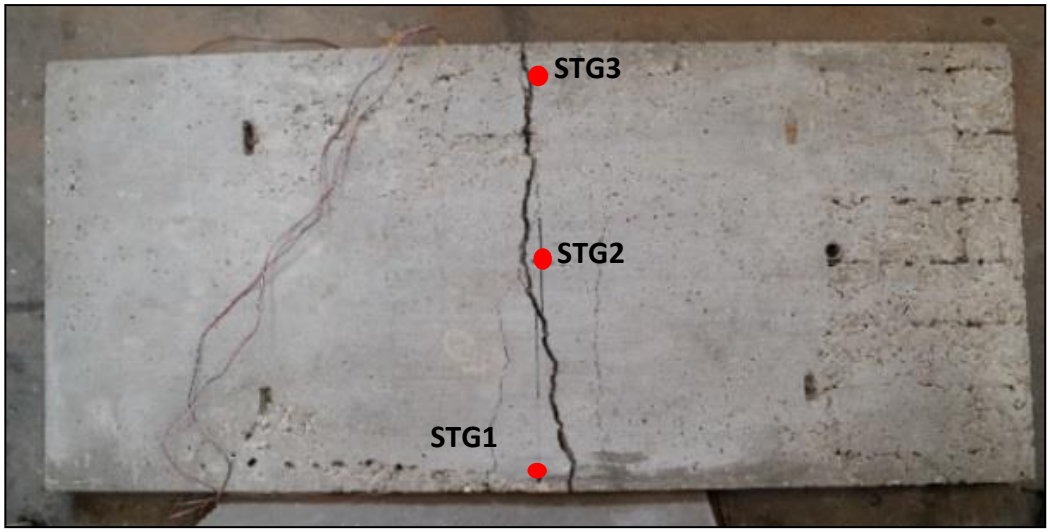

b) The crack pattern in the tension face of the slab and locations of the steel strain gauges (STG1, STG2 and STG3) on bars 1,2 and 3 respectively.

Figure 3-14: Stress-strain behaviour of concrete and steel and the crack pattern in the strengthened slab (QC1) under quasi-static test.

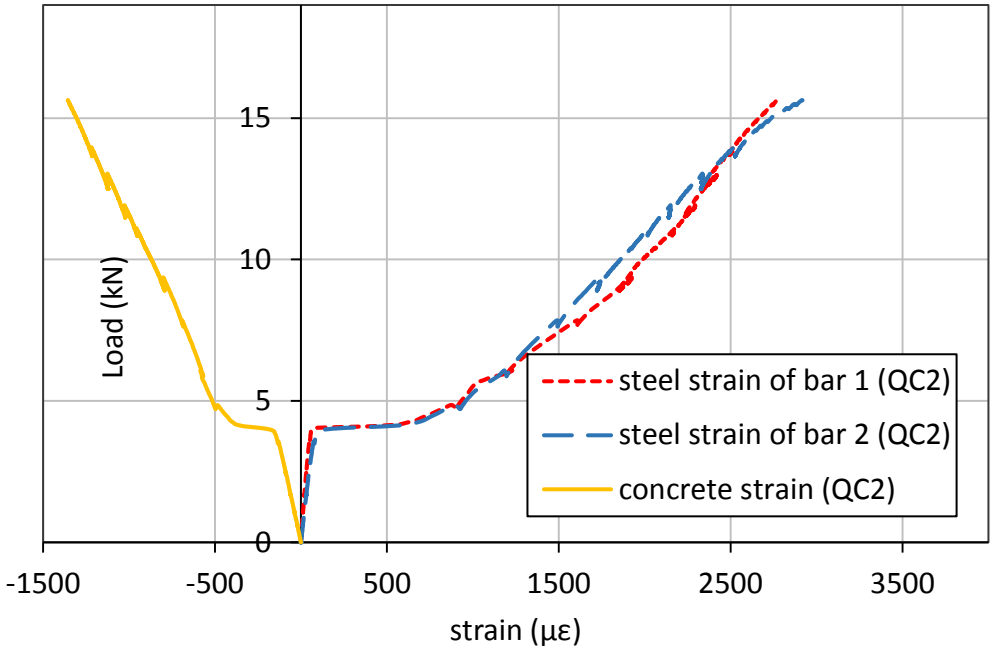

a) Stress-strain behaviour of concrete and steel bars.

b) The crack pattern in the tension face of the slab.

Figure 3-15: Stress-strain behaviour of concrete and steel and the crack pattern in the strengthened slab (QC2) under quasi-static test.

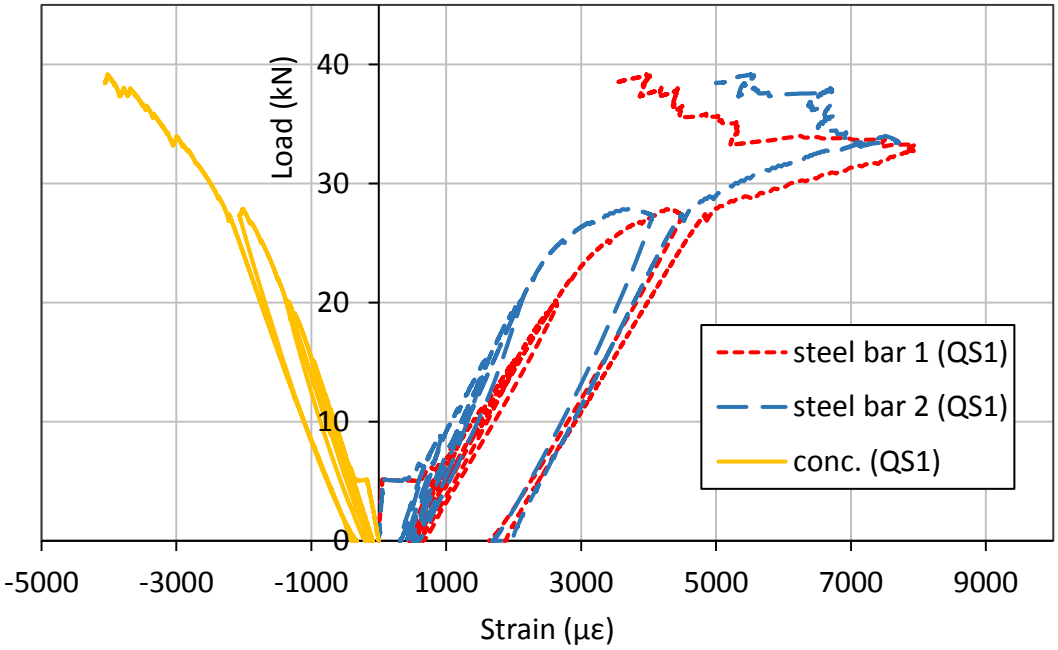

a) Stress-strain behaviour of concrete and steel bars.

b) The crack pattern in the tension face of the slab.

Figure 3-16: Stress-strain behaviour of concrete and steel and the crack pattern in the strengthened slab (QS1) under quasi-static test.

a) Crushing failure mode of slab QC1.

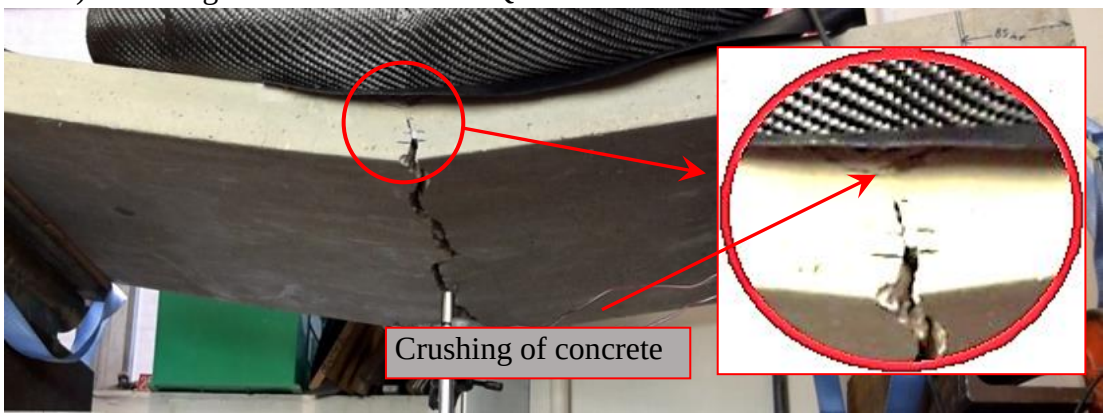

b) Crushing failure mode of slab QC2.

c) Shear failure mode of slab QS1.

Figure 3-17: Modes of failure in slabs; a) QC1, b) QC2 and QS1.

3.6 Discussion of the quasi-static test

A quasi-static test was conducted on RC slabs with and without NSM CFRP strengthening approach. In this test, the load was applied incrementally by using displacement control method. To spread the load on a wide area on the slab, an airbag rig was designed by using flexible balloons which are confined by a stiff fabric to increase the load capacity of the rig. For more load capacity. During the test, load, deflection and strains of steel and concrete at the mid-span of the slab were measured

simultaneously. The obtained results and the limitation of the quasi-static test is briefly presented in the following paragraph.

Based on the measured data of the load, deflection and strains in the low strain rate loading, it was found that applying the NSM CFRP strengthening approach on both faces of RC slab enhanced its moment capacity, ductility and energy dissipation. Where enhancing in the load capacity and the energy dissipation of about 200% was obtained when both faces of the slab were strengthened with 3 and 7 CFRP bars of 4 mm diameter respectively. Also, it was found that applying the NSM CFRP strengthening approach left his impact on the crack patterns at the end of the test by observing one opened major crack at the mid-span of the control slab compared to multi cracks in the strengthening slab. The latter crack pattern is desired as it contributes to reduce the maximum width of the cracks and spreading the plastic deformation in the steel bars rather than localizing it in one position. Where spreading the plastic deformation helps in increasing the dissipated energy in the slab. No debonding failure or slipping-off was observed in the NSM bars which confirming the less concerning about the delaminating or debonding failure in the NSM CFRP system compared to the EB system as mentioned in chapter 2.

The quasi-static test that conducted in this study was good in assessing the difference in the entire behaviour between the strengthened and the non-strengthened slab. However, some obstacles are involved in the test which limited the optimum utilizing of the obtained results that need to be overcame in the future work for more accurate assessment to the results. The most highlighted limitations in this test can be described as follows:

1. Despite the airbag rig seems apparently good in spreading the load uniformly on the slab, it is difficult to guarantee that the load is applied uniformly unless a pad pressure sensor is used under the airbag. Unfortunately, this instrument is not available in the current test.

2. The strain energy of the steel cannot be estimated based on the measured steel strain at the mid-length of the steel bars as it depends on the strain distribution profile along the steel bars which can be measured instrumentally by covering the entire length of each steel bar with strain gauge(s) which is difficult to be applied in the current study due to the limitation in the data logger system used in this study where

the maximum number of strain gauges is 8 when using one system and 16 when using two systems.

3. The ultimate state in the slab depends on the strain at the top fibre of concrete which can be estimated based on the critical section of the slab. However, it is also sensitive to the crack pattern in the tension face of the slab, where a premature crushing failure occurs when a wide major opened crack pattern happens in the slab. which lead to increasing the strain of concrete at the opened crack section.

4. Calculating the total and the dissipated energy of the slab by integrating the area under the load-deflection curve depending on the measured mid-span deflection is an estimating method. But, for more accurate energy estimating, the deflection-distance profile needs to be measured instrumentally in the test as nonproportional deflection and curvature distribution along the span occurs due to the nonlinearity in the properties of concrete.

3.6.1 The impact test results

3.6.1.1 Effect of the properties of the contact surface on the impact response.

Dropping a heavy body on a structural member produces an impact energy which is transferred as an impact load (transient load). This is a time-dependent function which takes an approximatly triangular shape with two factors: the peak value of the load (F_m) and the duration of the loading (t_d). Studying the effect of the shape of the impact function on the structural response of the member is needed. For this purpose, slab MC0, which is used as an elementary control slab, was subjected to multi-impact drops test by dropping a mass weighs 25 kg from a height of 0.5 m to hit the slab in the center point where the top load cell is located. The load is then spread on the slab by using the whiffletree. In the contact surface between the impactor and the load cell, different layers of rubber pads (1-3 layer) with a thickness of 12 mm were used which is equivalent to thickness of 12, 24 and 36 mm as shown in Figure 3-12. It was found that the same impact energy can produce different shapes of impact load function with different values of F_m and t_d based on the properties of the contact surface between impactor and the impacted bodies as shown in Figure 3-18.

Table 3-5 and Figure 3-18 show effect of the thickness of the rubber pad on variation of the impact load and the deflection with time of slab MC0 (preliminary test). They show that the peak force decreases and the duration of loading increases with the increase in the thickness of the rubber bad. As shown in Table 3-5, when the thickness of the pad increases from 12 to 24 mm (100%) the peak force dropped from 40.0 to 22.3 kN (56%) and the duration of loading increases from 6.2 to 10.0 ms (61%). Also, when the thickness increases from 12 to 36 mm (200%) the peak force dropped from 40.0 to 16.0 (40%) and the duration of loading increases from 6.2 to 13.0 ms (109%). A slight change in the magnitude of the measured impulse occurred when the thickness of the rubber pads changed, where the impulse increased from 91.3 to 98 (7%) when the thickness of the rubber increased from 12 to 24 mm (100%).

Although the impact impulse increased, a reduction in the maximum displacement response, from 8.56 to 8.19 (5%), was recorded when the thickness of the pad increased from 12 to 24 mm (100%). This indicates that the maximum displacement response to the applied impact load is sensitive to both the impact impulse and the peak force of the impact impulse (F_{peak}). Also, it was found that the time of the maximum response (t_m) increased from 11.6 to 15.0 ms (increase of 29%) when the peak force decreases from 40 to 22.3 kN (drop of 56%) indicating decreasing of the deflection rate with the decreasing of the impact peak force. As a result, the strain rate value increases with the increasing of the peak value of the impact force.

Based on the above results, three layers of rubber plates with a total thickness of 36mm were recommended and used in the subsequent impact tests to reduce the peak impact force obtained from dropping the mass with minimal loss in the impact impulse. This is useful for the integrity of the impact load cell to avoid any damage by exceeding its capacity (100 kN).

Table 3-5: Results of effect of thickness of the rubber pad on the load and deflection behaviour.

Mass. kg	Height of drop m	Thickness of the rubber. mm	The peak force (Fm) kN	Load period (t_d).	Impulse (NS)	Maximum displacement. mm	Time of the maximum (t_m). ms.
25	0.5	12	40.0	6.2	91.3	8.56	11.6
25	0.5	24	22.3	10.0	98.3	8.19	15.0
25	0.5	36	16.0	13.0	100.0	8.16	15.8

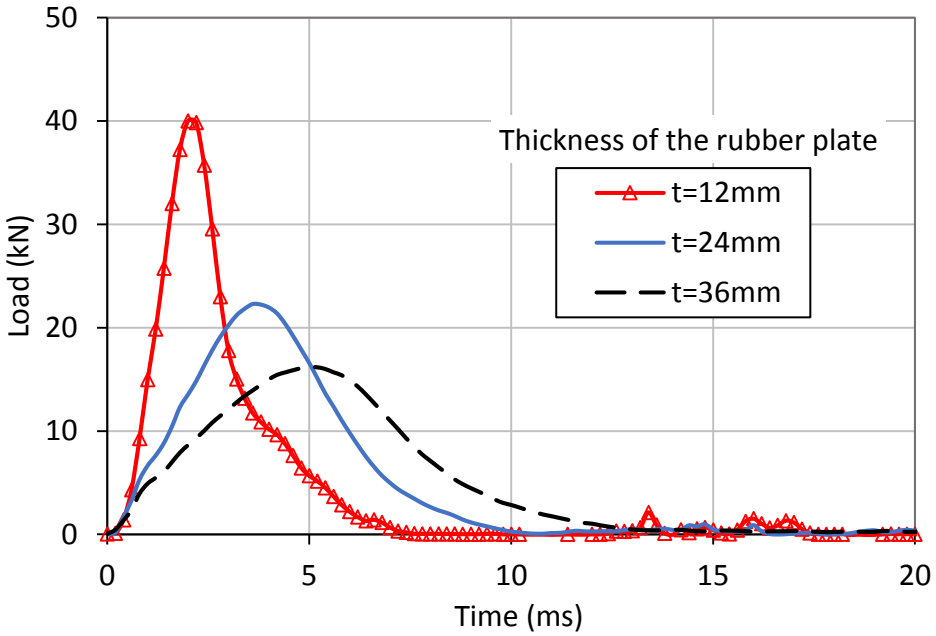

a) The impact impulse (I)

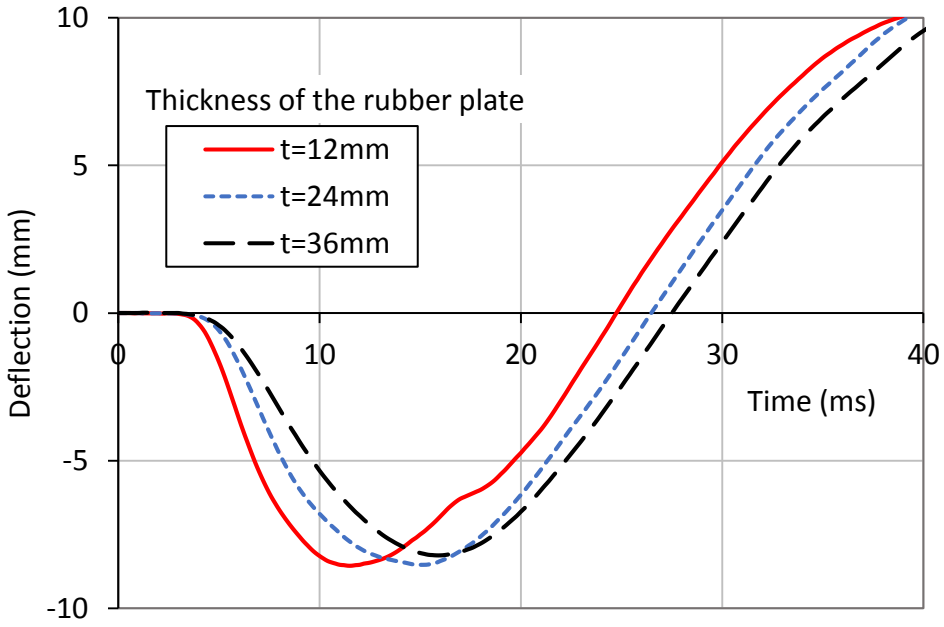

b) The deflection-time profile

Figure 3-18: Effect of the stiffness of the contact surface on (a) the impulse and (b) the deflection of the slab with the same impact energy applied on slab MC0.

3.6.1.2 The impact, reaction and deflection.

In the impact tests, the time history profiles of the impact force, reaction force and deflection were recorded continuously for the impact with a sampling frequency of 5 khz. Figure 3-19 and Figure 3-21 show all the three recorded data during the first drop of the control and the strengthened slab (MC and MS). It is noted that the reaction function lags the impact function by about 5 ms while the deflection function is found to be synchronous with the reaction function. Similar behaviour was reported by previous studies (Sangi, 2011, Batarlar, 2013, Saatci, 2007) where a lag between the impact and the reaction was attributed to the inertia forces of the member which start to resist the impact forces before the impact force is transmitted to the supports.

The impact pulse, with a peak load of 75-80 kN for MC1 and MS1 and 40-50 kN for MC2 and MS2 and loading time of about 9 ms for all, was found to be almost the same for both the control and the strengthened slabs in all drop tests which confirm the dependency of the impact load function on the properties of the contact surface as stated in section 3.6.1.1. In contrast, the reaction function showed different behaviour in each case taking a periodic function (non-uniform) with two different peaks and a total period of 26ms in MC-1 (control slab) and 22ms in MS1-1 and 25 ms for both MC2-1 and MS2-1. It should be noted that atypical reaction-deflection behaviour was obtained when repeating the impact test with same impact energy magnitude on each slab (MC and MS) as shown in Figure 3-20. By comparing the impact load function obtained in this test with the blast load function obtained by conducting real blast test as measured by previous work as presented in Figure 2-15 in chapter 2, a great similarity can be observed between them which indicating the adequacy of using impact loads as simulating to the blast loads.

In terms of the deflection-time profile, a difference of about 10 ms was noticed in the deflection period between MC1 and MS1. Also, a reduction in the maximum deflection under the same impact impulse, was noticed between MC-1 and MS-1 which dropped from 27.3 to 16.6 mm, representing a 39% drop as shown in Figure 3-19. While in the second test, there is no such change in the deflection behaviour of both MC2-1 and MS2-1 as shown in Figure 3-21. This was attributed to the partial crushing failure of the concrete in the compression face which led to increasing both the maximum deflection

and the duration of the deflection wave of slab MC1-1 compared to the other slabs where no crushing failure was detected during the first drop of each slab.

Figure 3-22 shows the historical deflection wave of the control slab based on different impact impulse which is used to calculate the deflection rate in the slab and to estimate the producing strain rates. It shows that the time of the maximum response remain almost constant when different magnitude of impact impulse is applied while the maximum deflection is proportional to the magnitude of the impulse. The independency between the deflection time response and the magnitude of the impulse is reasonable as the transient load was applied in a load control method rather than displacement control method. In this case, the maximum displacement time is sensitive to the natural period of a free vibrated element. Based on that, the deflection rate for the elements subjected to a transient load applied in a load control method is a geometrical dependent factor rather than a load-dependent factor. This seems to be conflicted with what has been stated in Figure 2-6 in chapter 2 where the strain rate regimes were classified based only on type of the loads with neglecting effect of the other factors such as the geometrical shape of the element and position of each structural material over the depth of the element and the natural period of the element which found to play a significant role in determining the deflection or the strain rates in the target elements.

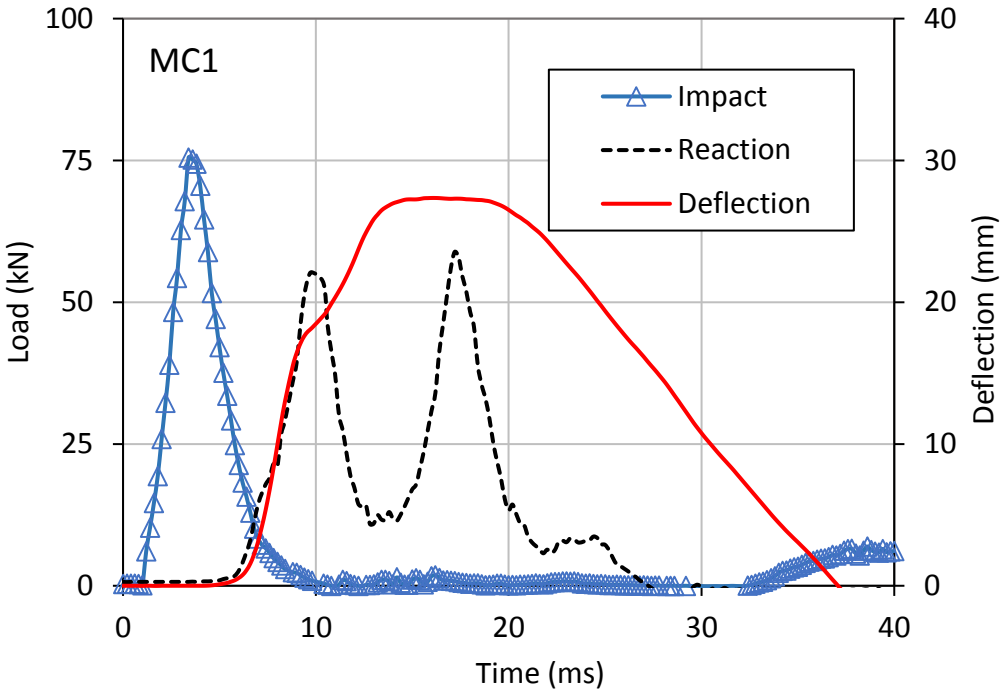

a) The control slab (MC1-1).

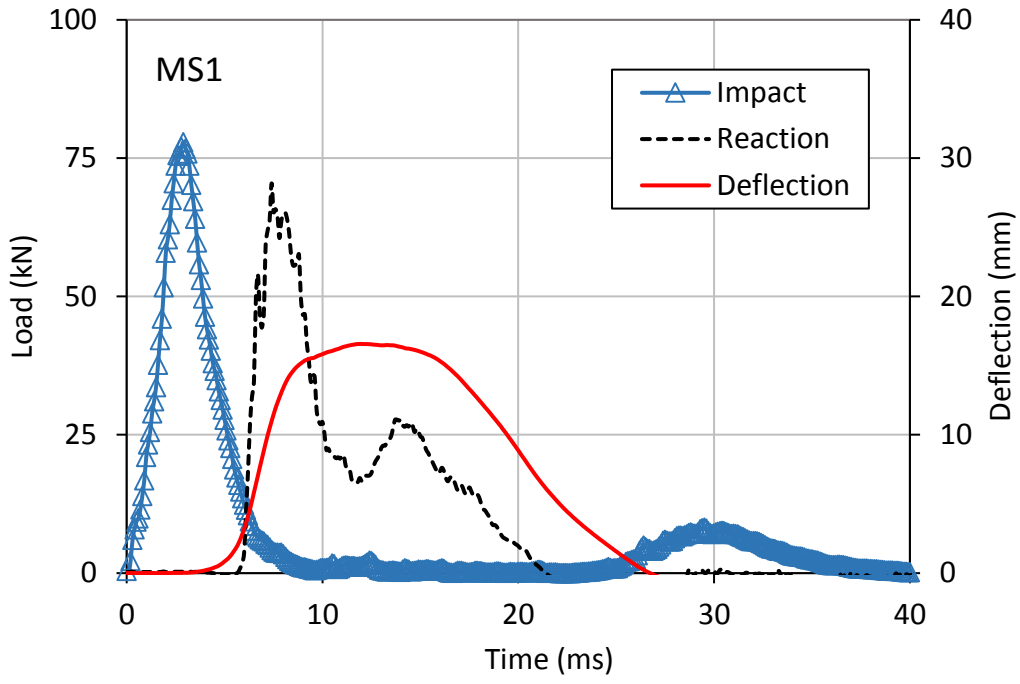

b) The strengthened slab (MS1-1)

Figure 3-19: History of deflection, impact load and reaction of a) the control (MC1-1) and b) the strengthened (MS1-1) slabs during the first impact blow.

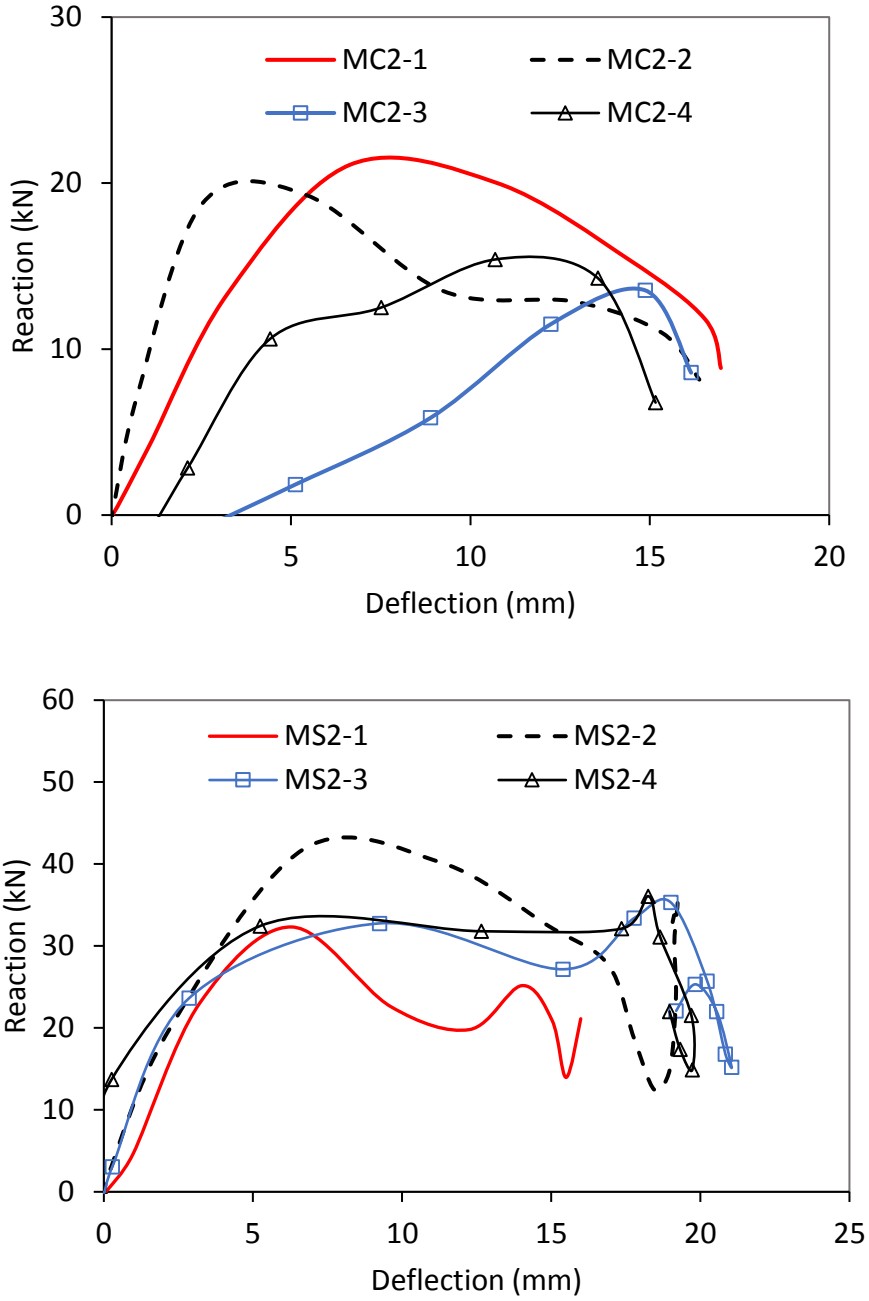

Figure 3-20: Different reaction-deflection behaviour (atypical) of slabs MC2 and MS2 under different impact drops with the same impact energy.

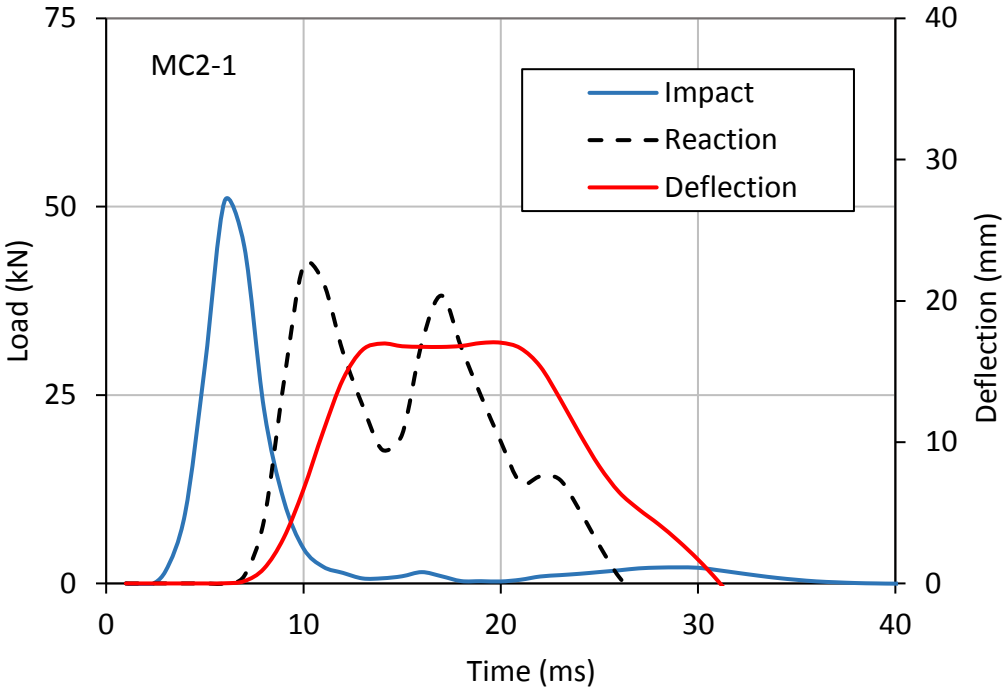

a) The control slab (MC2-1)

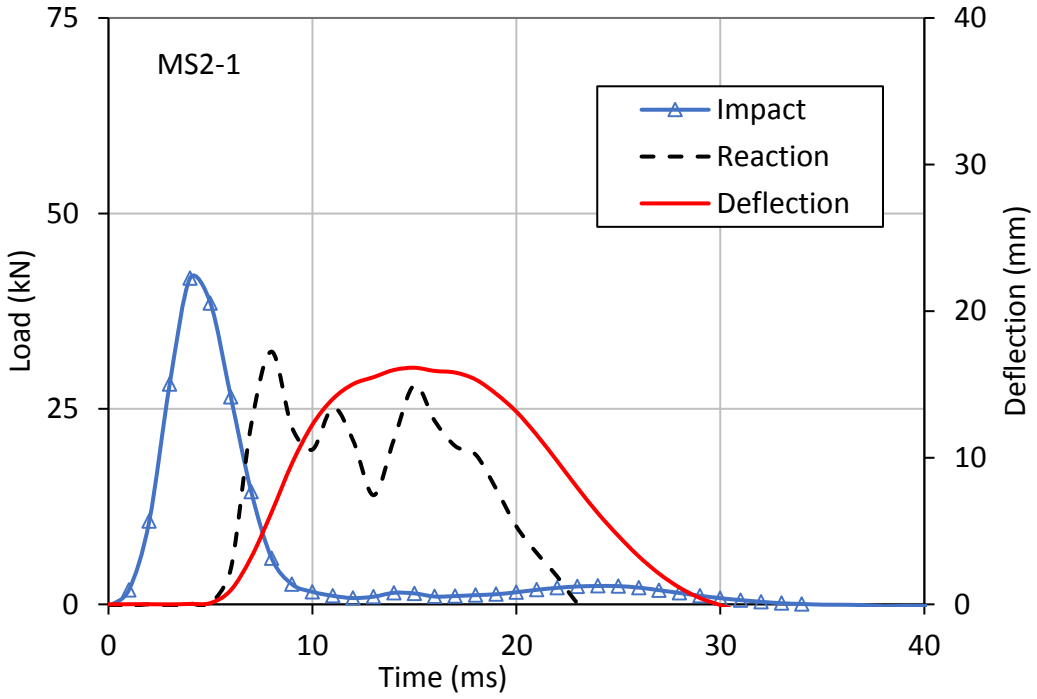

b) The strengthened slab (MS2-1)

Figure 3-21: History of deflection, impact load and reaction of a) the control (MC2-1) and b) the strengthened (MS2-1) slabs during the first impact blow.

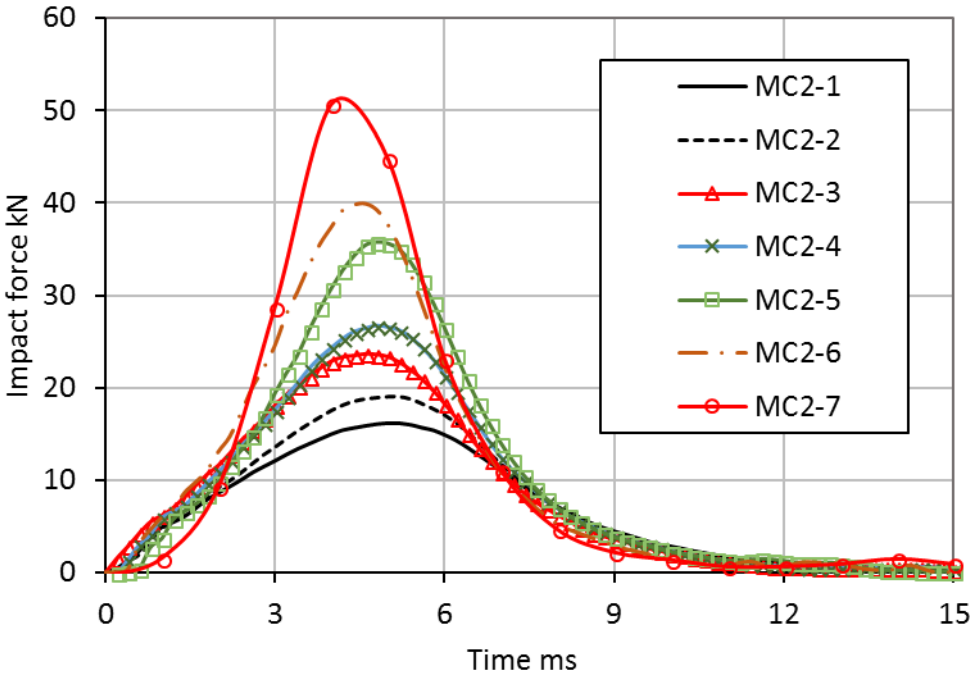

a) Impact force profile.

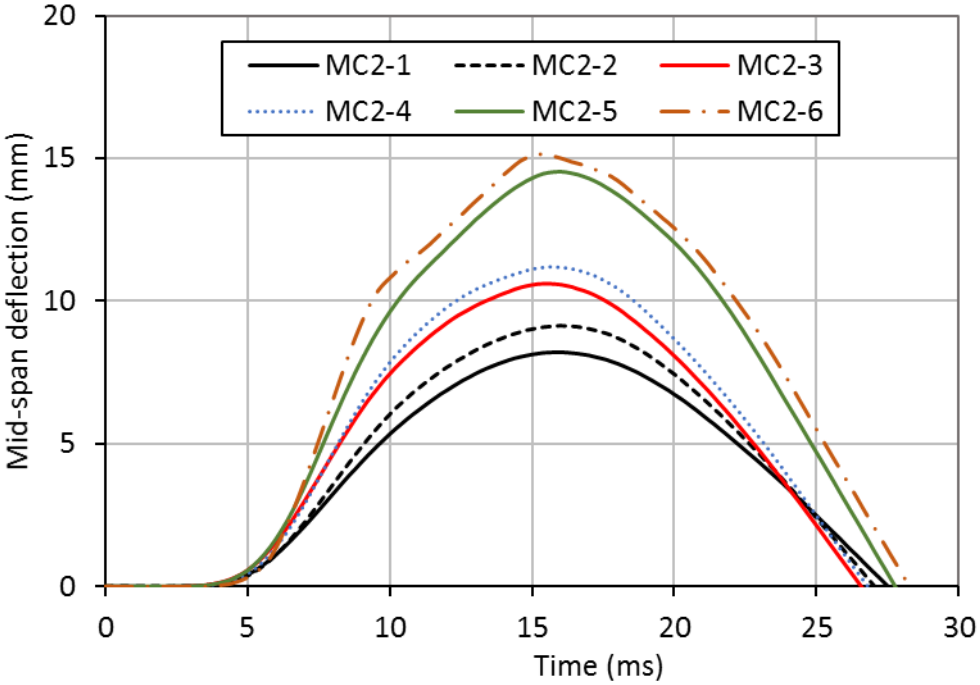

b) Mid-span deflection profile

Figure 3-22: The obtained history profiles of the impact force and the mid-span deflection of the control slab (MC) under various heights of dropping mass.

3.6.1.3 History of steel and concrete strain profile.

Figure 3-23 and Figure 3-24 present history of the steel and the concrete strains in both the control slabs (MC1 & MC2) and the strengthened slabs (MS1 & MS2) during the first impact drops. As shown, a sudden drop in the steel strain was detected in some of the steel bars at time 10 and 6.5 ms after initiation of the impact load for all slabs with no sign of any deflection drops at the same time, as shown with steel bar 1 in MC1-1. Similar behaviour was also noticed in the quasi-static test results as shown in Figure 3-14 -a and

Figure 3-16-a. This was attributed to the tension stiffening behaviour of the cracked reinforced concrete section where the strain profile along the steel bar is distributed non-uniformly when the surrounding concrete cracks. It takes a fluctuating shape with a peak value at the cracked section which drops in between cracks, as reported in many studies (Kaklauskas, 1999, Wu and Gilbert, 2008, Ng et al., 2010). Given that the cracks formed randomly along the member, this means that the position of the installed steel strain gauge along the bar (and hence relative to the nearest crack) played a significant role in the magnitude of strain detected. This explains why the steel strain in the subsequent impact blows recorded lower values, as shown in Figure 3-25, than those detected in the early stages of the 1st blow (before any open crack begins).

By comparing the historical steel strain profile obtained in this study by conducting impact test (Figure 3-23 and Figure 3-24) with the historical steel strain obtained by conducting real blast test as reported by previous test (Guo et al., 2017) as presented in Figure 2-14, it was found that there is quite similarity in the trend of both stating that the strain rates obtained by both, which depends on the historical steel strain profile, is quite similar. This indicates that conducting an impact test to simulate blast loads is reasonable in terms of the similarity in their effect on the target elements.

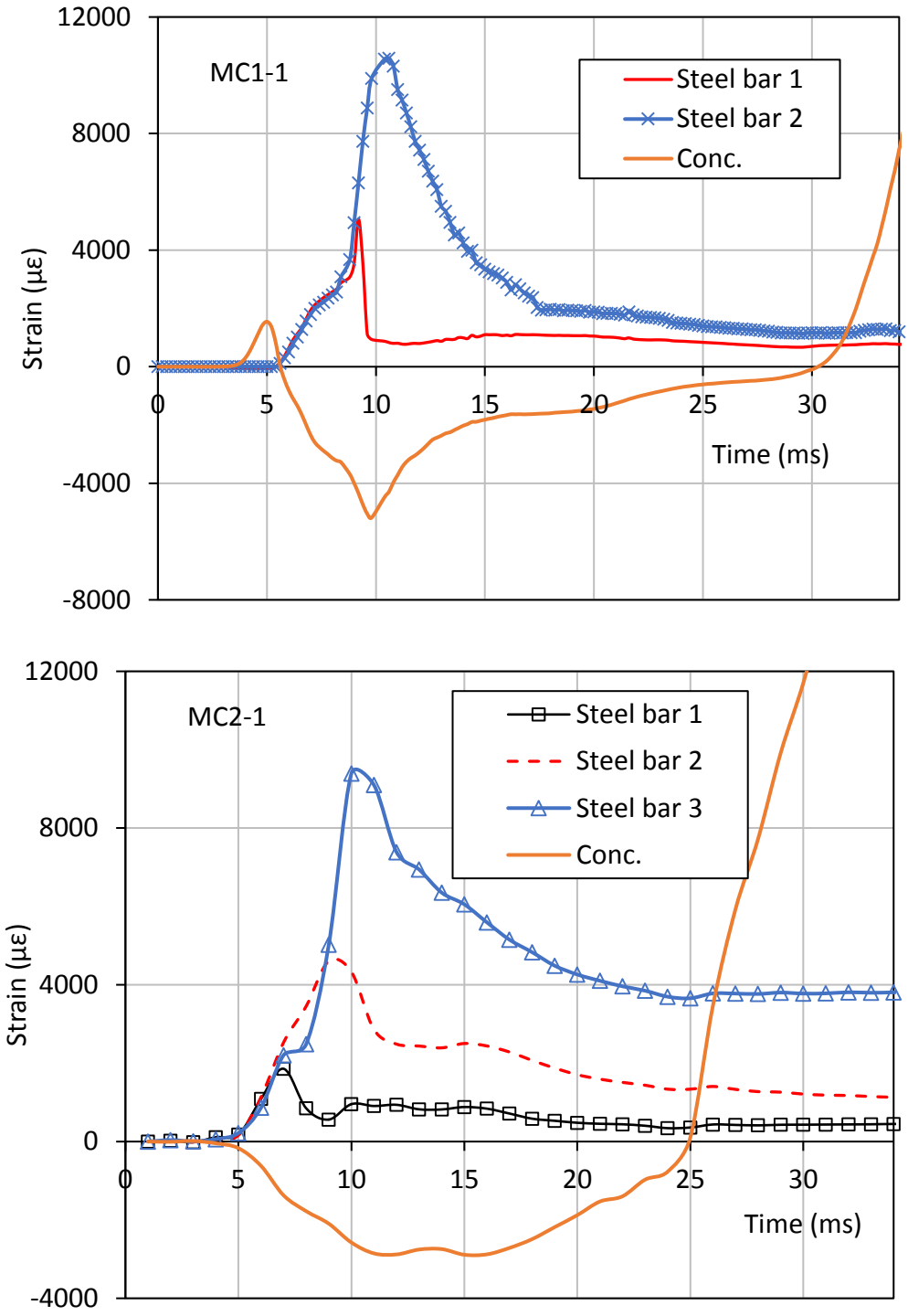

Figure 3-23: History of steel and concrete strain in the mid-span location of the control slabs MC1-1 and MC2-1 during the 1st impact drop.

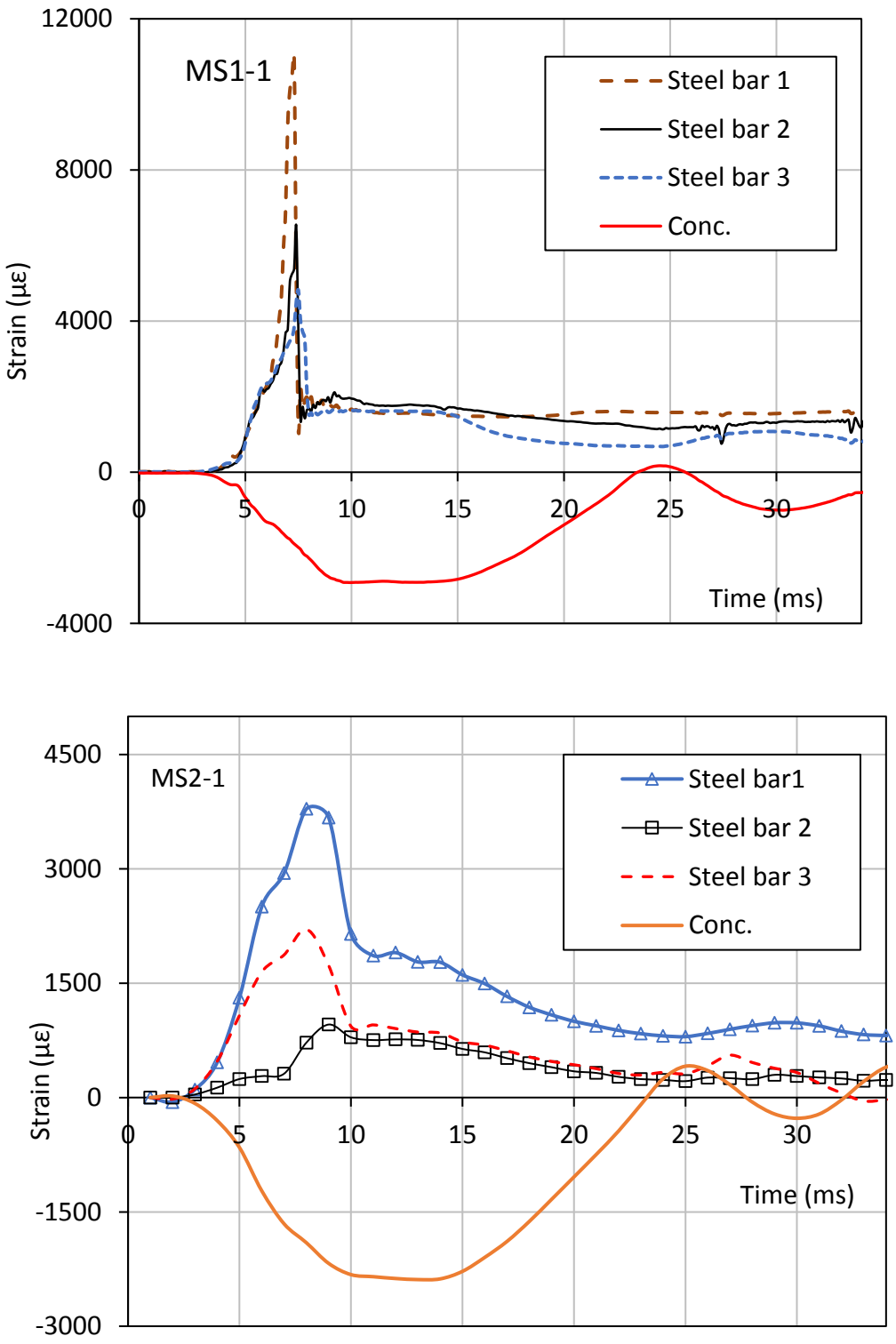

Figure 3-24: History of steel and concrete strain in the mid-span location of the strengthened slabs MS1-1 and MS2-1 during the 1st impact drop.

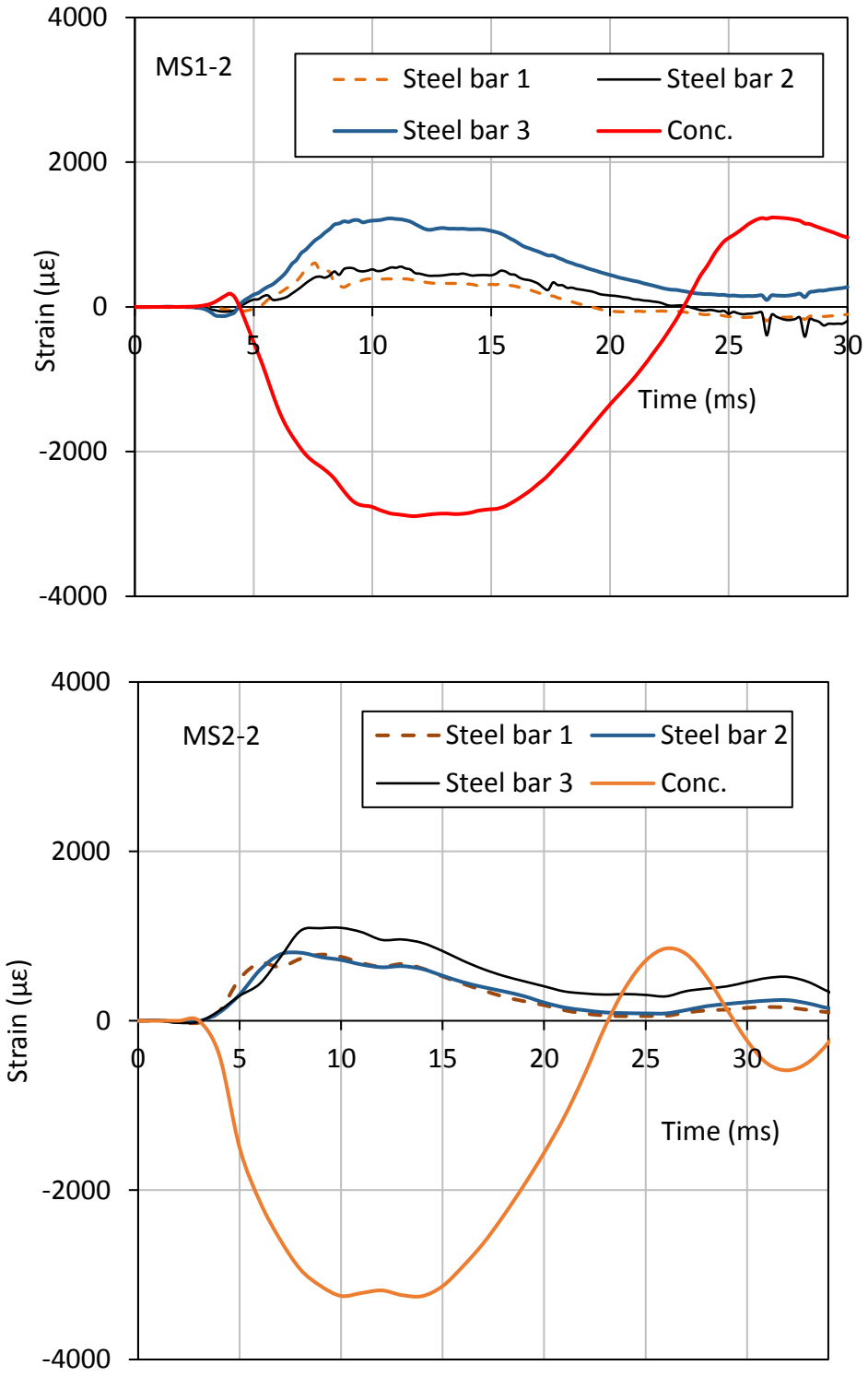

Figure 3-25: History of steel and concrete strain in the mid-span location of the strengthened slabs MS1-2 and MS2-2 during the 2nd impact drop.

3.6.1.4 Failure mode and crack pattern

Figure 3-26, Figure 3-27 and Table 3-6 present description of the compression damage and the crack pattern in both the control and the strengthened slabs after the first and the final impact drops. As shown, the control slab MC1-1 experienced a partial crushing failure in the compression zone (top face) accompanied by one major flexural wavy crack about the mid-span in the tension zone (bottom face) after the first impact drop. While after the second drop, the compression zone experienced a significant crushing failure in the top fibre of concrete accompanied by an increase in the width of the major crack in the tension face. In contrast, the strengthened slab MS1 showed different behaviour where the slab was subjected to 7 impact blows of the same impact energy (1000 J) with no sign of any damage in the compression face. Also, the crack pattern in the bottom face has turned from one major crack in the control slab (MC) to multiple cracks in the strengthened slab (MS) as described in Table 3-6. Similar failure mode and crack pattern behaviour was observed for both the control and the strengthened slabs MC2 and MS2 when repeating the multi-drop tests with lower impact load values except a higher number of drops, from 2 to 4, were needed to fail the control slab MC2 and from 7 to 11 drops for the strengthened slab MS2.

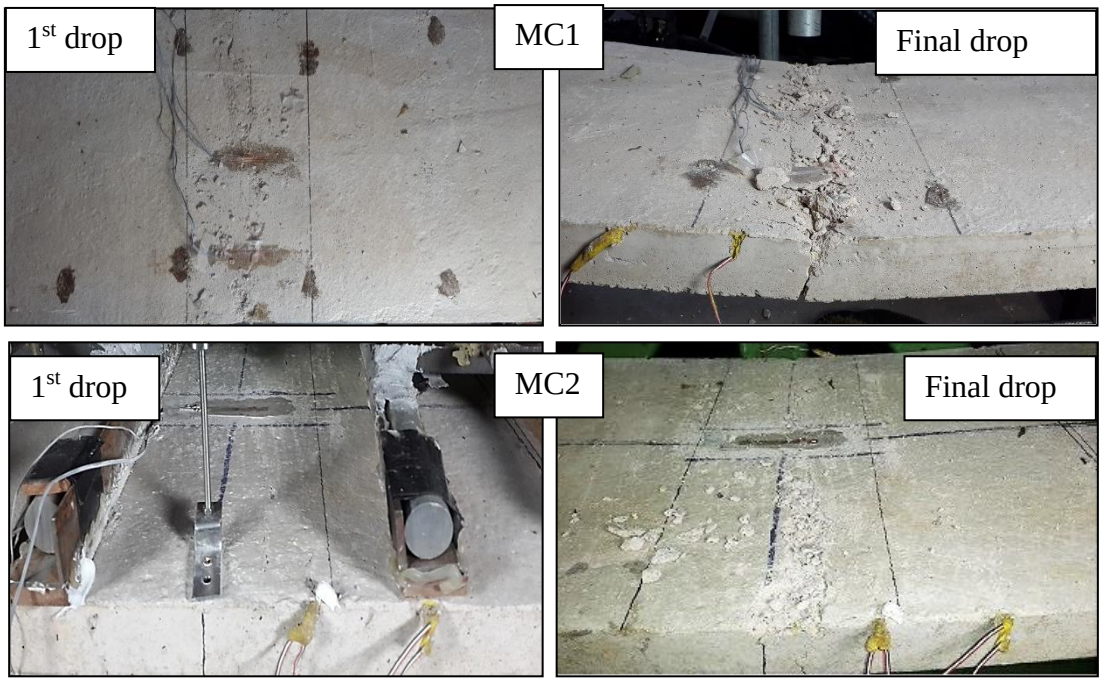

a) The compression face.

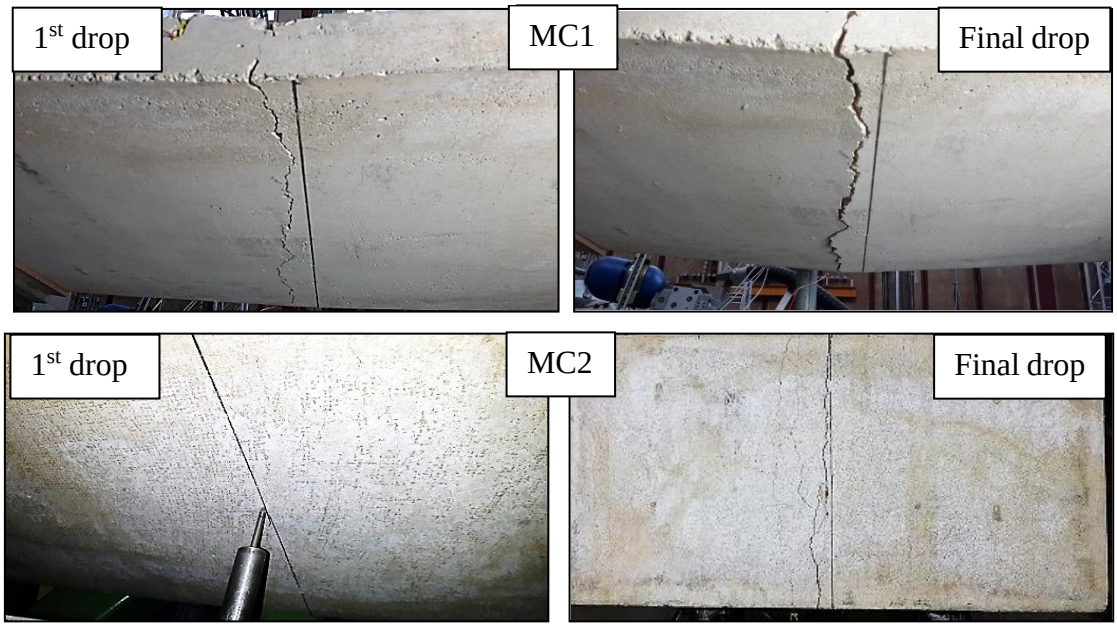

b) The tension face.

Figure 3-26: The damage of concrete at: a) the compression and b) the tension face of the control slabs (MC1 &MC2) after the first and the final impact drop test.

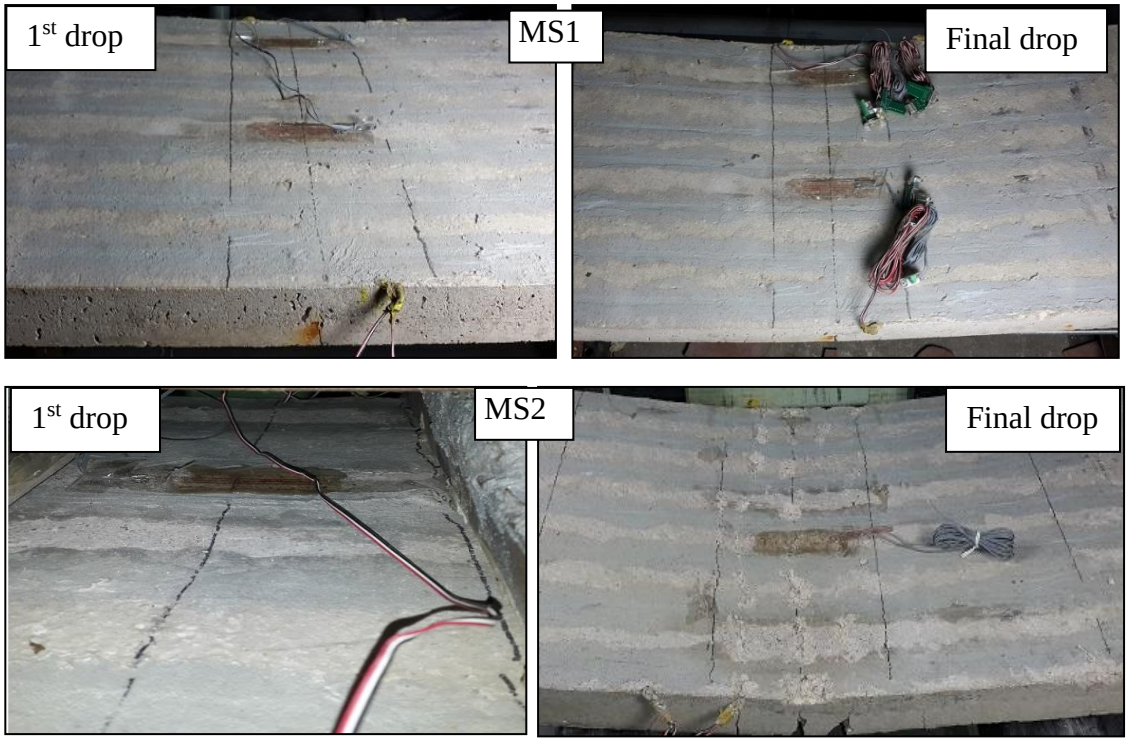

a) The compression face.

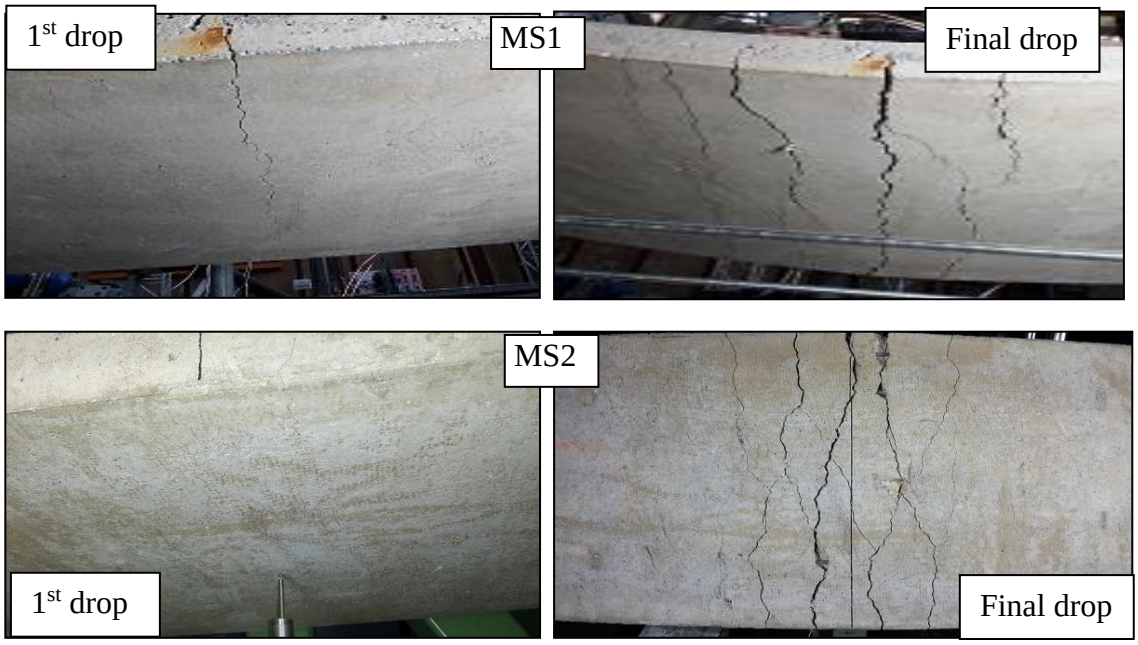

b) The tension face.

Figure 3-27: The damage of concrete at: a) the compression and b) the tension face of the strengthened slabs (MS1 &MS2) after the first and the final impact drop test.

3.6.1.5 Rebounding of the slab.

Based on the deflection-time profile measured for each test, it was found that the slab rebounds after the impact event which submits the slab to an inverse curvature and creates the second phase of the deflection as shown in Figure A. 8 and Figure A. 9 in appendix A. This phase was found to have a significant impact on the compression face of the control to resist the out-of-plane tension stresses when it is left without reinforcing, where many cracks were observed on the compression face of the control slab as compared to the strengthened slab where the top face was reinforced by CFRP NSM bars which resisted the out-of-plane tension forces during the second deflection phase. Figure A. 8 shows that the maximum deflection of the control slab in the second phase (the rebounding) was similar or higher than the maximum deflection in the first phase compred to the strengthened slab (MS2) where the maximum deflection in the second phase was lower than that in the first phase as shown in Figure A. 9 indicating the adequacy of using CFRP compression reinforcing on mitigating the rebounding effect in the element as a result to the oscillating of the element under impact and blast loading.

In case of the blast events, the second phase of the deflection time history function (rebounding) becomes more critical than the second deflection phase obtained from the impact events. This is because the pressure of the ambient increases extensively at the instance of the blast then drops dramatically to less than zero which causes sucking effect on the structure. The negative pressure (sucking) works as an inverse force acting in the same direction with the rebounding direction making the deflection in the second phase worse. This increases the need for strengthening the compression face of the slab to increase the ductility and to resist the reversing action.

Table 3-6: Crack patterns and failure modes of the specimens in the impact tests.

Case*	Max. strain of conc. με	Damage in tension zone	Damage in the compression zone
MC1-1	5100	One major crack about mid-span	Partial crushing of concrete at mid-span and hair cracks due to the rebounding behaviour
MC1-2	-	Extending of the one major crack about mid-span	Significant crushing of concrete at mid-span and hair cracks due to the rebounding behaviour
MS1-1	2900	One major crack at mid-span and two hair cracks on both sides	No damage or hair cracks were noticed
MS1-2	3800	Increasing width of the three cracks	No damage or hair cracks were noticed
MS1-3	4000	Increasing width of the previous cracks and initiating new cracks	No damage or hair cracks were noticed
MS1-4	4600	Increasing width of the previous cracks and initiating new cracks	No damage or hair cracks were noticed
MS1-5	5000	Increasing width of all cracks	No damage or hair cracks were noticed
MS1-6	4000	Increasing width of all cracks	No damage or hair cracks were noticed
MS1-7	3750	Increasing with of all cracks	No damage or hair cracks were noticed

M refers to Impact test, C1 refers to the 1st control slab, S1 refers to the 1st strengthened slab and the last number refers to the impact drop's number on the specimen.

3.6.1.6 Total and Dissipated energy

In the impact tests, the total and the dissipated energy for each impact drop were calculated by integrating the area under the load-deflection curve, where the load was either the impact load or the reaction force as mentioned in 3.5. To overcome the effect of the delay between the historical profile of the impact and the deflection profile, the impact profile was shifted forward to make it simultaneous with the deflection and the reaction waves. Figure 3-28 presents these load-deflection curves for both the control (MC1) and the strengthened slabs (MS1) under first and second blows.

Table 3-7 presents the results obtained from the impact test of slabs MC1 and MS1. It shows that based on the impact-deflection curves, the total energy increased from 2200 to 4949 J and the dissipated energy increased from 1083 to 1709 J. This corresponds to enhancing factors of 2.25 and 1.58 for the total and the dissipated energy respectively when the compression face of the slab is strengthened by 7 bars of CFRP NSM rods. When the reaction-deflection curves are used, the total energy increased from 1560 to 4790 J and the dissipated energy increased from 783 to 1645 J resulting in enhancing factors of 3.07 and 2.10 respectively. Both sets of results indicate that strengthening the compression face of the concrete slab enhances the impact resistance of the structure significantly in terms of both the total energy and the energy dissipation.

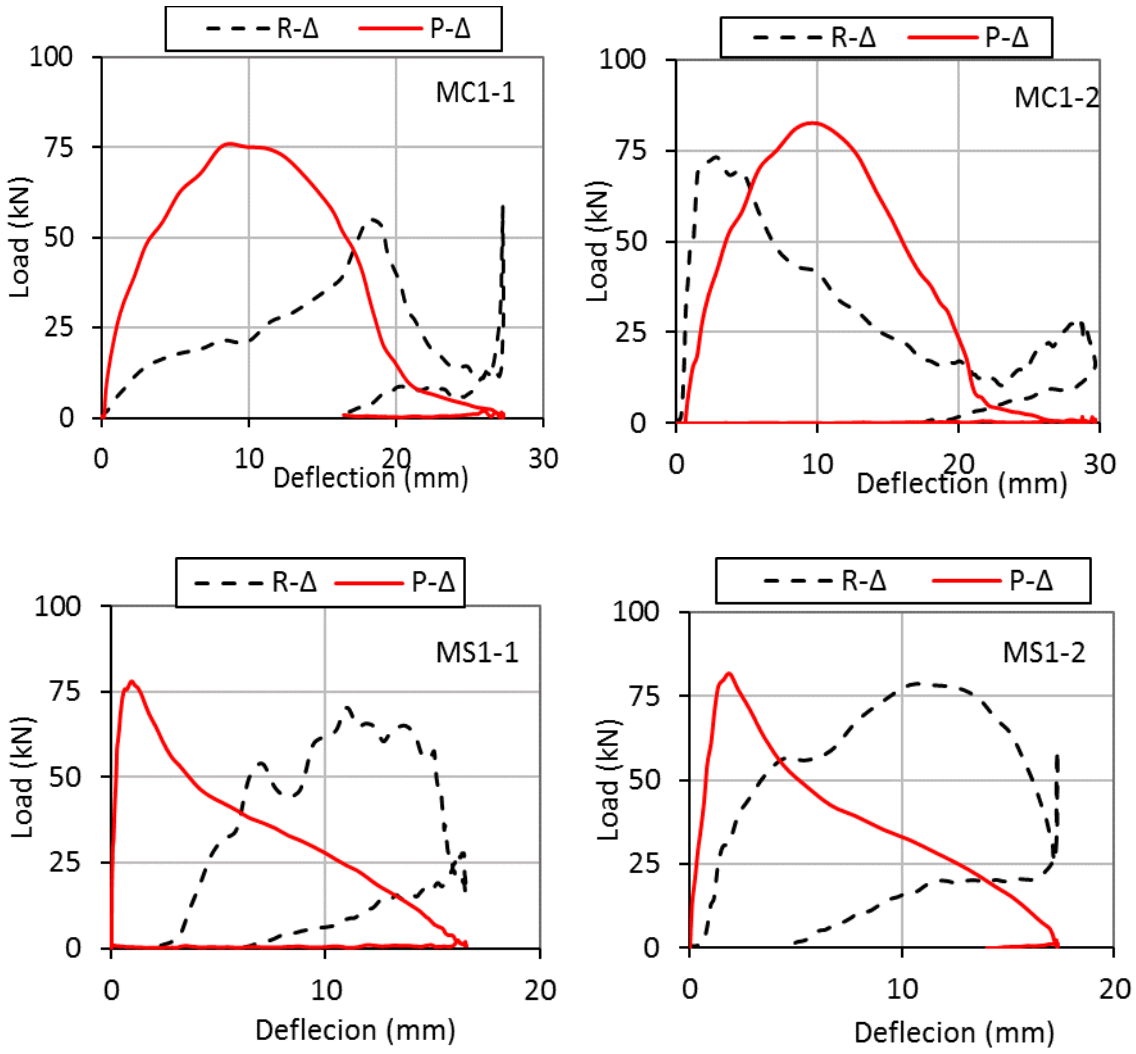

Figure 3-28: Impact (P) & Reaction (R) versus deflection (Δ) behaviour of slabs MC and Ms under 1st and 2nd.

Table 3-7: Results of the total and dissipated energy of both the control (MC1) and the strengthened (MS1) slabs based on both the impact and the reaction forces.

		MC1-1	MC1-2	MS1-1	MS1-2	MS1-3	MS1-4	MS1-5	MS1-6	MS1-7
Maximum deflection Δmax in each impact blow (mm)		27.35	29.67	16.57	17.33	17.31	17.96	15.18	14.36	21.16
Residual deflection Δres (mm)		12	16	7.5	8.1	4.3	5.7	4.2	4.2	5.7
Final deflection (mm)		41.67					55.66			
Ratio of the absorbed energy (Δmax-Δres/Δmax) %		0.56	0.46	0.55	0.53	0.75	0.68	0.72	0.71	0.73
Based on Impact-deflection curve	Total energy (J)	1050	1150	848	896	657	788	545	457	758
	Accumulated total energy (J)	2200					4949			
	Enhancement factor of the total energy					2.25				
	Absorbed energy	588	529	466	475	493	536	392	324	553
	Dissipated energy (J)	462	621	382	421	164	252	153	133	205
	Accumulated Dissipated energy (J)	1083					1709			
	Enhancement ratio of the dissipated energy %					1.58				

		MC1-1	MC1-2	MS1-1	MS1-2	MS1-3	MS1-4	MS1-5	MS1-6	MS1-7
Based on reaction-deflection curve	Total Reaction-deflection energy (J)	591	969	638	988	586	689	586	526	777
	Accumulated total energy (J)	1560.3					4790.5			
	Enhancement ratio of the total energy %					3.07				
	Absorbed energy	331	446	351	524	440	469	422	373	567
	Dissipated energy (J)	260	523	287	465	147	220	164	153	210
	Accumulated Dissipated energy (J)	783					1645			
	Enhancement ratio of the dissipated energy %					2.10				

Similar results were obtained when repeating the impact test with different pair of control and strengthened slabs (MC2 and MS2) by subjecting the slabs to impact impulse with lower impact peak force (P_{peak}). The impact and reaction forces versus deflection curves for all the impact drops are presented in Appendix A. In this test, the control slab (MC2) sustained four impact drops compare to 11 drops with the strengthened slab (MS2) before they fail in crushing of concrete. The enhancing factor of the dissipated energy was 2.08 when the slab was strengthened in the compression face by 7 CFRP bars by using the NSM approach. Details of the results are presented in Appendix A (Table A. 1 to

Table A. 3)

3.7 Discussion of the impact test

In this test, the specimens were subjected to multi-impact drops to assess the validity of the adopted NSM CFRP rods strengthening approach to resist loads with high loading rates such as impact and blast loads. The assessment was made in this study by comparing the results between the strengthened and the non-strengthened slabs in terms of the load, the deflection, the failure mode, the crack patterns, and the dissipated energy. The obtained results can be summarized as follows:

1- The impact impulse function obtained in this test is quite similar to the blast impulse function as measured by (Guo et al., 2017) as mentioned in chapter 2, indicating the adequacy of simulating the blast load by using impact test.

2- Conducting impact test as a non-explosive test to simulate the real blast test is valid based on the comparison between the obtained impact impulse and the steel strain profile with that found in the literature by conducting real blast test as reported by (Guo et al., 2017).

3- In addition to the dependency of the deflection rate and the produced strain rates to the loading rates, they also depend on the mechanical property of the element (the natural period) when a load control method is used in applying the load as is the case with the impact and blast loadings.

4- It was found that applying the NSM CFRP to strength the compression face of the element contributed to enhance its ductility and energy dissipated, where the maximum deflection of the slab increased from 41.67 mm to 55.66 mm (enhancing of 133%) and the dissipated energy enhanced by about 158-210%. The control slab sustained 2 impact drops before it fails compared 7 impact drops for the strengthened slab.

5- In terms of the crack patterns, in was found that strengthening the compression face of the slab by applying NSM CFRP approach contributed to change the crack patterns from one major opened crack pattern to multi-cracks in the tension face of the slab. this is similar to what has been observed in the quasi-static test.

Based on the obtained results, it can be stated that the impact test was feasible in assessing the resistance of the NSM CFRP system to the high loading rate such as impact and blast loads. However, some obstacles involved in the test limits the accuracy of the results which need to be overcome in the future work for more accurate assessment of the results. The most highlighted limitations in this test can be described as follows:

1- The whiffletree rig seems good in spreading the concentrated impact load on the slab to simulate the blast pressure and to prevent the localized failure which is the dominant failure mode in the hard contact events. However, it cannot be guaranteed that the load is distributed uniformly on the slab.

2- The sensitivity of the steel strain distribution to the position of the crack limited the utilization of the measured steel strain data in the mid-length of the steel bar especially when one or more cracks are opened. Similar to what has been observed with the quasi-static test, it is difficult to predict positions of the cracks exactly or to measure the steel strain profile along the entire length of the steel bars.

3- Although, no debonding in the CFRP bars was observed visually during the test, local or unnoticeable slipping of might occur in the test. So, for better assessment, the debonding or the slipping-off in the CFRP bars should be measured quantitively.

4- Due to the absence of any agreed method to calculate the dissipated energy of the RC element under dynamic loads and for the comparison reason, the dissipated energy of the slab in each individual drop was calculated based on either the impact-deflection or the reaction-deflection curves, where the deflection was measured in the mid-span of the slab. In reality, the total amount of the dissipated energy is affected by many factors such as the deflection-distance profile along the element and the crack patterns in the tension zone.

CHAPTER 4: ANALYTICAL AND NUMERICAL MODELLING

4.1 Introduction

Since it is difficult to obtain and measure all factors involved with the blast response instrumently due to many difficulties such as the constructive nature of the impact and blast loads which act on the structure within very short time, as found in chapter 3, and the inaccessibility of conducting real blast loading tests for many reasons as mentioned in chapter 2, the need to develop simulation processing analysis is crucial. For this purpose, this chapter present details of the nonlinear solutions used to predict the entire response of the one-way NSM CFRP system up to the ultimate failure under various strain rates. One of the main objectives of this study is to develop nonlinear models to estimate the static and dynamic response of one-way RC NSM CFRP system. This helps for more understanding to the blast response of the concrete structures. In this chapter, two nonlinear solutions were adopted to obtain this objective based on the analytical and numerical analysis. The reason for choosing the numerical solution is to validate the proposed analytical model to mitigate the limited experimental data available in this study or in the literature which is needed to validate any proposed model.

The first solution technique, presented in Section 4.2, is derived analytically by using a nonlinear layered method to derive the moment-curvature of the composite section then to predict the load-deflection curve up to the ultimate state by coupling the layered method with the moment area method. The obtained load-deflection curve was used to predict the statical displacement response at any given applied load. While the impact displacement response of the RC element was estimated by coupling the layered method with the SDOF method.

The second solution technique, presented in Section 4.3, uses numerical commercial software ABAQUS/CEA V. 6.14 (Abaqus, 2011). This comes in two versions - explicit and standard to simulate the static and dynamic response respectively. The strain rate factor is considered in both solutions to account its effect in the high loading rate regime such as blast and impact loads. While perfect bonding was assumed

between the CFRP and the concrete as less concern about the debonding failure in the NSM CFRP system as found and discussed in chapter 2.

This chapter presents details of the adopted models while the results obtained from these models and their validation with the experimental results are presented in chapter 5.

4.2 The analytical solution

The development of a nonlinear analytical procedure to predict the load-deflection relationship of one-way simply supported RC slab is based on modelling the section in several layers as shown in Figure 4-1 (Fujikake et al., 2009, Wu et al., 2009), where each layer has its own mechanical properties. The proposed analysis has two main steps: (1) determining the moment-curvature relationship of the RC slab section which utilizes the equilibrium equations and includes the effect of strain rate, (2) determining the load-deflection relationship of the RC slab based on the moment-curvature relationship.

4.2.1 Basic assumptions

To determine the moment-curvature relationship (m-k) of the member, the following classical assumptions are made:

1- Plane sections remain plane at any level of curvature.
2- Stress and strain at each layer in the sectional plane are assumed to be constant taking values of the centroid point of each layer.
3- Any deformation resulting from shear stresses is ignored.
4- Perfect bond between the bars and the surrounding concrete is assumed.
5- The stress-strain relationship for each of the constituent materials with its strain rate dependency is known.
6- The mid-span deflection rate is assumed to be constant by taking the average of the mid-span deflection rate which varies from 0 to the maximum mid-span deflection rate.

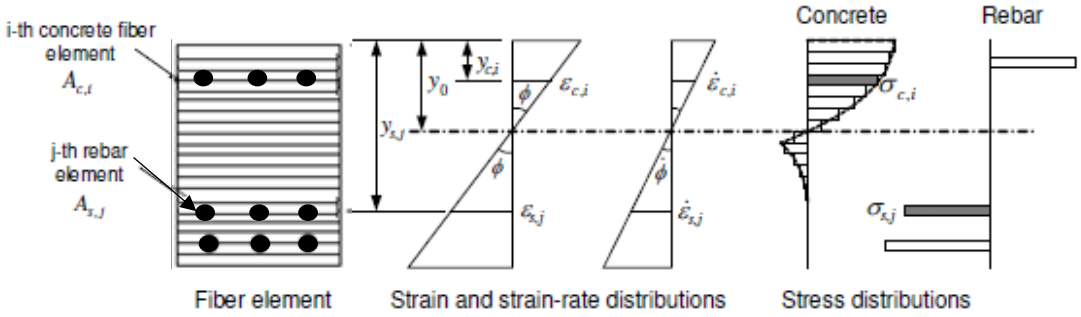

Figure 4-1: Details of the layered analysis method for the RC section without FRP strengthening material (Fujikake et al., 2009).

4.2.2 Constitutive materials modelling

The entire response of the member depends on the mechanical properties of the constituent materials. Each material has its unique stress-strain behavior for different type of stresses. In this study, only the compression and the tension stresses are considered. Therefore, the uniaxial behaviour of the constituent materials to these stresses are needed. Many models can be found in literature to idealize the stress-strain relationship for different structural materials (Reddiar, 2010, Youssef et al., 2007). In this study, the models of steel and CFRP were obtained from the uniaxial tensile tests carried out by the author. The model of concrete is taken from the literature as will describe in the following sections.

4.2.2.1 Concrete model in compression

In this study, the compression behaviour of concrete was simulated by using elasto-plastic model with strain softening behaviour. For this purpose, the model which proposed by Carreira and Chu was utilized as presented in 4-1 which was validated with the experimental behaviour of concrete (Carreira and Chu, 1985) :

$$\sigma_c = \frac{\gamma(\varepsilon_c / \varepsilon_c')}{\gamma - 1 + (\varepsilon_c / \varepsilon_c')^{\gamma}} f_c' \qquad 4\text{-}1$$

where σ_c=compressive stress in concrete; ε_c=strain in concrete; f'_c = quasi-static compressive strength of concrete; ε_c' =strain corresponding to f_c' (MPa) which is taken as 0.002; and γ is defined by:

$$\gamma = \left| \frac{f_c'}{32.4} \right|^3 + 1.55 \qquad 4\text{-}2$$

Figure 4-2 shows stress-strain curves for different type of concrete (C20, C30 & C40).

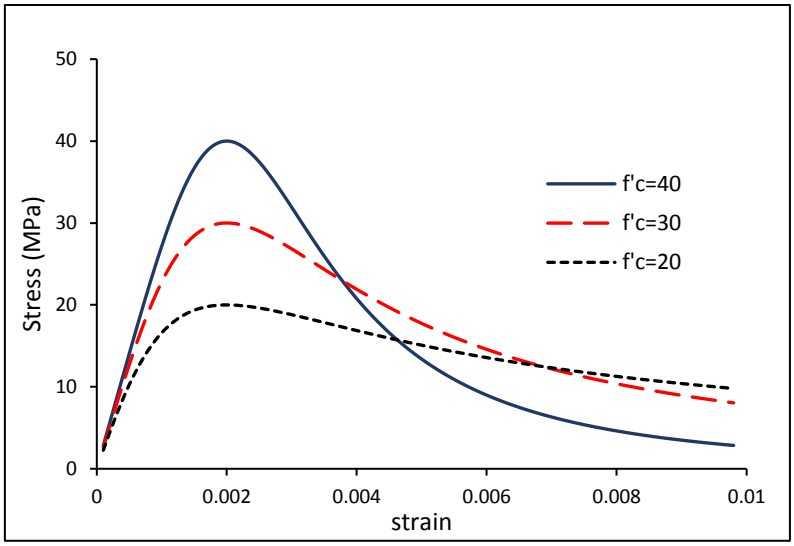

Figure 4-2: Stress-strain curves of different type of concrete based on the adopted model.

4.2.2.2 Concrete model in tension

In the tension zone of the member the behavior of the concrete and the reinforcement was modeled independently. In contrast to the plane concrete, tension stresses transfer between the cracks due to the existence of the reinforcement. This behaviour was simulated by using a tension stiffening model (Wu and Gilbert, 2008, Carino and Clifton, 1995a, Nayal and Rasheed, 2006). This model assumes that the average tension stiffening stress in the cracked zone gradually reduces with the increasing width of the crack. Figure 4-3 shows the stress-strain relationship in tension which assumes that the tensile stress increases linearly with the increase in tensile strain up to the cracking limit. Then, the tensile stress decreases to zero as the crack opens. The tension stiffening behavior depends on many factors, such as the density of reinforcing bars, the bond between the reinforcing bars and the surrounding concrete, the relative size of the aggregate compared to the diameter of the steel rebar, and the element mesh. In this study, following (Fujikake et al., 2009) a peak strain of 0.0004, beyond which the tension stiffening effect disappears, was assumed in establishing the tension stiffening

model. Thus, the stress-strain relationship of concrete in tension is represented by the following equations:

$$\sigma_t = E_o \varepsilon \qquad \varepsilon \le \varepsilon_{tcr} \qquad 4\text{-}3$$

$$\sigma_t = \frac{\varepsilon - \varepsilon_{tu}}{\varepsilon_{tu} - \varepsilon_{tcr}} f_t \qquad \varepsilon_{tcr} < \varepsilon \le \varepsilon_{tu} \qquad 4\text{-}4$$

$$\sigma_t = 0 \qquad \varepsilon > \varepsilon_{tu} \qquad 4\text{-}5$$

where f_t is tensile strength under static load (f_t=0.23$f_c'^{2/3}$) (Ueda, 2004), ε_{tcr} is the strain corresponding to the cracking stress (=f_t/E_o) ε_{tu}= 4.0 × 10^{-4} and $E_o = 3320\sqrt{f'c} + 6900$ (Fujikake et al., 2009).

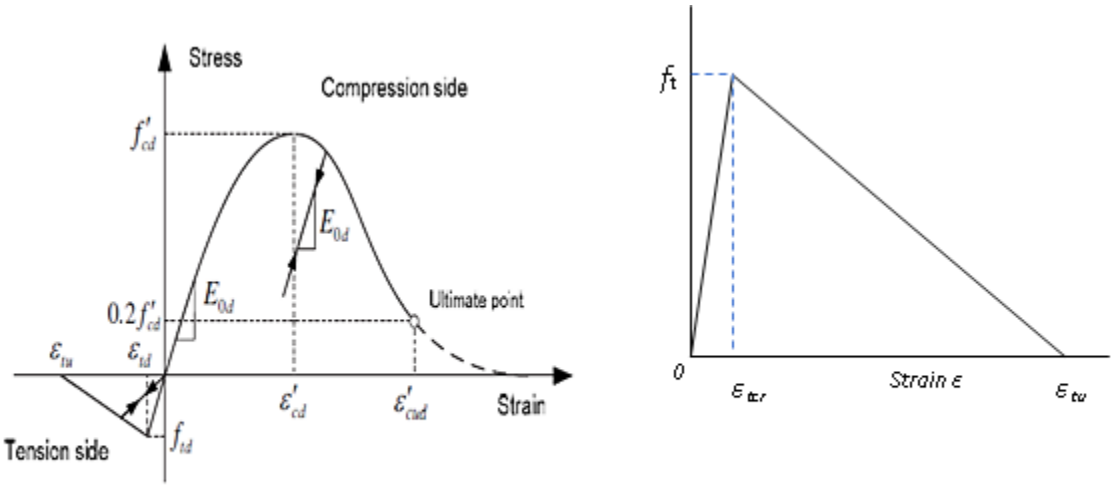

Figure 4-3: Stress-strain behaviour of concrete under compression and tension stresses.

4.2.2.3 Steel reinforcement model

In this study, each layer of steel reinforcing bars in the concrete member was modeled as a smeared layer with constant thickness. To simulate the stress-strain relationship of the steel, a bilinear stress-strain relationship, as shown in Figure 4-4a, was adopted. The modulus of elasticity (Es) and the modulus of plasticity (Ep) were obtained as the following:

$$E_s = \frac{f_{sy}}{\varepsilon_{sy}} \quad (4\text{-}6)$$

$$E_p = \frac{f_{su} - f_{sy}}{\varepsilon_{su} - \varepsilon_{sy}} \quad (4\text{-}7)$$

Where f_{sy} and f_{su} represent the yielding and the ultimate steel stress in MPa. And ε_{sy} and ε_{su} represent the yielding and the ultimate steel strain.

For better representation of steel behavior the stress-strain relationship of the steel was simulated by dividing the plastic range into three stages with three different elasto-plastic moduli (E_{p1}, E_{p2} & E_{p3}) based on the following proposed equations:

$$E_{p1} = f_1 E_p \quad (4\text{-}8)$$

$$E_{p2} = f_2 E_p \quad (4\text{-}9)$$

$$E_{p3} = f_3 E_p \quad (4\text{-}10)$$

Where f_1, f_2, and f_3 are factors to adjustment slope of E_{p1}, E_{p2} and E_{p3} based on the following proposed equations:

$$f_1 = 0.0008 E_p + 0.849 \quad (4\text{-}11)$$

$$f_2 = 1 \quad (4\text{-}12)$$

$$f_3 = -9 \times 10^{-5} E_p + 1.0144 \quad (4\text{-}13)$$

Since E_p depends on f_{sy} and f_{su} and both are found to be strain rate dependents (discussed in the next section) E_{p1}, E_{p2} and E_{p3} are strain rate dependents as well.

The proposed model of steel was validated with the experimental results of a direct tensile test on steel bar (D=6mm), as shown in Figure 4-4b, before it is used in this study.

4.2.2.4 Carbon Fibre model

To establish an accurate model to simulate the actual behaviour of CFRP, a direct tensile test was conducted on carbon fibre reinforcement bar (CFRP bar) to obtain the mechanical properties of the CFRP bars used in this research. Based on the obtained results, a linear stress-strain relationship up to the ultimate failure stress was assumed.

The ultimate stress was 1400 MPa and the ultimate strain was εu=0.01 as obtained from the test. Here, the failure mode was dominated by rupture of the CFRP bars. Figure 4-5 shows the actual and the idealized models.

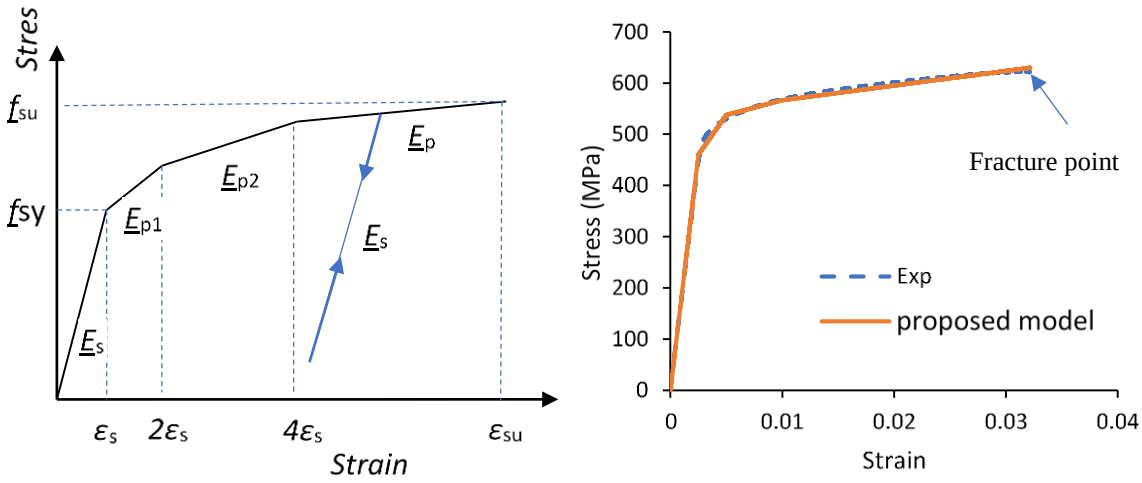

Figure 4-4: a) the proposed multi-linear stress-strain model of steel and b) the validation with the experimental results.

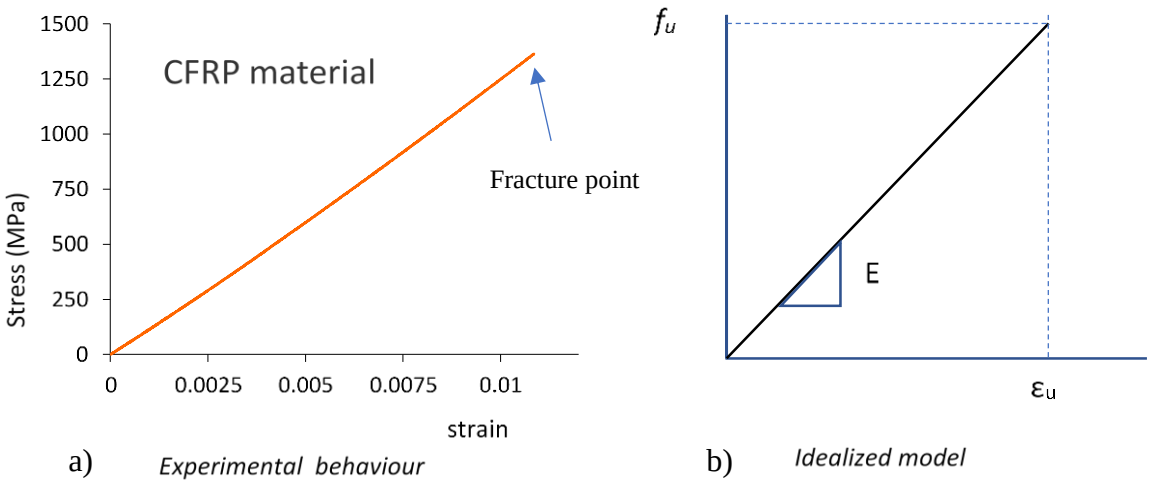

Figure 4-5: Stress-strain relationship of CFRP bar under direct tensile test: a) Experimental behavior, b) adopted model.

4.2.3 Strain rate dependency of the structural materials

The enhancing factor of the properties in the strain rate dependent materials is represented in form of the dynamic increase factor (DIF). Many models have been proposed to estimate the DIF of each structural material (Riisgaard et al., 2007, Malvar, 1998, Karim, 2005). In this study, the empirical formulas proposed by (Malvar and Crawford, 1998) is utilized to estimate the dynamic increase factor (DIF) of the tensile strength of concrete. In compression, the CEB model (CEB, 1993). For steel, the model by Malvar (1998) is utilized. The DIF for concrete and steel reinforcement at different strain rates is shown in Figure 4-6.

There is uncertainty about the strain rate effect on the mechanical properties of CFRP. (Ochola et al., 2004) have reported that CFRP is strain rate dependent under high strain rate values. (Orton et al., 2014) have reported that no strain rate effect on CFRP within range of 0.0015 to 7.86 S^{-1}. (Al-Hassani and Kaddour, 1998) have reported that strength of CFRP in the high strain rate regime in relation to the quasi-static regime is either unaffected, increased or decreased based on results obtained from different tests. As a result, no strain rate model was dedicated to simulating the strain rate dependency on CFRP. As mentioned in 2.4.2 the strain rate effect on CFRP is commonly neglected in most of the analytical calculations (Mutalib and Hao, 2010) especially for strain rates less than 100 s^{-1}. And the enhancing in the properties of CFRP is not significant for strain

rates range between 100-1000 s^{-1} (Langdon et al., 2014). Based on that, the strain rate dependency of the CFRP is neglected in this study as the maximum strain rate obtained in the impact test was less than 100 s^{-1}.

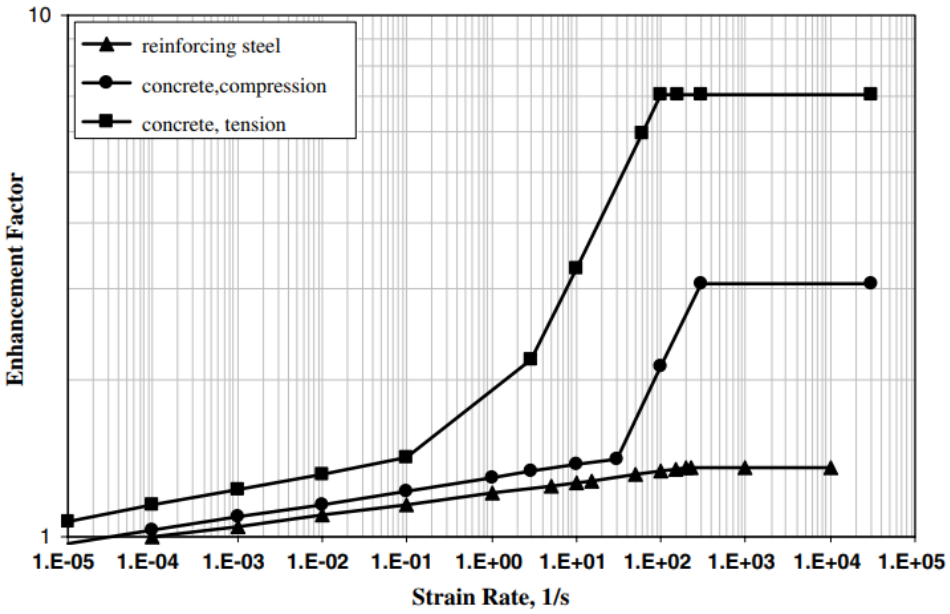

Figure 4-6: The dynamic increase factor (DIF) for both steel and concrete (Mutalib and Hao, 2010).

4.2.3.1 Strain rate dependency of the structural dynamic response

Under impact and blast loading, the strain rate value changes with time following the velocity of object which starts from zero, increases to reach the peak and then drops to zero when the deflection reaches the maximum value. Therefore, the strain rate value should be considered in the dynamic nonlinear analysis solution. No model was found in the literature to determine the entire response of the material under varied strain rate value. Furthermore, adopting such a model, if it exists, will add complexity to the nonlinear analysis. In this study, for simplicity and following (Fujikake et al., 2009), the strain rate value was assumed to be constant with the time up to the maximum deflection. This assumption is reasonable since the strain rate value has a linear effect on the mechanical properties of both steel and concrete as shown in Figure 4-6. Therefore, the average of the imposed strain rate value was used in the present analysis which can be calculated as:

$$\dot{\varepsilon}_{avr} = \frac{\dot{\varepsilon}_{max}}{2} = \frac{\varepsilon_{max}}{t_{max}} \qquad 4\text{-}14$$

Where: $\dot{\varepsilon}_{avr}$= average strain rate, $\dot{\varepsilon}_{max}$= maximum strain rate (the peak value); ε_{max} and t_{max} = strain and time (in seconds) at the maximum deflection.

4.2.3.2 Strain rate dependency of concrete in compression

The strain rate dependency in the compression behaviour of concrete was considered by including the Dynamic Increase Factor (DIF) based on the CEB model as follows (Coelho et al., 2015):

$$(DIF)_c = \left(\frac{\dot{\varepsilon}}{\dot{\varepsilon}_s}\right)^{1.026\alpha} \qquad for \dot{\varepsilon} \leq 30 s^{-1} \qquad 4\text{-}15$$

$$(DIF)_c = \gamma \left(\frac{\dot{\varepsilon}}{\dot{\varepsilon}_s}\right)^{1/3} \qquad for \dot{\varepsilon} > 30 s^{-1} \qquad 4\text{-}16$$

Where:$(DIF)_c$= dynamic increase factor of concrete in compression =f_{cd}/f_{cs}

f_{cd} = dynamic compression strength at $\dot{\varepsilon}$

f_{cs}= static compression strength at $\dot{\varepsilon}_s$

$\dot{\varepsilon}$= strain rate in the range of $30x10^{-6}$ to 300 s^{-1}

$\dot{\varepsilon}_s$= static strain rate ($30x10^{-6}$ s^{-1})

Log γ = 6.156 α-2

α = 1/(5+9 f_{cs}/ f_{co})

f_{co}= 10 MPa

This DIF formulation for concrete in compression has been validated with experimental data and accepted by most researchers as an accurate representation of the actual behavior of concrete in compression and adopted in the numerical analyses as stated by (Malvar and Crawford, 1998).

4.2.3.3 Strain rate dependency of concrete in tension

The dynamic increase factor (DIF) for the tensile strength under different strain rate value is given by:

$$(DIF)_t = \left(\frac{\dot{\varepsilon}}{\dot{\varepsilon}_s}\right)^{1.016\delta} \qquad for \dot{\varepsilon} \leq 30s^{-1} \qquad 4\text{-}17$$

$$(DIF)_t = \beta\left(\frac{\dot{\varepsilon}}{\dot{\varepsilon}_s}\right)^{1/3} \qquad for \dot{\varepsilon} > 30s^{-1} \qquad 4\text{-}18$$

Where:

(DIF)t= dynamic increase factor of concrete in tension =f_{td}/f_{ts}

f_{td} = dynamic tensile strength at $\dot{\varepsilon}$

f_{ts}= static tensile strength at $\dot{\varepsilon}_s$

$\dot{\varepsilon}$= strain rate in the range of $3x10^{-6}$ to 300 s^{-1}

$\dot{\varepsilon}_s$= static strain rate ($3x10^{-6}$ s^{-1})

Log β= 7.11δ-2.33

δ = 1/(10+6 f_{cs}/ f_{co})

f_{co}= 10 MPa

Figure 4-7 shows the predicted DIF of concrete in tension and compression for two types of concrete (C20 & C50) based on the adopted CEB model.

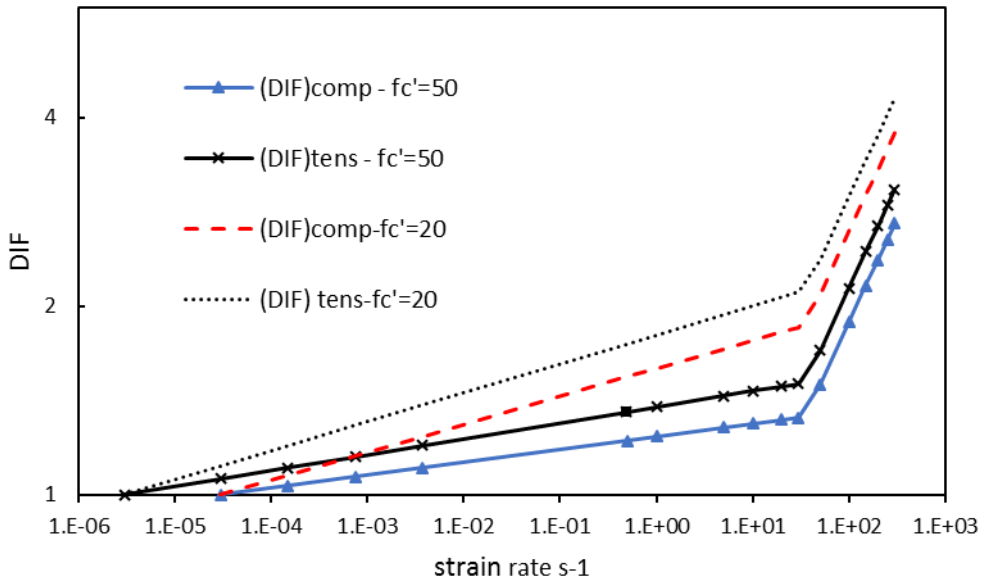

Figure 4-7: Dynamic increase factor of concrete in compression and tension based on the adopted CEB model.

4.2.3.4 Strain rate dependency of steel

Several strain rate dependent models of steel have been proposed in the literature. In the present study, strain rate dependent bilinear model with hardening behaviour is adopted. The strain rate dependency was considered by including the DIF of steel in compression and tension under strain rate effect based on Malvar's formulations (Malvar, 1998), the adopted DIF formulation for both yield and ultimate stress are:

$$DIF = \left(\frac{\dot{\varepsilon}}{\dot{\varepsilon}_s}\right)^{\alpha} \qquad 4\text{-}19$$

Where $\alpha = \alpha_{fy}$ for yielding stress and $\alpha = \alpha_{fu}$ for ultimate stress which can be calculated as:

$$\alpha_{fy} = 0.074 - 0.04\frac{fy}{414} \qquad 4\text{-}20$$

$$\alpha_{fu} = 0.019 - 0.009\frac{fy}{414} \qquad 4\text{-}21$$

This formulation is valid for fy varying from 290 to 710 MPa.

4.2.4 The relationship between Mid-span Deflection Rate and Curvature Rate

When a strain rate dependent sectional analysis is performed, the strain rate value at that section is needed to predict the response of each material. This means that in the layered method, the strain rate factor at each layer is needed. To estimate that, the relationship between the curvature rate ($\dot{\emptyset}$) and the mid-span deflection rate ($\dot{\delta}$) is required.

In a simply supported beam subjected to a rapid flexural load at mid-span with a constant speed, the relationship between the mid-span deflection and the curvature can be estimated based on the linear elastic theory as follows (Fujikake et al., 2009):

$$\emptyset = \frac{M}{EI} = \frac{12}{L^2}\delta \qquad 4\text{-}22$$

In the same way, similar relationship between the curvature rate $\dot{\emptyset}$ and the midspan deflection rate ($\dot{\delta}$) can be described as follows:

$$\dot{\phi} = \frac{12}{L^2}\dot{\delta} \qquad 4\text{-}23$$

4.2.5 Analytical Moment-Curvature Relationship

By dividing the cross section of the RC member into *nL* number of concrete layers and the reinforcing bars (steel or CFRP) into *m* layers, the total internal force and moment can be calculated based on the equilibrium equations as follows:

$$N = \int_A \sigma dA = \sum_{i=1}^{nL} \sigma_{c.j}\, A_{c.j} + \sum_{i=1}^{m} \sigma_{s.j} A_{s.j} \qquad 4\text{-}24$$

$$N = \int_A \sigma y dA = \sum_{i=1}^{nL} \sigma_{c.i}\, y_{c.i} A_{c.i} + \sum_{i=1}^{m} \sigma_{s.j} y_{s.j} A_{s.j} \qquad 4\text{-}25$$

where $\sigma_{c.i}$=stress acting on the individual concrete layer (i); $A_{c.i}$ =area of the individual concrete layer; $\sigma_{s.j}$=stress of the individual steel layer (j); $A_{s.j}$=area of the individual steel layer; $y_{i,j}$= the distance from the extreme top fiber of the section to the centroid of each layer. In a stable state, the summation of the internal forces is zero (N=0). This condition can be achieved by adjusting the neutral axis depth y_0 to satisfy the equilibrium condition.

The stress at each layer is calculated from the adopted constitutive material model based on the strain at that layer. The strain at each layer is calculated proportionally based on the strain of the top fiber of the section as linear strain distribution is assumed in the cross-section as shown in Figure 4-1. So, the strain of each layer is calculated as:

$$\varepsilon_{c.i} = (y_o - y_{c.i})\phi \qquad 4\text{-}26$$

$$\varepsilon_{s.j} = (y_o - y_{s.j})\phi \qquad 4\text{-}27$$

Where:

y_0=distance from the extreme compression fiber to the neutral axis.

$\emptyset$=curvature of the section ($\phi = \varepsilon_{top} / y_o$).

As a result of the linear variation of strain in the cross-section with the depth, the strain rates vary linearly with depth as well. Based on the curvature rate at the section,

which was given in Equation 4-23, the strain rate at each layer in the section is calculated as:

$$\dot{\varepsilon}_{c,i} = \left|\left(y_o - y_{c,i}\right)\right|\dot{\emptyset} \qquad 4\text{-}28$$

$$\dot{\varepsilon}_{s,j} = \left|\left(y_o - y_{s,j}\right)\right|\dot{\emptyset} \qquad 4\text{-}29$$

4.2.6 Analytical Load-Mid span Deflection Relationship

Once the moment-curvature m-k relationship of the RC member at any section is obtained based on the layered method, the curvature distribution over the entire length of the member can be calculated based on the moment diagram by considering the applied load and the boundary conditions of the member. The mid span deflection then can be calculated by double integrating the curvature distribution over one-half the length of the RC member. Due to the variation in the value of the strain rate factor along the member, a non-homogeneously state occurs along the member and m-k relationship at each section is needed. This is found to have an impact on the duration of the analysis as compared to the static analysis situation where m-k relationship is uniform along the member. In this study, the depth of the member was divided to 50 layers where thickness of each layer was taken as 1 mm for the slab with thickness of 50 mm to get better results.

For a uniformly distributed load over simply supported RC slab the bending moment diagram can be calculated based on the following equation:

$$M(x) = \frac{wL}{2}x - \frac{wx^2}{2} \qquad 4\text{-}30$$

Since the nonlinear analysis of the layered method is based on a given strain in the top fiber of the section, the strain in the mid-span ($\varepsilon_{c.m}$) is applied incrementally up to the maximum strain limit $\varepsilon_{cm(\max)}$ (0.0035). The strain rate distribution along the span is calculated as:

$$\dot{\varepsilon}_{c,x} = \dot{\varepsilon}_{c,m}\left(\varepsilon_{c,x}/\varepsilon_{c,m}\right) \qquad 4\text{-}31$$

$$\dot{\varepsilon}_{c,m} = \dot{\emptyset}_{mid}\, y_o \qquad 4\text{-}32$$

or $$\dot{\varepsilon}_{c,m} = \varepsilon_{c,m(max)}/t_{max} \qquad 4\text{-}33$$

Where:

$\varepsilon_{c.x}$ = strain in the top fiber of concrete at distance x from the support

$\varepsilon_{c.m}$ = strain in the top fiber of concrete at the mid-span section (L/2)

L= the shear length of the slab (mm)

x= distance from the element to the support (mm)

$\dot{\varepsilon}_{c,x}$= strain rate of the top fibre of concrete at each element.

$\dot{\varepsilon}_{c,m}$= strain rate of the top fibre of concrete at mid-span.

$\dot{\emptyset}_{mid}$ = average curvature rate at mid-span.

$\varepsilon_{cm(\max)}$ = strain of concrete at crushing

4.2.7 Effect of the opened cracks

The strain along the steel bar is distributed in proportion to the moment when no open crack occurs. But once a crack starts to open, the strain in steel is no more in the same proportion but it has a peak in the open crack position and lower strain in between the cracks as shown in Figure 4-8. Shin et al have studied the effect of localized and non-localized crack on the stiffness (Shin et al., 2015). They reported that the stiffness of the section drops when a crack is initiated, and it drops further when the crack is open or localized as shown in Figure 4-9.

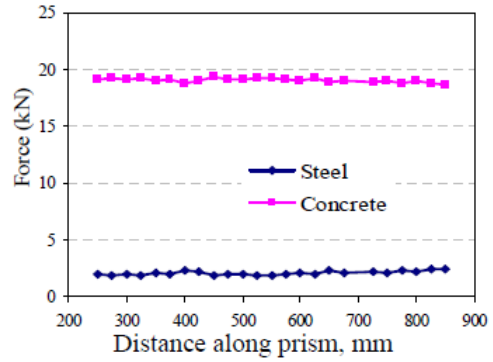

(a) Just before first cracking, $P = 21.1$ kN.

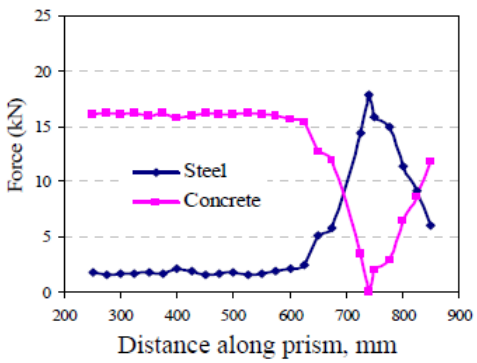

(b) Just after first cracking, $P = 17.8$ kN.

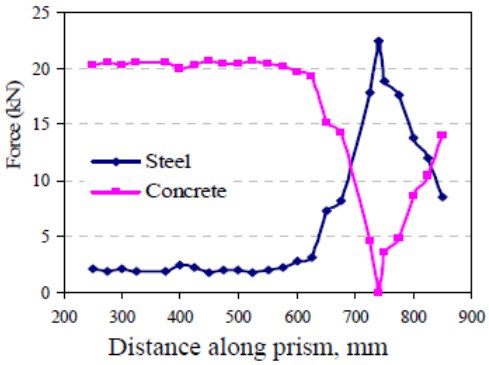

(c) Just before 2nd crack, $P = 22.4$ kN.

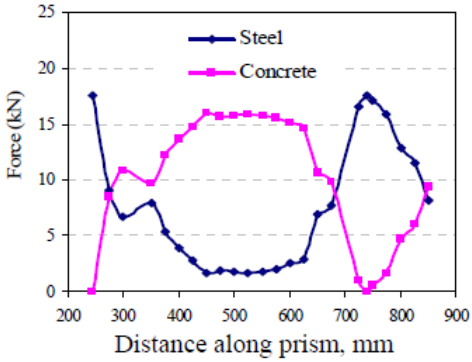

(d) Just after 2nd crack, $P = 17.4$ kN.

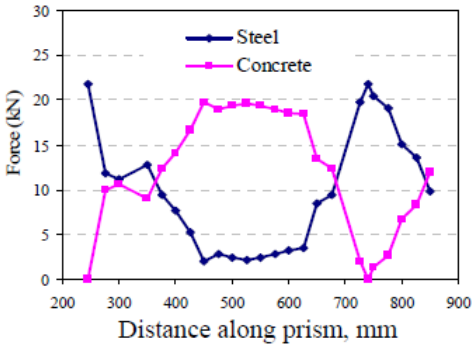

(e) Just before 3rd crack, $P = 21.8$ kN.

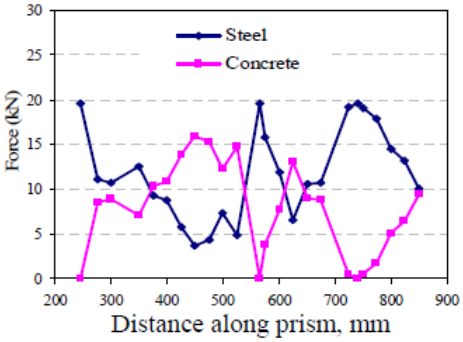

(f) Just after 3rd crack, $P = 19.6$ kN.

Figure 4-8: Variation of forces in steel and concrete at different stages of loading in a uniaxial tension test of an RC prism (Wu and Gilbert, 2008).

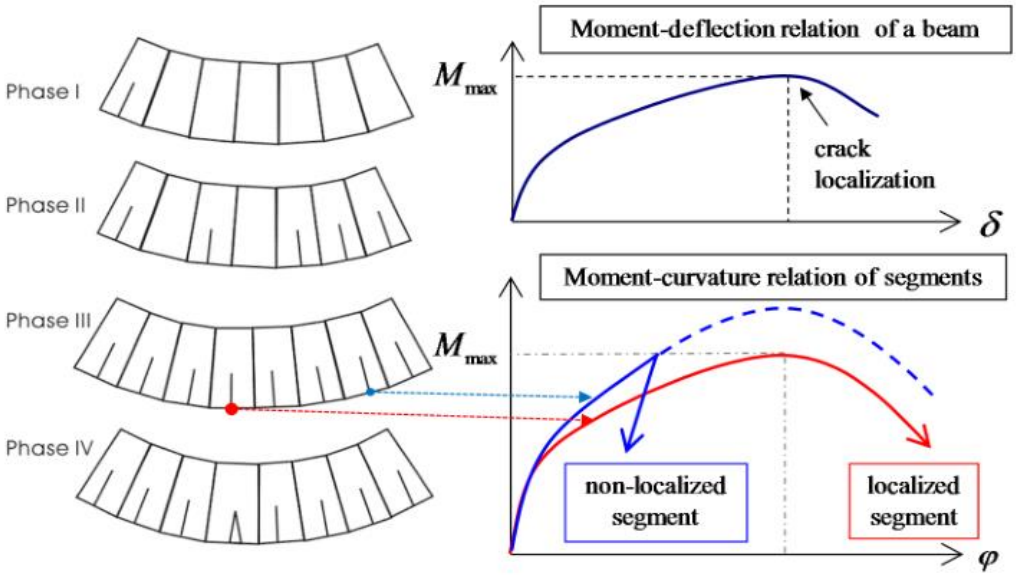

Figure 4-9: Deflection of Beam and curvature of segments with localized and non-localized crack (Shin et al., 2015)

In another study, Imai et al have studied the effect of the width of the crack on the strain enlargement of external CFRP sheet (Imai et al., 2010). They reported that the enlargement factor of the CFRP strain is highly affected by the width of the crack as shown in Figure 4-10. Based on that, a model to simulate the effect of the opened crack is needed.

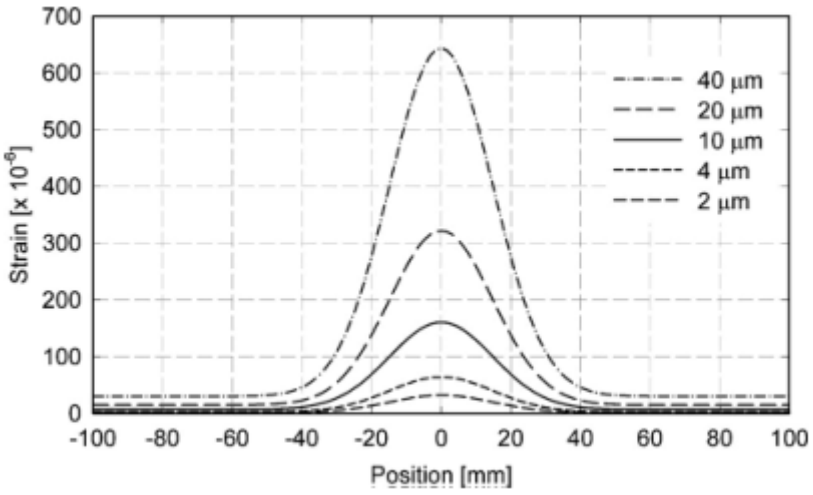

Figure 4-10: Strain distribution as measured by BOCDA-based optical fiber sensor (Imai et al., 2010)

4.2.7.1 Predicting width of the opened crack

Based on the analysis of measurements on RC beams, ACI Committee 224 (Abou-Zeid et al., 2001) reported that the flexural crack widths can be calculated based on the so-called Gergely-Lutz equation:

$$wcr = 2.2\,\beta\varepsilon_s\sqrt[3]{d_c A} \qquad 4\text{-}34$$

Where:

w_{cr} = most probable crack width (in)

β= ratio of the distance between the neutral axis and tension face to the distance between the neutral axis and reinforcing steel.

ε_s = strain in the steel reinforcement bar.

d_c = thickness of cover from the extreme tension fiber to the closest bar, in.

A= Area of concrete symmetric with reinforcing steel divided by number of bars (sq. in)

Figure 4-11 shows all the geometrical factors of the ACI crack model.

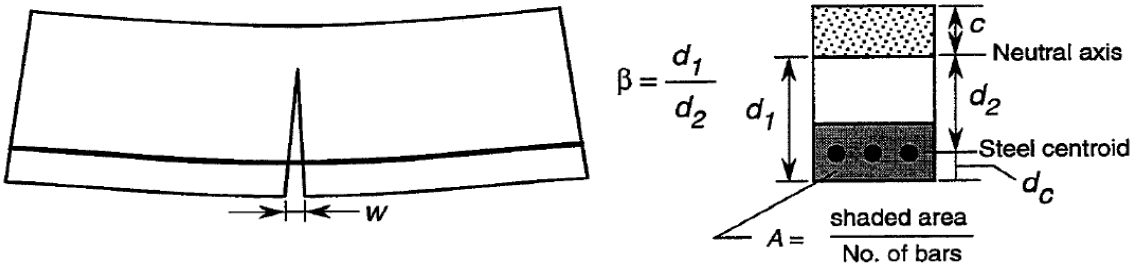

Figure 4-11: Geometrical factors in the ACI approach for control of flexural crack width (Abou-Zeid et al., 2001).

4.2.7.2 Predicting spacing of the cracks

The ACI Code does not consider the expected spacing between flexural cracks (Carino and Clifton, 1995b). So, the location of the cracks along the span should be predefined. One of the proposed model to predict the crack spacing is assumed based on the CEB/FIP approach as follows (Carino and Clifton, 1995b):

$$I_{s,max} = \emptyset\ 3.6\ \rho_{s,ef} \qquad 4\text{-}35$$

Where:

$I_{s,max}$= the maximum distance between cracks.

$\emptyset$ = bar diameter.

$\rho_{s,ef}$ = area of steel divided by effective area of concrete in tension (As/Ac_{ef}).

Ac_{ef} = equivalent to A in the ACI approach (equation 4-34).

According to the CEP/FIP bond-slip model, which is shown in Figure 4-12, intermediate cracks can occur only when the spacing between cracks exceeds $l_{s,\max}$. Thus, crack spacing will range from $l_{s,\max}$ to $0.5\,l_{s,\max}$. The average crack spacing $l_{s,avr}$ is taken to be approximately 2/3 of $l_{s,\max}$ which was also assumed in this study as follows:

$$l_{s,avr} = {}^{2}/_{3}\, l_{s,max} \qquad 4\text{-}36$$

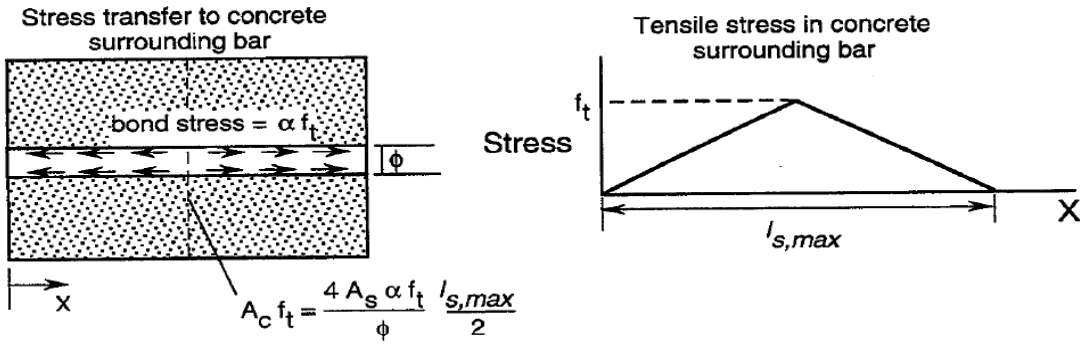

Figure 4-12: Model for computing slip length (Carino and Clifton, 1995b)

4.2.7.3 Modeling of the effect of the opened crack

In this section, the proposed model includes the effect of the width of the cracks on the distribution of curvature and strain is presented. Before any crack occurs, the angle of the curvature θ at each segment represents the average curvature at the segment times length of the segment as shown in the following equations (see Figure 4-13):

$$\theta_{SG1} = \frac{K_{n-1} + K_n}{2} dx \qquad 4\text{-}37$$

$$\theta_{SG2} = \frac{K_n + K_{n+1}}{2} dx \qquad 4\text{-}38$$

$$\theta_{SG1} = \frac{R_c}{L} = \frac{dx}{L} \qquad 4\text{-}39$$

$$L = \frac{dx}{\theta_{SG1}} \qquad 4\text{-}40$$

|When a crack opens at any node, θ at the contiguous segments (elements) is enlarged by a magnifying factor *Mf* as calculated below:

$$\theta_{SG1(cr)} = \frac{d_x + (w_{cr}/2)}{L} \qquad 4\text{-}41$$

$$= \theta_{SG1} + \frac{(w_{cr}/2)}{d_x/\theta_{SG1}}$$

$$= \theta_{SG1}\left(1 + \frac{(w_{cr}/2)}{d_x}\right)$$

Lets $$Mf(\theta_i) = \left(1 + \frac{(w_{cr}/2)}{d_x}\right)$$ 4-42

So $$\theta_{SG1(cr)} = \theta_{SG1} \times Mf\ (\theta_i)$$ 4-43

Where:

θ_{SG1} = Theta of segment 1 without a crack.

$\theta_{SG1(cr)}$ = Theta in segment 2 including the width of the crack.

K_n = Curvature at node *n*.

R_c= Curvature length along segment at the N.A line.

L= distance from N.A. to the intersection point.

dx= length of segment (element).

w= width of the crack.

$Mf\ (\theta)$ = Magnifying factor of theta in the segments contiguous to the crack.

To calculate the strain of the concrete and steel at the crack position (n), the following derivation can be applied:

$$\theta_{SGi(cr)} = \theta_{SGi} \times Mf(\theta_i)$$ 4-44

Based on Equation 4-37 the curvature at each node is:

$$K_n = \frac{2\theta_{SGi}}{dx} - K_{n-1}$$ 4-45

$$K_{n(cr)} = \frac{2\theta_{SGi(cr)}}{dx} - K_{n-1}$$ 4-46

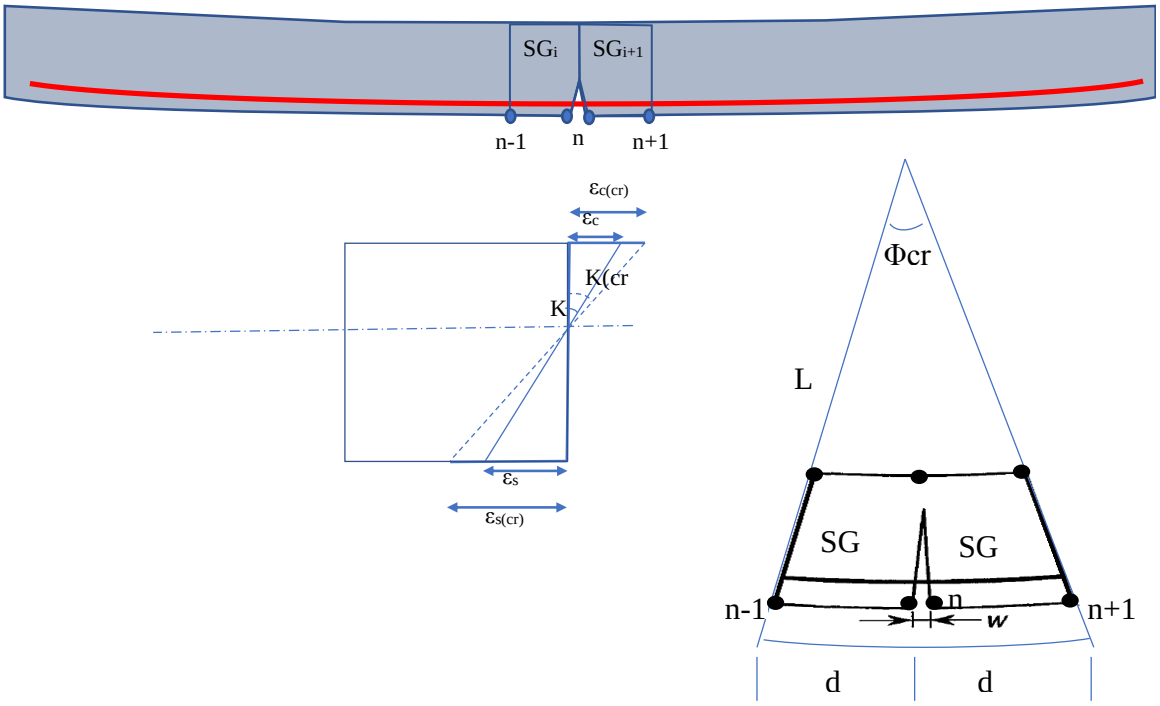

Figure 4-13: Effect of the width of the crack on the curvature.

By substituting equation 4-44 in equation 4-46:

$$K_{n(cr)} = \frac{2}{dx}(\theta_{SGi} \times Mf(\theta_i)) - K_{n-1} \qquad 4\text{-}47$$

By substituting equation 4-37 in equation 4-47:

$$K_{n(cr)} = \left[\frac{2}{dx}\left(\frac{K_{n-1} + K_n}{2} dx\right) \times Mf(\theta_i)\right] - K_{n-1} \qquad 4\text{-}48$$

$$K_{n(cr)} = [(K_{n-1} + K_n) \times Mf(\theta_i)] - K_{n-1} \qquad 4\text{-}49$$

$$K_{n(cr)} = \left[Mf\ (\theta_i)K_{n-1} + Mf(\theta_i)K_n)\right] - K_{n-1} \qquad 4\text{-}50$$

$$K_{n(cr)} = Mf\ (\theta_i)K_n + K_{n-1}[Mf(\theta_i) - 1]\ ) \qquad 4\text{-}51$$

From sectional strain distributions, the strain of steel and concrete can be calculated as:

$$\varepsilon_{c(n)} = K_n y_{o(n)} \qquad 4\text{-}52$$

$$\varepsilon_{c(n)cr} = K_{n(cr)}\ y_{o(n)} \qquad 4\text{-}53$$

$$\varepsilon_{s(n)} = K_n(d - y_o) \qquad 4\text{-}54$$

$$\varepsilon_{s(n)cr} = K_{n(cr)}(d - y_o) \qquad 4\text{-}55$$

Where:

$\varepsilon_{c(n)}$ and $\varepsilon_{s(n)}$ = strain of concrete and steel at node *n* without crack effect.

$\varepsilon_{c(n)cr}$ and $\varepsilon_{s(n)cr}$ = Strain of concrete and steel at node *n* by considering the opened crack.

$y_{o(n)}$ = Distance from N.A to the top fiber of concrete.

The nonlinear analysis procedure presented above is intended to obtain the load-deflection response of one-way RC member up to the ultimate failure load. So, it is capable to quantify the maximum values of the ultimate load, deflection, ductility, total energy and the dissipated energy under any constant strain rates (range between 10^{-4}-300 s^{-1}). The adopted procedure including all the above-mentioned equations was embedded in excel as subroutines by utilizing the visual basic VB editor. With one-click, the program starts running after pre-defining all the needed input data and the results will appear within 5-30 minutes based on the size of the element along the length and type of the analysis (static or dynamic). All the results will appear as tables and plots in a separate data spreadsheet in excel.

4.2.8 Structural response to the impact loading

In the quasi-static state, as a result of the slow loading rate, it is within reach to draw a uniform load-deflection curve to the member then to use it to predict the deflection, ductility, and energy based on any determined applied load. While, in the high loading rate state, such as blast and impact loading, it is complex to predict the dynamic response. The complexity arises from involving many factors in the dynamic response such as the material strain rate dependency, the fluctuation of the strain rate value, the nonlinearity in the inelastic behavior of the material and the uncertainties in the actual

function of the dynamic loads which is a time-dependent function. As such, it is not possible to draw a uniform load-deflection curve for a member to represent its dynamic response to the rapid transient load at variance to the static state. Therefore, to develop any analytical procedure, many assumptions should be imposed. In the following paragraphs, details of the procedure and the imposed assumptions are presented.

In this study, two steps were adopted to predict the dynamic nonlinear response under any determined short transient rapid load (impulse with determined *Fm* and t_d). The first step comprises following the nonlinear layered method, as presented in the previous sections, to obtain the elastic strength (Ru) and the maximum elastic deflection (y_e). While the second step is dedicated to estimate the maximum displacement response (y_m) under the applied impulse. If only the ultimate response of the member is requested, only the first step is applied by applying incremental strain in the top fibre of concrete up to the crushing value 0.0035. This should be enough to determine the ultimate values of load, ductility, total and dissipated energies of the member which is the main aim in this study. In case of the multi-impact case where the dissipated energy for each drop is needed, both the steps should be followed to obtain the results.

In the second step, many assumptions are made to estimate the maximum response of the structural member. The fundamental assumptions were made by considering the structural response of the system as that of a single degree of freedom (SDOF) system. The applied load function was idealized as a triangular shape with known values of peak force and load duration. This found to be reasonable to simulate the impact impulse based on the comparison with the measured impact impulse as will be shown later. Also, this idealization was approved to be adequate in simulating the blast and impact impulse by many researchers (Fujikake et al., 2009, Ngo et al., 2007a, Mosalam and Mosallam, 2001). Also, the dynamic response of the member was assumed to be elastic-perfectly plastic by neglecting the hardening effect.

The dynamic load factor of the applied load was included by establishing a link between the duration of the load and the natural period of the member. In this procedure, two methods are adopted to predict the maximum deflection of the SDOF system, one is used when the total behaviour is within the elastic range, and another is used when a plastic response is expected in the SDOF system. Details of both methods are given in the following sections.

4.2.8.1 Elastic SDOF system

The simplest way to simulate the dynamic response of a member subjected to a suddenly applied load is by means of the SDOF approach. The structure is represented by a system of a concentrated mass M which is subjected to a suddenly applied load as an impulse *F*(*t*). While the resistance of the member to the applied load is represented by a weightless spring with an equivalent stiffness K as illustrated in Figure 4-14. Based on that, the equation of motion of the un-damped elastic SDOF system is given by Biggs (1964) as:

$$M\ddot{y} + Ky = F(t) \qquad 4\text{-}56$$

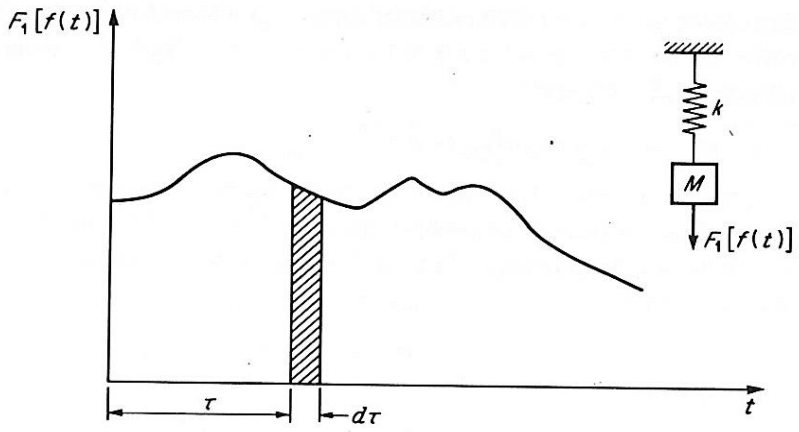

Figure 4-14: General load function of the dynamic applied load.(Biggs and Biggs, 1964).

The solution of this second order differential equation is very complex if the applied load was varying with time and often numerical solution is needed. To begin with a simple case, the suddenly applied load is assumed to have a constant magnitude with infinite duration time. In this case, the solution for equation 4-56 is:

$$y = C1\ \sin\omega t + C2\ \cos\omega t + \frac{F(t)}{K} \qquad 4\text{-}57$$

$$\dot{y} = C1\ \cos\omega t - C2\ \sin\omega t \qquad 4\text{-}58$$

Where ω represent the natural frequency of the member which can be calculated as:

$$\omega = \frac{2\pi}{T} = \sqrt{\frac{K}{M_{equ}}} \qquad 4\text{-}59$$

C1 and C2 can be calculated by applying the initial conditions of the state. By assuming that the member is moving from the rest, the initial conditions are taken as t=0 and y_o=0. So, C1 and C2 are represented as:

$$C1 = \dot{y}_o \qquad 4\text{-}60$$

$$C2 = y_o - \frac{F(t)}{K} \qquad 4\text{-}61$$

If the load function is represented as a function of a constant force (F1), which represent the peak force, then the load function can be described as F1[f(t)]. So, the general solution for equation 4-62 becomes (Biggs and Biggs, 1964):

$$y = y_o \cos \omega t + \frac{\dot{y_o}}{\omega} \sin \omega t + y_{st}\, \omega \int_0^t f(t) \sin \omega (t - \tau) d\tau \qquad 4\text{-}62$$

Where y_{st} represents the static deflection due to the peak force F1 and can be represented as:

$$y_{st} = \frac{F1}{K} \qquad 4\text{-}63$$

Where:

$y(t)$ = the maximum deflection at time t.

$\dot{y}$(t)= velocity of the deflection at time t.

F1= the peak value of the impact load.

K= stiffness of the structural member.

ω = the natural frequency of the structural member.

t= time in the deflection- time function

τ= time in the load-time function.

t_d= the loading period of the impact impulse(I).

T = the natural period of the structural member.

The stiffness of the simply supported member is calculated based on the elastic theory as:

$$K = \frac{f\ EI}{L^3} \qquad 4\text{-}64$$

Where *f* is constant and taken as 48 for uniformly distributed load and 76.8 for the concentrated load acting in the mid-span. In this study, since the load is distributed uniformly on part of the entire length Le (partially distributed load) the factor *f* was taken as 68 based on the ratio of the equivalent loaded length to the total length (Le/L).

The dynamic load factor (DLF) is defined as the ratio of the maximum elastic dynamic deflection to the maximum elastic static deflection of the member under the same magnitude of the force. So, the maximum elastic dynamic deflection of any member can be estimated based on the DLF as a reference to the maximum static deflection. The DLF can be simplified to be a nondimensional factor as follows:

$$DLF = \frac{y_{\max(d)}}{y_{\max(s)}} = \frac{y_{\max(d)}}{F_m / K} = \psi(\omega t_d) = \psi \times 2\pi\left(\frac{t_d}{T}\right) \qquad 4\text{-}65$$

Where $y_{max\ (d)}$ and $y_{max\ (s)}$ represent the maximum deflection under dynamic and static effect of load with a peak magnitude of Fm.

The DLF can be introduced as a curve based on the ratio t_d/T. Biggs (Biggs and Biggs, 1964) proposed different curves for different simulations of loading function such as constant, linear, rectangular, triangular and equilateral triangular. It was found that the triangular model fits the blast loading due to the finite rising time of the blast loading. In the present study, the equilateral triangular model was used to predict the maximum impact response since the measured impact load function was found to be similar to the equilateral triangular shape. The DLF curve of the equilateral triangular load function proposed by Biggs (Biggs and Biggs, 1964) is shown in Figure 4-15.

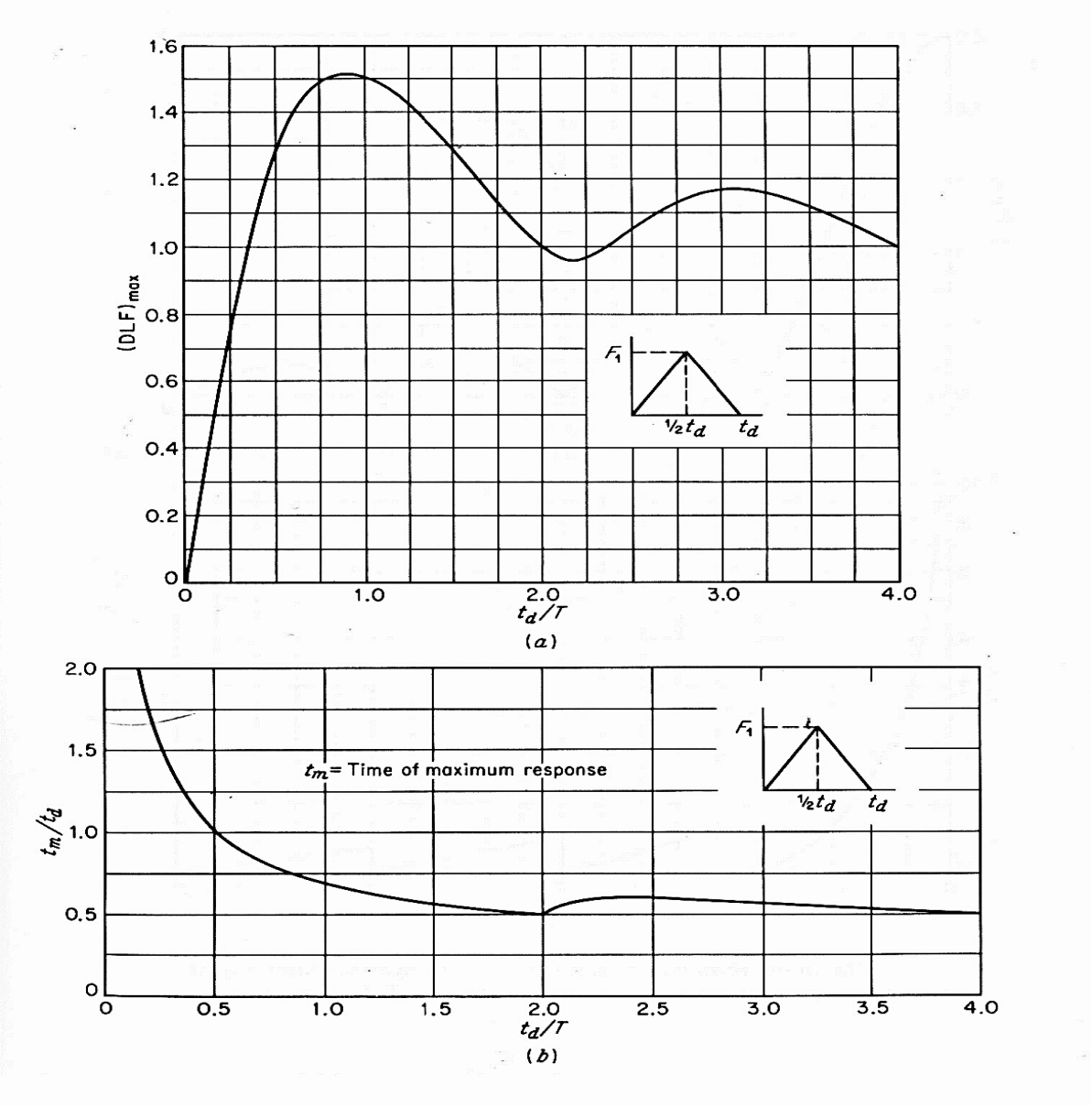

Figure 4-15: Maximum response of one-degree elastic systems (undamped) subjected to equilateral triangular load pulse, a) the DLF curve, b) time of the maximum response (Biggs and Biggs, 1964).

4.2.8.2 Elasto-plastic SDOF system:

When the structural elements are expected to exhibit large plastic deformation under high impulse loadings, the elastic SDOF is not capable to predict the entire response of the member. Predicting the entire dynamic response is only possible by following step-by-step numerical solution by using a nonlinear dynamic finite element analysis software. However, an ideal elasto-plastic SDOF system is commonly used to predict both the dynamic transint loading (Impulse) and the resulting deformation with uncertainty about

the degree of the accuracy (Biggs and Biggs, 1964, Ngo et al., 2007a). The proposed ideal dynamic response was made based on a predicted ductility factor ($\mu = y_m/y_e$) which was estimated based on the ratio of the applied dynamic load to the dynamic yielding strength of the member (*Ru*) as shown in Figure 4-16. For example, if the structural member with a determined dynamic resistance (*Ru*) is subjected to a dynamic rapid equilateral triangular load pulse with a peak force value of F_m, the result of the maximum deformation (y_m) can be estimated based on the predicted ductility factor. Biggs (Biggs and Biggs, 1964) proposed charts including set of curves to estimate the ductility factor based on the idealized load function. Figure 4-17 shows chart of the equilateral triangular load function as presented by Biggs (Biggs and Biggs, 1964).

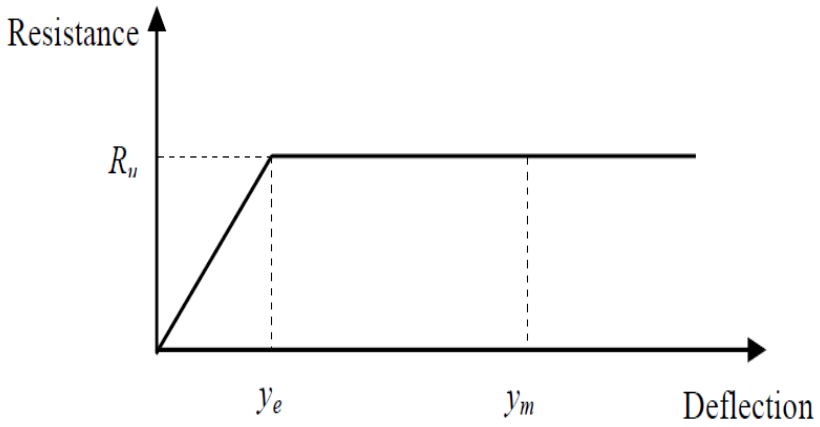

Figure 4-16: Simplified resistance function of an elasto-plastic SDOF system (Biggs and Biggs, 1964).

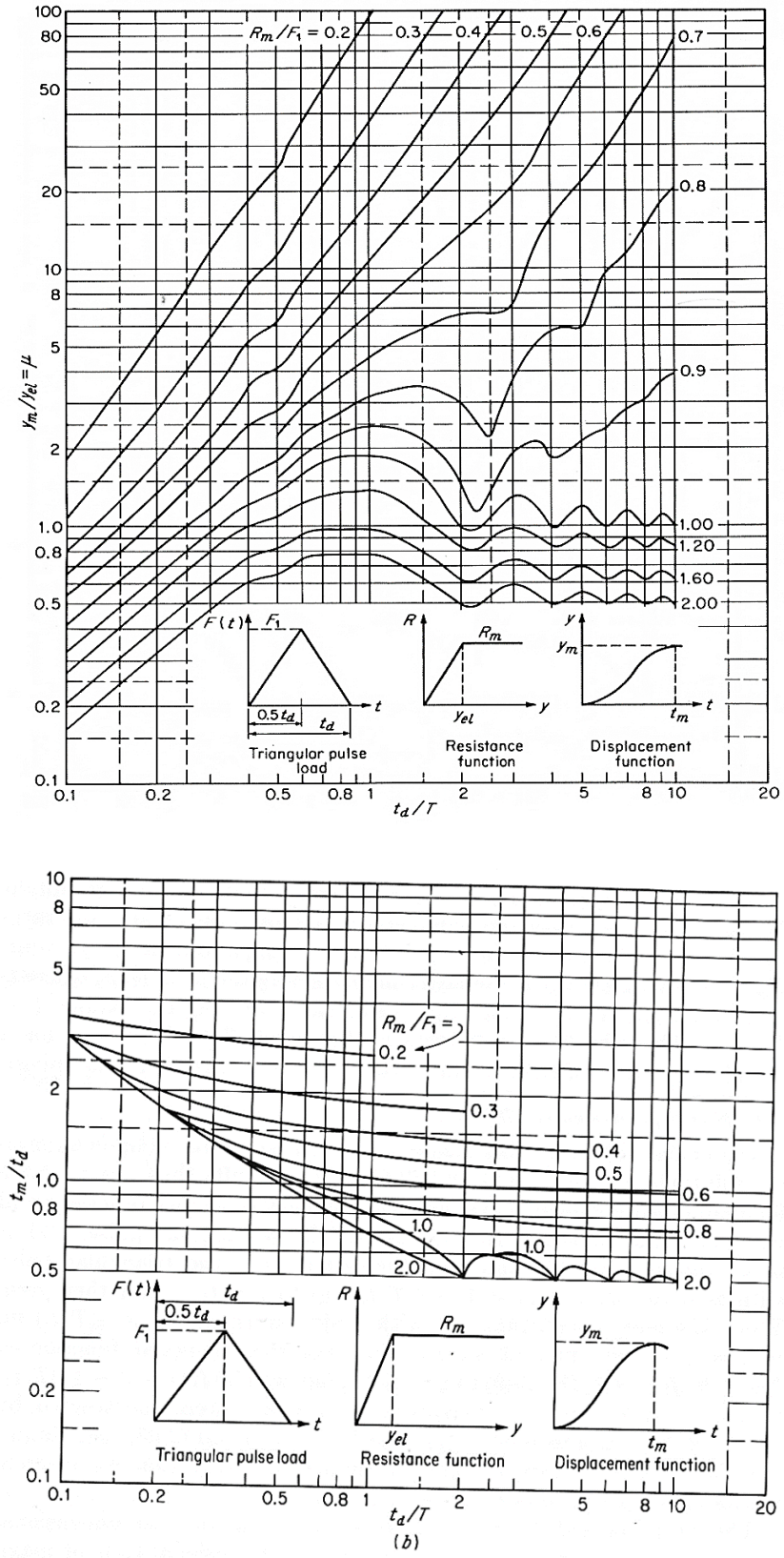

Figure 4-17: Maximum response of elasto-plastic SDOF system to a triangular load (Ngo et al., 2007b).

4.3 The numerical analysis

The numerical analysis, popularly known as finite element analysis (FEA), is widely used to study the response of the structural member under different conditions. The popularity of the FEM technique is attributed to its ability to provide solutions for problems involving complexity. Material and geometric nonlinearities, strain rate effect, and irregularity in the load applied are examples to the complexity of the structural response to the static and dynamic loading. Many commercial finite element codes are available to simulate the nonlinear structural response. In this study, ABAQUS/CAE FE software (v 6.14) (Abaqus, 2011) is selected to be used to simulate the structural response of the RC one-way slab with the NSM technique. This FEM code has two types of analysis procedure: standard which is dedicated for the static problems, and explicit which is designed for the dynamic problems including response to very short transient loads such as blast and impact. Abaqus code also has ability to model problems involving contact between surfaces such as the impact of a falling mass. This software has a wide range of material models and types of meshes in its library with the options to include user defined material model which make it possible to simulate different types of materials such as concrete, steel, and CFRP. In the following sections, details of the material models, meshes, element types, failure models, loading method and other parameters which are implemented in the current study are discussed.

4.3.1 Modelling of reinforced concrete member

In Abaqus, the concrete block can be modelled as 2D or 3D solid or shell element as shown in Figure 4-18. For complicated problem such as impact response 3D element is found to be more accurate in representing the three-dimensional stresses. Reinforcing bars can be modelled by either a discrete or embedded element as shown in Figure 4-19. With the discrete element, which can take solid beam element, the bond between the reinforcement bar and the concrete is assumed to be perfect unless idealized linkage elements having a spring stiffness with a defined bond-slip relationship are used. the drawback of the discrete approach is that the mesh discretization is restricted at the location of the reinforcement which could be complicated in some cases. With the embedded option available in Abaqus this problem is overcome by allowing the compatibility in the displacement between the concrete and the reinforcement in any layout without any complication in the meshing process. The embedded method is

advantageous in simulating most of RC structures which have reinforcement with complex layout scheme.

In this study, 3D hexahedron brick element with eight nodes (C3D8R) was selected to model the concrete block. An embedded 3D truss element with two nodes (T3D2) was selected to model the steel and CFRP bars assuming perfect bond between the reinforcing bars and the concrete. By utilizing the symmetry of the one-way RC slab in the two directions, a quarter of the slab is meshed in Abaqus to reduce the running time. Figure 4-18 shows the FE models used for the concrete and the reinforcing bars on the quarter of the slab.

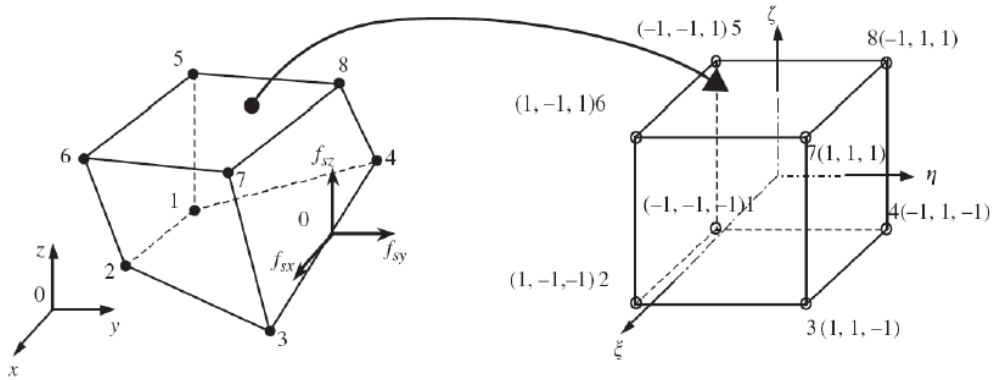

Figure 4-18: Eight node hexahedron brick element (Sangi, 2011, Barros et al., 2006).

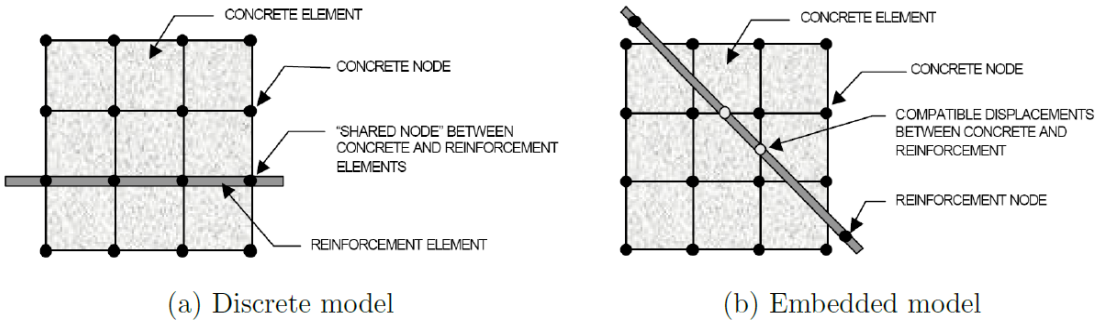

Figure 4-19: Representation of reinforcement in concrete model (Sangi, 2011).

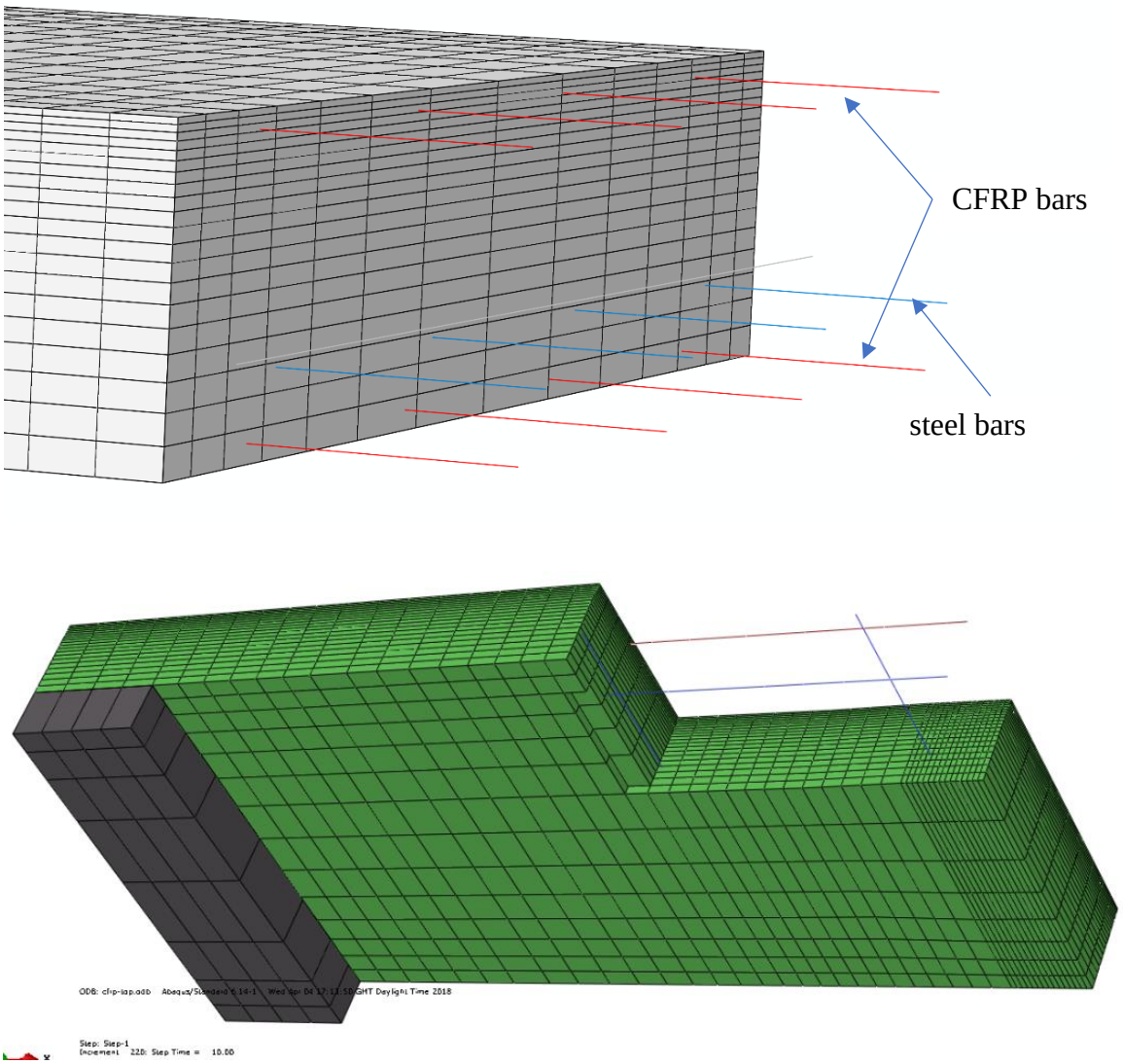

Figure 4-20: The adopted FE model of the RC slab showing concrete, steel and CFRP bars.

4.3.2 Material constitutive modelling

Since the stress-strain relationship of the constitutive material plays a significant role in the structural response of the member to the applied load, defining this relationship is crucial in any numerical analysis approach. Abaqus has many models to define different types of materials having different physical state and mechanical properties.

4.3.2.1 The constitutive model of concrete

Concrete has a compression stress-strain relationship which consists of elastic and plastic regimes with hardening and softening strain behaviour. While in tension, linear

elastic stress-strain behaviour up to the cracking limit is represented. The failure mode of concrete is brittle either in compression which is represented by crushing failure or in tension which is represented by cracking failure. In tension, when the cracked concrete element is reinforced with steel bars the best way to simulate the tension behaviour is by adopting tension stiffening model. In Abaqus, two type of concrete material models are included: the smeared crack model and the Concrete Damage Plasticity model (CDP). The latter model is more accurate in estimating the response to the dynamic loads such as impact, blast and cyclic loading. In this study, CDP model is used to simulate the material behaviour of concrete for both static and dynamic loading conditions. In this model, the isotropic elastic behaviour of concrete in compression up to the proportional limit is defined by identifying Young's modulus, density, and Poisson's ratio. The plastic behaviour is defined by providing the stress-plastic strain values in a tabular form as an input parameter data. The same should be done to define the post-cracking stress-strain behaviour of concrete in tension by pre-defining the stress-strain data from a proper tension stiffening model

In addition to the basic parameters to define the stress-strain behaviour, parameter to define the microstructure of concrete is needed. In Abaqus, these parameters are defined by the dilation angle ψ, flow potential eccentricity ϵ, the ratio of initial biaxial to the uniaxial compression stress $\sigma_{co}/\ \sigma_{bo}$, the ratio of the second stress invariant on tensile meridian K_c and the viscosity parameter μ. In this study, the default parameters of the failure shape which were recommended by (Kmiecik and Kamiński, 2011), as shown in Table 4-1, are used. In this study, if the viscosity parameter is taken as 0, a convergence problem occurs when the first crack initiated. So, value of 0.005 S was selected to conduct the numerical study after fitting with the experimental result.

Table 4-1: Default parameter of CDP model under compound stress (Kmiecik and Kamiński, 2011)

Dilation angle	Eccentricity	$\sigma_{co}/\ \sigma_{bo}$	K_c	Viscosity parameter (sec)
36	0.1	1.16	0.667	0*

*: Replaced by 0.005 in this study to overcome the convergence problem

When the concrete member is subjected to dynamic, such as impact, recycle blast and earthquake, the concrete element at the member is expected to experience reversal in

the applied stresses with time due to rebound or vibration of the member. Considering this, the stress-strain relationship during the reloading state changes due to the relative damage in the concrete element based on the level of the plasticity at each stage. This behaviour is considered in CDP model by defining the relationship between the damage level and the plastic strain in compression and in tension. Based on that, a modification stress-strain relationship is used in CDP model to consider the level of damage d_c and d_t in both compression and tension part as shown in Figure 4-21.

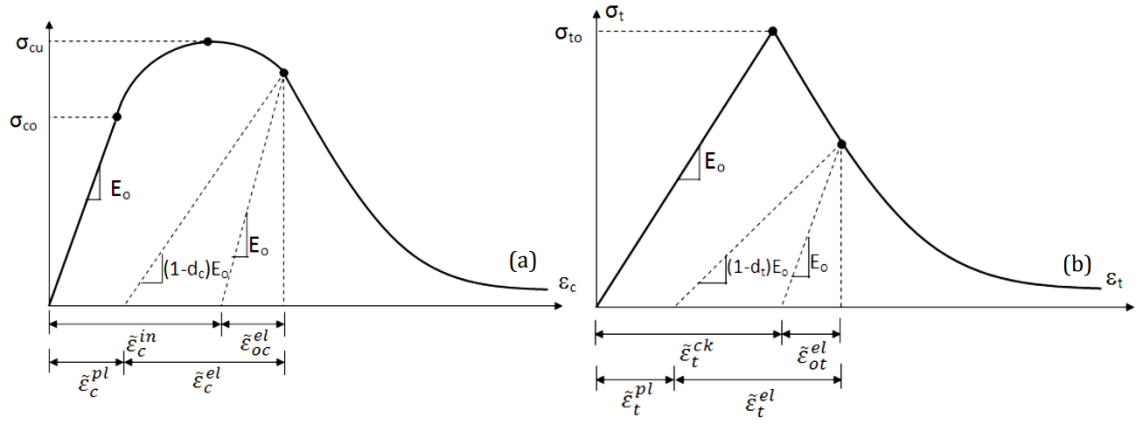

Figure 4-21: The Modified stress-strain curve of concrete in the CDP model (Abaqus, 2011).

The stress-plastic strain data is obtained based on the same equation which was used in the analytical procedure , i.e. proposed by Carreira (Carreira and Chu, 1985), was used. The strain obtained from this equation is converted to inelastic strain then to plastic strain based on the following equations:

$$\varepsilon_c^{pl} = bc\varepsilon_c^{in} \qquad 4\text{-}66$$

$$\varepsilon_c^{in} = \varepsilon_c - \sigma_c E_c^{-1} \qquad 4\text{-}67$$

The compression damage factor dc is then calculated based on the following equation:

$$dc = 1 - \frac{\sigma_c E_c^{-1}}{\varepsilon_c^{pl}\left(\frac{1}{bc} - 1\right) + \sigma_c E_c^{-1}} \qquad 4\text{-}68$$

Where b_c is a model parameter for unloading uniaxial compression test within a range of 0 to 1 used to estimate the ratio of the plastic to the inelastic strain as shown in Figure 4-22.

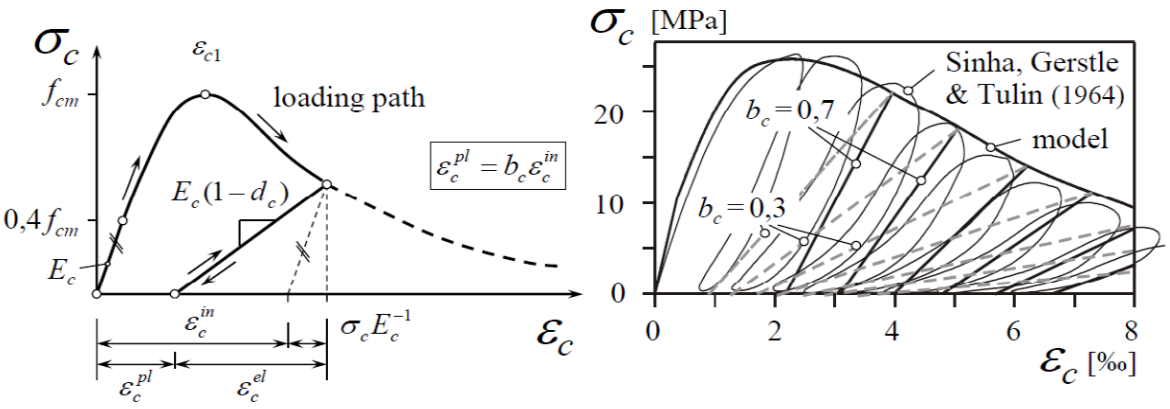

Figure 4-22: The relationship between the plastic and the inelastic strain with the consideration of the damage parameter dc (Sinha et al., 1964).

In the RC member and when fine element size is used in the tension zone the analysis is found to be sensitive to the elements when there is no reinforcement in them as in the concrete cover. So, converting the tensile stress-strain relationship to a tensile stress-displacement relation is recommended, where the displacement in the displacement field represents width of the crack w_c which is obtained from the following equations:

$$\frac{\sigma_t}{f_{ct}} = [1 + (c_1 w/w_c)^3]e^{-c_2\frac{w}{w_c}} - \frac{w}{w_c}(1 + c_1^3)e^{-c_2} \qquad 4\text{-}69$$

$$w_c = 5.14\,\frac{G_F}{f_{ct}} \qquad 4\text{-}70$$

Where w= width of the equivalent crack, wc= width of the equivalent crack at the complete release of the tension stress or the fracture energy, σt= the tensile stress normal to the direction of the crack, GF= the fracture energy needed to create a stress-free crack over a unit are, fct= tensile strength of concrete, c1 and c2 are constants factors which are taken as 3 and 6.93. When there is no test data, fct and GF can be calculated based on the following CEB-FIP (Code, 1993) equations:

$$f_{ct} = 0.23\ \bar{f_c}^{2/3} \quad \text{4-71}$$

$$\text{GF} = (0.0469 d_a^2 - 0.5 d_a + 26)\ \left(\frac{\bar{f_c}}{10}\right)^{0.7}\ , \text{Nm/m}^2 \quad \text{4-72}$$

Where d_a= maximum aggregate size (mm) and $\bar{f}c$= strength of concrete (MPa). In this study, da was taken as 20 mm based on the measured data.

4.3.2.2 The constitutive model of steel bar

Steel is simulated as an isotropic material with elastic-strain hardening plastic behaviour under both tension and compression stresses. In Abaqus, the elastic and the plastic behaviour are modeled separately. The elastic behaviour is modeled by defining the modulus of elasticity and Poisson's ratio and the plastic range is modeled by defining the yielding stress and the corresponding plastic strain up to the rupture limit. These two models are available under "Elastic" and "Plastic" options from the material library modes. The strain rate effect is included in the plastic range behaviour as it is available within the plastic model. The stress-strain relationship in the plastic regime should be provided in a tabular form. In this study, the stress-strain data was provided based on the piecewise linear steel model which was proposed in the analytical analysis which has been validated with the measured data. The failure in the steel was modeled by selecting the "Ductile Damage" which is available in Abaqus for defining failure of ductile material by specifying the fracture strain value with the strain rate dependency. In this study, the fracture strain was taken to be 0.035 based on the measured data. No strain rate effect on the fracture strain was assumed according to the proposed steel model.

4.3.2.3 Constitutive model of CFRP bars

CFRP composite material has an orthotropic material behaviour based on the orientation of the Carbon fibres in the composite. So, if it is used as a 2D or 3D strengthening material (sheet or strip), the orthotropic mechanical properties need to be defined. If the CFRP designed to work as a unidimensional strengthening material, such as CFRP rods, then an isotropic behaviour can be assumed. In this study, since the implemented NSM CFRP technique uses the composite as a one-dimensional reinforcing bar and the geometry is modeled by using truss element, an isotropic behaviour is assumed to model the CFRP material. Based on that, a linear elastic stress-strain model

was selected to model the CFRP material by defining its modulus of elasticity and Poisson's ratio. Brittle failure model was used to model the failure by defining the fracture strain of CFRP which was taken as 0.011 as obtained from the direct tensile test (Section 3.2.2.3).

4.3.3 Simulating the applied load

In Abaqus, the load can be simulated either by a load control or a displacement control method. The load control method is the general method and used to simulate different type of loading such as concentrated, distributed and partially distributed loads. While in the displacement control method, simulating the non-concentrated load is complicated. The displacement control method outstands the load control method in simulating the softening behaviour in the entire load-deflection behaviour. In this study, the load control method is used in applying the distributed for the ease of simulating the non-concentrated loads (such as the partially uniformly distributed load) and the difficulty of predefining the velocity of deflection wave which is needed in case of using the displacement control method. However, simulating the nonlinear response of the structural element by using displacement control method can overcome the convergence problemes which occurs when the resistance of the element drops due to cracking or softening behaviour. In the standard version of Abaqus, which is used for the static analysis, the load is applied incrementally up to the maximum load. In the Explicit version, which is used to analyse the dynamic problems, a rapid transient load is applied by defining the load-time function in a tabular form which is available in Abaqus to simulate the transient loads.

4.3.4 Predicting the crack pattern

In terms of the crack patterns, both the analytical and the numerical crack patterns were compared with the experimental crack pattern which was assessed based on visual observation at the ultimate state. In the analytical procedure, the crack pattern was estimated by calculating the width of the cracks at any potential position of a crack as presented in Section 4.2.7. For the comparison, only four cracks were considered along half of the symmetrical span in this study. Figure 4-23 shows the typical predicted crack pattern along the span of each slab. While in the numerical procedure the plastic strain distribution at the tension face of the slab is used to estimate the crack pattern along the span length.

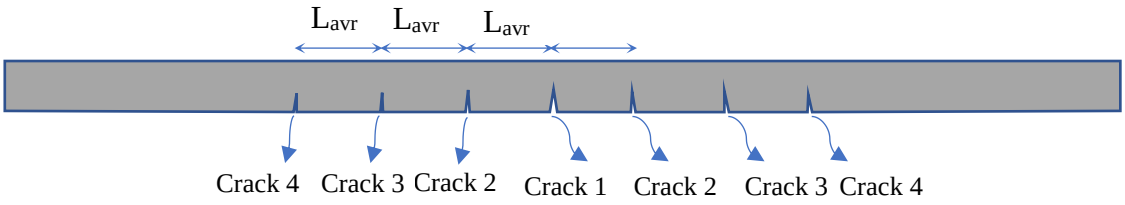

Figure 4-23: The typical crack pattern of the slabs based on the average crack spacing.

4.4 Summary

One of the objectives in this study is to introduce nonlinear solution to simulate the static and dynamic response of NSM CFRP system. In this chapter, two nonlinear solutions were presented; analytical and numerical solutions. The analytical solution was derived based on the layered method where all the adopted equations were imbedded in an excel data spreadsheet by using VB code. While the numerical method was done by adopting the commercial FEA software ABAQUS/CEA (Abaqus, 2011) where both the standard and the explicit versions were used in analysing the static and dynamic problems. All the assumptions and the constitutive material models which are adopted in both solutions are presented in detail in this chapter. While the results obtained from both procedures are presented in the next chapter. The analytical solution is dedicated for simulating the static and dynamic response of the one-way structural member. However, the basic assumptions adopted in the analysis limit its wide application and more improvement is needed to cover all the aspects in the structural response. The adopted assumptions include neglecting the shear stresses, assuming perfect bonding properties in the contact surfaces between the concrete and the reinforcing materials, assuming constant strain rates during the dynamic response. In the numerical solution, the debonding in the reinforcement was neglected as perfect bond was assumed in the bonding area. Also, the constitutive material models were assumed based on predefined stress-strain relationships for all the structural materials and for different values of strain rates then to obtain the relationship for any determined strain rate based on the interpolation processing.

CHAPTER 5: RESULTS AND DISCUSSION

5.1 Introduction

One of the main objectives in this study is to provide nonlinear solution models to simulate the blast and impact response of the one-way RC NSM CFRP system to give better understand to the entire behaviour of the system and to study and investigate all the potential factors involved in the structural response which cannot be covered or studied experimentally due to the destructive and the extremely short duration loads. As mentioned in chapter 2, limited research was conducting in the modelling of the blast resistance of FRPs composites in both the analytical and the numerical simulating. However, due to the variety in properties and shapes of the FRPs materials, no numerical or analytical model found to be outstanding or comprehensive in simulating the FRPs composites. This was reflected in the absence of any design guideline for the blast resistance field.

In this study, two models were introduced to simulating the blast and impact response of the one-way RC NSM CFRP system by adopting analytical and numerical solution techniques. Details of the adopted nonlinear solutions were presented in chapter 4. To validate the adopted models, the predicted results were compared with the experimental results obtained in this study by conducting quasi-static and impact tests as presented in chapter 3.

This chapter presents the comparison between the predicted results of both the theoretical and the numerical analysis procedures and the experimental results to validate the adopted models. The verification was divided into two parts based on the strain rate regime, one for the low strain rate regime represented by the quasi-static loading, and the other for the high strain rate regime represented by the impact loading. Following that, parametric studies were carried out theoretically by using both the analytical and the numerical procedure by assuming different strengthening ratio of CFRP reinforcing on both faces of the one-way RC slab to investigate the potential affecting factors in the RC NSM system. The obtained results are presented and discussed in the following sections.

5.2 Validating the nonlinear analysis procedures in the quasi-static regime

5.2.1 The load-deflection behaviour

To validate the developed analytical and numerical procedures in the low strain rate regime (quasi-static state) both slabs (QC1 and QS1) were analyzed and compared with the experimental results presented in Table 3-4. Table 5-1 shows all the experimental and the predicted results of both QC1 and QS1.The results using the analytical procedure are calculated with and without the effect of the width of the cracks (i.e. discrete and smeared crack techniques), where the discrete crack technique was used by including with of the opened crack based on the proposal opened crack model as presented in section 4.2.7.3 while this effect was neglected in the smeared crack technique. It shows that including the width of the cracks contributes to a slight increase in the predicted deflections and as a result on the predicted total and dissipated energy.

For the slab QC1 it shows that the measured yielding load is 18.8 kN while the predicted yielding load is 19.04 and 17.68 kN from the analytical and the numerical models respectively. Both the predicted yielding loads are close to the measured value with difference factor ranges between 1 to 6%. In terms of the yielding deflection, a predicted value of about 7.7 mm was obtained from both solutions which was close to the measured value of 7.0 mm. In terms of the ultimate state, the predicted ultimate load was 22.9 kN and 24.6 kN for the analytical and the numerical solution respectively as compared to the measured value of 23.5 kN indicating good match between the experimental and the two modelling procedures. The predicted ultimate deflection of slab QC1 when the concrete reached the crushing strain in compression was 16.9 mm and 18.5 mm for the analytical and numerical solutions respectively, while the measured ultimate deflection is 19.7 mm. Figure 5-1 shows the entire load-deflection curves of slab QC1 up to the ultimate state from the analytical and the numerical procedures and the physical experiment. It shows that both solutions are in good agreement with the experimental load-deflection behaviour up to the ultimate state of the slab.

To validate both the predicted solutions with the experimental results of the strengthened slab QS1, the comparisons are made as above. The predicted yielding load is 23 kN for both the analytical and the numerical solutions while the measured yielding load was 22 kN. This indicates that both procedures are good in estimating the yielding load within a margin of 5%. In terms of the ultimate state, both the analytical and the

numerical predicted ultimate loads (40.8kN and 38.5kN), were close to the experimental ultimate load (38.7kN) within a range of 5%. The ultimate deflection at the crushing failure was 26.5 mm, 26.9 mm and 24.5 mm for the analytical, numerical and experimental procedures respectively.

Figure 5-2 shows both the predicted analytical and numerical load-deflection behaviour in comparison with the recorded load-deflection behaviour of slab QS1. It shows that both the analytical and the numerical procedures are in good agreement with the experimental load-deflection behaviour up to the ultimate state.

5.2.2 The total and the dissipated energy

Table 5-1 and Figure 5-3 show the quasi-static results of the total and the dissipated energy of slabs QC1 and QS1 obtained from analytical, numerical and experimental procedures which are calculated based on integrating the area under the load-deflection curve as described in Section 3.5. The enhancement factor of each energy value is presented in Table 5-1 as well.

For the control slab QC1, while the experimental results of the total and the dissipated energy were 354 J and 253 J respectively, the predicted total and dissipated energies were 292 J and 180 J for the analytical procedure and 262 J and 155 J for the numerical procedure. The predicted values are quite close to each other and both are lower than the experimental total and dissipated energy of about 16% and 65% respectively indicating that both the predicted models give good estimation in terms of the ultimate total energy for the control slab. While both procedures are underestimate the ultimate dissipated energy of the slab by about 65%. It is worth mentioning that the ultimate dissipated energy was calculated experimentally based on the measured strain of concrete which gives the average strain along the 60 mm concrete strain gauge while in the maximum strain of concrete was depended to define the ultimate state theoretically.

For slab QS1, while the experimental results of the total and the dissipated energy were 614 and 310 J respectively, the predicted total and dissipated energies were 740 and 385 J for the analytical procedure and 599 and 327 J for the numerical procedure. As shown in Figure 5-3, the numerical predicting of both energies is so close to the obtained results with a difference factor of about 2% and 5% respectively. While the difference between the analytical results of both the total and the dissipated energies were 20% and

24% respectively. This indicates that the accuracy of the numerical procedure is more than that of the analytical procedure in estimating the total and the dissipated energy of the strengthened slab QS1. However, the accuracy of the theoretical procedure gave good estimating of the energy with an accepted percentage of error (20-25%).

Table 5-1 shows that when the slab was strengthened in both faces with NSM CFRP system the total and the dissipation energy were enhanced with an enhancing factor in the quasi-static condition. The measured enhancing factor of the total and the dissipated energy was 1.73 and 1.23 compared to a predicted enhancing factor of the total and energy dissipation of 2.58 and 2.14 in the analytical procedure and 2.29 and 2.11 in the numerical procedure as shown in columns h and j of Table 5-1 . Overall, both the procedures are adequate to predict the entire response of the NSM CFRP system within an acceptable percentage of error.

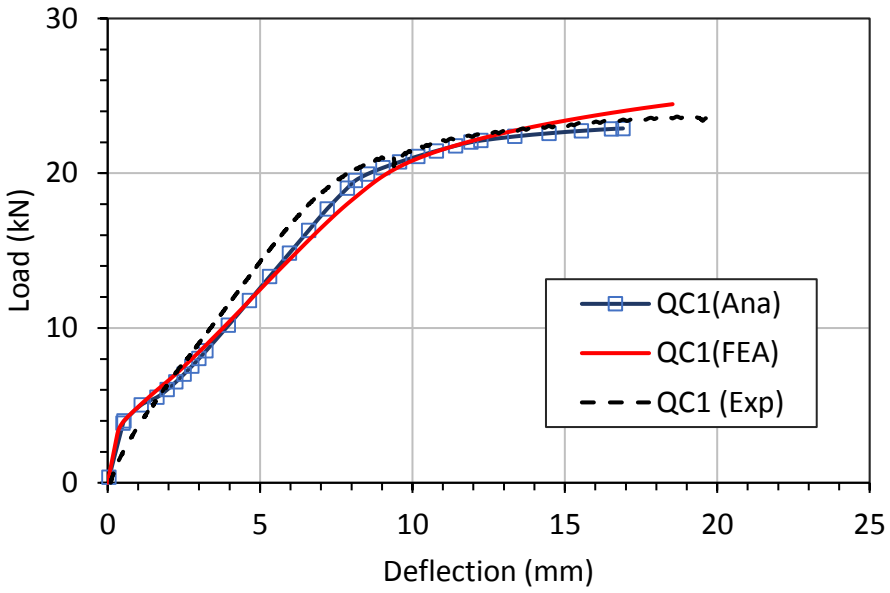

Figure 5-1: Comparison of the analytical and the numerical load-deflection behaviour with the experimental behaviour of the control slab (QC1)

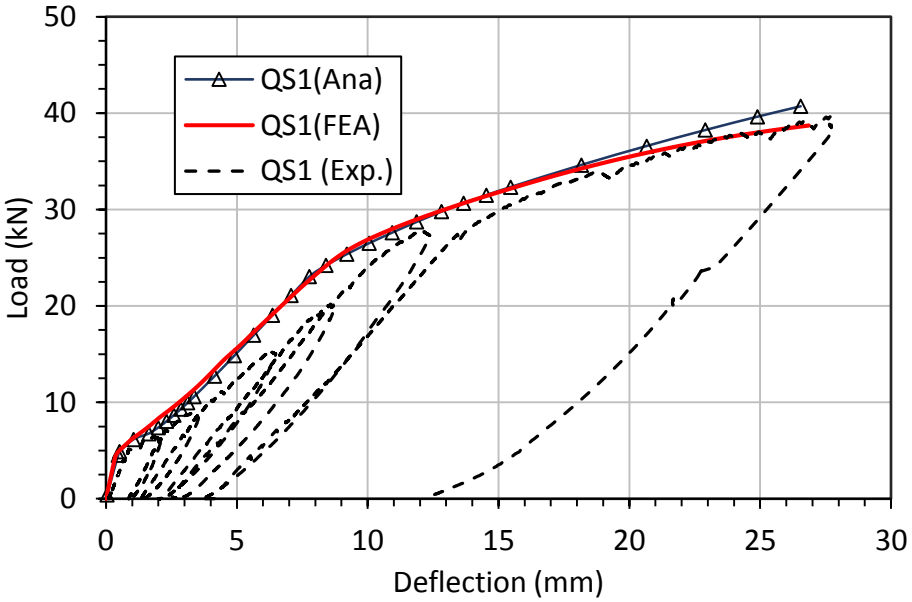

Figure 5-2: Validation of the analytical and the numerical load-deflection behaviour with the experimental behaviour of the strengthened slab (QS1)

Table 5-1: The experimental and the predicted results of the tested slabs QC1 and QS1

a	b	c	d	e	f	g	h	i	j
Slab	Yeilding load P_y kN	Yeilding deflection Δ_y mm	Ultimate load P_u kN	Ultimate deflection Δ_u mm	Ductility factor (Δ_u/Δ_y)	Total Energy (E_t) J	Enhancing factor of Et	Dissipated Energy (E_d) J	Enhancing factor of E_d
	The analytical results (Smeared crack technique)								
QC1	19.04	7.87	22.9	16.9	2.15	279	2.58	169	2.24
QS1	23	8	40.7	26.5	3.31	720		378	
	The analytical results (Discrete crack technique)								
QC1	19.7	7.87	22.9	16.9	2.15	292	2.53	180	2.14
QS1	23	8	40.8	26.7	3.34	740		385	
	FEA results								
QC1	17.68	7.6	24.6	18.5	2.43	262	2.29	155	2.11
QS1	27.6	8	38.7	26.9	3.36	599		327	
	The experimental results								
QC1	18.8	7	23.5	19.7	2.81	354	1.73	253	1.23
QS1	22	10	38.7	24.5	2.45	614		310	

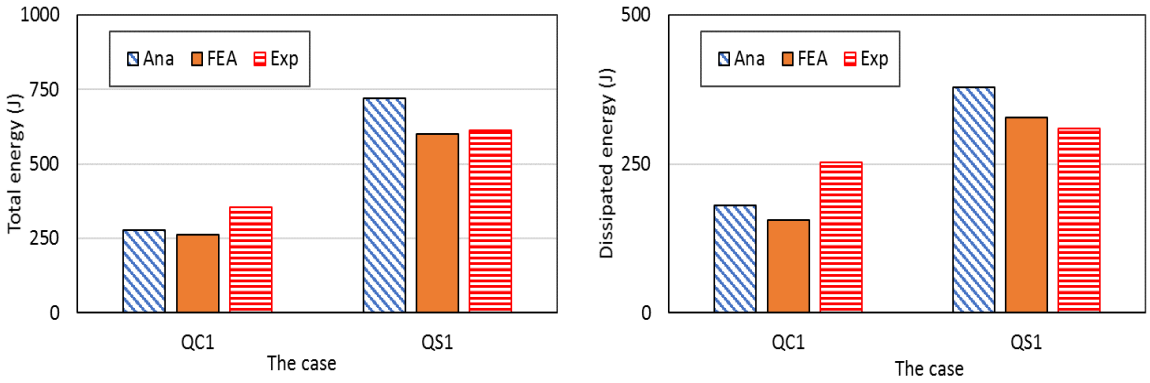

a) The total Energy b) The dissipated Energy

Figure 5-3: Comparison of the a) total and b) dissipated energy of each slab (QC1 & QS1) obtained from each procedure.

5.2.3 The crack patterns

As mentioned in Section 4.3.4, since no measured data was obtained experimentally to identify the crack patterns in the slab, the comparison between the predicted and the experimental crack pattern was made based on the visual observation to the final crack pattern in each slab after the test.

Based on the observation from the quasi-static test, there is obvious difference in the crack pattern between the control and the strengthened slabs QC1 and QS1, where the crack pattern is represented by one major opened crack in slab QC1 and by multi cracks in slab QS1 as shown in

Figure 5-4. In the analytical procedure, almost similar behaviour was detected between slab QC1 and QS1 as shown in Figure 5-5 where the opened cracks turn to be distributed in slab QS1 and concentrated in the mid-span in slab QC1. This change in the crack pattern might be attributed to the difference in the steel strain distribution along the span between QC1 and QS1 as shown in Figure 5-9(a) since the width of the crack in any position depends on the steel strain. The numerical procedure didn't show any change in the crack pattern between QC1 and QS1 as shown in Figure 5-6. The crack pattern is almost the same in both slabs which is represented by one or two opened crack(s) near the mid-span and hairy cracks away from the mid-span line.

Table 5-1 shows that a small increase in the ultimate deflection and energy was obtained when the effect of the crack pattern (discrete method) is included in the

calculation for both the slabs. In contrast, a noticeable change was detected in the strain and curvature distribution along the span as shown in Figure 5-7 and Figure 5-8 where spikes along the steel strain-distance profile were noticed at the potential locations of the cracks. Since concrete is assumed to be perfectly homogenous, the first crack is expected to be occur in the mid-span section where the maximum tensile strain occurs. In practice due to many other factors, such as the shrinkage effect and lack of the perfect homogenous properties of concrete, positions of the cracks show small shifts from the predicted positions and they take a wavy shape along the cross-section as shown in Figure 5-4.

Figure 5-4: The observed Crack patterns in the tension face under quasi-static load for slabs QC1 and QS1.

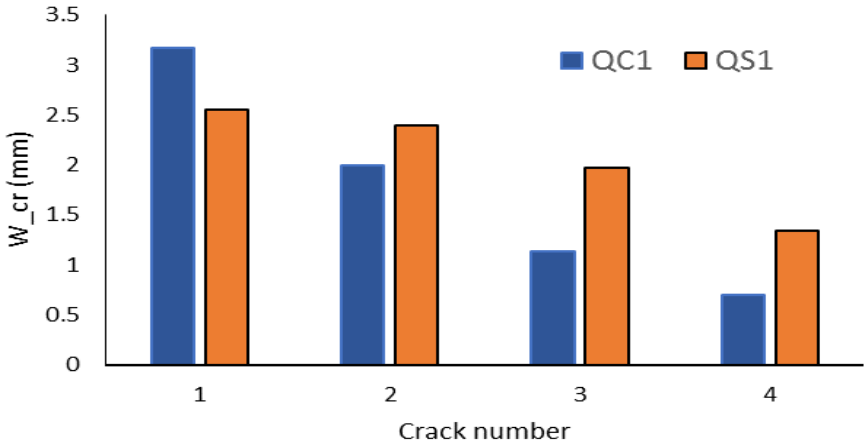

Figure 5-5: Comparison between the analytically predicted width of the four sequent cracks at each slab (QC1 &QS1) at the ultimate state of the analytical method.

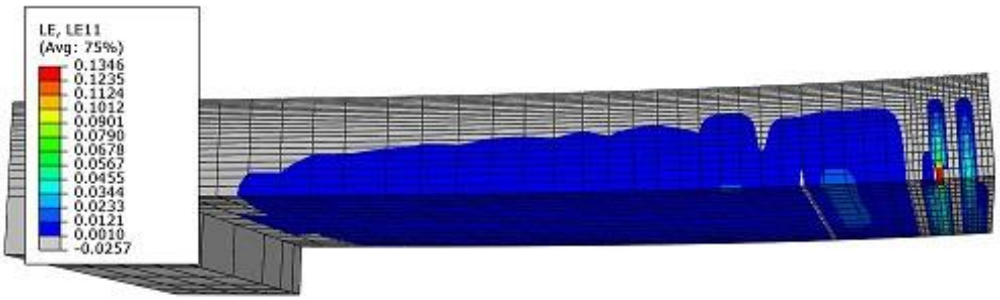

a) QC1

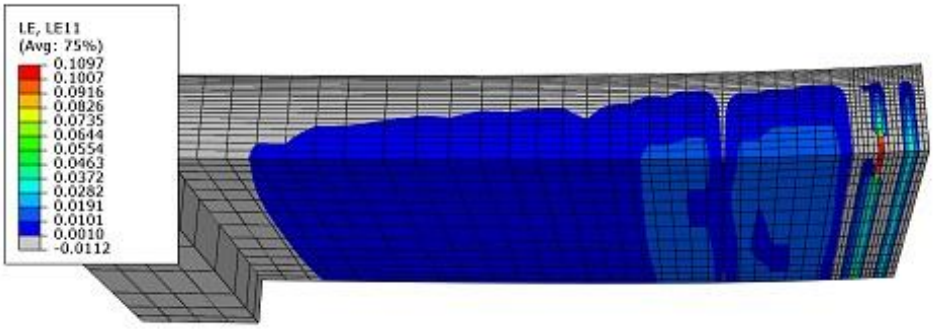

b) QS1

Figure 5-6: The numerical plastic strain distribution at the ultimate state at the bottom face of slab (a) QC1 and (b) QS1

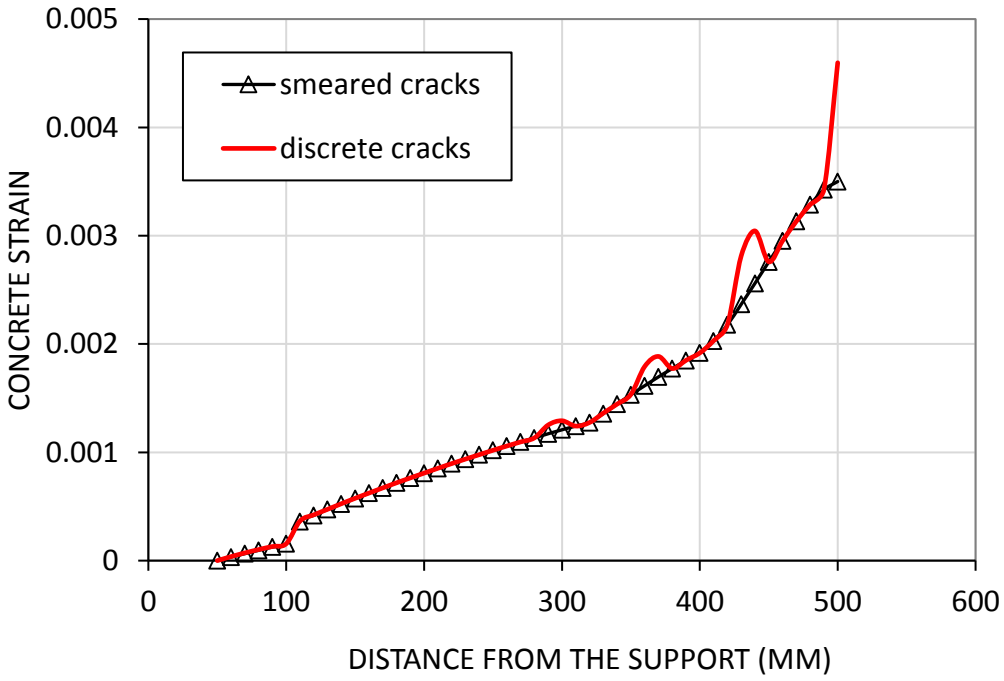

a)

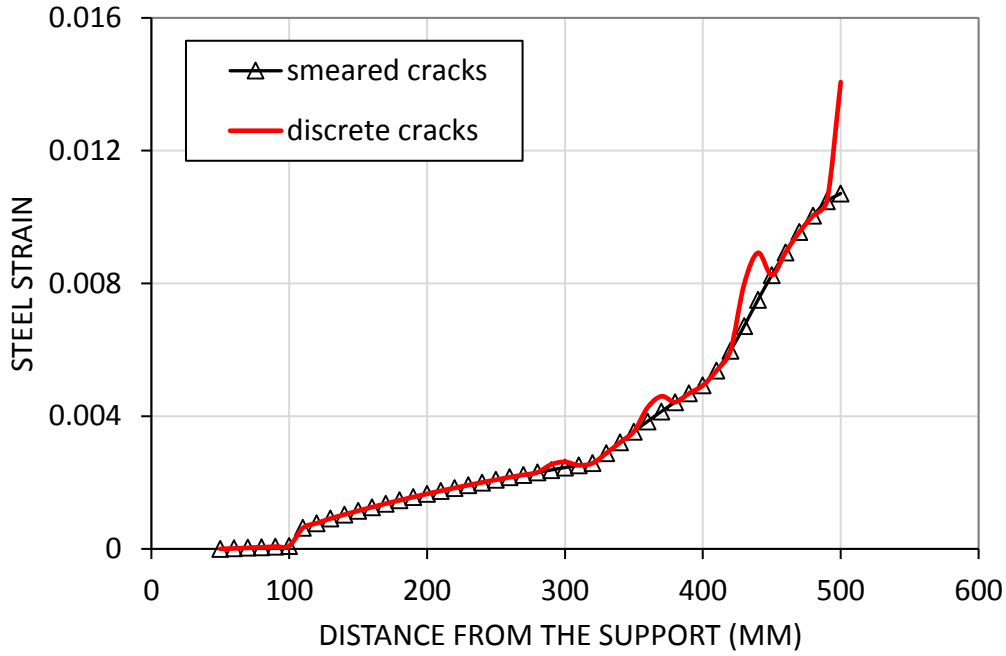

b)

Figure 5-7 The predicted strain distribution of a) concrete and b) steel along half of the span length of slab (QC1) under quasi-static load at the ultimate state.

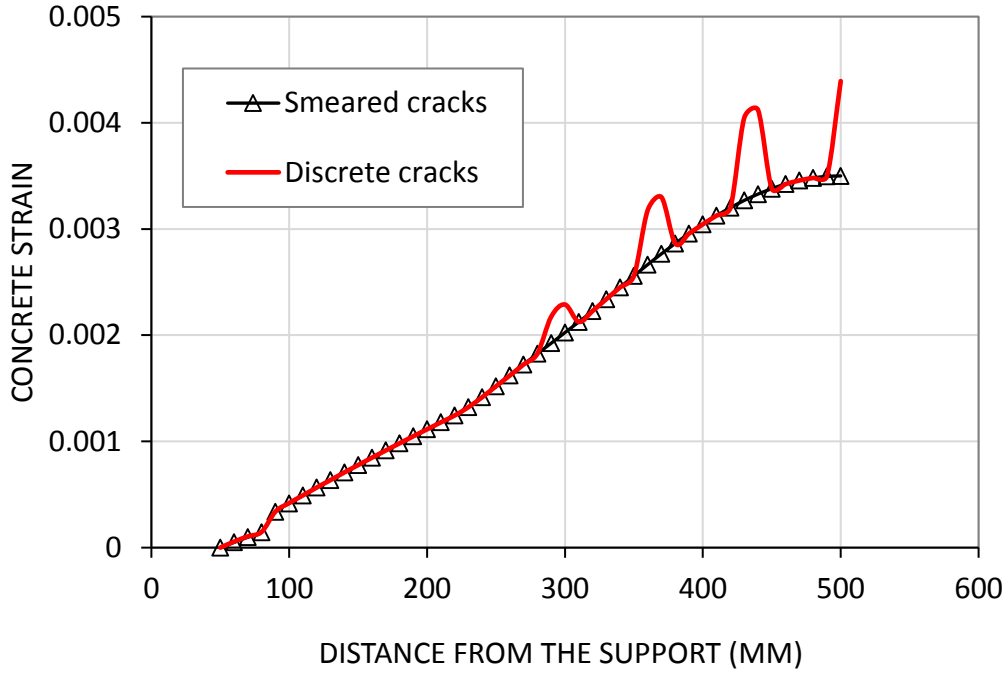

a) Concrete strain profile along the span length of the slab

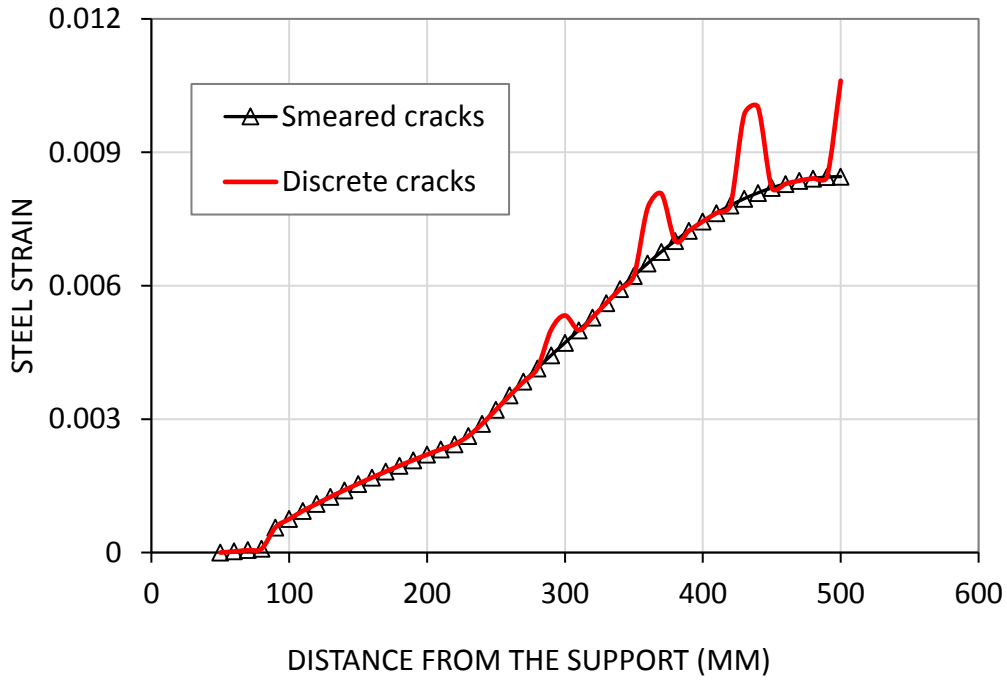

b) Steel strain profile along the span length of the slab

Figure 5-8: The predicted strain distribution of a) concrete and b) steel along half of the span length of slab (QS1) under quasi-static load at the ultimate state.

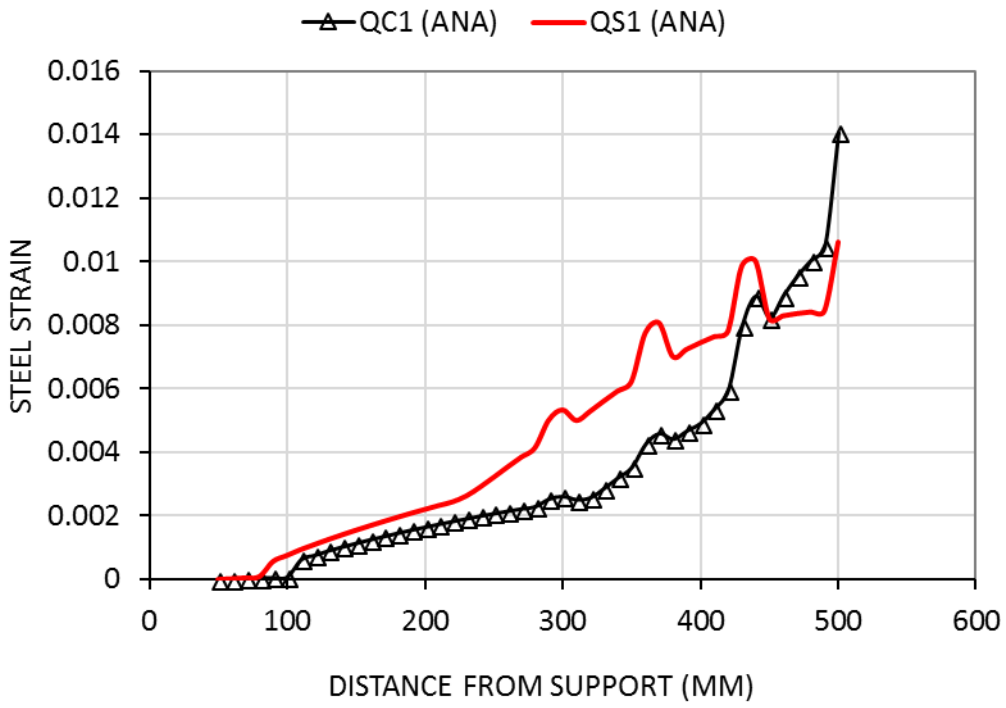

a) Analytical procedure

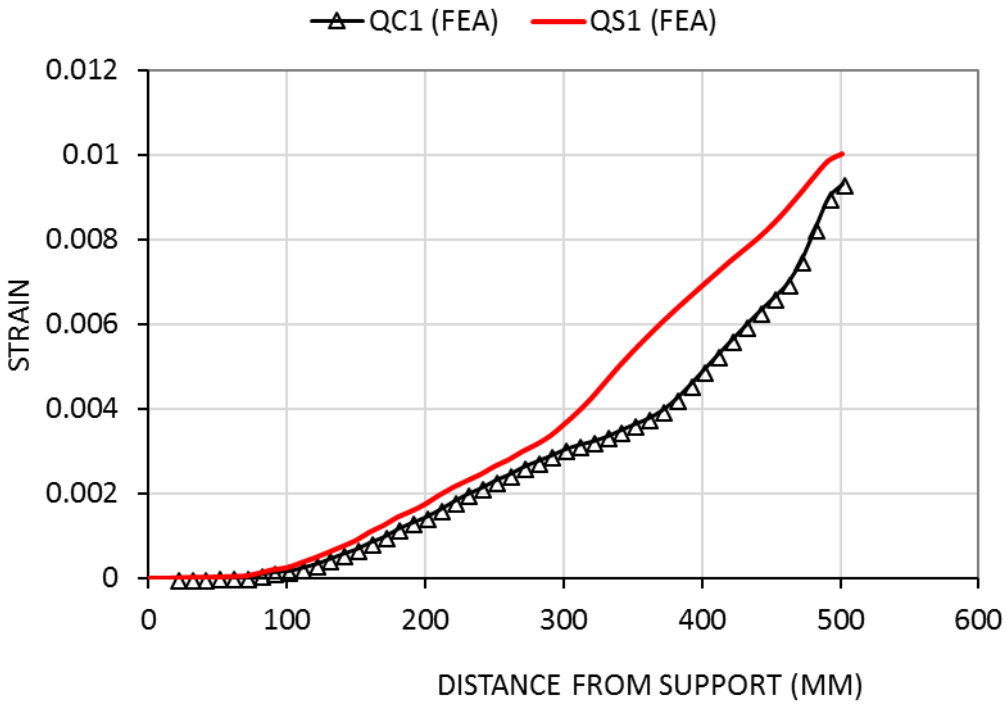

b) Numerical procedure

Figure 5-9: Comparison between the a) analytical and b) the numerical predicted steel strain distribution along half of the span of the control QC1 and the strengthened slab QS1 under static load.

5.3 Validating the nonlinear solution procedures in the high strain rate regime

To validate the developed analytical and numerical procedures in the high strain rate regime, the predicted results are compared with the measured results that are obtained from conducting impact tests on the two different slabs: control slab MC2 and strengthened slab MS2. Properties and details of each slab were presented in chapter 4. A comparison between the predicted and the measured data is presenting in the following section.

5.3.1 The impact maximum deflection

The maximum response of each slab under different impact load magnitudes is considered to validate the developed procedures with the recorded results. Figure 3-22 shows the recorded historical impact load and deflection corresponding to different heights of dropping mass. Table 5-2 presents the analytical maximum response and its corresponding time based on the SDOF elasto-plastic method which described in Section 4.2.8.2. The yielding strength and deflection of the slab (Ru & Ye) which are needed as input factors in this method are obtained from Figure 5-11 which is obtained by adopting the layered method (Section 4.2) for any determined time of the maximum response (t_{m2}). Table 5-3 presents both the analytical and the numerical results of the maximum response and its corresponding time in comparison with the experimental results for both the control MC2 and the strengthened slab MS2 under various impact forces. Figure 5-10 presents the comparison between the measured and the predicted maximum response of the slabs in a bar chart form. They indicate that the analytical predicted maximum response differs from the measured response within 15-30%. While the numerical predicted maximum response found to be very close to the measured values with a less than 10% error when the slab experiences medium or high plastic deformation range. It is also found that the analytically predicted deflections were higher than the measured deflections in all cases, and the difference between them increases with the increasing plastic deformation produced by increasing the applied impact load. This might be attributed to the basic assumption made in the analytical procedure where an elastic-perfect plastic load-deflection behaviour was assumed by neglecting the hardening behaviour which may have led to overestimating the predicted maximum deflection.

In terms of the time of the maximum response, both the analytical and the numerical procedures gave an estimated value of about 10-11 ms which is very close to the measured time which was about 10 ms for all the cases. In general, good agreement between the predicted and the actual results for both the analytical and the numerical procedures was observed. This indicates that the analytical procedure can be adopted to analyse one-way slab with and without NSM CFRP bars within an accepted percentage of error. The predicted results obtained from both the adopted procedures are found to be significantly sensitive to the duration of loading (t_d), this highlights the need to assuming the loading time exactly to get accurate results.

5.3.2 The Resistance-deflection behaviour

Since the impact impulse represents the properties of the contacted surfaces during the impact event and the total reaction at the support represents the response of the member to the total of the applied forces (the impact forces and the initial forces), the total reaction was used to represent the resistance-deflection behaviour of the member. Figure 5-12 shows the resistance-deflection behaviour of slab MC2-8 obtained from the three adopted procedures. A good agreement was achieved between the analytical and the numerical behaviour despite the use of differernt incremental method to apply the load, while different behaviour was obtained from the impact test as presented in Figure 5-12. It should be noted that it is difficult to validate the predicted reaction-time profile with the measured one as atypical reaction-deflection behaviour was obtained experimentally when repeating the impact test with same impact energy magnitude on each slab (MC and MS) as shown in Figure 3-20.

Table 5-2: the experimental and the predicted maximum deflection Ym and the corresponding time t_m.

	Measured data		calculated		From Figure 4-17b	From Figure 5-11 based on t_{m2}			From Figure 4-17a	
slab	Peak force F_m (kN)	Loading period t_d (ms)	Periodic time T (ms)	t_d /T	Time of the maximum response t_{m2} (ms)	Elastic resistance Ru (kN)	Y_e (mm)	Ru/Fm	Y_m/Y_e	Maximum deflection Y_m mm
MC2-1	16.2	9	24	0.38	10-12	25.2	10.5	1.56	0.9	9.45
MC2-2	19.0	9	24	0.38	10-12	25.2	10.5	1.33	1.1	11.55
MC2-3	23.6	9	24	0.38	10-12	25.2	10.5	1.1	1.2	12.6
MC2-4	26.6	9	24	0.38	10-12	25.2	10.5	0.95	1.3	13.65
MC2-5	35.3	8	24	0.33	10-12	25.3	10.5	0.72	1.6	16.8
MC2-6	39.9	7.7	24	0.32	10-12	25.3	10.5	0.63	1.8	18.9
MC2-7	50.7	7.0	24	0.29	10-12	25.3	10.5	0.5	2.0	21
MS2-1	41.7	8	24	0.33	10-12	25.5	10.5	0.61	2	21
MS2-2	52	7	24	0.29	10-12	25.5	10.5	0.49	2.2	22.05
MS2-3	65.7	6.0	24	0.25	10-12	25.5	10.5	0.39	2.4	26.25

Table 5-3: Comparison between the measured and the predicted maximum response of the control slab (MC2) under different impact load values.

Case	F_m (kN) Exp	t_d Exp	Δ_{max} (mm) Exp.	Ana.	Error %	FEA	Error %	t_m (ms) Exp.	Ana.	FEA
MC2-1	16.2	9.0	8.2	9.5	15	5.6	-32	10	11	10
MC2-2	19.0	9.0	9.1	11.6	27	6.9	-24	10	11	10.2
MC2-3	23.6	9.0	10.6	12.6	19	9.2	-13	10	11	10.5
MC2-4	26.6	9.0	11.2	13.7	22	10.7	-4	10	11	10.5
MC2-5	35.3	8.0	14.5	16.8	16	14.5	0	10	11	10.6
MC2-6	39.9	7.7	15.1	18.9	25	16.6	10	10	11	10.6
MC2-7	50.7	7.0	17.5	21.0	20	17.1	-2	10	11	10.6
MS2-1	41.7	8.0	16.1	21.0	30	17.0	6	10	11	10.5
MS2-2	54.0	7.0	19.2	22.1	15	17.5	9	10	11	10.5
MS2-3	65.7	6.0	22.9	26.3	15	21.5	-6	10	11	10.5

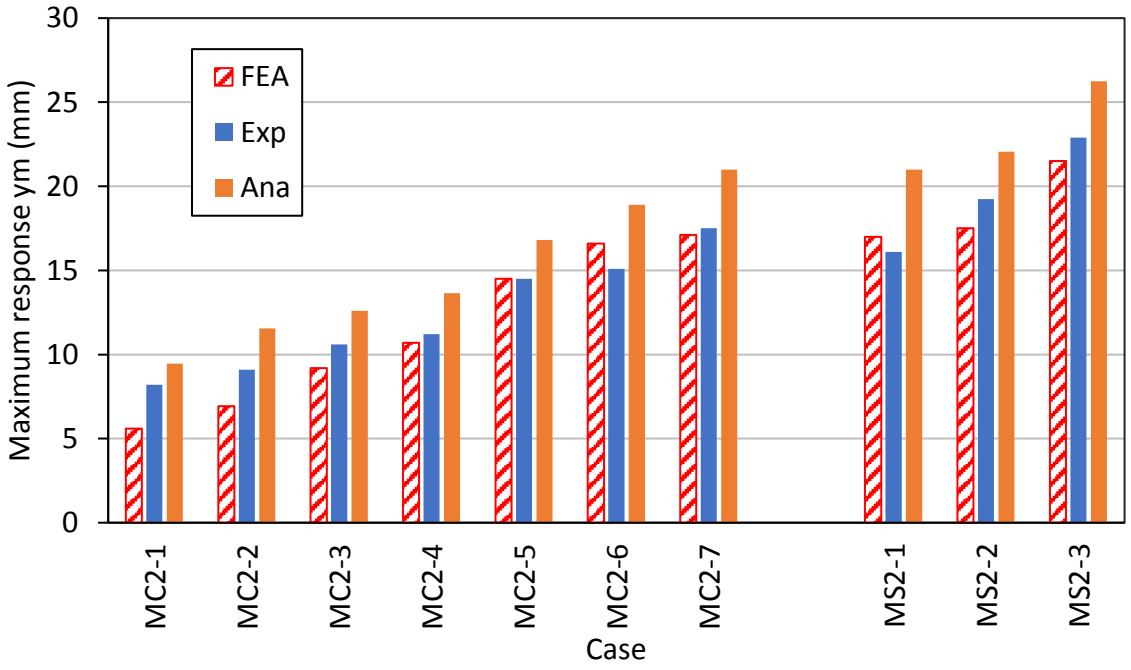

Figure 5-10: Validation of the analytical and the numerical maximum response with the experimental results under different impact load magnitudes for slab MC2 and MS2.

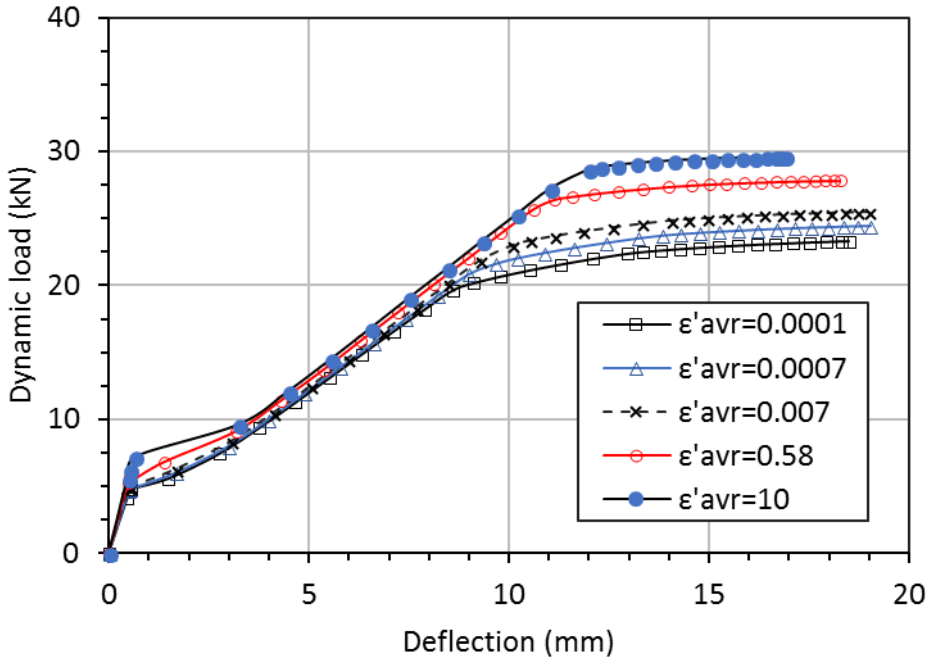

Figure 5-11: The predicted analytical load-deflection response of the control slab (MC2) under different strain rate values.

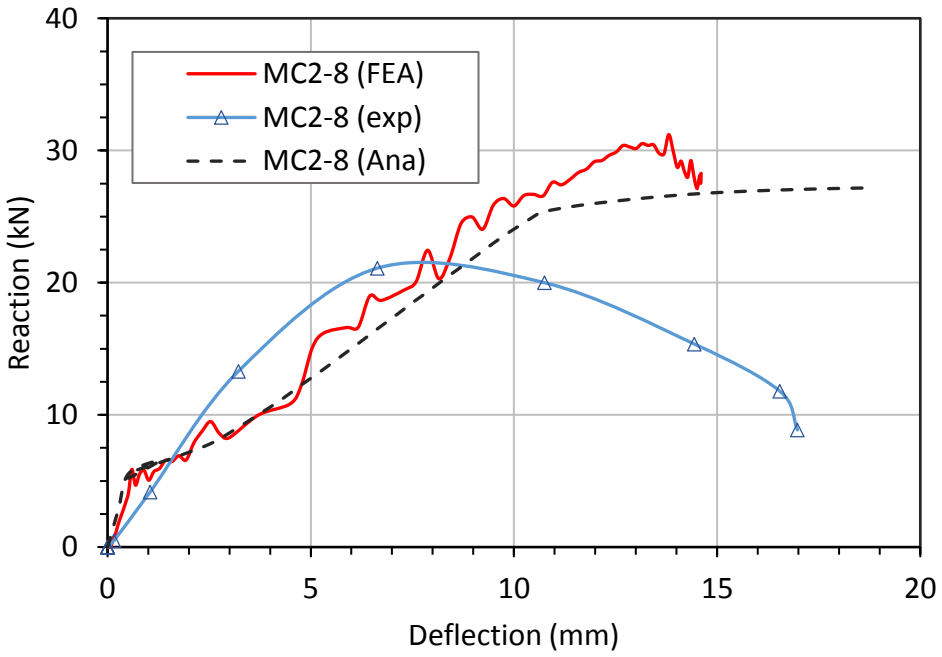

Figure 5-12: Comparison between the predicted reaction-deflection behaviour with the recorded behaviour of slab MC2

5.3.3 The crack patterns

The procedure which was used in the static analysis was also used in the dynamic analytical procedure to predict width of the cracks in four potential positions as described in section 4.2.7. Figure 5-13 shows the predicted width of the cracks in both the control and the strengthened slabs (MC2 & MS2). As shown, width of the major cracks (wcr1 and wcr2) at the ultimate state increases when the compression face of the slab is strengthened with NSM CFRP bars, where wcr1 increases from 3.75 to 4.9 mm and wcr2 increases from 1.9 to 3 mm. This is similar to what has been visually observed in the impact test as shown in Figure 5-14 where width of the crack increases with the compression face was strengthened. This indicates that the analytical procedure is capable to detect the change in the width of the cracks when applying the NSM CFRP approach in the high loading rate regime too in addition to the low loading rate regime which was approved in section 5.2.3. Similar behaviour was also detected in the numerical procedure where the predicted strain of the two major cracks at the ultimate state of slab MS2 was higher than the corresponding strain of slab MC2 as shown in Figure 5-15 indicating increasing width of the cracks.

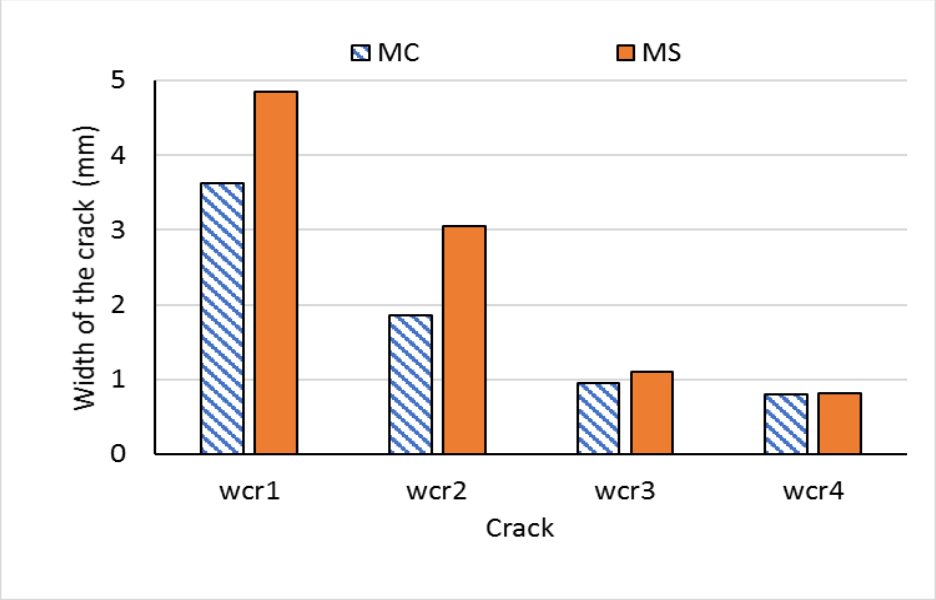

Figure 5-13: The analytical width of the four consequent cracks at the ultimate state of slabs MC and MS under rapid loading.

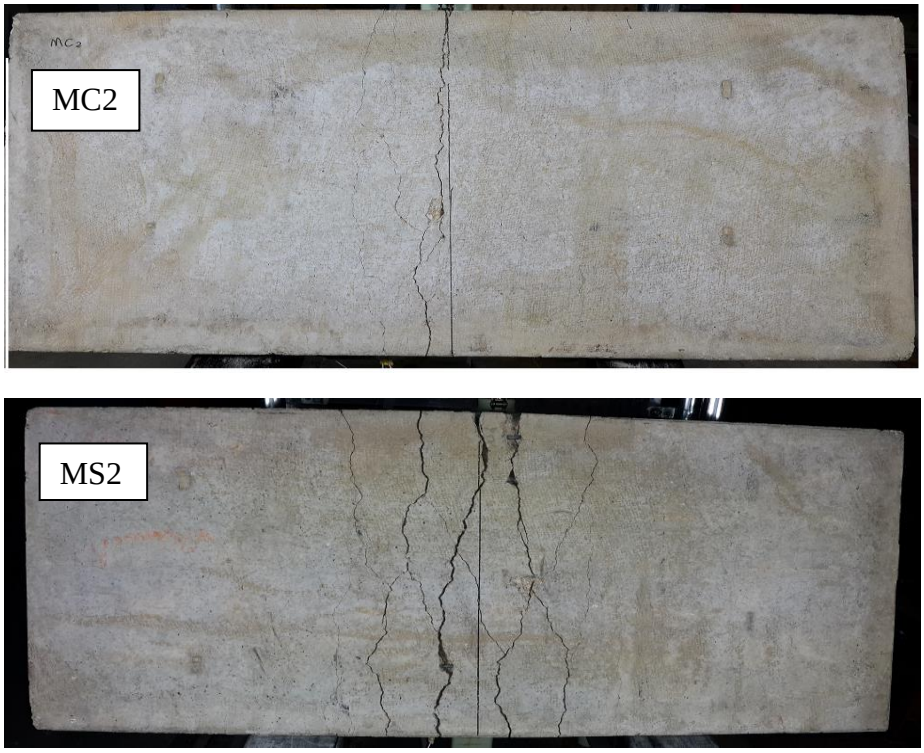

Figure 5-14: The actual crack pattern which observed at the ultimate state of the impact test of each slab (MC2 and MS2).

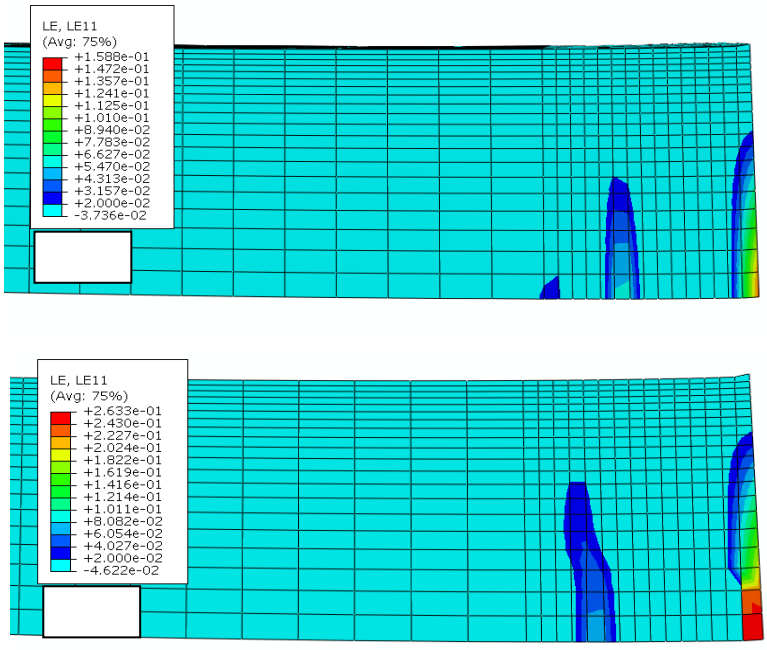

Figure 5-15: The numerical crack pattern of slab MC2 and MS2 at the ultimate state of the impact analysis.

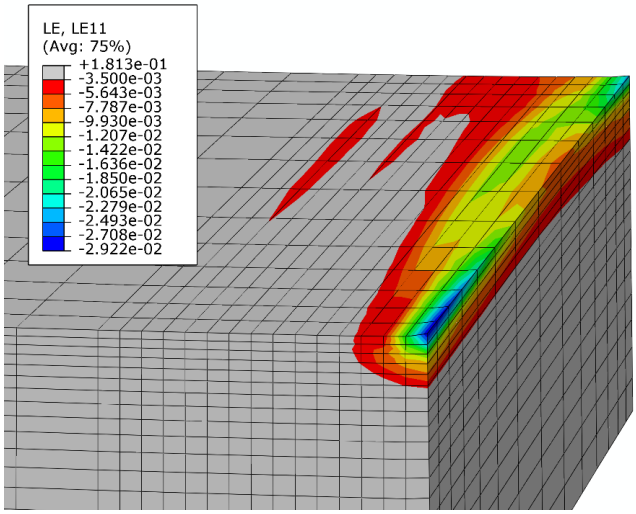

Figure 5-16: The compression strain at the top fibre of concrete at the mid-span section at the ultimate state of case MS2.

5.4 Strength and limitations of the two used procedures

Based on the results of the validation analysis which were presented in the previous sections and conducted on both the analytical and the numerical models, it was found that both the adopted models are in good agreement with the experimental results in terms of the load-deflection behaviour and the total and the dissipated energy in the low strain rate regime, where both models were capable to detect the cracking, yielding and the ultimate loads closely. Also, both models were capable to detect the change in the entire load-deflection behaviour when applying NSM CFRP approach. In terms of the total and the dissipated static energy, there is quite match between the predicted results obtained from both models and both overestimated the experimental results with different convergence factor as presented in Table 5-1. There is also match in the enhancing factor of the total and the dissipated energy obtained from both models when applying NSM CFRP approach.

It was found that including the proposed opened crack model (discrete crack model) in the analytical model does not change the entire load-deflection behaviour significantly, but it has impact on the strain distribution profile in the steel bars and the concrete which is used as an indication to the locations and widths of the propagated opened cracks along the span length of the slab. No such similar behaviour was detected in the numerical model making the analytical model outstanding in this aspect. This feature was utilized in detecting the change in the crack patterns when the slab is

strengthened by NSM CFRP approach. Based on the assumptions adopted in the analytical model, effect of shear forces, deformations and multi-direction stresses are neglected in the analytical model making the numerical model outweighs that analytical model in this aspect.

In the high strain rate regime, the predicted results were validated with the experimental results based on the maximum displacement response under each impact pulse. It was found that both models are in good agreement with the experimental results. However, the numerical model gave better estimating to the maximum response than the analytical model where the average percentage of error was 15-30% for the analytical analysis and 10% for the numerical analysis. It was found that with the analytical solution, the less plastic deformation imposed in the system the more accurate estimating of the maximum displacement obtained. This is attributed to the basic assumption used in the analytical model by assuming perfect plastic behaviour by neglecting the hardening behaviour. However, this limitation should not affect on the estimating the total and the dissipated energy at the ultimate state as no need to use the elasto-plastic SDOF method in this case. It is worth mentioning that the analytical model depends on the displacement control method during the analysis which is used to estimate the load for all distributing form of loading based on the equation of moment, while the load control method was used in the numerical method to simulate the loads since it is difficult to use the displacement method when non-unique concentrated load is applied. Thus, the analytical model is capable to simulate the softening behaviour in the load-deflection curve up to the ultimate state, while the numerical model only can continue the analysis when there is hardening behaviour in the load-deflection curve. This limitation in the numerical model should be considered in the analysis.

To extend the study, parametric study was conducted to investigate effect of the potential involved factors in the NSM CFRP system as presented in the following sections.

5.5 Parametric study

As both of the adopted nonlinear procedures were validated with the experimental results and found to be adequate in simulating the response of the NSM CFRP system to the applied flexural load with various loading rate value, the models can be used for a parametric study to study effect of the potential affecting factors on the entire behaviour

of the RC NSM CFRP system as one of the main objective in this study is to develop an analytical model than can be used to investigate and predict the entire behaviour of the RC NSM system theoretically especially when studying that experimentally could be difficult or expensive . In this study, many factors which are expected to have impact on the entire response of the NSM CFRP system are studied, such as the CFRP strengthening ratio, effect of deflection rate on the entire behaviour, effect of the stiffness of the CFRP. Studying effect of these factors aims to investigate effect of each factor for the optimum performance of the NSM strengthening approach.

For more understanding to the difference in the analysis between the two adopted models, the first factor in the parametric study was conducting by using both the analytical and the numerical models. While the remaining factors were studied by conducting only the analytical model due to its ability to detect the change in the entire behaviour of the NSM CFRP system, which is main aim of this study, and due to the low time of running compared to the numerical analysis especially in the static analysis where the analytical analysis completed within 5 minutes compared to 30 minutes and more for the numerical analysis. In addition to that, the deflection rate factor (strain rate effect) can only be controlled in the analytical model where the displacement control method is used where the strain rate values can be changed by imposing different constant deflection rate value which can be estimated based on the time of the maximum response (t_m). This is out of reach when the load-control method is used in the analysis which is adopted in the numerical model. Details of the parameters and the results are presented in the following sections.

5.5.1 Effect of strengthening ratio of CFRP

Effect of the external strengthening reinforcement ratio of the NSM CFRP rods in both the tension and the compression faces of the slab was studied in this study, where 16 cases of one-way RC slab were analysed analytically and numerically by considering different strengthening ratio in each face. The reason for the comparison between these procedures is to investigate the difference between these two models in detecting the difference in the entire behaviour of the slab under different strengthening ratio. This was achieved by changing number of CFRP bars in each face (0, 3, 5 and 7); the steel reinforcing ratio and the geometrical and mechanical properties of the concrete block is kept the same. For ease of understanding of each case (Table 5-4), the number of CFRP

bars on each face is included in the name scheme of each case which is S(t, c) where S refers to slab, t refers to number of CFRP bars in the tension face and c refers to number of CFRP in the compression face.

The results of these cases were compared based on the entire load-deflection behaviour and the total and the dissipated energy up to the ultimate state of each case. The ultimate state of each case is reached when the top fibre of concrete in the mid-span reaches to the ultimate concrete strain which is assumed to be 0.0035 in this study. Table 5-4 and Table 5-5 present details of the strengthening ratio and the obtained results of each case using the analytical and the numerical solution respectively. The applied load was assumed to be an impact impulse with a peak magnitude of 80 kN and duration of 10 ms. Thus, the dynamic analysis procedure of each nonlinear solution was used here. The strain rate effect was included in both procedures by assuming a constant deflection rate in the analytical procedure and various deflection rates in the numerical procedure which were calculated automatically during the analysis.

From the results of the analytical procedure, presented in Table 5-4, it was found that when only the compression face of the slab is strengthened, the maximum deflection, the total and the dissipated energy increase proportionally with an increase in the strengthening ratio of the CFRP bars. As shown in Table 5-4 and Figure 5-17, when the compression face is strengthened by 3, 5 and 7 CFRP bars, i.e. for the cases S(0,3), S(0,5) and S(0,7), the total energy increased by a factor of 1.22, 1.39 and 1.51 as compared to S(0,0) and the dissipated energy increased by a factor of 1.35, 1.63 and 1.84. The optimum enhancing factor in the total energy among the cases was obtained in S(5,7) by recording 2.05. The optimum enhancing factor in the dissipated energy was obtained in S(3,7) by recording 2.18 where rupture of CFRP in tension face contributed to increase the dissipated energy dramatically in addition to the contribution of the plastic deformation energy of the steel bars. This is clearly indicated in case S(3,0) and S(3,3) where the enhancing factor of the dissipated energy jumped from 0.72 to 1.76 due to the rupture in the CFRP compared to smaller increase, from 1.24 to 1.38, in the enhancing factor of the total energy. This indicates that the dissipated energy of the slab either decrease or increase with the increasing in the strengthening ratio of CFRP in the tension face based on the ratio of the CFRP to the ductility available in the slab as the rupture in the CFRP bars in the tension face occurs only if the concrete does not experienced crushing failure (within the available ductility range of the slab).

The analytical results also show that there is no change in the yielding strength and a small increase in the ultimate strength of the slab is detected with the increase in the CFRP in the compression face. Both the yielding and the ultimate strength increase dramatically with the increasing of the ratio of CFRP in the tension face as shown in Table 5-4 and Figure 5-18. The ultimate deflection of the slab is found to be sensitive to ratios of the CFRP in both faces where increasing the CFRP in the compression face leads to increase the ultimate deflection while increasing the CFRP in the tension face leads to decrease the ultimate deflection.

Table 5-5 presents the results of the same 16 cases which were analysed using the numerical procedure. Figure 5-22 to Figure 5-26 show the comparison between the analytical and the numerical results where the results of the deflection, load and the energy were obtained at the ultimate state. As shown in Figure 5-22 and Figure 5-23 there are only small differences between the analytical and the numerical resistance-deflection curves despite the difference in the assumption of applying the dynamic load whereas a constant deflection rate is assumed with the analytical procedure.

Figure 5-24 shows that in both procedures the ultimate deflection increases with the increase in the compression strengthening ratio of CFRP with good agreement in the predicted values of both models. Figure 5-25 shows that there is no effect on the ultimate resistance of the slab if just the compression face is strengthened. While if the tension face is strengthened with CFRP bars, the ultimate resistance increases with the increase in the compression strengthening. This is attributed to the hardening behaviour in the load-deflection response of the slab which is achieved by strengthening the tension face while almost steady plastic load is achieved when only steel reinforcement bars is used in the tension face. As a result to the hardening behaviour, both the ductility and the plastic load increase with the increasing in the ratio of CFRP in the compression face.

Figure 5-26 shows both the total and the dissipated energy for each case obtained by the analytical and the numerical procedures. It shows that the total and the dissipated energy increase with the increasing of the compression strengthening ratio for any constant tension strengthening ratio. It also shows that the total and the dissipated energy increase dramatically when the CFRP in the tension face ruptures which is desired to dissipate more energy before the strengthened element fails by crushing of concrete to reduce the fragmentation in the concrete as much as possible for the integrity of both the

structure and the occupants. This rupture can be achieved by controlling both the tension and the compression strengthening ratio as shown in case S(3,5) and S(3,7) where increasing the compression strengthening ratio contributed to increase in the ductility of the slab and as a results extending the reachable strain in the tension strengthening CFRP bars more than the rupture strain as shown in Figure 5-19 where increasing the compression strengthening in slabs S(3,3), S(3,5), S(3,7) led to take the strengening CFRP in the tension face to the rupture compared to the slab S(3,0) which contributes to more energy dissipation in the element in addition to the steel strain energy dissipation achieved by enhancing the ductility. Figure 5-26 also shows that the analytical results of the total and the dissipated energy were higher than the numerical results despite the similarity in the trend. This was a results to the difference in the resistance-deflection behaviour obtained from each procedure as shown in Figure 5-22 and Figure 5-23 which was attributed to the difference in applying the dynamic load as described earlier.

In general, both the numerical and the analytical procedures found to be able to detect the change in the entire response of the one-way NSM CFRP system with the changing of the strengthening ratio of both the compression and the tension strengthening CFRP bars. This justifies the efficiency of adopting only the analytical model in conducting the remaining parametric studies in addition to the reasons that mentioned in Section 5.4. The predicted results obtained by conducting this parameter study indicated that both the ratio of the CFRP on each face plays a significant role in the amount of the dissipated energy achieved in the strengthened element where the CFRP in the tension face enhances the strength and the plastic load of the element while the CFRP in the compression face enhances the level of the ductility in the element and the dissipated energy in the element enhances with the enhancing of both the plastic load and the level of the ductility in the element.

Table 5-4: The analytical results of different cases study with different strengthening ratio of NSM CFRP bars in both faces.

Case	No. of CFRP bars		Yeilding load P_y (kN)	Yeilding deflection Δ_y mm	Ultimate load P_u (kN)	Ultimate deflection Δ_u mm	Total energy E_t. (J)	Enhancing factor*	Dissipated energy E_d. (J)	Enhancing factor*
	Comp. face	Ten. face								
S(0,0)	0	0	25.3	10.7	27.2	18.7	362	0.00	207	0.00
S(0,3)	3	0	25.5	10.8	27.7	21.4	442	1.22	279	1.35
S(0,5)	5	0	25.6	10.8	28.1	23.5	502	1.39	337	1.63
S(0,7)	7	0	25.6	10.6	28.4	25.0	547	1.51	380	1.84
S(3,0)	0	3	32.1	10.9	40.8	18.5	450	1.24	240	1.16
S(3,3)	3	3	32.1	10.9	28.4	19.3	499	1.38	364	1.76
S(3,5)	5	3	32.1	10.9	28.7	20.6	546	1.51	409	1.98
S(3,7)	7	3	32.1	10.9	29.0	22.0	590	1.63	452	**2.18**
S(5,0)	0	5	35.1	11.2	46.1	18.0	561	1.55	220	1.06
S(5,3)	3	5	35.1	11.2	47.5	21.8	659	1.82	299	1.44
S(5,5)	5	5	35.0	11.0	48.7	22.4	694	1.92	322	1.56
S(5,7)	7	5	35.5	11.1	50.0	23.3	742	**2.05**	351	1.70
S(7,0)	0	7	38.6	11.5	49.4	17.0	582	1.61	200	0.96
S(7,3)	3	7	38.9	11.4	51.5	20.0	633	1.75	245	1.18
S(7,5)	5	7	38.8	11.3	53.2	20.9	684	1.89	274	1.32
S(7,7)	7	7	39.4	11.4	54.8	21.6	729	2.01	295	1.43

*: Case S(0,0) was used as a reference to calculate the enhancing factors in all cases.

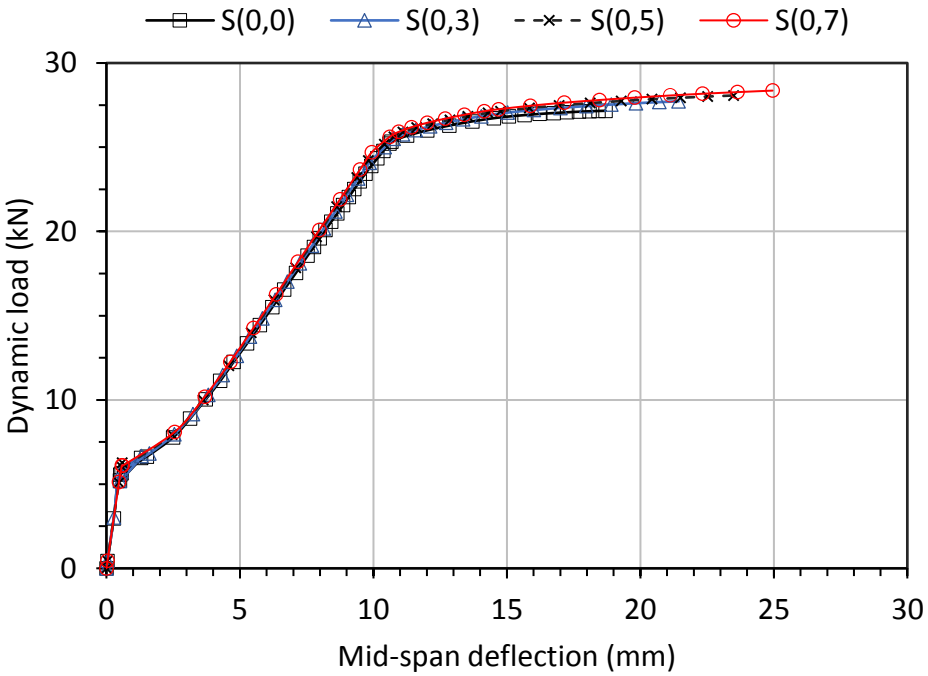

Figure 5-17: The analytical load-deflection response of the slab under different strengthening ratio in the compression face only with no CFRP bars in the tension face.

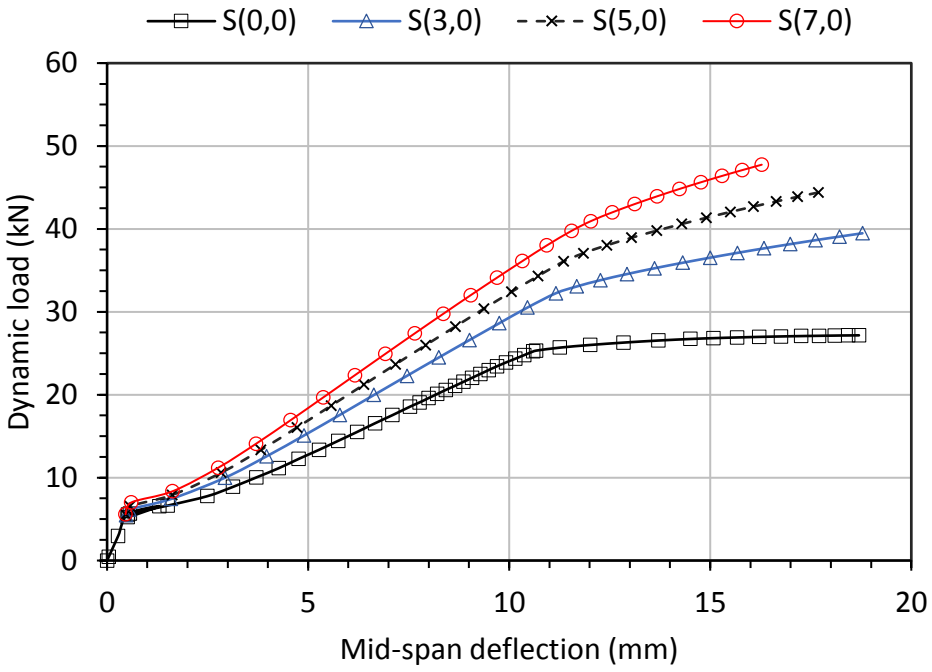

Figure 5-18: The analytical load-deflection response of the slab under different strengthening ratio of CFRP in the tension face only.

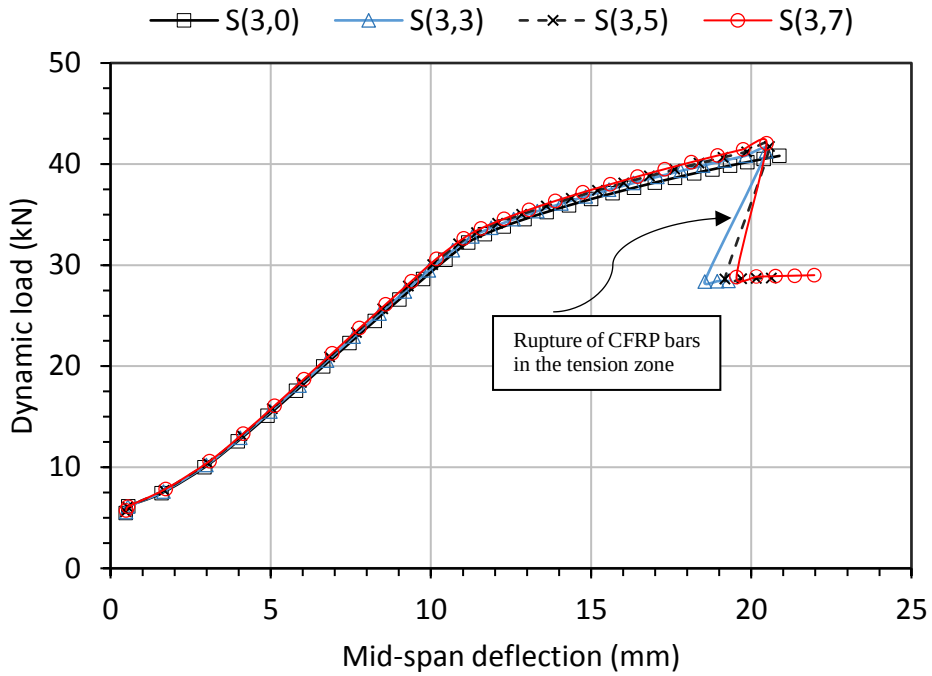

Figure 5-19: The analytical load-deflection response of the slab under different compression strengthening ratio with 3 CFRP bars in the tension face

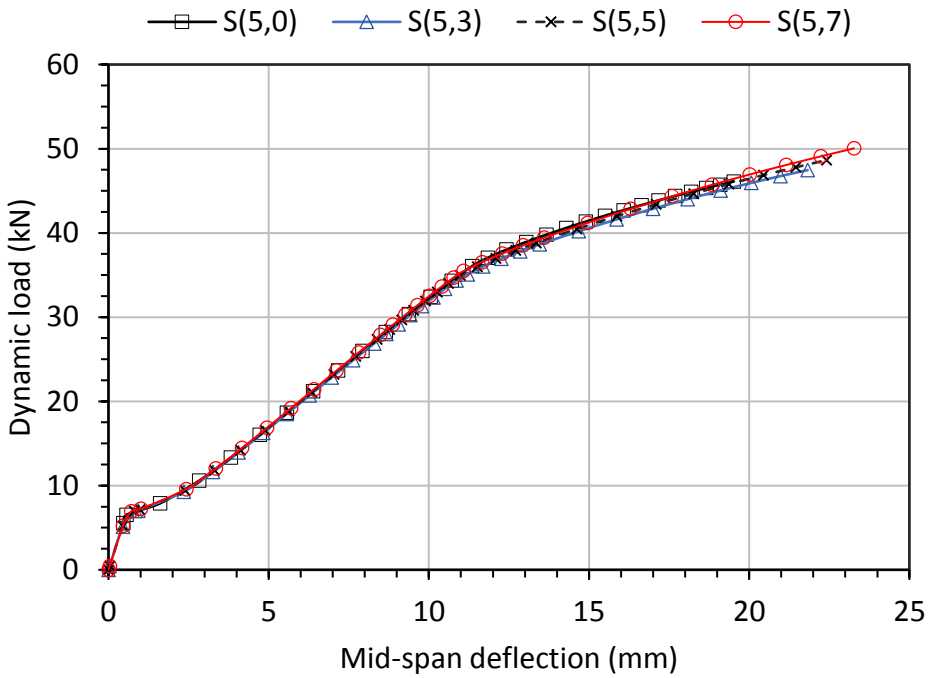

Figure 5-20: The analytical load-deflection response of the slab under different compression strengthening ratio with 5 CFRP bars in the tension face.

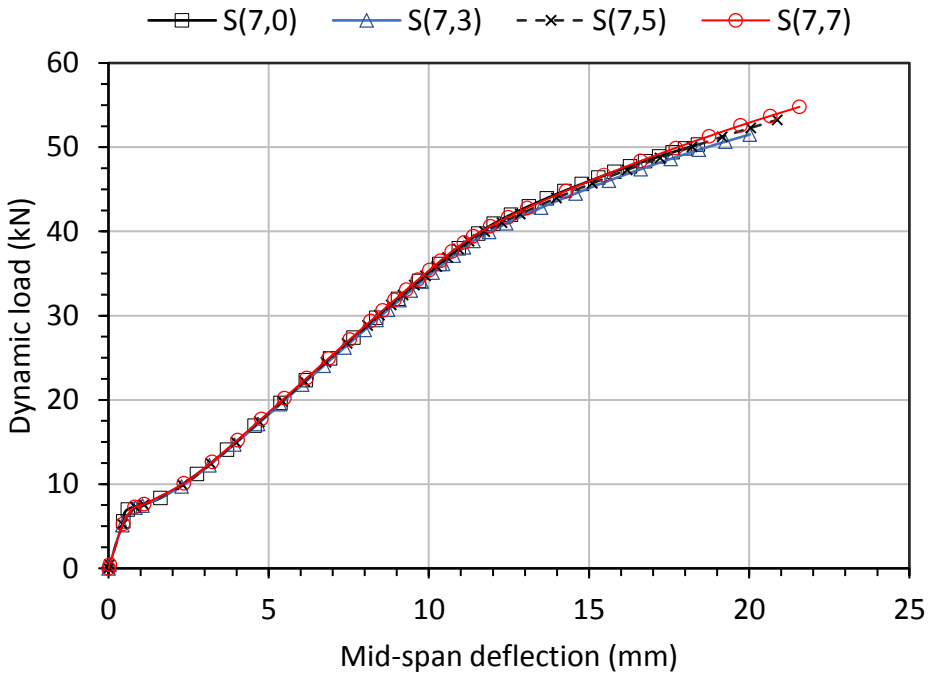

Figure 5-21: The analytical load-deflection response of the slab under different compression strengthening ratio with 7 CFRP bars in the tension face.

Table 5-5: The numerical results of different cases study with different strengthening ratio of NSM CFRP bars in both faces.

Case	No. of CFRP bars		Yeilding load Py (kN)	Yeilding deflection Δ_y mm	Ultimate load P_u (kN)	Ultimate deflection Δ_u mm	Total energy E_t. (J)	Enhancing factor*	Dissipated energy E_d. (J)	Enhancing factor*
	Comp. face	Ten. face								
S(0,0)	0	0	26.2	13.1	28.4	22.6	360.6	1.00	209.1	1.00
S(0,3)	0	3	26.4	12.8	28.7	23.6	391.0	1.08	230.5	1.10
S(0,5)	0	5	26.2	11.8	28.8	24.1	399.8	1.11	237.4	1.14
S(0,7)	0	7	26.9	11.7	28.2	25.5	433.2	1.20	274.4	1.31
S(3,0)	3	0	31.4	12.9	37.5	17.0	307.0	0.85	116.7	0.56
S(3,3)	3	3	32.8	13.4	36.9	18.1	341.9	0.95	136.4	0.65
S(3,5)	3	5	25.7	9.8	29.2	23.7	487.1	**1.35**	301.6	**1.44**
S(3,7)	3	7	34.0	14.5	26.0	26.1	542.6	**1.50**	362.0	**1.73**
S(5,0)	5	0	37.3	14.1	40.0	15.7	295.9	0.82	98.3	0.47
S(5,3)	5	3	27.7	10.0	43.0	18.3	350.0	0.97	124.0	0.59
S(5,5)	5	5	25.8	9.5	41.9	18.2	370.9	1.03	139.8	0.67
S(5,7)	5	7	34.2	12.6	43.5	19.2	418.9	1.16	155.4	0.74
S(7,0)	7	0	29.14	10.00	42.8	15.7	320.2	0.89	105.7	0.51
S(7,3)	7	3	32.10	12.56	46.1	17.1	375.2	1.04	126.8	0.61
S(7,5)	7	5	26.18	13.13	46.0	18.1	419.1	1.16	144.7	0.69
S(7,7)	7	7	30.66	9.93	48.0	19.3	464.7	1.29	164.4	0.79

*: Case S(0,0) was used as a reference to calculate the enhancing factors in all cases.

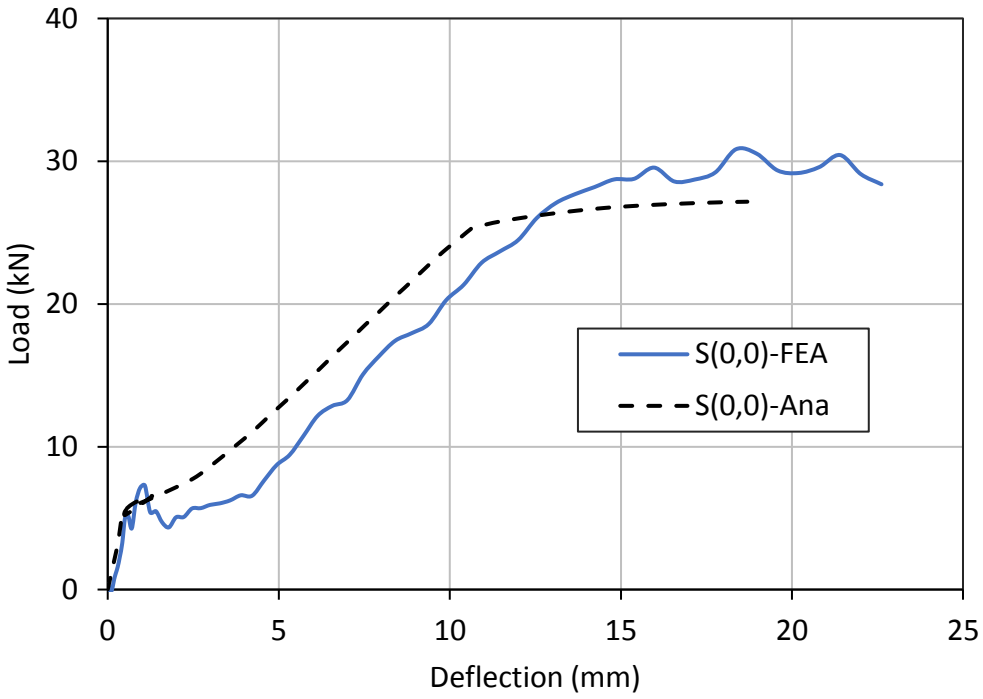

Figure 5-22: Comparison between the analytical and the numerical Reaction-deflection behaviour of case S(0,0) which is used to calculate the energy.

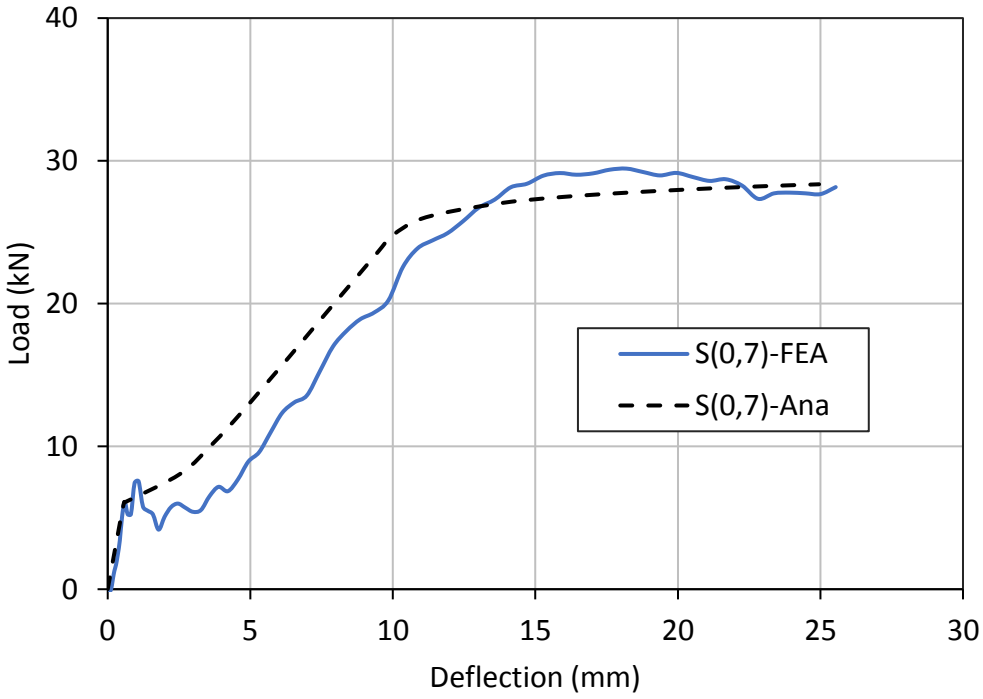

Figure 5-23: Comparison between the analytical and the numerical Reaction-deflection behaviour of case S(0,7) which is used to calculate the energy.

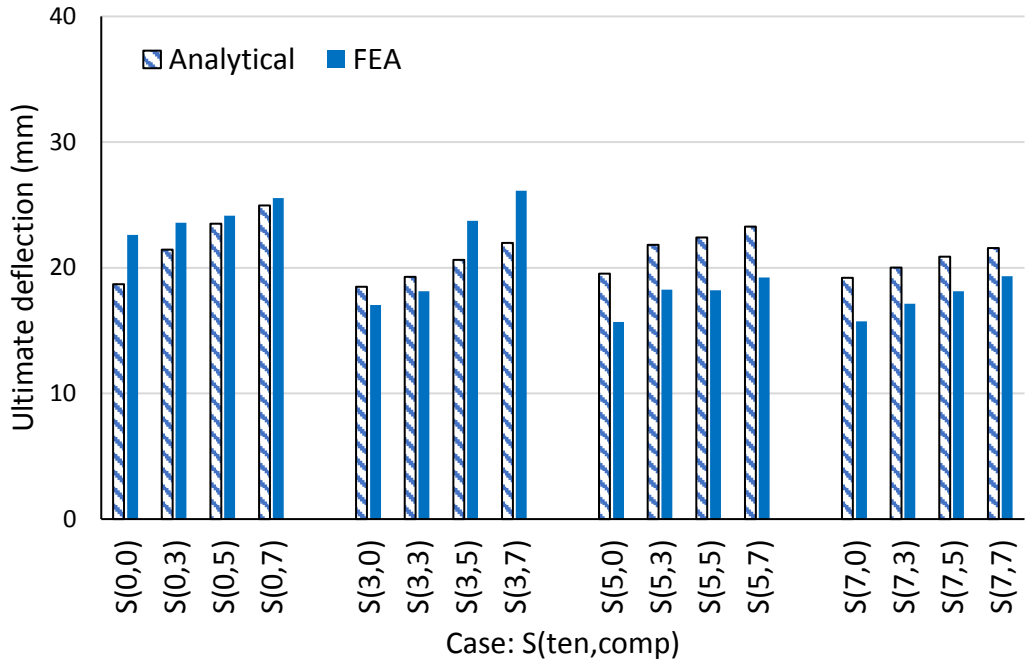

Figure 5-24: The predicted ultimate deflection value at each case study obtained from the analytical and the numerical procedures.

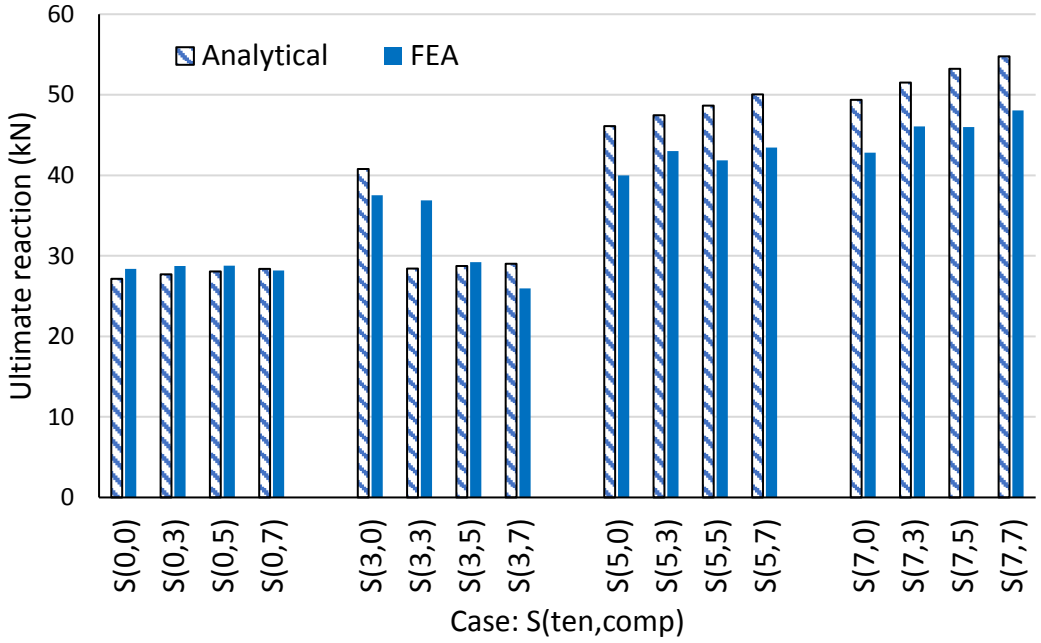

Figure 5-25: The predicted ultimate Load at each case study obtained from the analytical and the numerical procedures.

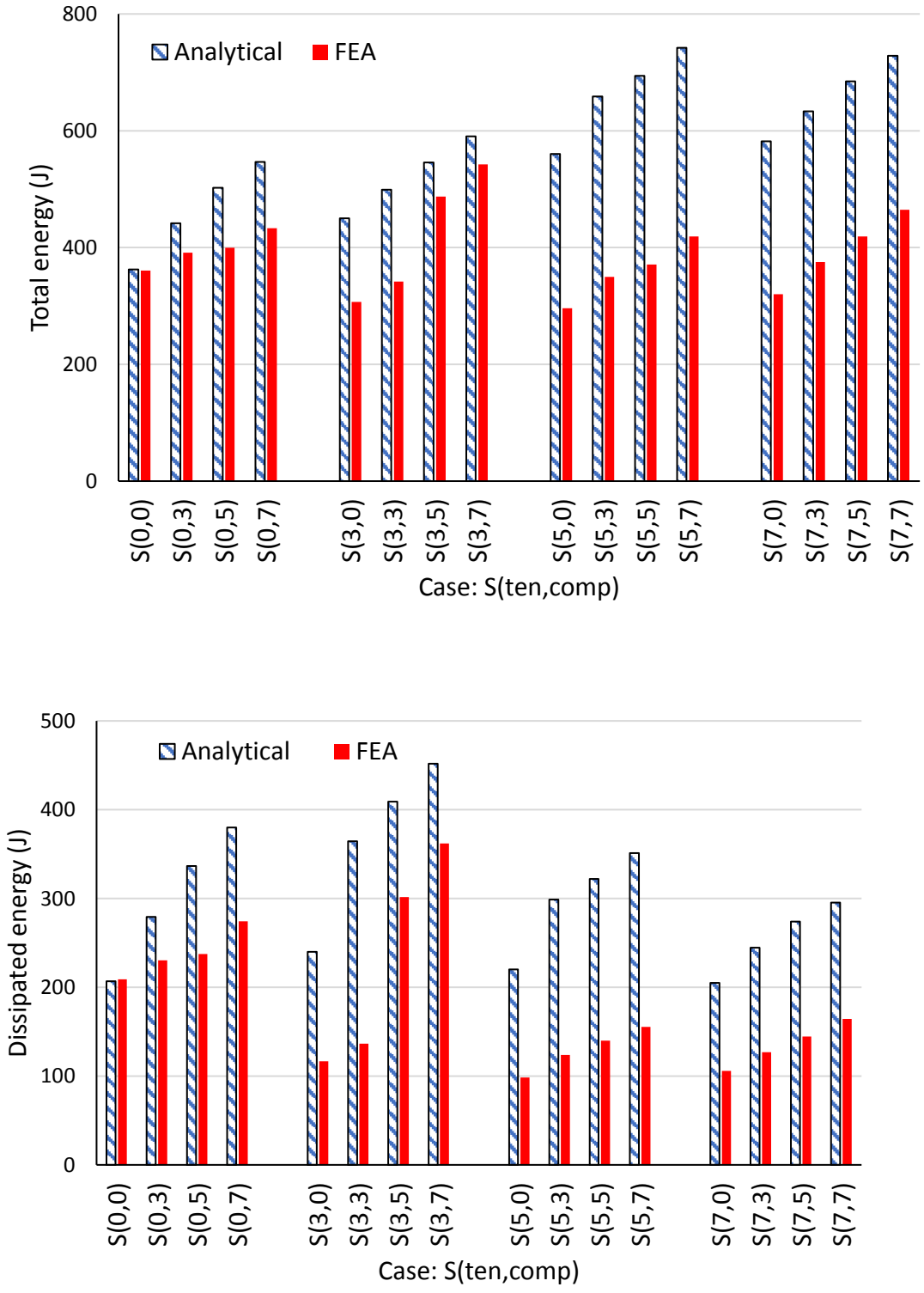

Figure 5-26: The total and the dissipated energy of different cases with different number of CFRP bars obtained from the analytical and the numerical procedures.

5.5.2 Effect of deflection rate on the total and the dissipated energy

In this section, the impact of the strain rates on the entire load-deflection response and the energy dissipated of the strengthened slab is studied. Slab S(0,7), i.e. strengthening only the compression face of the slab is considered in conducting this parametric study as the main aim in this study is to enhance the energy dissipation rather than the strength capacity. Based on the results of the comparison between the results of the analytical and the numerical solutions as presented in the previous sections which show that both procedures are in good agreement in many aspects and both were able to detect the entire behaviour of the NSM CFRP system,

Figure 5-27 shows the entire load-deflection response of slab S(0,7) with different t_m values. It shows that the yielding strength increases with the increase in the deflection rate value. The plastic load was also found to be increasing with the increase of the deflection rate. Increasing the yielding strength contributes to increasing the elastic energy and as a result a decrease in the dissipated energy. On the other hand, increasing the plastic load contributes to increasing the dissipated energy. Since the entire dissipated energy is a function to both the yielding strength and the plastic load, the entire dissipated energy either increases or decreases with the increasing of the deflection rate based on the effect of each factor. This is shown in Figure 5-28 where the dissipated energy increased from 315 J at t_m=100 (quasi-static state) to 337 J at t_m=0.1 s then drops to 332 J when t_m = 0.01 s. However, no significant change in the dissipated energy was obtained when the deflection rate changes.

Figure 5-29 shows the enhancing factor of the dissipated energy (compared to the quasi-static state) under a wide range of deflection rate. It shows that the enhancing factor of the dissipated energy ranges from 1 to 1.07 for various deflection rate value. Based on this, it can be concluded that the strain rate effect has a slight impact on the energy dissipation of the slab when a sufficient range of ductility is allowed. Based on this result and for time-saving of the analysis, the next parametric studies are conducting under quasi-static condition since including the strain rate effect in the analysis increases the time of the analysis as the m-k relationship is atypical in the slab due to the changing in the strain rates which highlight the need to calculate the m-k relationship for each layer and at each section.

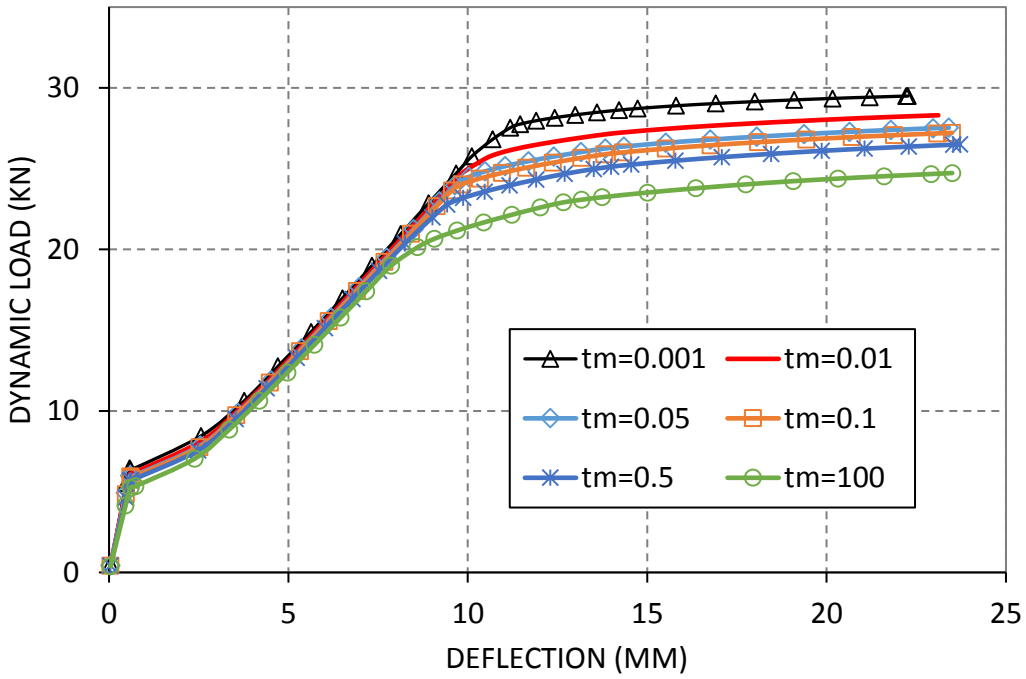

Figure 5-27: The load-deflection behaviour of slab S(0,7) for different deflection rate values where t_m refers to the time of the maximum deflection.

5.5.3 Effect of the stiffness of CFRP on the energy dissipation

To study the effect of stiffness of the CFRP bars on the energy dissipation of the slab, a one-way RC slab is analysed by using the analytical procedure. The slab is strengthened on the compression face only with a different number of CFRP bars (3,5,7 and 9) each with 4mm diameter. The corresponding equivalent strengthening area of CFRP is 37.68, 62.8, 87.92 and 113.04 mm^2. Slab QC1 is selected to represent the reference slab. As such, the results obtained in this analysis were calculated based on the geometrical and mechanical properties of the structural material used in slab QC1. In each slab, the analysis was conducted by assuming different values of modulus of elasticity for the CFRP bars varied from 50 to 250 GPa by representing the actual range of stiffness of CFRP bars commercially available, which depends on the ratio of the carbon fibers to the resin used in the composite.

Figure 5-30(a) shows that the dissipated energy of the slab achieved by adopting the NSM technique increases linearly with the increasing of the stiffness of the CFRP reinforcing bars. It was also found that the slope of the linear portion increases when the area of the CFRP increases. Figure 5-30(b) shows that the enhancing factor of the dissipated energy of the tested slab, with respect to the reference slab, ranges between 1 and 3.1. This indicates that both the reinforcing area and the stiffness of the CFRP bars play a significant role in increasing the amount of the dissipated energy in the CFRP NSM strengthening approach.

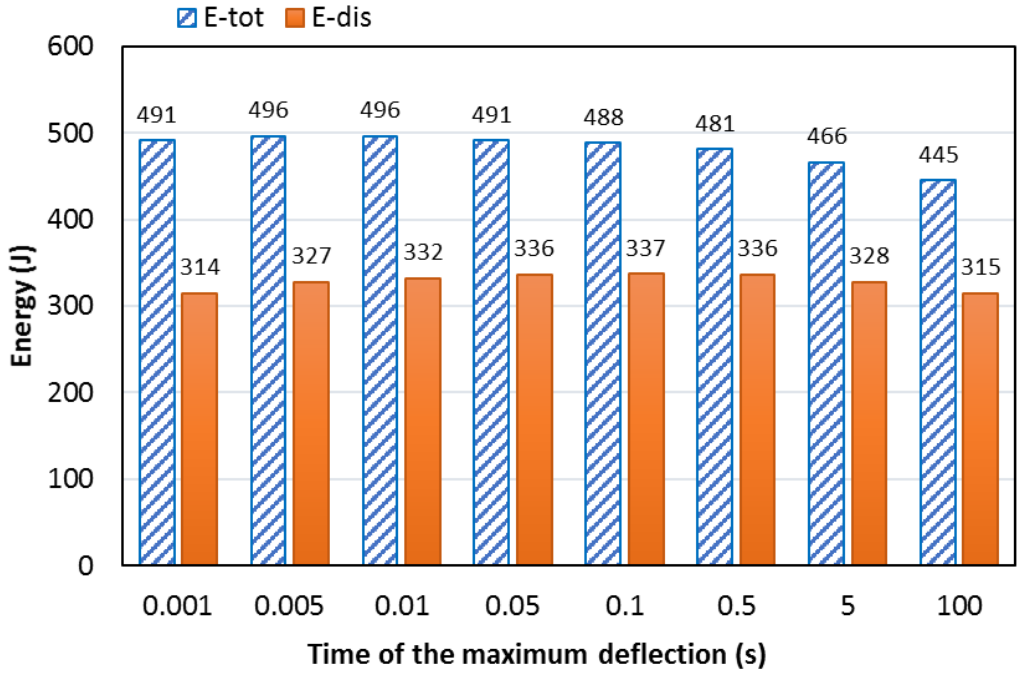

Figure 5-28: The total and the dissipated energy of slab S(0,7) for different deflection rate value.

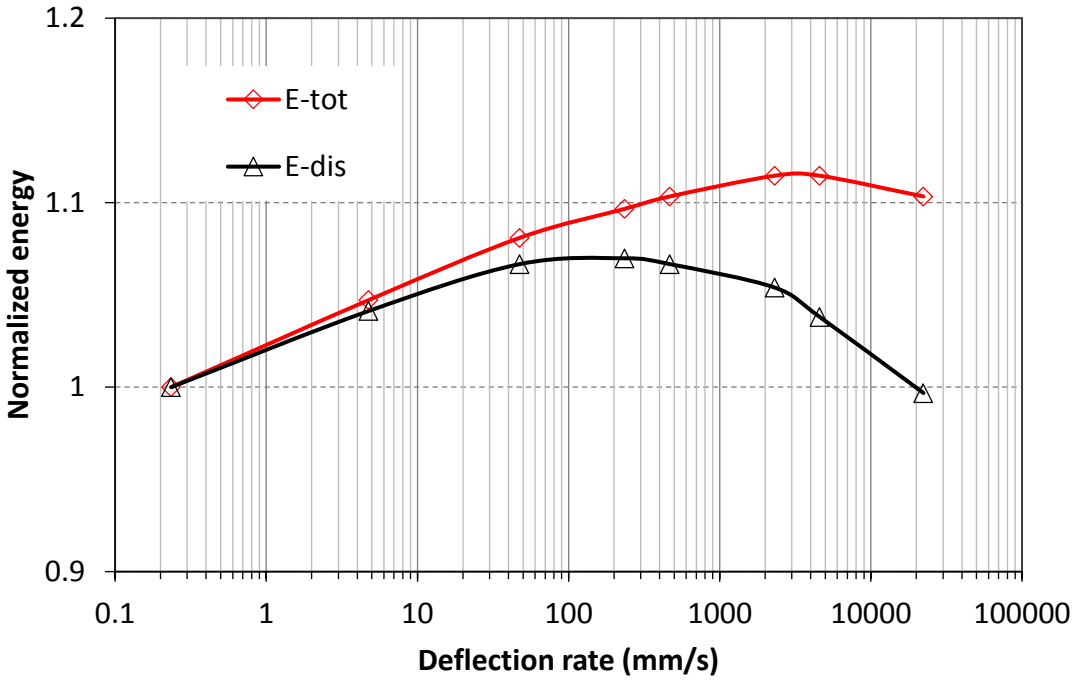

Figure 5-29: The relationship between the normalized total and dissipated energy (to the quasi-static state) and the deflection rate value of slab S(0,7).

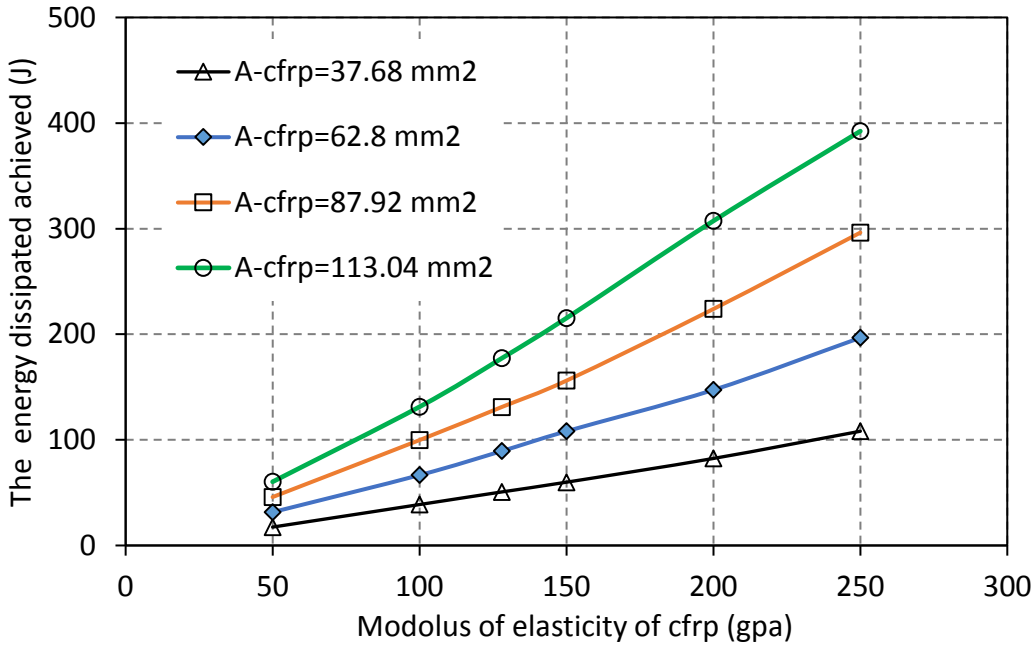

a) The amount of the energy dissipated

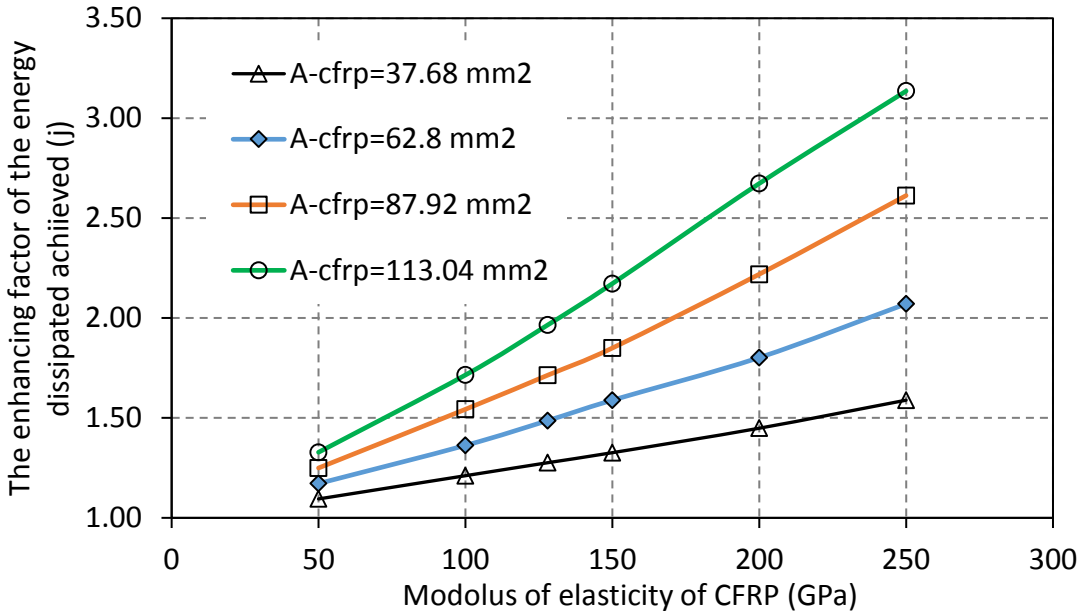

b) The enhancing factor of the dissipated energy

Figure 5-30: Effect of the modulus of the elasticity of the CFRP on: a) the amount and b) the enhancing factor of the dissipated energy of the slab by using different compression strengthening ratio.

5.5.4 Effect of dimensions of the one-way slab on the energy dissipation

To study the effect of the geometrical dimensions of the one-way slab on the amount of the dissipated energy obtained by adopting the NSM CFRP technique, different values of shear length and thickness of the one-way slab were imposed. The obtained results were compared with the results of the reference slab QC1.

The parametric study was conducted by applying different shear span length varying from 900 to 3150 mm and different thickness from 50 to 125 mm. Details of the steel and CFRP reinforcement are left without change in all the cases. The concrete cover of the steel reinforcement is assumed to be 10 mm for all cases. Thus, the effective depth of the slab increases linearly with the depth of the slab. The strengthening technique is assumed to be as slab S(0,7) by applying 7ϕ4mm CFRP bars in the compression face while the tension face is left without strengthening.

Figure 5-31(a) shows the amount of the dissipated energy achieved for each strengthened slab case in addition to the dissipated energy of the reference case. It shows that the dissipated energy achieved by applying the same quantity of CFRP bars is sensitive to both the shear span and the thickness of the slab and the amount of the dissipated energy achieved increases linearly with the increasing of both length and thickness of the slab. Increasing the dissipated energy with the increasing of the span length is attributed to the increase in the length of the plastic zone in the slab which allows for more plastic deformation in the steel reinforcement since the plastic zone length is a ratio to the shear span length. While increase in the dissipated energy achieved in the strengthened slab with the increasing thickness is attributed to the increasing of the distance between the steel reinforcement bars and the neutral axis of the cross-section which led to increasing the additional steel strain due to shifting up of the neutral axis b.

Figure 5-31(b) shows that the enhancing factor of the dissipated energy of the strengthened slab compared to the control slab is sensitive to the effective depth of the slab. The shear length has no impact on the enhancing factor which indicates that the ratio of the plastic zone to the shear span is constant.

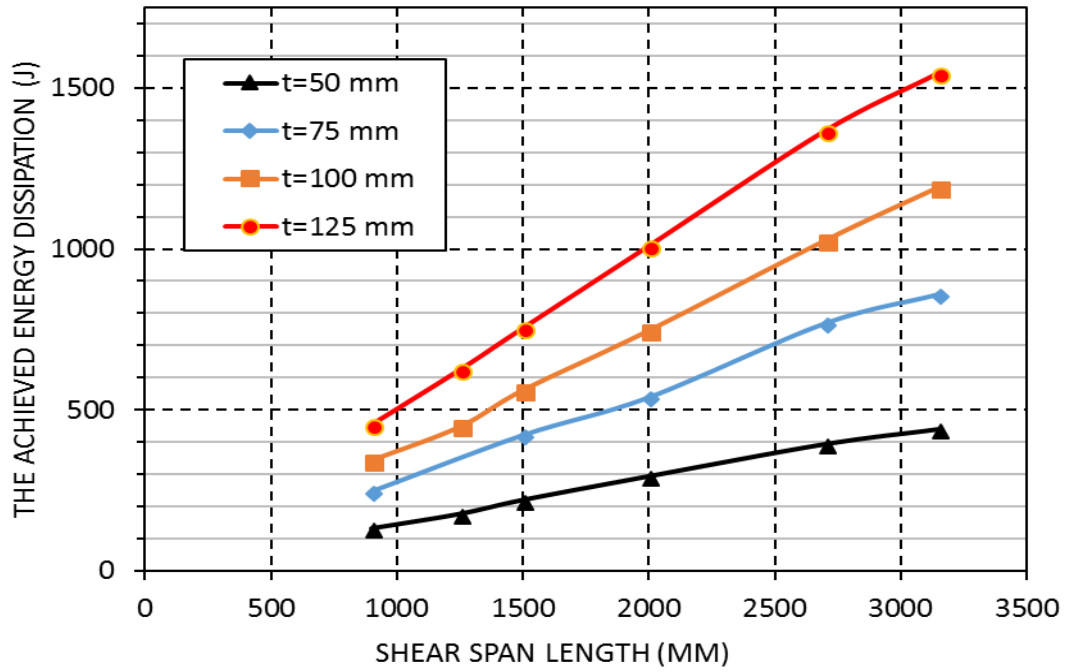

a) Energy dissipation with different thickness.

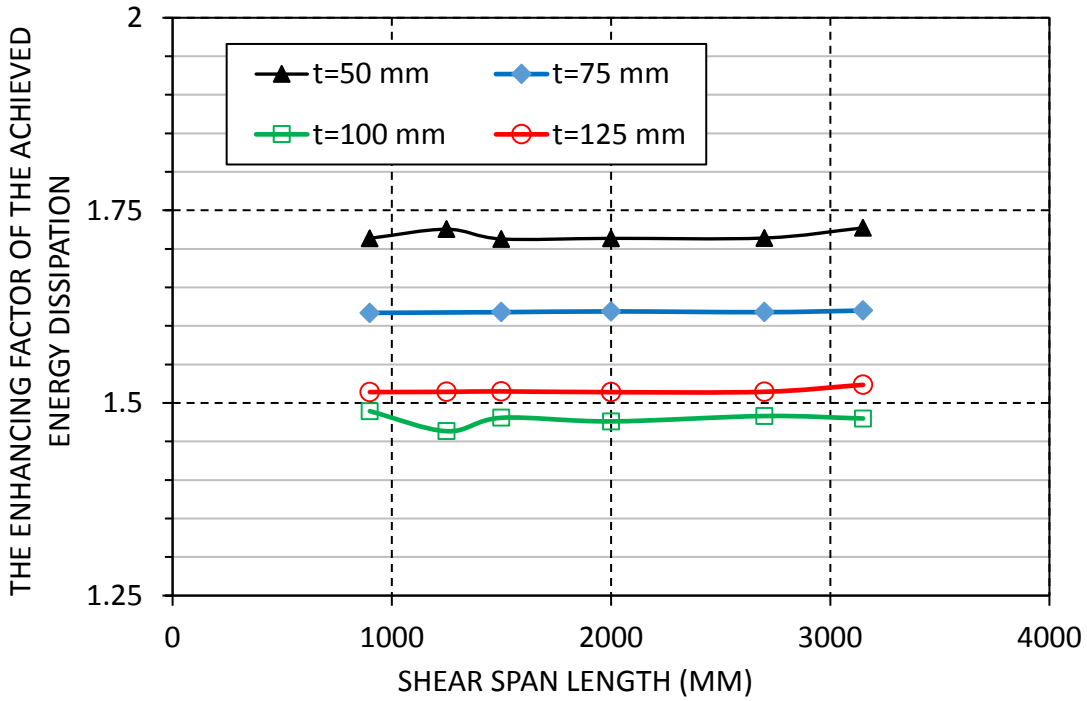

b) Enahncing factor of the energy dissipation with different thickness.

Figure 5-31: The amount of (a) the energy dissipation and (b) its enhancing factor of the strengthened slab S(0,7) compared to the control slab S(0,0) for different values of thickness and shear length.

5.5.5 Effect of the reinforcing area of steel and CFRP on the energy dissipation

In this case study, the effect of the steel and CFRP reinforcing area was studied. To give more flexibility to increasing both reinforcing areas without any concern about exceeding the minimum and the maximum limit of the steel reinforcing, the geometrical dimensions of the slab for all cases are taken as 2000 x 500 x 100 mm for the shear length, width, and the thickness respectively. The size of the steel and the CFRP bars are taken as 8 and 4 mm respectively for all cases. In this study, five values of the steel reinforcing area are assumed which range from 301 to 553 mm^2 with different values of CFRP reinforcing area ranging from 0 to 125.6 mm^2.

Figure 5-32-a presents the dissipated energy achieved in the strengthened slab when different steel and CFRP are used. It indicates that when the slab is strengthened, the achievable dissipated energy increases with the increasing of the CFRP reinforcing area and the decreasing of the steel reinforcing area. Increasing the CFRP area led to shifting up in the neutral axis which contributes to increasing the strain of steel and as a result increasing the dissipated energy. Increasing the steel reinforcing area in the section leads to decreasing the distance between the steel reinforcing and the neutral axis (to achieve balance in the internal forces) which contributes to mitigating the effect of the CFRP as stated in Section 5.5.4. Figure 5-32-b shows that the enhancing factor of the dissipated energy is sensitive to the CFRP area while the effect of the steel area is mitigated. Figure 5-33-a shows that the amount of the dissipated energy increases linearly with the increasing of the ratio of CFRP/steel area for all the cases.

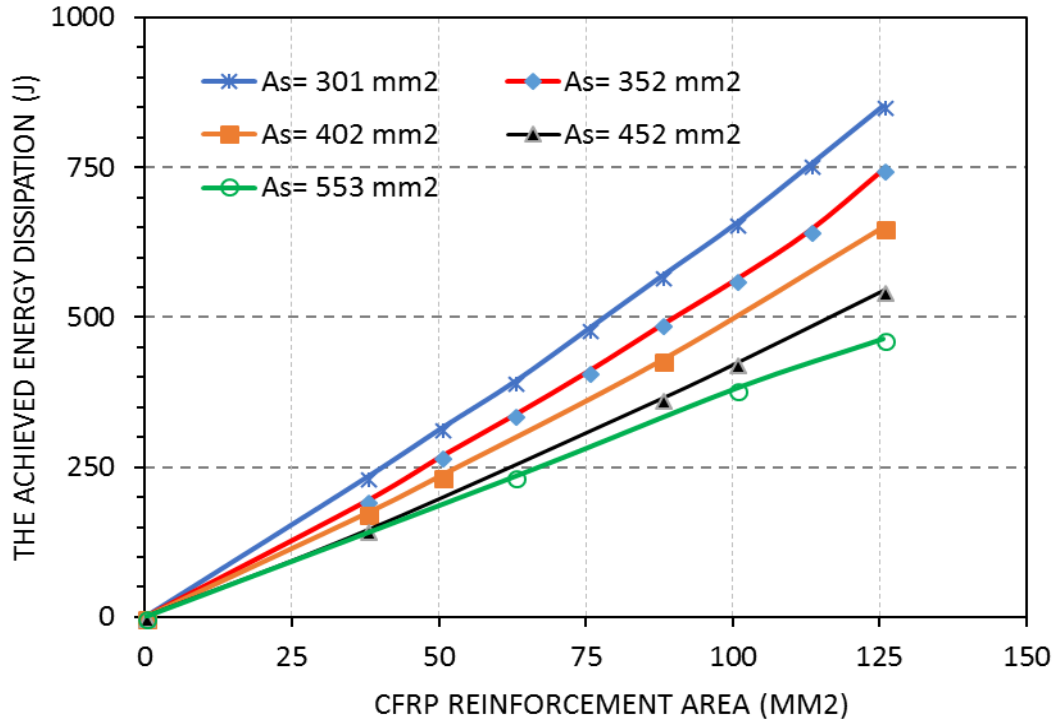

a)

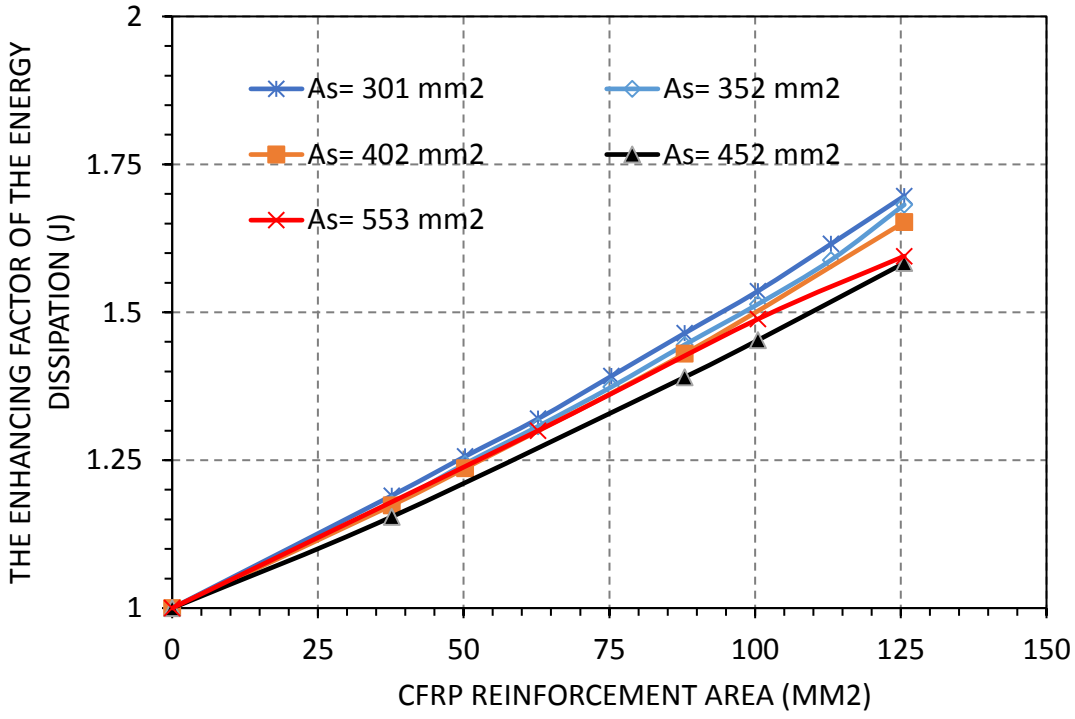

b)

Figure 5-32: The amount and the enhancing factor of the energy dissipated of the strengthened slab with different steel and CFRP reinforcing area.

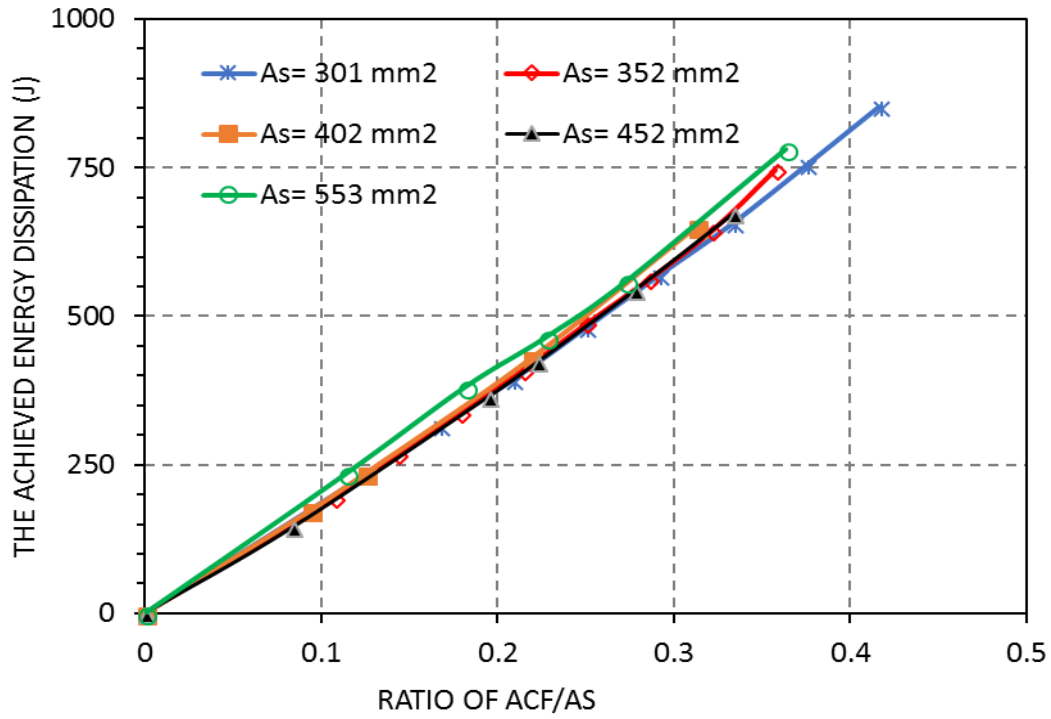

a) Energy dissipation with different steel ratio.

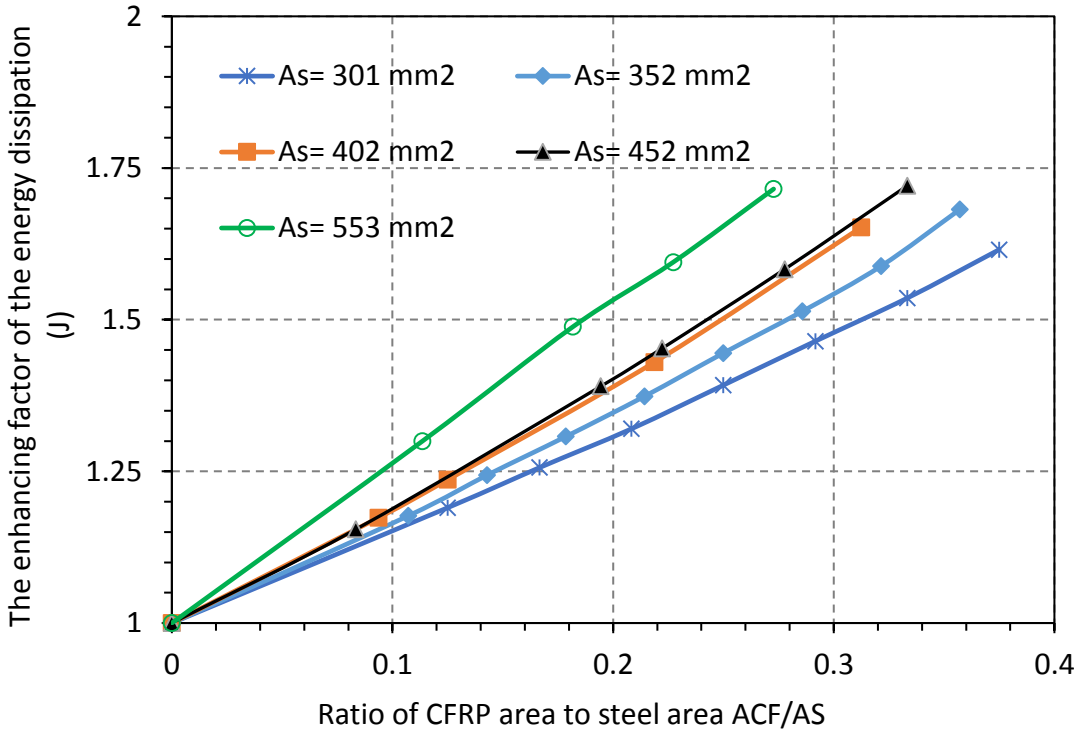

b) Enhancing factor of the energy dissipation with different steel ratio.

Figure 5-33: The amount and the enhancing factor of the energy dissipated of the strengthened slab with different ratio of CFRP to steel reinforcing.

5.6 Conclusion

This chapter contains the predicted results obtained from analysing one-way RC NSM CFRP system up to the ultimate state by using two models; analytical and numerical which are presented in chapter 4. Firstly, the adopted models were validated with the experimental results which is presented in chapter 3. The obtained results of the validation analysis indicated the adequacy of both models to simulate the NSM CFRP system in the low strain rate regime in terms of predicting the entire load-deflection behaviour and the enhancing in the energy dissipation in the RC member. No significant difference was obtained between these two models. While in the high strain rate regime (impact state) the numerical model was more accurate in estimating the maximum displacement response for any known impact impulse where the average percentage of error between the numerical and the measured maximum deflection response was 10% compared to 20% was obtained with the analytical model. This was attributed to the basic assumption adopted in the analytical model by assuming elastic-perfect plastic behaviour in the load-deflection curve by neglecting the hardening behaviour.

In terms of the pattern of the cracks, the proposed opened crack model which was adopted in the analytical model was capable to detect the change in the pattern of the cracks between the control and the strengthened slab which was observed in the experimental test. While the numerical model did not detect any change in the pattern of the crack. However, this change in the pattern of the cracks has slight effect on the energy dissipation based on the predicted results. As the displacement control criteria method is used in the analytical model compared to the load control criteria method during the analysis, the softening behaviour in the load-deflection curve can only be simulated in the analytical model while a convergence problem occurs during the numerical analysis when the load drops.

Based on the parametric study that conducted to investigate the effect of some potential involved factors, it was found that the amount of the dissipated energy achieved by strengthening either one or both faces of the slab is affected by many factors, such as the ratio of CFRP reinforcing in the section, stiffness of the CFRP composite, ratio of the main steel reinforcement, and thickness of the element, where the amount of the enhancing in the energy dissipated increases with the increase of these factors.

The results obtained in this study from both the experimental and the analysis procedures indicated the adequacy of retroffiting the RC slabs on one or both faces by using NSM CFRP approach in enhancing the blast resistance of the slab significantly in terms of the strength, ductility and the energy dissipationwith no debonding failure was observed in the CFRP composite material. This is different that what has been reported by (Wu et al., 2007) where no significant enhancement in the blast resistance of the RC slab was obtained when a close-in explosion event was applied as reviewed in chapter 2. It was noticed that in most of real blast tests close-in explosion events are applied to reduce the weight of the explosive charge and to increase the reflected pressure to fail the specimen. This has an effect on the failure mode obtained in the slab where a scabbing, shear and debonding of the FRP material were the dominant failure modes due to localizing the load in the centre of the specimen (Wu et al., 2007, Wu et al., 2009). While these failure modes are rarely obtained in cae of far explosion events. In the current study, spreading the concentrated load on a wide area of the slab by using load spread rigs helped to avoid these types of failure and as a results simulating the far explosion events to overcome the limitations engaged with the real blast tests.

CHAPTER 6: SUMMARY AND CONCLUSION

6.1 Summary

In this research, the need for enhancing the blast resistance of a structural building is highlighted. Firstly, a review of the studies on improving the blast resistance of the structural elements by using different techniques has been presented with focus on the recent strengthening methods which utilize the innovative FRP materials. Then the strengths and limitations of each technique were highlighted before identifying the areas in the blast protection field that need to be investigated more to enrich the existing knowledge in this field.

In this study, the entire behaviour of the one-way RC NSM CFRP system that is subjected to loads with low and high loading rates has been studied. The study was carried out by conducting experimental and theoretical programs by strengthening one-way RC slabs on one or both faces by using NSM CFRP rods. To simulate the blast load effect, both the static and the impact loads were spread along the slab. In case of static loading, the strengthening technique was applied on both faces to investigate the feasibility of using NSM CFRP technique for increasing both the load capacity and the ductility of the elements. In case of impact loading, the strengthening technique was applied only on the compression face of the strengthened slabs to investigate its effectiveness in enhancing the energy dissipation of the slab to dissipate the impact and the blast energy applied on the structural elements to eliminate or mitigate the amount of the energy at the crushing point of the concrete to prevent the progressive collapse and reduce the fragmentation in the concrete.

Then the NSM system was modelled analytically and numerically. The analytical modelling was carried out by coupling the traditional nonlinear sectional layered method with the moment area method to predict the load-deflection behaviour of the system under loads with different loading rates by adopting strain rate dependent material models for both the concrete and the steel reinforcement. In the impact simulation, the nonlinear layered method was coupled with the elasto-plastic SDOF method to estimate the maximum impact response of the one-way slab and the entire load-deflection response

which was used to calculate the total and the dissipated energy of the slab up to the maximum response. Then, to gain confidence in the analytical model, the analytical results were compared with the nonlinear FE model results which were obtained by using the Abaqus software which is well known in simulating the impact and the blast response. All the obtained results were presented and discussed in detail in terms of the failure modes, ultimate strength, crack patterns and the total and the dissipated energy.

6.2 Conclusion

The following conclusions can be drawn from this research:

6.2.1 Literature review study

Most of the previous studies were conducted on increasing the strength capacity of the RC elements by using EB FRP strips. Despite the significant enhancement in the strength of the elements to the static, impact and blast loads, many drawbacks were identified with this technique, such as the premature debonding failure of the FRP strips and the reduction in the ductility of the strengthened elements. Although enhancing strength capacity of the element helps to prevent failure or collapse of the elements in many cases, catastrophic damages and human losses can occur as a result to the brittle failure of the elements when the applied load exceeds the load capacity of the elements. Thus, enhancing the ductility and the energy dissipation of the elements especially under massive out-of-plane loading such as blast and impact is important. Limited studies have been conducted on enhancing the ductility and the energy dissipation of the elements by adopting the EB FRP methods. In the previous studies limited enhancement in the ductility was obtained when the compression face of the element was strengthened. This was due to the premature failure of the FRP strips.

In the last 10 years, NSM FRP technique has become a promising strengthening technique as an alternative to the EB FRP method since it overcomes the above-mentioned drawbacks of the latter. Most of the studies on the NSM technique, studied its effectiveness to the static loads with limited focus on the dynamic response. Furthermore, enhancing the ductility and the energy dissipation of the elements was still not covered sufficiently.

6.2.2 Physical experiments

1. In the low strain rate loading regime, applying the NSM CFRP strengthening approach on both faces of RC slab enhanced its moment capacity, ductility and energy dissipation. While the load capacity increased from 25.1 to 49.4 kN (nearly 200%) and the energy dissipation increased from 424 to 901 J (nearly 210%) when both faces of the slab were strengthened with 3 and 7 CFRP bars of 4 mm diameter respectively.

2. In the high strain rate regime, strengthening the compression face of the RC slab improved both the total energy and the energy dissipation with an enhancing ratio of 320% and 230% respectively, thus suggesting good effectiveness of this strengthening method to enhance the structural resistance to the impact and blast loads. No debonding failure in the NSM CFRP occurred which could lead to a premature failure and reducing the utilization of the strong FRP material as occurs with the EB technique.

3. Based on the comparison between the measured impact pulse and the blast impulse it was found that the measured impact load function compared well in its form with the blast load function obtained from real blast test (Guo, Xu et al. 2017). Both are transient loads acting within a very short time taking a triangle load function with two factors: the peak force, and the duration of the load. The strain rate induced on the element depends on these two factors. Thus, response of the structural elements to each of these loads is almost similar as long as the peak force and the duration of the load are similar. This finding is outstanding as it indicates that conducting impact test as a non-explosive blast test is reasonable to estimate the response of the element to the blast loading. This helps to increase number of the experimental tests that can be done in this field by avoiding the difficulty involving in conducting explosive tests.

4. Spreading the concentrated quasi-static and impact loads on the specimens by either of the adopted loading layout rigs, that is airbag and whiffletree, helped in avoiding the local and the shear failure which is expected with the concentrated loads. This helped to conduct the non-explosive test (impact test) to simulate the real blast test which otherwise is difficult to conduct. So far, no similar studies

were found in the literature that tried to spread the impact load by either of the adopted methods or others to simulate the blast loading.

5. Strengthening the compression face of RC slab by using NSM approach had a significant impact on the crack pattern of the tension face by changing its pattern from one major crack to multiple cracks in both low and high strain rate regime. The multi-crack pattern helped to control the width of each crack and to increase the energy dissipation which is attributed to the plastic deformation in the steel at each crack.

6. In the high strain rate loading test, no cracks occurred in the strengthened slab due to the presence of the CFRP bars in the compression face. Thus, applying NSM CFRP in the compression face of RC slabs helps to cope with any out-of-plane tensile stresses in the non-reinforced faces.

7. No debonding failure was observed in the CFRP rods in both the tension and the compression faces which is attributed to the sufficient development length and the high parameter/section area ratio provided by using 4mm size of CFRP bars.

6.2.3 Analytical and numerical results

8. In the quasi-static case, both the analytical and the numerical models showed good agreement with the experimental results in predicting the entire load-deflection response of the slab. In terms of the estimated dissipated energy, the difference factors of the dissipated energy were 20-35% and 2-30% for both the analytical and the numerical simulation respectively.

9. The nonlinear layered analysis method is good in establishing the moment-curvature relationship of one-way element member for various loading rates if proper strain rate dependent material models are adopted. Also, coupling the nonlinear layered analysis method with the nonlinear moment area method is effective in predicting the load-deflection behaviour of the element for different loading rates.

10. Coupling the nonlinear layered method with the SDOF method was approved to be adequate in predicting the impact displacement response of the RC element

at any level of plastic deformation. However, the percentage of error increases with the increasing in the level of the plastic deformation.

11. The numerical simulation model was better than the analytical model in predicting the maximum response of the slab under impact load, but no significant change was found where the average difference factor of the numerical predicting was 10% compared to 20% for the analytical when compared with the experimental impact test results.

12. The analytical model overestimates the maximum impact displacement response of the control slab by 20%. This might be due to assuming elastic-perfect plastic load-deflection behaviour neglecting the hardening behaviour in the load-deflection curve which contributes to absorb energy and reduce the maximum displacement response if it is included in the analysis.

13. In the quasi-static state, the sudden reduction in the stiffness of the slab which was experimentally obtained when the first crack initiated can be detected in the analysis if a proper tension stiffening model with dramatic exponential decay branch is used. However, a convergence problem during the analysis occurs when the viscosity parameter of the concrete (unit of second) is taken as zero in the numerical modeling. Thus, the viscosity parameter of the concrete should be more than zero to overcome this problem. In this study, value of 0.005 s was depended in the numerical analysis as found to be fit with the experimental results.

14. The proposed discrete crack model which is adopted in the analytical solution is capable to predict the crack patterns for both the strengthened and the control slab. However, including the width of the cracks in the calculation led to a slight increase in the predicted deflection and, as a result, the predicted total and dissipated energy.

6.2.4 Parametric study

15. Based on the parametric study using the analytical model, increasing the deflection rate led to an enhancement in the elastic strength of the slab as a result to the strain rate dependency of the component material.

16. No significant change in the amount of the dissipated energy gained by strengthening the compression face with the changing in the applied loading rate was obtained. This stating the strain-rate independency of the enhancing factor in the dissipated energy when using NSM CFRP approach.

17. The amount of the energy dissipation achieved by strengthening the compression face of the slab depends on many factors, such as the thickness of the slab, steel reinforcing ratio, the stiffness of the CFRP rods and ratio of the CFRP. The energy dissipation increases with the increasing values of these factors.

18. The optimum amount of the energy dissipation can be achieved when both faces of the slab are strengthened by NSM CFRP rods and by allowing the CFRP in the tension face to rupture if the crushing or the shear failure of concrete can be controlled.

19. The maximum amount of the dissipated energy achieved by strengthening the slab depends on the level of the steel reinforcing ratio based on the ratio of the used to the available ductility in the slab. For over-reinforced elements, just low amount of the ductility is used which can be utilized by strengthening the compression face of the element by NSM CFRP system if the shear and the debonding failure in the slab are controlled.

6.3 Limitation of the work

The results gathered from both the experimental and the theoritical programs in terms of the load, deflection, steel and concrete strains were sufficient to assess the validity of using NSM CFRP approach to enhance the ductility, loading capasity and energy dissipation in the existing concrete building. However, some limitations are involved in both procedures and should be considered before generalising thier obtained results. The limitations involved in this study are described as follows:

1. As small scale elements were used in the tests, to be within the limit capasity of the equipment used in the tests, only way slab and one layer of CFRP strengthening bars on either the tension or the compression face of the slab were adopted. So, the results and the conclusions obtained from this study is valid for only the one way elements.

2. The displacement in both the static and impact tests were measured only in the middle of the slab by fixing LVDT underneath the slab by using glue or bolt. In some cases the LVDT was detached from the specimens in the impact test due to the high oscillation of the specimen as a results to the impact response. For more accurate results, accelerators are preferred to bedistributed in many points to record the displacement profile along the slab rather than recording only the mid-span displacement.
3. The steel strain was measured only in the mid-length of the steel bar. While it was found that the steel strain is sensitive to the cracks pattern. Therfore, for more utilization of the steel strain, the strain needs to be measured along the steel bar by spreading many strain gauges. This helps to better estimating to the steel strain profile along the bar which can be used to calculate the steel strain energy dissipation.
4. The theoretical method adopted in this study was developed for one-way element such as beam or one way slab with neglecting the shear effect and the debonding failure of the reinforcements which in some cases cause premature failure in the structural element. So, the analytical procedure needs to be developed by including these important factors.

6.4 Future work

1. Future research could try to improve and develop a model to predict the change in the crack patterns and their contribution to the energy dissipation under different loading rates. This can be achieved by conducting more experimental tests with measuring width, number and positions of the cracks instrumently then using them to improve a proper opened crack model.

2. Future work could measure the slip in the CFRP bars quantitively rather than depending on the post-test observation since including slipping of the CFRP bars has an impact on the distribution of the stresses in the element if not enough bonding area is provided as a result to the lack of the development length or when large size of CFRP bar is used. Little slipping off if it exists could delay the rupture in the CFRP bars in the tension zone.

3. More studies are needed in the validity of conducting non-explosive tests, such as impact and rapid pressure, to resemble the real blast tests (which are not easily accessible) with high accuracy. This can be achieved for example by improving more sophisticated rigs to spread the load uniformly on the entire area of the slab to simulate distribution of the blast loads.

4. Future work could consider enhancing the bonding behaviour of the NSM CFRP bars by adopting proper anchoring systems. This helps to improve the bonding properties in case of the lack of the bonding area available in the system such as at the beam-column joint position.

5. Since the amount of the dissipated energy achieved by strengthening one or both faces of the slab is controlled by its shear resistance, research is needed to enhance the shear strength of the slab.

6. The SDOF method can be improved by including the hardening behaviour of the load-deflection curve for better estimating the maximum response of the slab under impact loads.

7. Research is needed to examine the feasibility of enhancing the ductility of the continuous slabs where the critical section occurs in the hogging zone (at the support) and using NSM could be challenging due to insufficient development length being available for the CFRP rods.

8. Since the strong epoxy Sikadure is expensive, investigating efficiency of different locally made bonding and filling materials on the entire behaviour of the strengthened member is needed.

REFERENCES

ABAQUS, F. 2011. Analysis User's Manual 6.14. *Dassault Systemes Simulia Corp., Providence, RI*.

ABOU-ZEID, M., FOWLER, D. W., NAWY, E. G., ALLEN, J. H., HALVORSEN, G. T., POSTON, R. W., BARLOW, J. P., HANSEN, W., RHOADS, R. J. & BRANDER, M. E. 2001. Control of Cracking in Concrete Structures. *Report, ACI Committee,* 224**,** 12-16.

ABRAHAMSON, G. & LINDBERG, H. 1976. Peak load-impulse characterization of critical pulse loads in structural dynamics. *Nuclear engineering and design,* 37**,** 35-46.

ACI 2008. "Guide for the design and construction of externally bonded FRP systems for strengthening concrete structures.". *Technical committee document 440.2R-02, American Concrete Institute (ACI), Committee 440, 45 pp.*

ADHIKARY, S. D., LI, B. & FUJIKAKE, K. 2015. Parametric study of RC beams under a wide range of loading rates. *Proceedings of the Institution of Civil Engineers-Structures and Buildings,* 168**,** 729-746.

AL-HASSANI, S. & KADDOUR, A. Strain rate effects on GRP, KRP and CFRP composite laminates. Key engineering materials, 1998. Trans Tech Publ, 427-452.

AL-MAHMOUD, F., CASTEL, A., FRANÇOIS, R. & TOURNEUR, C. 2009. Strengthening of RC members with near-surface mounted CFRP rods. *Composite Structures,* 91**,** 138-147.

ALHADID, M. M., SOLIMAN, A. M., NEHDI, M. L. & YOUSSEF, M. A. 2014. Critical overview of blast resistance of different concrete types. *Magazine of Concrete Research,* 66**,** 72-81.

ALKHRDAJI, T. & NANNI, A. Surface bonded FRP reinforcement for strengthening/repair of structural reinforced concrete. Proc., ICRI-NRCC Workshop, Baltimore, MD (USA), Oct, 1999. 19.

ALKHRDAJI, T., NANNI, A., CHEN, G. & BARKER, M. 1999. Upgrading the transportation infrastructure: solid RC decks strengthened with FRP. *Concrete International,* 21**,** 37-41.

ASPLUND, S. Strengthening bridge slabs with grouted reinforcement. Journal Proceedings, 1949. 397-406.

AUTODYN, A. 2005. Theory manual revision 4.3. *Century Dynamics, Concord, CA*.

BAKER, W. E., KULESZ, J., RICKER, R., BESSEY, R., WESTINE, P., PARR, V. & OLDHAM, G. 1975. Workbook for predicting pressure wave and fragment effects of exploding propellant tanks and gas storage vessels.

BAKER, W. E., KULESZ, J. J., WESTINE, P. S., COX, P. A. & WILBECK, J. S. 1981. A manual for the prediction of blast and fragment loadings on structures. USDOE, Albuquerque Operations Office, Amarillo Area Office.

BAKIS, C. E., GANJEHLOU, A., KACHLAKEV, D. I., SCHUPACK, M., BALAGURU, P., GEE, D. J., KARBHARI, V. M., SCOTT, D. W., BALLINGER, C. A. & GENTRY, T. R. 2002. Guide for the design and construction of externally bonded FRP systems for strengthening concrete structures. *Reported by ACI Committee,* 440.

BARROS, J. A., FERREIRA, D. R., FORTES, A. S. & DIAS, S. J. 2006. Assessing the effectiveness of embedding CFRP laminates in the near surface for structural strengthening. *Construction and Building Materials,* 20**,** 478-491.

BATARLAR, B. 2013. *Behavior of reinforced concrete slabs subjeted to impact loads.* İzmir Institute of Technology.

BATRA, R. & HASSAN, N. 2007. Response of fiber reinforced composites to underwater explosive loads. *Composites Part B: Engineering,* 38**,** 448-468.

BENMOKRANE, B., CHAALLAL, O. & MASMOUDI, R. 1995. Glass fibre reinforced plastic (GFRP) rebars for concrete structures. *Construction and Building Materials,* 9**,** 353-364.

BERGER, J., HEFFERNAN, P. & WIGHT, R. 2008. Blast testing of CFRP and SRP strengthened RC columns. *Structures Under Shock and Impact,* 98**,** 95-104.

BIGGS, J. M. & BIGGS, J. M. 1964. *Introduction to structural dynamics,* McGraw-Hill College.

BOURNAS, D. & TRIANTAFILLOU, T. Flexural strengthening of RC columns with near surface mounted FRP or stainless steel reinforcement: experimental investigation. The 14th World Conference on Earthquake Engineering, October12-17, 2008. 2.

BRANDT, A. M. 2008. Fibre reinforced cement-based (FRC) composites after over 40 years of development in building and civil engineering. *Composite structures,* 86**,** 3-9.

BUCHAN, P. & CHEN, J. 2007. Blast resistance of FRP composites and polymer strengthened concrete and masonry structures–A state-of-the-art review. *Composites Part B: Engineering,* 38**,** 509-522.

CARINO, N. J. & CLIFTON, J. R. 1995a. *Prediction of cracking in reinforced concrete structures,* US Department of Commerce, National Institute of Standards and Technology.

CARINO, N. J. & CLIFTON, J. R. 1995b. Prediction of cracking in reinforced concrete structures. *Report NISTIR,* 5634.

CARREIRA, D. J. & CHU, K.-H. Stress-strain relationship for plain concrete in compression. Journal Proceedings, 1985. 797-804.

CEB, C. 1993. Model code 1990. Comité Euro-International du Béton, Thomas Telford Services Ltd., London, England.

CHOCK, J. M. K. 1999. *Review of methods for calculating pressure profiles of explosive air blast and its sample application.* Virginia Tech.

CODE, C.-F. M. 1993. Thomas Telford, London. CEB-FIP.

COELHO, M. R., SENA-CRUZ, J. M. & NEVES, L. A. 2015. A review on the bond behavior of FRP NSM systems in concrete. *Construction and Building Materials,* 93**,** 1157-1169.

DAVID, E. & NEUNER, J. Environmental durability studies for FRP systems: definition of normal conditions of use of FRP for structural strengthening applications. FRP Composites in Civil Engineering. Proceedings of the International Conference on FRP Composites in Civil Engineering., 2001.

DAVIDSON, J. S., PORTER, J. R., DINAN, R. J., HAMMONS, M. I. & CONNELL, J. D. 2004. Explosive testing of polymer retrofit masonry walls. *Journal of Performance of Constructed Facilities*.

DE LORENZIS, L. & TENG, J. 2007. Near-surface mounted FRP reinforcement: An emerging technique for strengthening structures. *Composites Part B: Engineering,* 38**,** 119-143.

DE SOUZA NETO, E., PERIĆ, D. & OWEN, D. 1998. Continuum modelling and numerical simulation of material damage at finite strains. *Archives of Computational Methods in Engineering,* 5**,** 311.

DIAS, S., BARROS, J. & JANWAEN, W. 2018. Behavior of Rc Beams Flexurally Strengthened with Nsm Cfrp Laminates. *Composite Structures,* 201**,** 363-376.

DOLCE, F., MEO, M., WRIGHT, A., FRENCH, M. & BERNABEI, M. 2010. Structural response of laminated composite plates to blast load. *Plastics, Rubber and Composites,* 39**,** 180-188.

DRAGANIĆ, H. & SIGMUND, V. 2012. Blast loading on structures. *Technical Gazette,* 19**,** 643-652.

ESHWAR, N., NANNI, A. & IBELL, T. J. 2008. Performance of two anchor systems of externally bonded fiber-reinforced polymer laminates. *Materials Journal,* 105**,** 72-80.

EWEN, K. A. 2005. *Ductility in FRP rods for concrete reinforcement by interfacial shearing.* Master of applied science, University of Ottawa.

FORET, G. & LIMAM, O. 2008. Experimental and numerical analysis of RC two-way slabs strengthened with NSM CFRP rods. *Construction and Building Materials,* 22**,** 2025-2030.

FORGHANI, A. & VAZIRI, R. 2009. Computational modeling of damage development in composite laminates subjected to transverse dynamic loading. *Journal of Applied Mechanics,* 76**,** 051304.

FRANGOU, M., PILAKOUTAS, K. & DRITSOS, S. 1995. Structural repair/strengthening of RC columns. *Construction and building materials,* 9**,** 259-266.

FUJIKAKE, K., LI, B. & SOEUN, S. 2009. Impact response of reinforced concrete beam and its analytical evaluation. *Journal of structural engineering,* 135**,** 938-950.

GARDNER, N. & SHUKLA, A. 2011. The blast response of sandwich composites with a functionally graded core and polyurea interlayer. *Dynamic Behavior of Materials, Volume 1.* Springer.

GIMÉNEZ, E., ADAM, J., IVORRA, S., MORAGUES, J. & CALDERÓN, P. 2009a. Full-scale testing of axially loaded RC columns strengthened by steel angles and strips. *Advances in Structural Engineering,* 12**,** 169-181.

GIMÉNEZ, E., ADAM, J. M., IVORRA, S. & CALDERÓN, P. A. 2009b. Influence of strips configuration on the behaviour of axially loaded RC columns strengthened by steel angles and strips. *Materials & Design,* 30**,** 4103-4111.

GUO, Z., XU, Z., CHEN, C., ZHANG, B., LEHMAN, D. E. & CAO, S. 2017. Behavior of GFRP retrofitted reinforced concrete slabs subjected to conventional explosive blast. *Materials and Structures,* 50**,** 236.

HA, J.-H., YI, N.-H., CHOI, J.-K. & KIM, J.-H. J. 2011. Experimental study on hybrid CFRP-PU strengthening effect on RC panels under blast loading. *Composite Structures,* 93**,** 2070-2082.

HANSSEN, A., ENSTOCK, L. & LANGSETH, M. 2002. Close-range blast loading of aluminium foam panels. *International Journal of Impact Engineering,* 27**,** 593-618.

HAWILEH, R. A. 2012. Nonlinear finite element modeling of RC beams strengthened with NSM FRP rods. *Construction and Building Materials,* 27**,** 461-471.

HEARLE, J. W. 2001. *High-performance fibres,* Elsevier.

HETHERINGTON, J. & SMITH, P. 2014. *Blast and ballistic loading of structures,* CRC Press.

HOSSEINI, M. M., DIAS, S. J. & BARROS, J. A. 2014. Effectiveness of prestressed NSM CFRP laminates for the flexural strengthening of RC slabs. *Composite Structures,* 111**,** 249-258.

HUI, T. & OSKAY, C. 2012. Computational modeling of polyurea-coated composites subjected to blast loads. *Journal of Composite Materials,* 46**,** 2167-2178.

ICARDI, U. & FERRERO, L. 2010. Optimization of sandwich panels to blast pulse loading. *Journal of Sandwich Structures & Materials,* 12**,** 521-550.

IMAI, M., NAKANO, R., KONO, T., ICHINOMIYA, T., MIURA, S. & MURE, M. 2010. Crack detection application for fiber reinforced concrete using BOCDA-based optical fiber strain sensor. *Journal of structural engineering,* 136**,** 1001-1008.

JOHNSON, C., SLAWSON, T., CUMMINS, T. & DAVIS, J. 2004. Concrete masonry unit walls retrofitted with elastomeric systems for blast loads. DTIC Document.

JONES, J., WU, C., OEHLERS, D., WHITTAKER, A., SUN, W., MARKS, S. & COPPOLA, R. 2009. Finite difference analysis of simply supported RC slabs for blast loadings. *Engineering Structures,* 31**,** 2825-2832.

KAKLAUSKAS, G. 1999. A New Stress-Strain Relationship for Cracked Tensile Concrete in Flexure. *Statyba,* 5**,** 349-356.

KAPTAN, K. 2017. Effectiveness of externally bonded FRP systems in strengthening of RC structures in seismic areas. *Proceedings of the Institution of Civil Engineers-Structures and Buildings,* 170**,** 362-375.

KARIM, M. R. 2005. *Constitutive modeling and failure criteria of carbon-fiber reinforced polymers under high strain rates.* University of Akron.

KIM JHJ, Y. N., KIM SB, ET AL 2009. Experimental study onblast loading response of retrofitted RC slab structures. *Asia-Pacific conference on FRP in structures (edJ Sim).* Seol, Korea,.

KMIECIK, P. & KAMIŃSKI, M. 2011. Modelling of reinforced concrete structures and composite structures with concrete strength degradation taken into consideration. *Archives of civil and mechanical engineering,* 11**,** 623-636.

KNOX, K. J., HAMMONS, M. I., LEWIS, T. T., PORTER, J. R. & BRANCH, F. P. 2000. Polymer materials for structural retrofit. *Force Protection Branch, Air Expeditionary Forces Technology Division, Air Force Research Laboratory, Tyndall AFB, Florida*.

KRAJCINOVIC, D. 2000. Damage mechanics: accomplishments, trends and needs. *International Journal of Solids and Structures,* 37**,** 267-277.

KRAUTHAMMER, T., ASSADI-LAMOUKI, A. & SHANAA, H. 1993. Analysis of impulsively loaded reinforced concrete structural elements—I. Theory. *Computers & Structures,* 48**,** 851-860.

KRISTOFFERSEN, M., PETTERSEN, J. E., AUNE, V. & BØRVIK, T. 2018. Experimental and numerical studies on the structural response of normal strength concrete slabs subjected to blast loading. *Engineering Structures,* 174**,** 242-255.

LAN, S., LOK, T.-S. & HENG, L. 2005. Composite structural panels subjected to explosive loading. *Construction and Building Materials,* 19**,** 387-395.

LANGDON, G., CANTWELL, W., GUAN, Z. & NURICK, G. 2014. The response of polymeric composite structures to air-blast loading: a state-of-the-art. *International Materials Reviews,* 59**,** 159-177.

LEE, S. K., CHEN, Z., NG, M., TANG, J., WAN, L., LIU, M. & LEE, L. 2008. Evaluation of CFRP, GFRP and BFRP Material Systems for the Strengthening of RC Slabs. *Journal of reinforced plastics and composites*.

LI, Q. & MENG, H. 2002. Pressure-impulse diagram for blast loads based on dimensional analysis and single-degree-of-freedom model. *Journal of engineering mechanics,* 128**,** 87-92.

LI, S., LI, X., WANG, Z., WU, G., LU, G. & ZHAO, L. 2017. Sandwich panels with layered graded aluminum honeycomb cores under blast loading. *Composite Structures,* 173**,** 242-254.

LI, S., WANG, Z., WU, G., ZHAO, L. & LI, X. 2014. Dynamic response of sandwich spherical shell with graded metallic foam cores subjected to blast loading. *Composites Part A: Applied Science and Manufacturing,* 56**,** 262-271.

LIBRESCU, L., OH, S.-Y. & HOHE, J. 2004. Linear and non-linear dynamic response of sandwich panels to blast loading. *Composites Part B: Engineering,* 35**,** 673-683.

LIMAM, O., FORET, G. & EHRLACHER, A. 2003. RC two-way slabs strengthened with CFRP strips: experimental study and a limit analysis approach. *Composite Structures,* 60**,** 467-471.

LIU, I., OEHLERS, D. J., SERACINO, R. & JU, G. 2006. Moment redistribution parametric study of CFRP, GFRP and steel surface plated RC beams and slabs. *Construction and Building Materials,* 20**,** 59-70.

LIU, X., TIAN, X., LU, T. & LIANG, B. 2014. Sandwich plates with functionally graded metallic foam cores subjected to air blast loading. *International Journal of Mechanical Sciences,* 84**,** 61-72.

LONGINOW, A. & ALFAWAKHIRI, F. 2003. Blast resistant design with structural steel. *Modern Steel Construction,* 43**,** 61-66.

LUCCIONI, B., AMBROSINI, R. & DANESI, R. 2004. Analysis of building collapse under blast loads. *Engineering structures,* 26**,** 63-71.

MALVAR, L. J. 1998. Review of static and dynamic properties of steel reinforcing bars. *Materials Journal,* 95**,** 609-616.

MALVAR, L. J. & CRAWFORD, J. E. 1998. Dynamic increase factors for concrete. Naval Facilities Engineering Service Center Port hueneme CA.

MALVAR, L. J., CRAWFORD, J. E., WESEVICH, J. W. & SIMONS, D. 1997. A plasticity concrete material model for DYNA3D. *International journal of impact engineering,* 19**,** 847-873.

MANUAL, A. U. S. 2000. Ansys inc. *Cannonsburg, PA.*

MAO, L., BARNETT, S., BEGG, D., SCHLEYER, G. & WIGHT, G. 2014. Numerical simulation of ultra high performance fibre reinforced concrete panel subjected to blast loading. *International Journal of Impact Engineering,* 64**,** 91-100.

MARCHAND, K., COX, P. & PETERSON, J. 1991. Blast analysis manual, Part I–Level of protection assessment guide–Key asset protection program construction option (KAPPCO). *Southwest Re-search Institute, Final report for the US Army Corps of Engineers, Omaha District.*

MAYS, G. 1995. *Blast effects on buildings: design of buildings to optimize resistance to blast loading,* Thomas Telford.

MEISAMI, M. H., MOSTOFINEJAD, D. & NAKAMURA, H. 2013. Punching shear strengthening of two-way flat slabs using CFRP rods. *Composite Structures,* 99**,** 112-122.

MERRIFIELD, R. 1993. *Simplified calculations of blast induced injuries and damage*, Health and Safety Executive, Technology and Health Sciences Division.

MOON, N. N. 2009. *Prediction of blast loading and its impact on buildings.* Doctoral dissirtation, NATIONAL INSTITUTE OF TECHNOLOGY ROURKELA.

MORI, L., LEE, S., XUE, Z., VAZIRI, A., QUEHEILLALT, D., DHARMASENA, K., WADLEY, H., HUTCHINSON, J. & ESPINOSA, H. 2007. Deformation and fracture modes of sandwich structures subjected to underwater impulsive loads. *Journal of mechanics of materials and structures,* 2**,** 1981-2006.

MOSALAM, K. M. & MOSALLAM, A. S. 2001. Nonlinear transient analysis of reinforced concrete slabs subjected to blast loading and retrofitted with CFRP composites. *Composites Part B: Engineering,* 32**,** 623-636.

MOSALLAM, A. S. & MOSALAM, K. M. 2003. Strengthening of two-way concrete slabs with FRP composite laminates. *Construction and Building Materials,* 17**,** 43-54.

MUKHOPADHYAYA, P. & SWAMY, N. 2001. Interface shear stress: a new design criterion for plate debonding. *Journal of Composites for Construction,* 5**,** 35-43.

MUSSELMAN, E. 2007. *Characterizing blast and impact resistance of long carbon fiber reinforced concrete.* The Pennsylvania State University.

MUSZYNSKI, L. C. & PURCELL, M. R. 2003. Composite reinforcement to strengthen existing concrete structures against air blast. *Journal of Composites for Construction,* 7**,** 93-97.

MUTALIB, A. A. & HAO, H. 2010. Numerical analysis of FRP-composite-strengthened RC panels with anchorages against blast loads. *Journal of Performance of Constructed Facilities,* 25**,** 360-372.

NAM, J.-W., KIM, H.-J., KIM, S.-B., YI, N.-H. & KIM, J.-H. J. 2010. Numerical evaluation of the retrofit effectiveness for GFRP retrofitted concrete slab subjected to blast pressure. *Composite Structures,* 92**,** 1212-1222.

NAYAL, R. & RASHEED, H. A. 2006. Tension stiffening model for concrete beams reinforced with steel and FRP bars. *Journal of Materials in Civil Engineering,* 18**,** 831-841.

NG, P. L., LAM, J. Y. & KWAN, A. K. 2010. Tension stiffening in concrete beams. Part 1: FE analysis. *Proceedings of the Institution of Civil Engineers: Structures and Buildings*.

NGO, T., MENDIS, P., GUPTA, A. & RAMSAY, J. 2007a. Blast loading and blast effects on structures–an overview. *Electronic Journal of Structural Engineering,* 7**,** 76-91.

NGO, T., MENDIS, P., GUPTA, A. & RAMSAY, J. 2007b. Blast loading and blast effects on structures–an overview. *Electronic Journal of Structural Engineering,* 7**,** 76-91.

OCHOLA, R., MARCUS, K., NURICK, G. & FRANZ, T. 2004. Mechanical behaviour of glass and carbon fibre reinforced composites at varying strain rates. *Composite Structures,* 63**,** 455-467.

ORTON, S. L., CHIARITO, V. P., RABALAIS, C., WOMBACHER, M. & ROWELL, S. P. 2014. Strain rate effects in CFRP used for blast mitigation. *Polymers,* 6**,** 1026-1039.

PANTUSO, A., NEUBAUER, U. & ROSTASY, F. Effects of thermal mismatch between FRP and concrete on bond. Minutes of 4th concretefibrecrete meeting, Lille, France, 2000.

PHAM, T. M. & HAO, H. Review of concrete structures strengthened with FRP against impact loading. Structures, 2016. Elsevier, 59-70.

PICHANDI, S., RANA, S., OLIVEIRA, D. & FANGUEIRO, R. 2013. Fibrous and composite materials for blast protection of structural elements—A state-of-the-art review. *Journal of Reinforced Plastics and Composites,* 32**,** 1477-1500.

QIU, X., DESHPANDE, V. & FLECK, N. 2004. Dynamic response of a clamped circular sandwich plate subject to shock loading. *Journal of Applied Mechanics,* 71**,** 637-645.

RABINOVITCH, O. & FROSTIG, Y. 2002. Strengthening of RC slabs with circular composite patches–a high-order approach. *Composite structures,* 55**,** 225-238.

RAJAMANI, A. & PRABHAKARAN, R. 1980. Response of composite plates to blast loading. *Experimental Mechanics,* 20**,** 245-250.

RAMAN, S. N., NGO, T. & MENDIS, P. 2011. A review on the use of polymeric coatings for retrofitting of structural elements against blast effects. *Electronic Journal of Structural Engineering,* 11**,** 69-80.

RAMANA, V., KANT, T., MORTON, S., DUTTA, P., MUKHERJEE, A. & DESAI, Y. 2000. Behavior of CFRPC strengthened reinforced concrete beams with varying degrees of strengthening. *Composites Part B: Engineering,* 31**,** 461-470.

RAZAQPUR, A. G., CONTESTABILE, E. & TOLBA, A. 2009. Experimental study of the strength and deformations of carbon fibre reinforced polymer (CFRP)

retrofitted reinforced concrete slabs under blast load This article is one of a selection of papers published in the Special Issue on Blast Engineering. *Canadian Journal of Civil Engineering,* 36**,** 1366-1377.

RAZAQPUR, A. G., TOLBA, A. & CONTESTABILE, E. 2007. Blast loading response of reinforced concrete panels reinforced with externally bonded GFRP laminates. *Composites Part B: Engineering,* 38**,** 535-546.

REDDIAR, M. K. M. 2010. *Stress-strain model of unconfined and confined concrete and stress-block parameters.* Texas A & M University.

REMENNIKOV, A. M. 2003. A review of methods for predicting bomb blast effects on buildings.

RIEDEL, W., THOMA, K., HIERMAIER, S. & SCHMOLINSKE, E. Penetration of reinforced concrete by BETA-B-500 numerical analysis using a new macroscopic concrete model for hydrocodes. Proceedings of the 9th International Symposium on the Effects of Munitions with Structures, 1999. Berlin-Strausberg Germany, 315-322.

RIISGAARD, B. Finite element analysis of Polymer reinforced CRC columns under close-in detonation. 6th European LS-DYNA Users' Conference, 2007.

RIISGAARD, B., NGO, T., MENDIS, P., GEORGAKIS, C. & STANG, H. Dynamic increase factors for high performance concrete in compression using split Hopkinson pressure bar. 6th International Conference on Fracture Mechanics of Concrete and Concrete Structures, 2007.

SAATCI, S. 2007. *Behaviour and modelling of reinforced concrete structures subjected to impact loads*.

SANGI, A. J. 2011. *Reinforced concrete structures under impact loads.* Heriot-Watt University.

SASTRANEGARA, A., ADACHI, T. & YAMAJI, A. 2005. Improvement of energy absorption of impacted column due to transverse impact. *International journal of impact engineering,* 31**,** 483-496.

SAYED-AHMED, E., BAKAY, R. & SHRIVE, N. 2009. Bond strength of FRP laminates to concrete: state-of-the-art review. *Electronic Journal of Structural Engineering,* 9**,** 45-61.

SEBASTIAN, W. M. 2001. Significance of midspan debonding failure in FRP-plated concrete beams. *Journal of Structural Engineering,* 127**,** 792-798.

SENA-CRUZ, J. 2005. *Strengthening of concrete structures with near-surface mounted CFRP laminate strips.* PhD, Universidade do Minho

SEYHAN, E. C., GOKSU, C., UZUNHASANOGLU, A. & ILKI, A. 2015. Seismic behavior of substandard RC columns retrofitted with embedded aramid fiber reinforced polymer (AFRP) reinforcement. *Polymers,* 7**,** 2535-2557.

SHAHAWY, M., BEITELMAN, T., AROCKIASAMY, M. & SOWRIRAJAN, R. 1996. Experimental investigation on structural repair and strengthening of damaged prestressed concrete slabs utilizing externally bonded carbon laminates. *Composites Part B: Engineering,* 27**,** 217-224.

SHIN, K.-J., JANG, K.-H., CHOI, Y.-C. & LEE, S.-C. 2015. Flexural Behavior of HPFRCC Members with Inhomogeneous Material Properties. *Materials,* 8**,** 1934-1950.

SIKADUR-31CF Product data sheet of Sikadur 31-CF.

SILVA, P. F. & LU, B. 2007. Improving the blast resistance capacity of RC slabs with innovative composite materials. *Composites Part B: Engineering,* 38**,** 523-534.

SIMONELLI, G. 2006. *Finite element analysis of RC beams retrofitted with fibre reinforced polymers.* Università degli Studi di Napoli Federico II.

SINHA, B., GERSTLE, K. H. & TULIN, L. G. Stress-strain relations for concrete under cyclic loading. Journal Proceedings, 1964. 195-212.

SOLIMAN, S. M., EL-SALAKAWY, E. & BENMOKRANE, B. 2010. Flexural behaviour of concrete beams strengthened with near surface mounted fibre reinforced polymer bars. *Canadian Journal of Civil Engineering,* 37**,** 1371-1382.

STANDARD, B. 1881. Part-116 (1983) Method for Determination of Compressive Strength of Concrete Cubes, London. *British Standard Institution*.

STANLEY, M., METZGER, J., MARTINEZ, R. & KOENIG, J. 2005. UL-like testing of commercial off-the-shelf products that enhance the blast and ballistic resistance of structures, quick look Report 2. *New Mexico Tech, Energetic Materials Research and Testing Center, Karagozian & Case, Burbank, CA*.

SU, H. & MCCONNELL, J. 2013. Energy Response of Idealized Composite Sandwich Panels under Blast Loads. *Journal of Engineering Mechanics,* 140**,** 20-30.

SU, R., SIU, W. & SMITH, S. T. 2010. Effects of bolt–plate arrangements on steel plate strengthened reinforced concrete beams. *Engineering Structures,* 32**,** 1769-1778.

TABATABAEI, Z. S., VOLZ, J. S., GLIHA, B. P. & KEENER, D. I. 2012. Development of long carbon fiber-reinforced concrete for dynamic strengthening. *Journal of Materials in Civil Engineering,* 25**,** 1446-1455.

TÄLJSTEN, B., CAROLIN, A. & NORDIN, H. 2003. Concrete structures strengthened with near surface mounted reinforcement of CFRP. *Advances in structural engineering,* 6**,** 201-213.

TEDESCO, J. W., MCDOUGAL, W. G. & ROSS, C. A. 1999. *Structural dynamics: theory and applications*, Addison-Wesley Menlo Park, CA.

TEKALUR, S. A., SHUKLA, A. & SHIVAKUMAR, K. 2008. Blast resistance of polyurea based layered composite materials. *Composite Structures,* 84**,** 271-281.

TENG, J., CHEN, J., SMITH, S. T. & LAM, L. 2003. Behaviour and strength of FRP-strengthened RC structures: a state-of-the-art review. *Proceedings of the institution of civil engineers-structures and buildings,* 156**,** 51-62.

THIAGARAJAN, G., HSIA, K. & WALTERS, W. Blast simulation of armor plate behavior using the virtual internal bond model. 16th ASCE Engineering Mechanics Conf., Seattle, USA, 2003.

UEDA, T. 2004. Standard Specifications for Concrete Structures-2002. *JSCE, Hokosha Co., Ltd, Japan***,** 24-32.

VO, T., GUAN, Z., CANTWELL, W. & SCHLEYER, G. 2012. Low-impulse blast behaviour of fibre-metal laminates. *Composite Structures,* 94**,** 954-965.

WANG, E., GARDNER, N. & SHUKLA, A. 2009. The blast resistance of sandwich composites with stepwise graded cores. *International Journal of Solids and Structures,* 46**,** 3492-3502.

WANG, S.-Y. & WANG, Z.-Y. 2013. Mechanism of improving ductility of high strength concrete T-section beam confined by CFRP sheet subjected to flexural loading. *Journal of Central South University,* 20**,** 246-255.

WANG, Z., LU, Y., HAO, H. & CHONG, K. 2005. A full coupled numerical analysis approach for buried structures subjected to subsurface blast. *Computers & Structures,* 83**,** 339-356.

WU, C., OEHLERS, D., REBENTROST, M., LEACH, J. & WHITTAKER, A. 2009. Blast testing of ultra-high performance fibre and FRP-retrofitted concrete slabs. *Engineering structures,* 31**,** 2060-2069.

WU, C., OEHLERS, D. J., WACHL, J., GLYNN, C., SPENCER, A., MERRIGAN, M. & DAY, I. 2007. Blast testing of RC slabs retrofitted with NSM CFRP plates. *Advances in Structural Engineering,* 10**,** 397-414.

WU, H. & GILBERT, R. 2008. An experimental study of tension stiffening in reinforced concrete members under short-term and long-term loads. *UNICIV Report no*.

YI, N.-H., KIM, J.-H. J., HAN, T.-S., CHO, Y.-G. & LEE, J. H. 2012. Blast-resistant characteristics of ultra-high strength concrete and reactive powder concrete. *Construction and Building Materials,* 28**,** 694-707.

YOO, D.-Y. & YOON, Y.-S. 2014. Influence of steel fibers and fiber-reinforced polymers on the impact resistance of one-way concrete slabs. *Journal of Composite Materials,* 48**,** 695-706.

YOUSSEF, M. N., FENG, M. Q. & MOSALLAM, A. S. 2007. Stress–strain model for concrete confined by FRP composites. *Composites Part B: Engineering,* 38**,** 614-628.

YUSOF MA, N. N., ISMAIL A, ET AL 2010. Development of blast resistant concrete. *J Defense Secur,* 1**,** 238–250.

ZHANG, S. S., YU, T. & CHEN, G. 2017. Reinforced concrete beams strengthened in flexure with near-surface mounted (NSM) CFRP strips: Current status and research needs. *Composites Part B: Engineering,* 131**,** 30-42.

ZHOU, X., KUZNETSOV, V., HAO, H. & WASCHL, J. 2008. Numerical prediction of concrete slab response to blast loading. *International Journal of Impact Engineering,* 35**,** 1186-1200.

APPENDICES

Appendix A: The experimental results obtained from the impact test on slabs MC2 and MS2.

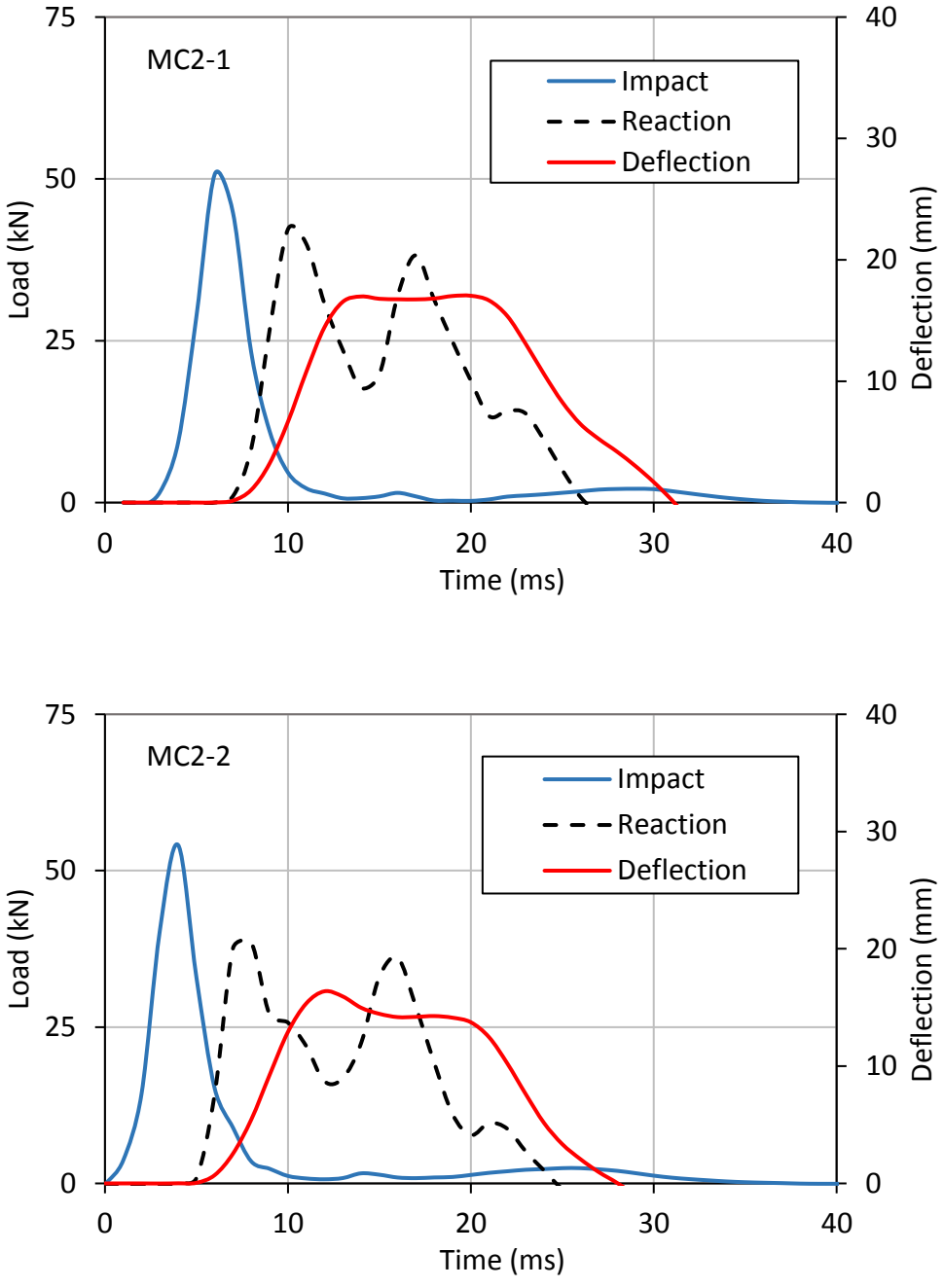

Figure A. 1: Time history profile of the impact load, reaction and deflection of cases MC2-1 and MC2-2 during the first deflection phase.

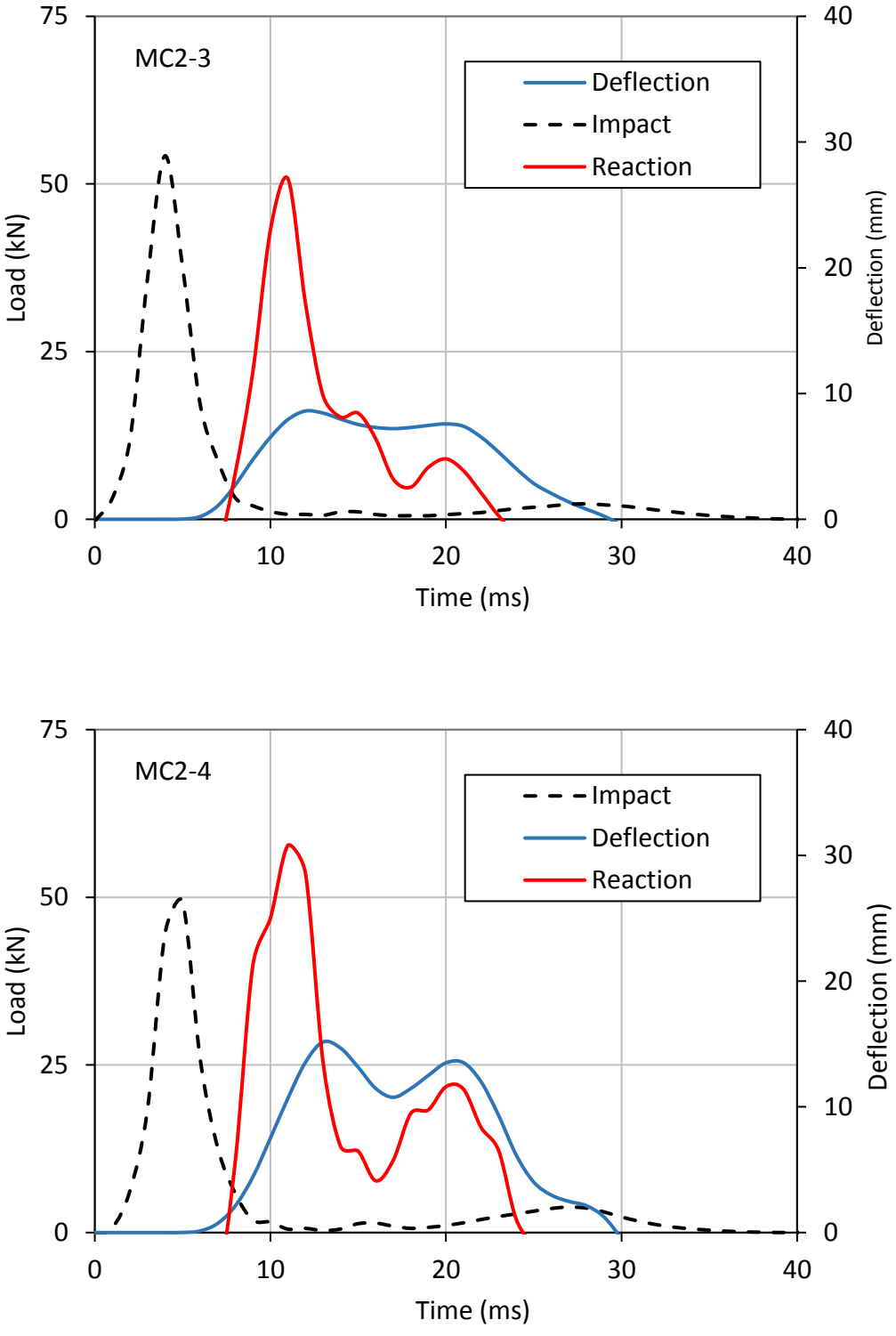

Figure A. 2: Time history profile of the impact load, reaction and deflection of cases MC2-3 and MC2-4 during the first deflection phase.

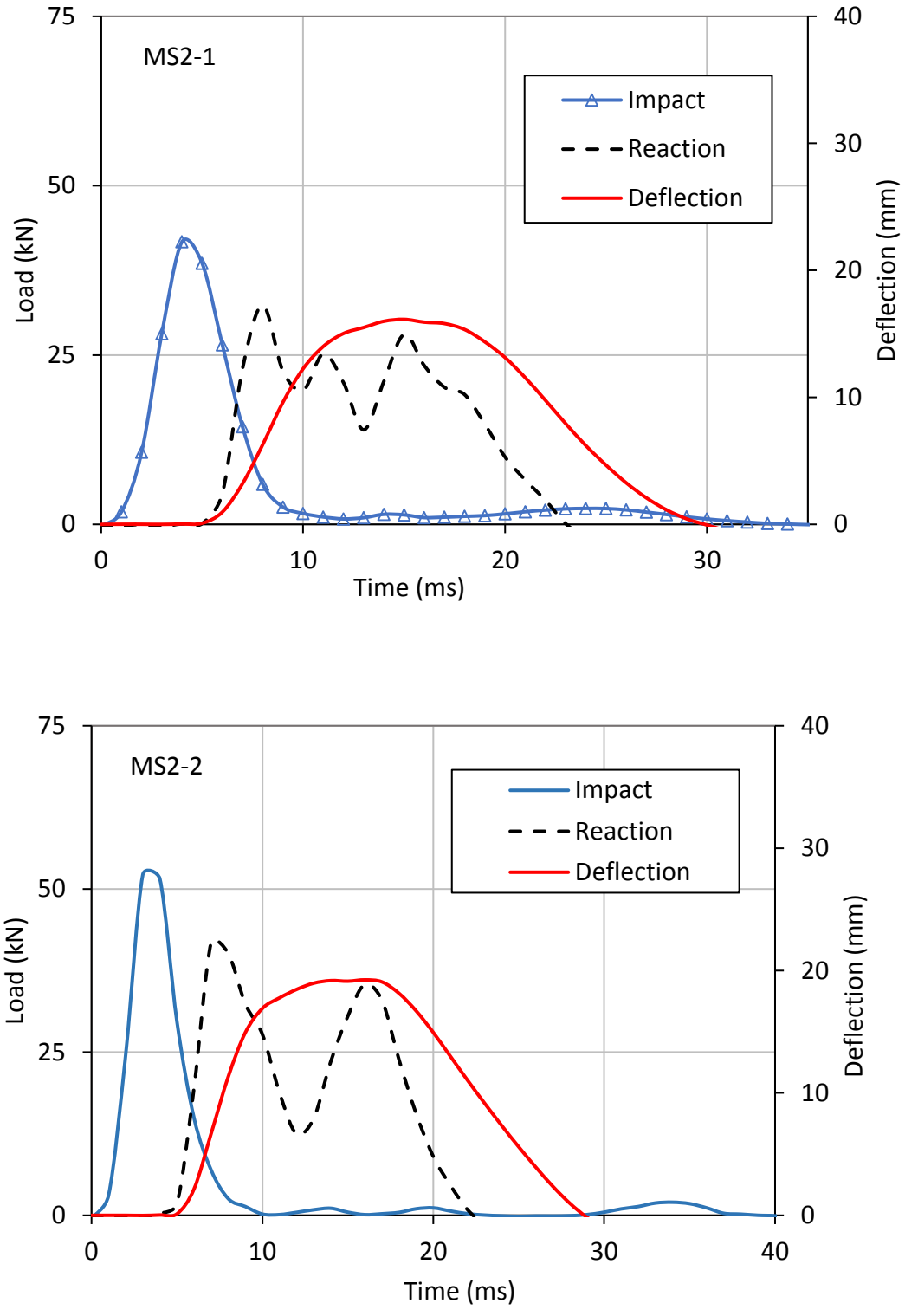

Figure A. 3: Time history profile of the impact load, reaction and deflection of cases MS2-1 and MS2-2 during the first deflection phase.

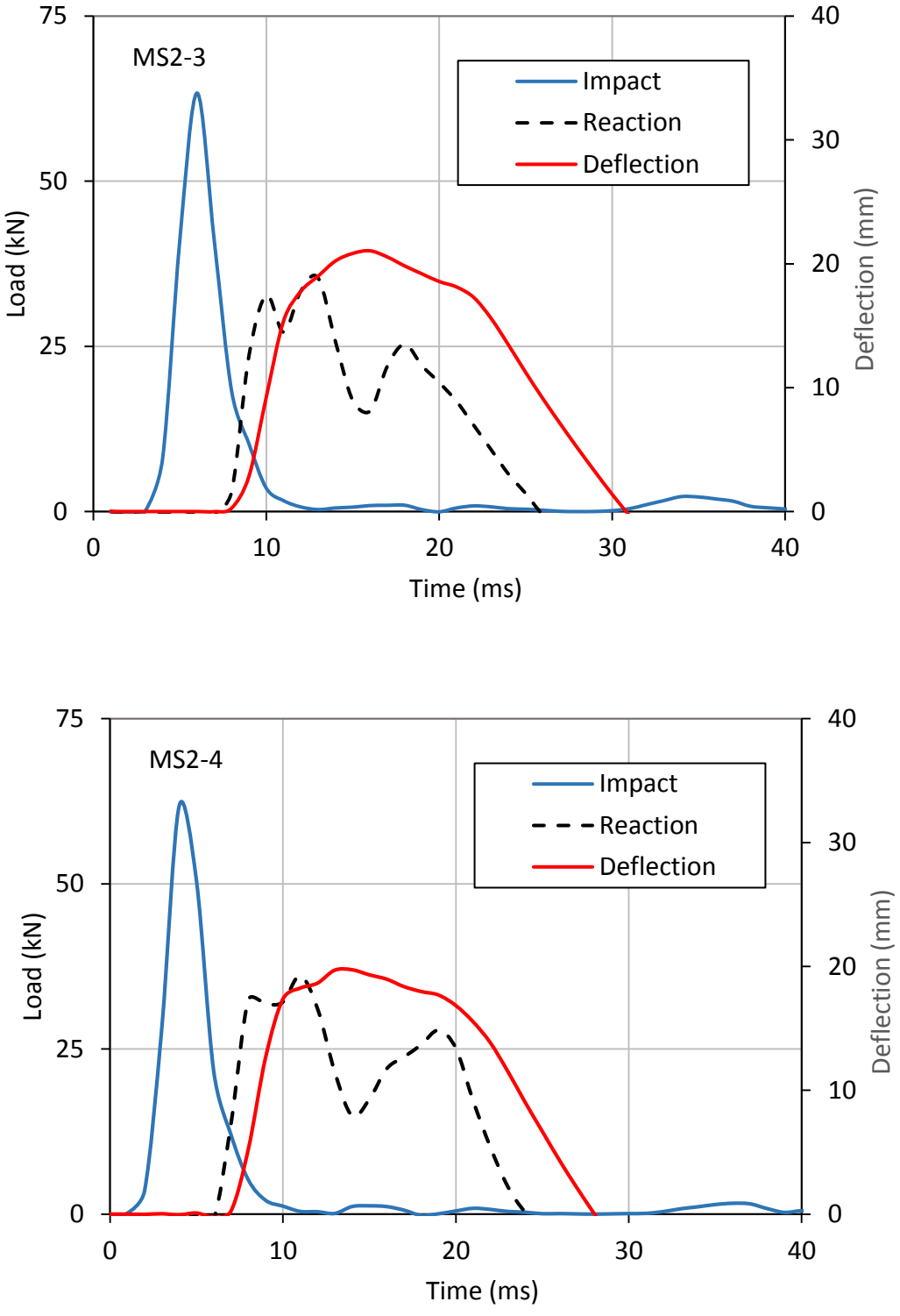

Figure A. 4: Time history profile of the impact load, reaction and deflection of cases MS2-3 and MS2-4 during the first deflection phase.

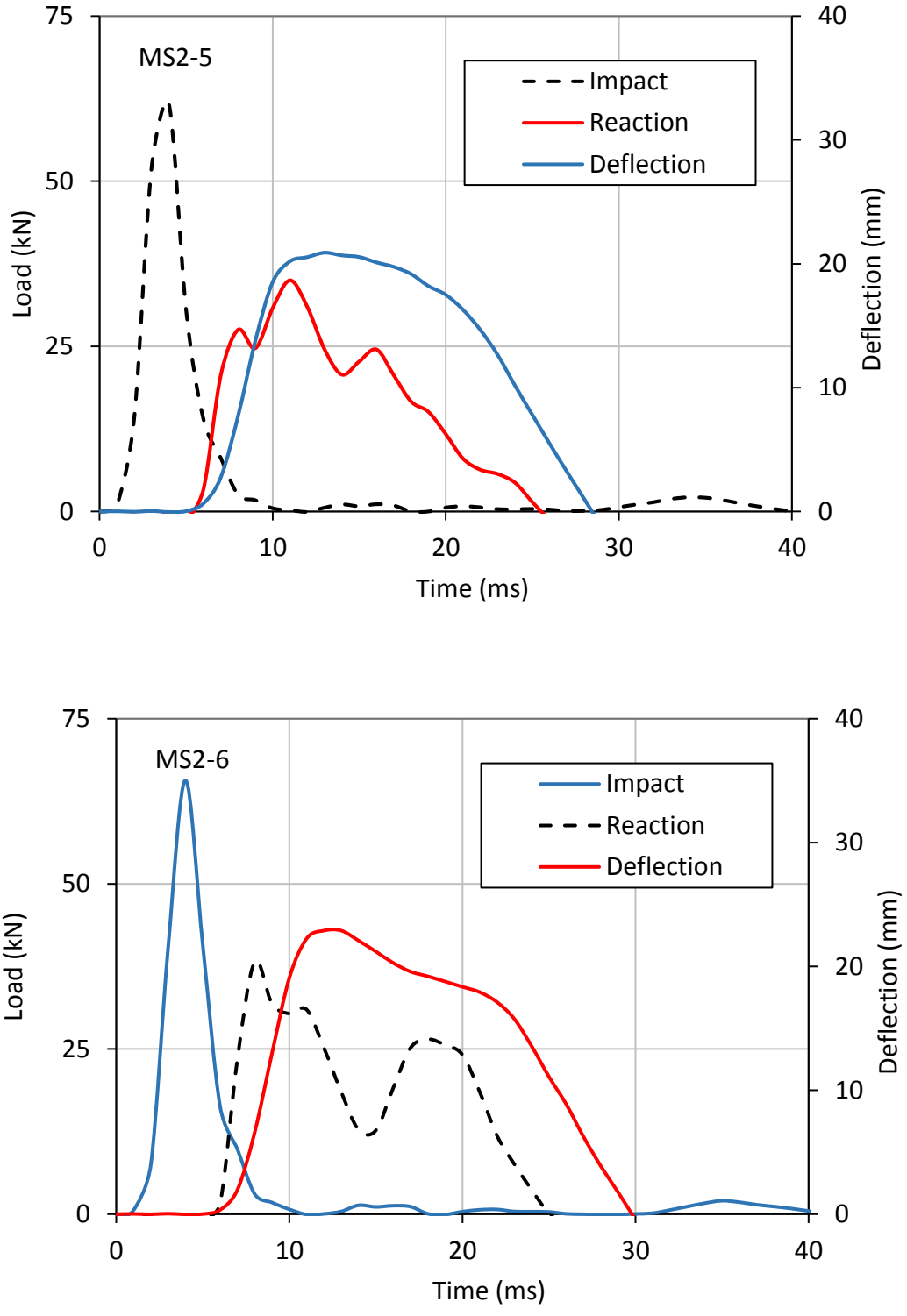

Figure A. 5: Time history profile of the impact load, reaction and deflection of cases MS2-5 and MS2-6 during the first deflection phase.

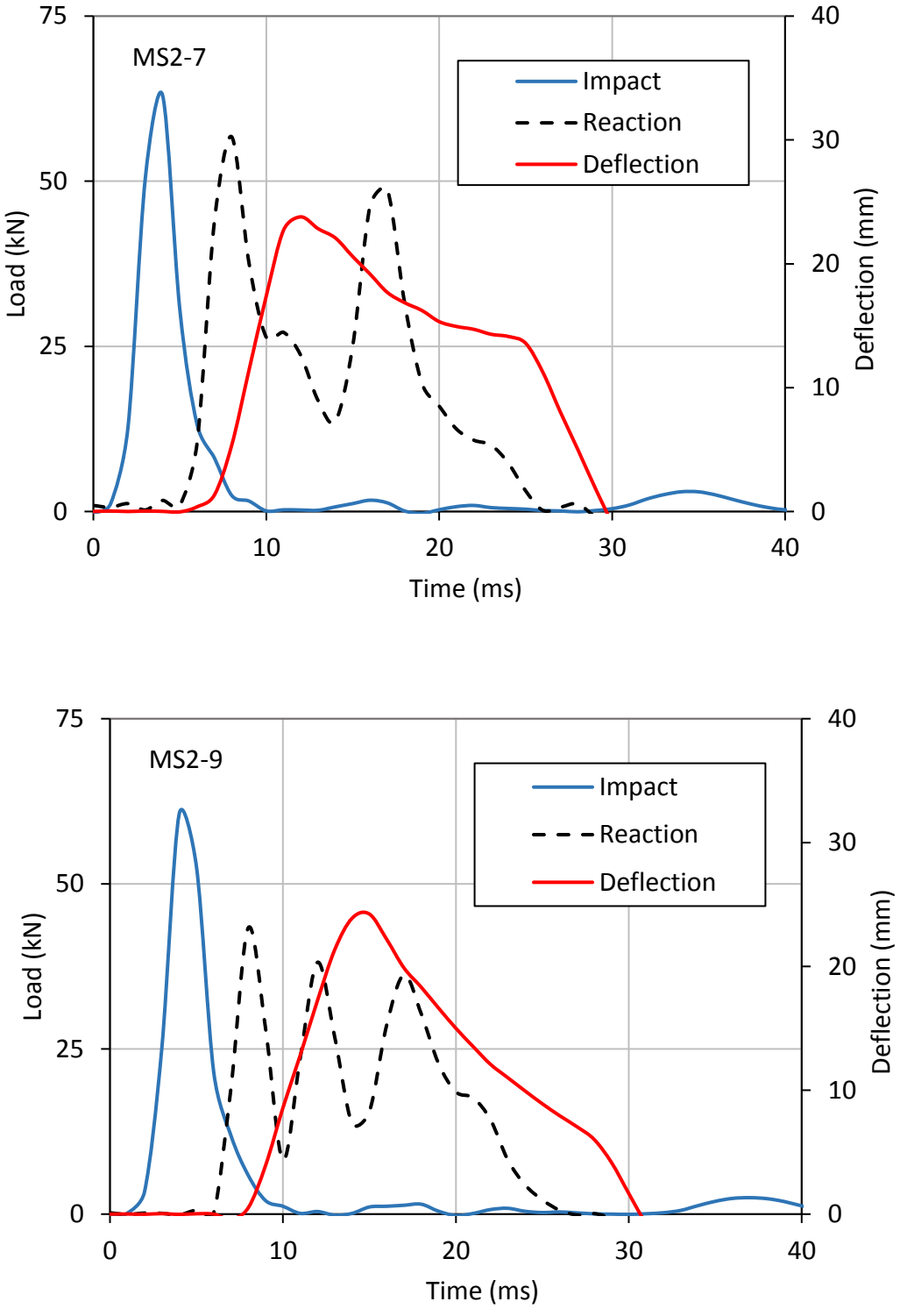

Figure A. 6: Time history profile of the impact load, reaction and deflection of cases MS2-7 and MS2-9 during the first deflection phase.

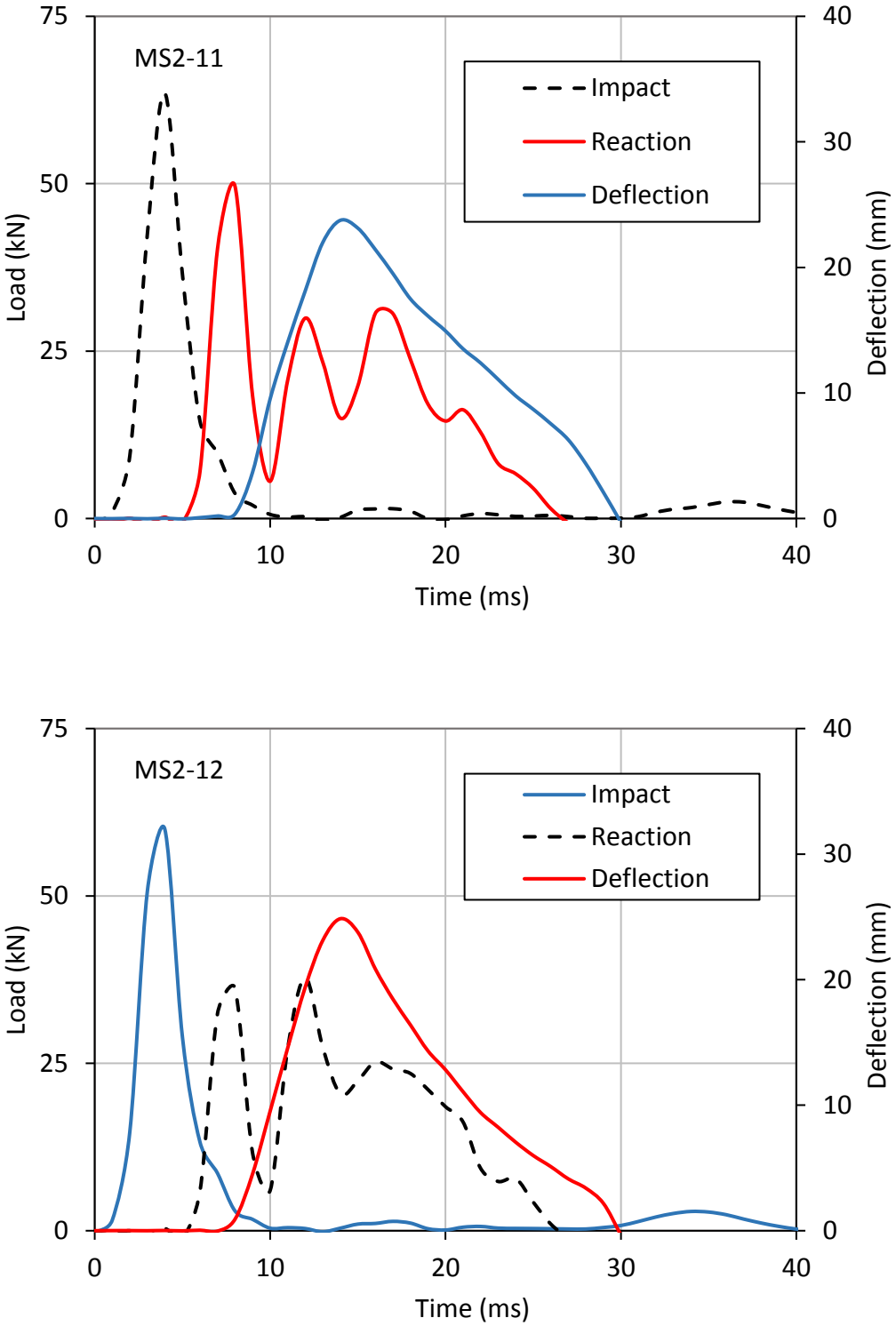

Figure A. 7: Time history profile of the impact load, reaction and deflection of cases MS2-11 and MS2-12 during the first deflection phase.

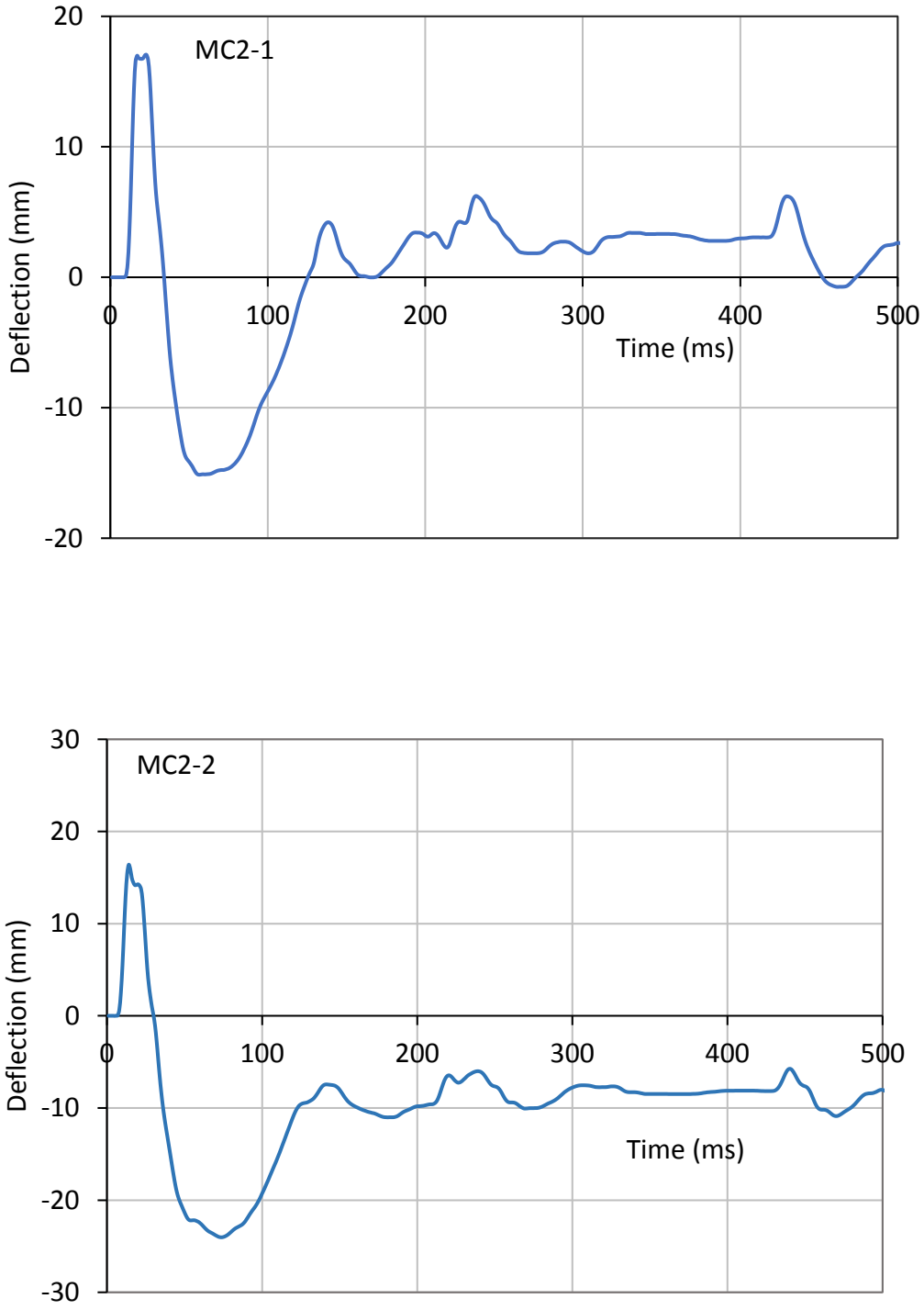

Figure A. 8: The hystorical deflection wave of the control slab (MC2) for the first and the second impact drops.

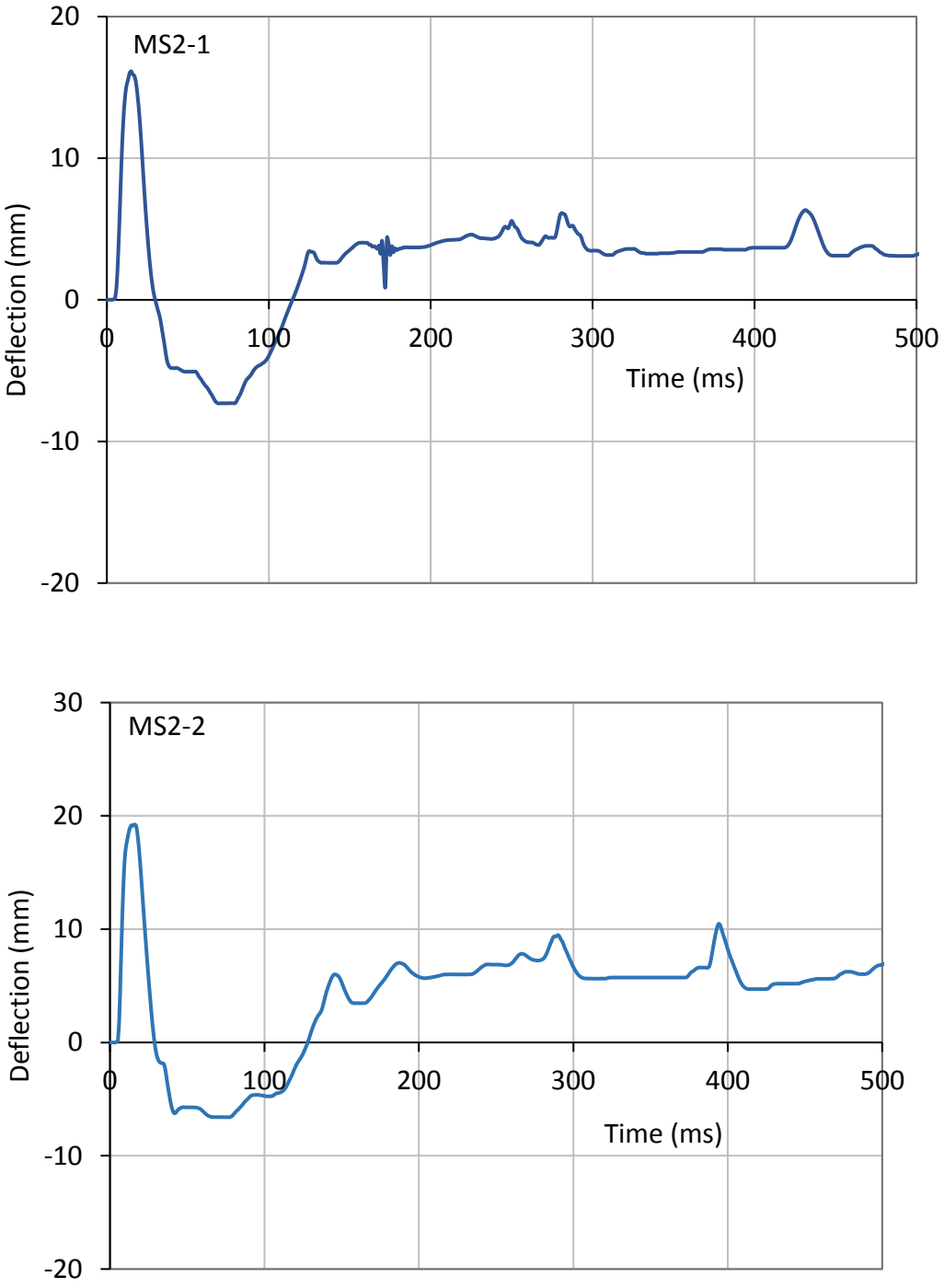

Figure A. 9: The hystorical deflection wave of the strengthened slab (MS2) for the first and the second impact drops.

Table A. 1: Results of the impact tests on the control slab MC2 under different impact drops.

Description		MC2-1	MC2-2	MC2-3	MC2-4
Maximum deflection Δ_{max} in each impact blow (mm)		17.04	16.38	16.15	15.16
Residual deflection Δ_{res} (mm)		5.7	9.36	5.1	3.58
Final deflection (mm)		23.74			
Ratio of the absorbed energy ((Δ_{max}-Δ_{res})/Δ_{max}) %		0.67	0.43	0.68	0.76
Based on reaction-deflection curve	Total Reaction-deflection energy (J)	525.3	462	450	309.3
	Accumulated total energy (J)	1746.66			
	Absorbed energy	349.6	198	307.9	236.3
	Dissipated energy (J)	175.7	264	142.1	73
	Accumulated Dissipated energy (J)	654.9			

Table A. 2 Results of the impact tests on the control slab MS2 under different impact drops.

Description		MS2-1	MS2-2	MS2-3	MS2-4	MS2-5	MS2-6	MS2-7	MS2-8	MS2-9	MS2-10	MS2-11	MS2-12
Maximum deflection Δ_{max} in each impact blow (mm)		16.1	19.1	21.1	19.7	20.9	22.9	23.8	23	24.2	23	23.8	24.9
Residual deflection Δ_{res} (mm)		4.2	6.9	7.2	3.7	5.0	5.0	4.1	5.7	3.4	2	2.1	1.7
Final deflection (mm)		51.04											
Ratio of the absorbed energy (Δ_{max}-$\Delta_{res}/\Delta_{max}$) %		0.74	0.64	0.66	0.81	0.76	0.78	0.83	0.75	0.86	0.91	0.91	0.93
Based on reaction-deflection curve	Total Reaction-deflection energy (J)	349	585	567	579	512	692	877	500	625	450	482	565
	Accumulated total energy (J)	6782.35											
	Absorbed energy	257	375	373	470	389	540	725	376	537	411	438	528
	Dissipated energy (J)	92	210	194	109	123	151	152	124	88	39	43	38
	Accumulated Dissipated energy (J)	1361.9											

Table A. 3: The maximum deflection and the dissipated energy of each slab at the end of the impact test on slabs MC2 and MS2.

Slab	MC2	MS2
Accumulated deflection	23.7	51.0
Accumulated dissipated energy	655	1362
Enhancement ratio of the dissipated energy %	2.08	

Appendix B: Design of the specimens

Specification of the specimens:

In designing the specimes in the experimental part of the current study, the following points were considered:

1- The specimens were cast as one way slab with the geometrical dimention of 1000 x 500 x 50 mm as small scale specimens.
2- The specimens were reinforced by using 7 deformed steel bars with diameter of 6 mm. This reinforcement provides reinforcing area of 197mm^2 in the cross section of the specimen which is equivalent to a reinforcing ratio of 0.0078 (0.78%).
3- For the strengthened specimens, the specimens were post strengthened (after reached to the hardening state) by using CFRP bars with size of 4 mm.

Justification of the selected specifications:

The following factors were considered in designing the specimens:

1- The specimens should be lightweight to be easy to move and lift them without the need to any havy lifting machine. This helps to speed up the test.
2- The specimens should have limited strength capasity for both the yielding and the ultimate resistance under static and dynamic conditions. This is attributed to the limitation in the capasity of the instruments (load cells, LVDT) available in the lab where most of them having load capasity of about 80-100 kN. Also due to the limitation in the capasity of the equipments used in the test such as the airbag rig and the impact test equipment where the weight and the hight available in the dropping mass test were limited.
3- Size of the steel and CFRP bars should be compatible with the thickness and the concrete cover that available in the specimens. So, size of 6 and 4mm were selected for the steel and the CFRP bars as the thickness of the slab was selected to be 50mm.

4- The strengthening approach should be applied after the concrete in the specimen get hard. This is necessary as the aim of the study is to strengthening the existing (old) buildings where the blast resistance was encountered in their design.

5- A Sufficient bonding area for each bar should be ensured to avoid any debonding failure that might occurs in both the steel or the CFRP as the debonding failure or slipping of the bars was not considered in this study.

6- The steel reinforcing ratio should be within the range between the minimum and the maximum ratio As the main aim in this study is to enhance the flexural resistance of the one-way slab in terms of the load capacity, ductility and the dissipated energy. Steel ratio very close to the minimum ratio should be avoided as no spare ductility available in the slab to be targeted by strengthening the compression face of the slab. Also, reinforcing ratio close to the maximum ratio should be avoided as it increasing the shear stresses in the slab which has limited shear resistance. Based on that, steel ratio of 0.78% was taken in the design.